Metrology with trapped atoms on a chip using non-degenerate and degenerate quantum gases

Vincent Dugrain

LABORATOIRE KASTLER BROSSEL
LABORATOIRE DES SYSTÈMES DE RÉFÉRENCE TEMPS–ESPACE

THÈSE DE DOCTORAT DE
L'UNIVERSITÉ PIERRE ET MARIE CURIE

Spécialité : Physique Quantique
École doctorale de Physique de la Région Parisienne - ED 107

Présentée par
Vincent Dugrain

Pour obtenir le grade de
DOCTEUR de l'UNIVERSITÉ PIERRE ET MARIE CURIE

Sujet :

Metrology with Trapped Atoms on a Chip using Non-degenerate and Degenerate Quantum Gases

Soutenue le 21 Décembre 2012 devant le jury composé de:

M.	Djamel	ALLAL	Examinateur
M.	Denis	BOIRON	Rapporteur
M.	Frédéric	CHEVY	Président du jury
M.	Jozsef	FORTAGH	Rapporteur
M.	Jakob	REICHEL	Membre invité
M	Peter	ROSENBUSCH	Examinateur

Remerciements

Mes premiers remerciements s'adressent à mes deux encadrants de thèse, Jakob Reichel et Peter Rosenbusch. Jakob, mon directeur de thèse, pour m'avoir initié à la beauté des atomes froids sur puce puis intégré dans son équipe en tant que doctorant. J'ai bénéficié de ses multiples conseils, expérimentaux et autres. Aux côtés de Peter, responsable de la manip Horloge sur Puce au Syrte, j'ai énormément appris, des astuces expérimentales aux conseils de présentation orale en passant par la gestion de projet. La relation de confiance que nous avons su développer au cours de ces trois années a été un élément important pour l'établissement d'une ambiance de travail agréable et stimulante.

Je voudrais en second lieu exprimer ma gratitude envers les membres de mon jury pour avoir accepté de prendre part à mon évaluation en cette dangeureuse journée de fin du monde: les rapporteurs, Joszef Fortagh et Denis Boiron, ainsi que Frédéric Chevy et Djamel Allal.

Les membres de l'équipe TACC méritent une mention toute particulière, et pas seulement pour leur qualités artistiques: Wilfried Maineult, notre post-doc, collègue plein de ressources ayant toujours un sujet de discussion nouveau sous la main; Christian Deutsch pour m'avoir passé les rênes de la manip avec succès; Ramon Szmuk, mon successeur sur la manip, à qui je souhaite bonne chance pour sa thèse. Konstantin Ott nous a également rejoint vers la fin de ma thèse et c'était un plaisir d'interagir avec lui. J'en profite pour féliciter également les premiers contributeurs au projet, Friedmann Reinhard, Clément Lacroûte et Fernando Ramirez, pour avoir construit une expérience remarquable dont la stabilité m'étonne encore. J'ai, indirectement, beaucoup profité de votre ingéniosité et de vos efforts, ils ont largement permis l'acquisition des résultats présentés dans cette thèse. Les stagiaires de notre équipe, Itamar Sivan, Philip Oertle, Thomas Chaigne, Constantin De Guerry, Barbara Bensimon ont aussi contribué à leur échelle et je les en remercie.

J'ai eu la chance de passer ces trois années de thèse en interaction très forte avec les membres de deux laboratoires: le SYRTE et le LKB. Je tiens à remercier leurs directeurs respectifs, Noël Dimarcq pour l'un et Paul Indelicato ainsi que Antoine Heidmann pour l'autre, pour m'y avoir accueilli. Il est difficile de citer sans en oublier tous les chercheurs, personnels, post-doc et étudiants qui ont contribué de près ou de loin au bon déroulement de cette thèse. De manière générale, je remercie toutes ces personnes pour leur disponibilité et leur accueil. Je me contenterai d'une liste non exhaustive, en commençant, côté SYRTE, par Sébastien Bize et Rodolphe Letargat pour, entre autres, leurs precieux conseils quant a ma soutenance. Les discussions -scientifiques ou autres- avec Andre Clairon, Giorgio Santarelli (il vous dira qu'il n'a pas le temps mais le prendra quand meme), Pierre Ulrich (ou le gardien de la variance d'Allan), Arnaud Landragin, Yann Le Coq (expert en formation express sur les cavites optiques), Franck Pereira Dos Santos (un style inimitable), Michel Abgrall, Emeric Declerq,

Daniele Rovera (un collègue du weekend), Carlos Garrido Alzar, Philippe Laurent, Stefane Guerandel, Christine Guerlin, Joseph Ashkar, John MacFerran ont été particulièrement formatrices. D'autres membres ont été la pour un échange de materiel, une discussion, un café ou simplement un sourire: Ouali Acef, Marie-Christine Angonin, Christian Borde, Nicola Chiodo, Baptiste Chupin, Luigi De Sarlo, Pacôme Delva, Jocelyne Guéna, Jerôme Lodewyck, Sébastien Merlet, Frédéric Menadier, Philippe Tuckey, Peter Wolf, Natascia Castagna, Yves Candela, Berangère, Daniele Nicolodi. Mentions speciales pour leur disponibilité et leur réactivité, ce qui rend la vie de laboratoire plus agréable: aux membres du service électronique, Jose Pintos-Fernandes, Laurent Volodimer, Jean-Francois Roig et Michel Lours (la bonne humeur incarnée); à ceux du service informatique: Gilles Sakoun (le sherif) et Pascal Blondé; aux membres du service administratif: Marine Pailler, Anne Quezel et Pascale Michel; au service Ultravide et Mécanique: Annie Girard, Florence Cornu, David Holleville, Bertrand Venon, Jean-Pierre et Jean-Jacques. Je voudrais remercier les gens de la cantine (mention speciale a Corinne) et de l'accueil, qui contribuent largement à la bonne ambiance au sein de l'Observatoire.

Il est difficile de ne pas mentionner le fabuleux groupe de doctorants du SYRTE, en croissance exponentielle lors de mes années de thèse, qui contribuent pour beaucoup au cadre de travail chaleureux et accueillant du laboratoire. D'abord les "'vieux"' que j'ai vu soutenir, Thomas Lévèque, Philippe Westergaard, Arnaud Lecaillier, Sinda Mejri, Amale Kanj, Quentin Bodard, Sophie Pelisson, Olga Kozlova entre autres. Les "'jeunes"', que je remercie notamment pour la prise en charge du pot de thèse: Adèle Hilico, Anthony Bercy, Jean-Marie Danet, Indranil Dutta, Tristan Farah, Mikhail Gurov, Jean Lautier, Mathieu Meunier, Bruno Pelle, Rinat Tyumenev, Wenhua Yan. Bon vent à chacun pour la thèse.

Côté LKB, j'aimerais remercier tout particulièrement les membre de l'équipe Microcircuits à Atomes: Jérôme Éstève (la force tranquille) et Alice Sinatra, notamment pour m'avoir guidé dans la compréhension des BECs, Romain Long pour la préparation à la soutenance, et, pêle-mêle, les collègues post-docs et doctorants avec qui j'ai eu beaucoup de plaisir a travailler: Jürgen Volz, Roger Gehr, Kenneth Maussang, Guillhem Dubois, Dominique Maxein, Florian Haas, Benjamin Besga, Claire Lebouteiller, Krzysztof Pawlowski, Sébastien Garcia, Hadrien Kurkjian. J'exprime également ma reconnaissance aux personnes du service administratif, notamment Christophe Bernard, Thierry Tardieu et Dominique Delande, et à Jean-Michel Isaac du service mécanique.

J'ai eu l'occasion d'interagir avec de nombreux chercheurs d'autres laboratoires que je ne pourrai pas tous citer. Je voudrais simplement mentionner ici la contribution de Christophe Texier au calcul du bruit associé aux pertes d'atomes et l'en remercier.

Je voudrais remercier Coralie (mon canard en sauce) et Clément pour la relecture de ce manuscript. J'en profite pour remercier les amis de la chorale de La Clé des Chants Ensemble, et son chef de choeur Benoît, non seulement pour la performace remarquable lors du pot de la soutenance, mais aussi pour tous les bons moments passés pendant et après les répétitions: Élodie, Christophe, Anne, Stéphanie, Etienne, Christian, Morganne, Pascal, Gilles, Constance... et les autres. Je veux aussi mentionner la bande des gros, j'ai nommé Adam, Gatien, Rémi (un hommage particulier pour ses nombreuses citations non publiées) et les compatriotes du Master élargi. Merci aux copains venus du Grand Nord et d'ailleurs pour leur virées impromptues a Paris.

Je voudrais remercier ma famille pour leur soutien sans faille au cours de cette thèse: mes parents Jean-Pierre et Edith pour leur présence affectueuse et indéfectible, les brozers Olivier et Francois ainsi que leur tribus respectives: Cris et Mowgli, Sophie et Swann. Grosse pensée pour Marie, je suis sûr que tu aurais adoré être là.

Enfin je voudrais remercier tout spécialement ma fiancée Amrit pour les longues heures passées à relire le manuscript et corriger les trop nombreuses erreurs d'anglais, pour sa patience, mais surtout pour avoir constamment été là pendant ces trois ans.

Contents

Introduction

Atomic clocks have undergone tremendous development over the past 60 years. They give a good illustration of the application of quantum physics to everyday life. Mobile phone networks, for example, are synchronized to the signal of atomic clocks. Satellite navigation is another prime example. By equipping each satellite with a set of atomic clocks the Global Positioning System (GPS) can localize, by triangulation, a point on Earth to a resolution of a few meters. Fast and reliable telecommunication is increasingly at the core of society and the need for stable frequency references will certainly continue to grow in the future.

Atomic clocks also provide today's best primary frequency standards: since 1968 the SI second has been defined as the *duration of 9 192 631 770 periods of the radiation corresponding to the transition between the two hyperfine levels of the ground state of the caesium 133 atom* [1]. This definition was refined in 1997 to account for recent technical advances by underlining that *this definition refers to a caesium atom at rest at a temperature of 0 K* [2]. Nowadays, the SI second is realized by atomic fountains operating in various places around the world. The fantastic accuracy of these devices has other interests for fundamental physics: for example, in the accurate measurement of the ground state hyperfine splitting [3] or constraining the temporal variations of fundamental constants [4].

The search for ultimate accuracy is not yet over. Currently the most accurate fractional frequency measurements are obtained on optical transitions in trapped neutral ensembles or single ions. With stabilities of $3 \times 10^{-15}/\sqrt{\tau}$ these systems can reach total uncertainties in the 3×10^{-17} range [5, 6]. It becomes possible to observe the change of an atom's frequency occurring during a displacement of 33 cm in the Earth's gravitational field [7]. In the future these devices could be used to map the gravitational field around a planet [8].

Besides these extremely accurate devices there are atom clocks, although more modest in performance, that have greater potential to be made compact. Based on well-established technologies, the aim is to be able to industrially produce these compact devices for them to be used in onboard systems such as satellites, submarines or space missions [9]. Several projects (references will be given later in this manuscript) are currently under development that all target the realization of liter-sized devices with frequency stabilities in the low $10^{-13}/\sqrt{\tau}$.

The Trapped Atom Clock on a Chip (TACC) is one such project. At its core, cold ^{87}Rb atoms are trapped below a micro-structured chip and interrogated by a microwave signal. Numerous properties motivate the selection of ^{87}Rb: its collision properties, favorable for both cooling and spectroscopy: a rather large hyperfine splitting; the possibility for magnetic trapping; the existence of a magic field around which the clock frequency dependence on the magnetic field cancels to first order. Structurally the atom chip is the key for compactness:

technologies for cooling, trapping, interrogating and manipulating atoms are progressively integrated [10], as witnessed by the on-chip microwave guide used in our experiment.

However, TACC is not only an atomic clock, it is also a dedicated system for fundamental studies and for developing tools to manipulate atoms. Among other features it offers the possibility to work with either non-degenerate (thermal clouds) or degenerate quantum gases (Bose-Einstein condensates or BECs). This property makes it the ideal experiment for assessing the potential of each of these two regimes for time metrology, and, more widely, for high-resolution measurements. As shown in the work of my predecessors [11] thermal clouds can be operated in a regime where the exchange collisions keep the atomic spins synchronized for extremely long times, in the order of one minute. BECs obey a dramatically different physics: given their much higher typical densities (typically a factor ~ 100 higher than thermal clouds), interactions become dominant and can no longer be treated as a perturbation. As strongly correlated systems, they also constitute a good starting point for quantum metrology beyond the standard quantum limit.

Another open question is the application of the long interrogation times to portable atom interferometers with large sensitivities: atomic clocks, but also atomic force sensors (gravimeters, gyrometers, magnetometers) or more practical devices such as portable powermeters.

This thesis aims to make several contributions to the growing field of on-chip atom clocks and interferometers. It reports a number of metrology experiments carried out with trapped cold atoms on a chip, with either non-degenerate or degenerate quantum gases. These experiments range from fundamental studies of atomic properties to the development and demonstration of tools for producing and manipulating atoms on a chip.

This manuscript is organized as follows:

- We begin by introducing the global context of on-chip metrology with trapped atoms. After recalling the founding principles of time and frequency metrology and the current status of compact atomic frequency references we briefly present the concept of magnetic microtraps for neutral atoms. We expose the properties of ^{87}Rb among which is the existence of a pseudo-magic magnetic trap. Finally, we describe the two main effects of atomic interactions: the frequency collisional shift and the identical spin rotation effect (ISRE).

- The second chapter deals with experimental methods. We give a description of the setup and focus on the special features of our experiment. We describe in particular two double-state detection methods, one of which was established during this thesis. As we work with very dilute traps, the existence of residual cloud oscillations in the clock interrogation trap becomes an issue that we also discuss.

- The third chapter is a characterization of the frequency stability of the clock operated with non-condensed gases. The clock frequency is affected by technical noise that is under investigation. After a description of the analysis tools we list all known mechanisms that produce noise on the clock frequency. We then report on our experimental investigation of the noise sources and amplitudes. Our research points out the existence of shot-to-shot fluctuations of the cloud temperature and places upper bounds on several other contri-

butions. We finally present the best clock stability observed so far and suggest ideas for the next steps of the characterization.

- Degenerate gases is the focus of the fourth chapter. We study the potential of Bose-Einstein condensates for metrology. BECs are useful resources in the case of high spatial resolution measurements and entanglement-assisted quantum metrology. The study starts with the measurement and modeling of the state-dependent spatial dynamics, a well-known phenomenon in BECs. One consequence of the dynamics is the modulation of the Ramsey contrast in time, as it depends on the wavefunction overlap between the two states. The coherence of BECs is studied as a function of the interrogation time, atom number and clock frequency spatial inhomogeneity. We show evidence for noise in the data that could be related to an elongation of the collective spin state in the Bloch sphere.

- In the fifth chapter we report on the manipulation of the atomic external state by inhomogeneous interrogation fields. This study was carried out with thermal clouds. We show an illustration of pulse engineering used to control the red/blue sideband asymmetry. In the non-sideband resolved case we observe interferences between atoms transferred on the carrier and on the sideband.

- In the sixth chapter we give an experimental proof-of-principle of the realization of an atomic microwave powermeter by characterizing the response of our system over a microwave power range of 80 dB. This work employs the concept of using trapped atoms as a microwave power (secondary in our case) standard which could, in the long term, be useful in metrology applications.

- Finally, in the seventh chapter we report on the experimental investigation of fast alkali pressure modulation under ultra-high vacuum conditions. Modulating the alkali pressure above 1 Hz is a conceptually simple technique for boosting the repetition rate of cold-atom based systems. One of its requirements is the design of fast sources. We demonstrate the realization of a device for modulating the pressure modulation on the 100 ms timescale and loading of a MOT (magneto-optical trap) within 1.2 s. Both the short and the long term behavior of the source are investigated. Adsorption and desorption processes appear to play a major role and will be considered. We also present alternative fast sources based on laser-heated and reduced thermal mass rubidium dispensers.

Chapter 1

Atom trapping on a chip: a tool for metrology

This chapter aims to provide the reader with an introduction to the founding concepts of the Trapped Atom Clock on a Chip (TACC). We will begin with a brief discussion of the basic principles and advantages of atomic time keeping and will include an overview of compact atomic clocks with specific focus on the benefits of trapped atoms for application in metrology. We will then describe the idea of atom trapping on microstructures, also called atom chips. In trapped atom clocks interactions play a leading role, this will be referred to and expanded upon in the concluding part of this chapter. In particular we will focus on two effects that play crucial roles in our experiment: the collisional shift of the clock frequency and the identical spin rotation effect.

1.1 Basic concepts of time metrology

1.1.1 Atomic clocks

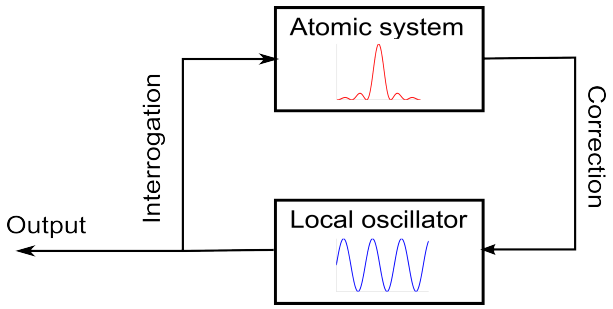

Figure 1.1: *Locking principle of an oscillator on a atomic resonance. This scheme illustrates the basic principle of atomic clocks. The locked local oscillator provides the useful signal.*

An atomic clock is essentially constituted of two elements: a local oscillator and an atomic reference. The general idea is to lock the local oscillator frequency f_{LO} on an atomic transition of frequency f_{at}. The response of the atom gives the difference between the two frequencies which is used as an error signal (figure 1.1). Ideally, the frequency of the local oscillator reproduces the atomic frequency exactly.

An atomic transition is the most stable frequency reference currently available. This is because it does not drift in time due to the fact that atoms are stable objects within the limit of their radioactive disintegration time (47.5×10^9 yr for ^{87}Rb). The atomic transition is selected to have a very narrow natural linewidth such that the width of the spectroscopy is limited by the interrogation time (Fourier-limited). The atomic response is the dependance of the state populations on the detuning $f_{at} - f_{LO}$, and changes with the interrogation scheme (Ramsey or Rabi spectroscopy). To make the atomic response as steep as possible, and thus provide the most sensitive frequency measurement, long interrogations times are needed.

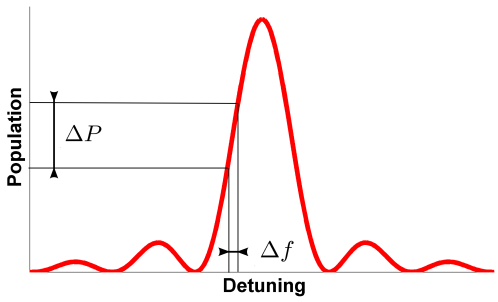

Figure 1.2: *Example of the atomic response in the case of Rabi interrogation. Long interrogation times are needed to make the atomic response steep and provide high sensitivity to frequency changes.*

The resolution we are able to achieve when measuring an atomic frequency is fundamentally limited by the atomic shot noise. However, in the real world, the atomic line position can fluctuate under the influence of interatomic interactions or external fields causing fluctuations of the local oscillator frequency.

Clock accuracy and clock stability When the clock is locked, the local oscillator frequency can be written

$$f_{LO}(t) = f_{at}\left[1 + \epsilon + y(t)\right], \tag{1.1}$$

where $y(t)$ may fluctuate, but its average is equal to 0. The *accuracy* of the clock is the error of the offset ϵ: this denotes how well the clock reproduces the atomic frequency of the atom isolated from the outside world. The ability to build accurate ^{133}Cs clocks is one reason for its choice as the international time reference. Primary frequency standards need to be accurate clocks.

The fluctuating part $y(t)$ characterizes the *stability* of the clock. It must be as small as possible. It is fundamentally limited by the atomic shot noise, which arises from the measurement process.

A clock with unknown accuracy but with $y(t)$ of small amplitude and averaging to zero can be used as a secondary frequency standard. Such a clock delivers a signal at the clock frequency $f_{at}(1+\epsilon)$. The offset ϵ can be calibrated against a primary standard. In fact most applications

of atomic clocks require frequency stability rather than accuracy since they can be calibrated periodically. The Trapped Atom lock on a Chip aims to be a highly stable secondary frequency standard.

1.1.2 Atom-field interaction

The interaction between the local oscillator and the atom is treated in the near-resonant case. The atom can be reduced to the 2 clock levels and the general theory of a two-level atom interacting with an electromagnetic field applies. We call Ω the Rabi frequency of the atom/field coupling, and $\delta = f_{LO} - f_{at}$ the detuning.

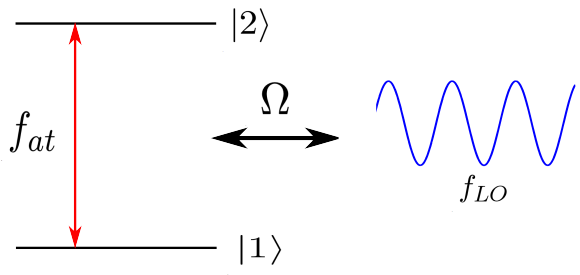

Figure 1.3: *Model of the two-level atom interacting with an electromagnetic field. Ω is the Rabi frequency.*

1.1.3 Ramsey and Rabi spectroscopy

Two interrogation schemes are commonly used [12].

- **Rabi** spectroscopy involves interrogating the atoms with one pulse of constant amplitude and duration T. The atomic response, defined as the probability of the atom to transfer from state $|1\rangle$ to state $|2\rangle$ is given by

$$P_2 = \frac{\Omega^2}{\Omega^2 + 4\pi^2\delta^2} \sin^2\left(\sqrt{\Omega^2 + 4\pi^2\delta^2}\frac{T}{2}\right). \tag{1.2}$$

- **Ramsey** interrogation consists of applying two short pulses separated by a free evolution time T_R. The pulses used have an area of $\pi/2$. If the pulse durations are omitted the atomic response is given by

$$P_2 = \frac{1}{2}\left[1 + \cos\left(2\pi\delta T_R\right)\right] \tag{1.3}$$

In the Bloch sphere picture, the first pulse of the Ramsey interrogation is equivalent to placing the atom in the equatorial plane. During the Ramsey time, T_R, the atom evolves freely corresponding to a precession of the pseudospin along the equator at the frequency f_{at}. The second pulse converts the accumulated phase into population difference of $|1\rangle$ and $|2\rangle$.

For equal interrogation times the Ramsey method provides an atomic response ~ 1.6 times more sensitive to frequency changes than the Rabi scheme. Another major advantage of the

Ramsey interrogation is that the atom is not subject to the interrogation field during the phase evolution (to our level of approximation Ω does not appear).

1.1.4 Compact frequency references

In this section we provide an overview of the various different types of compact atomic clocks and their applications in order to give the reader a broader perspective of our continued interest in researching and building atomic clocks.

Applications of compact atomic clocks

Global positioning system Now available in almost every car or smartphone, GPS consists of a set of satellites that continuously broadcast their position and time, exact to a billionth of a second. A GPS receiver takes this information and uses it to calculate the car's or phone's position on the planet. For this it compares its own time with the time sent by three satellites. This method requires that both the satellites and the receiver carry clocks of remarkable accuracy. However, by picking up a signal from a fourth satellite the receiver can compute its position using only a relatively simple quartz clock. To ensure time accuracy each satellite carries four atomic clocks, which are periodically re-calibrated when passing over the control stations [13].

Very Large Baseline Interferometry This is a technique that uses distant antennas pointing to the same radiofrequency stellar source (for example quasars) to increase angular resolution. The useful information is contained in the difference of the signal arrival times on each of the two antennas. These arrival times need to be known accurately on both remote devices. The needs, in terms of clock stability, are so stringent that most stations use hydrogen masers for the synchronization [14].

Geophysics Atomic clocks may be applied and utilized in studies of the Earth's rotation and the movements of tectonic plates for earthquake detection. [9].

Other fields such as space missions, meteorology and environment (monitoring of the atmosphere) might also benefit from the development of compact atomic frequency references [9]. There is no doubt that further applications of compact and stable atomic clocks will appear in the future.

Current status of compact atomic clocks

In this subsection we do not provide a complete overview of the field of compact atomic clocks, rather, we focus on a few projects that target performances similar to ours in terms of size and frequency stability.

Pulsed, optically pumped clock (INRIM) This clock is composed of a vapor cell placed in a microwave cavity. It uses the Ramsey scheme with interrogation times of a few milliseconds due to the short coherence time of the atoms. First, an intense laser pulse pumps the atoms into one of the two states. The microwave transition is driven and a second laser pulse detects the atomic population. Recently, a short-term stability of $1.7 \times 10^{-13}/\sqrt{\tau}$ was demonstrated,

with an integrated instability of $\sim 5 \times 10^{-15}$ and drifts below $\sim 10^{-14}$ per day [15].

Coherent population trapping (CPT) These clocks also interrogate the hyperfine transition in an atomic vapor. They do not involve microwaves but two phase-coherent laser beams that are detuned by the clock frequency. Under these conditions the atoms can be pumped into a dark state where their resonance peaks sharply and may be used for locking the local oscillator. The SYRTE CPT clock is operated in pulsed mode for a reduced sensitivity to laser power. Its latest status is a short term stability of $7 \times 10^{-13}/\sqrt{\tau}$ integrating down to $4 \times 10^{-14}/\sqrt{\tau}$ [16].

Trapped mercury ion clock This project is being developed at the Jet Propulsion Laboratory. Mercury ions are captured in a linear multipole trap, where microwave spectroscopy of the hyperfine transition is performed. The population is detected with a discharge lamp. In the last publication (2009) [17], a short-term stability of $2 \times 10^{-13}/\sqrt{\tau}$ was reported , integrating down to $\sim 10^{-15}$ in one day for a $\sim 3\,\mathrm{L}$ physics package.

Cold atoms in an isotropic cavity (HORACE) This project is being developed at SYRTE. The basic idea is to use a spherical cavity to both cool and interrogate the atoms. Optical molasses is created inside the cavity and a Ramsey spectroscopy is performed on the free falling atoms. Atoms are recaptured at the end of each cycle and cycle times of 80 ms can be achieved. The current status of this project is a short term stability of $2.2 \times 10^{-13}/\sqrt{\tau}$, limited by the atomic shot noise, and frequency instability of $\sim 3 \times 10^{-15}$ after 10^4 seconds of integration [18].

The TACC project also targets a stability of $\gtrsim 10^{-13}/\sqrt{\tau}$. As explained later in this thesis, the discovery of the effect of spin self-rephasing [11, 19] gives hope that this target may even be surpassed. In the next section we discuss the advantages and drawbacks of using trapped atoms for metrology.

1.1.5 Using trapped atoms for metrology

The interest of using trapped atoms for metrology lies in the long interrogation times that can be achieved whilst keeping the system compact. However, special traps must be engineered in order to disturb the two clock states energies in the same way, as we will see in this section. Traps also enable one to cancel the atom's recoil from the interrogation photon as in optical clocks.

Extended interrogation times

In atomic fountains the atoms are under free fall. The upper limit of the interrogation time is given by the size of the apparatus. By launching the atoms up against gravity one can gain a factor of 2, but the slow scaling of the free fall time $t = \sqrt{2h/g}$ with the size of the apparatus h makes it hard to gain. We note, however, that recently an atomic fountain exceeding 10 m was proposed for testing general relativity [20, 21].

By trapping the atoms one can achieve arbitrarily long interrogation times. The new limitations to the interrogation time become the coherence time of the superposition (T_2^* in the language of the nuclear magnetic resonance), the lifetime of the atomic trapped cloud, the natural linewidth of the transition or the coherence time of the local oscillator.

Cancelation of the effect of the trap on the clock frequency

Magic traps for accurate clocks Atom trapping consists of giving the atomic state's energy a spatial dependance while metrology implies insensitivity to external fields. The apparent contradiction can be solved if we consider situations where the energy varies with the external field *for both clock states in the same way.* In such a trap the *energy difference* between the two clock states becomes insensitive to the trapping field to first order, and the frequency of the trapped atom is identical to the atomic frequency in free space (see figure 1.4). Such traps are called *magic traps*, and are the primary requirement in achieving clock accuracy.

A magic optical trap can be created by choosing a *magic* wavelength [22] at which both clock states have identical electric polarizabilities. For microwave clocks (typically Cs or Rb) there have been proposals to combine the polarization of the trapping light with a magnetic field in order to eliminate the effect of the optical trap on the clock frequency [23], however, this is at the expense of an increased magnetic field sensitivity.

Magic traps for stable clocks The clock stability at the standard quantum limit is proportional to $1/C$ where C is the fringe contrast. When operating with thermal atomic clouds one faces the issue of atom dephasing. In this regime the atoms are all independent and the precession speed in the Bloch sphere is different for each of them: it depends on the clock frequency landscape experienced by an atom during its trajectory. As time passes atoms will dephase from each other which will reduce the contrast of the Ramsey fringes. Dephasing is greatly reduced in a magic trap as a result of the clock frequency being independent of position (or atom's coordinates). Magic traps are tools for building stable clocks.

A second feature of magic traps is that they make the clock frequency insensitive to fluctuations of the external field, leading to a reduction in the technical noise associated with these fluctuations.

Pseudo-magic traps We define a *pseudo-magic trap* as a trap that possesses the following two properties: (1) no dephasing and (2) clock frequency insensitivity to changes of the trap amplitude, but does not reproduce the free-space frequency (see figure 1.4). Such a trap is the starting point for constructing a secondary frequency standard: (1) high clock quality factors are accessible as a result of long dephasing times and (2) the clock frequency is insensitive to trap magnitude fluctuations, which removes a source of technical noise.

This gives the philosophy of the Trapped Atom Clock on a Chip (TACC). As mentioned, TACC relies on the existence of a pseudo-magic magnetic trap for ^{87}Rb, the details of which are elaborated on further in this manuscript.

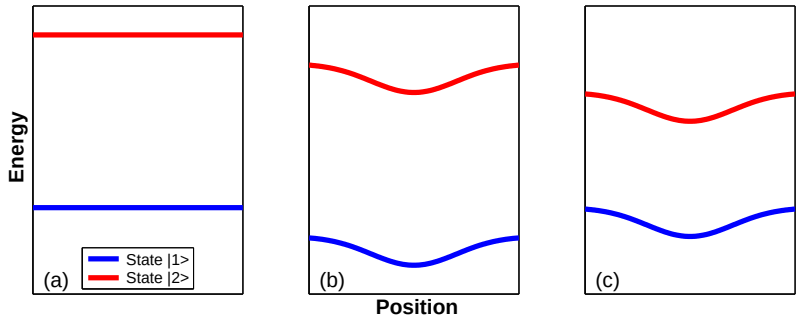

Figure 1.4: *(a) Atomic levels in free space. (b) A magic trap reproduces the free space atomic frequency. (c) A pseudo-magic trap does not reproduce the free space atomic frequency.*

Cancelation of the photon recoil

When an atom emits or absorbs a photon of wave vector $\mathbf{k}$ from a plane wave, it recoils with the momentum $\hbar\vec{k}$. This recoil can provoke a Doppler shift of the atomic transition frequency and introduce a bias on the frequency measurement. This recoil effect can be inhibited [24] if the trap frequency $\omega/(2\pi)$ and the mass of the atoms m obey (Lamb-Dicke regime):

$$\eta = \sqrt{\frac{\hbar k^2}{2m\omega}} \ll 1. \tag{1.4}$$

η is the Lamb-Dicke parameter.

Operating in such a regime is particularly crucial for clocks based on optical transitions, for which the recoil momentum is 10^5 times larger than for a microwave clock. This is one reason for choosing optical traps for such clocks, with typical trap frequencies of 100 kHz.

For a microwave clock, the Lamb-Dicke condition is less stringent and magnetic traps, which are typically less confining than optical traps, can be used. In the case of ^{87}Rb, a trap frequency of 10 Hz gives a Lamb-Dicke parameter of 3×10^{-4}.

1.2 Neutral atom trapping on a chip

This section will include a brief account of the principles of magnetic trapping of neutral atoms with particular consideration of ^{87}Rb for which a pseudo-magic magnetic trap exists. We will also give an overview of the basic concept of atom trapping on chips including examples of some trap configurations.

1.2.1 Magnetic trapping

Neutral atoms interact with the magnetic field via their magnetic dipole moment $\boldsymbol{\mu}$. In low magnetic fields (i.e. causing energy shifts much smaller than the hyperfine splitting) the atomic dipole moment is directly proportional to the total angular momentum $\mathbf{F}$ with the

proportionality constant $-\mu_B g_F$ (g_F is the Lande factor). The interaction energy in a magnetic field $\mathbf{B}$ takes the form

$$U = -\boldsymbol{\mu} \cdot \mathbf{B} = \mu_B g_f \mathbf{F} \cdot \mathbf{B} = \mu_B g_F m_F |B|. \tag{1.5}$$

Maxwell's equations allows only the existence of local minima of the magnetic field B in space. Thus, only atoms with a magnetic dipole moment antiparallel to the field (low field seekers) can be trapped, in minima of the magnetic field.

To keep the atoms in the trap, it is important that their dipole moment adiabatically follows the local direction of the magnetic field. The criteria is that the rate of change of the field's direction θ (in the reference frame of the moving atom) must be smaller than the Larmor frequency [10]:

$$\frac{d\theta}{dt} \ll \omega_L = \frac{\mu_B |g_F| B}{\hbar}. \tag{1.6}$$

In regions of very small magnetic fields this condition is violated, resulting in atom losses (Majorana losses).

1.2.2 A pseudo-magic trap for ^{87}Rb

Equation 1.5 is only approximate, and a rigorous derivation of the magnetic energy must include the hyperfine splitting. For states of $J = 1/2$, the hamiltonian can be diagonalized analytically and leads to the Breit-Rabi formula, which gives the eigenenergies as a function of the magnetic field. At low fields, the eigenstates are very close to the $|F, m_F\rangle$ states, and in the rest of the manuscript they are considered as equal.

The magnetic energy of the two trappable states $|1\rangle = |F = 1, m_F = -1\rangle$ and $|2\rangle = |F = 2, m_F = 1\rangle$ can be calculated. In particular there is a field B_m around which the energy of these two states have identical dependence to the magnetic field to first order. Around this *magic field* the corresponding energies can be expanded:

$$U_1(\mathbf{r}) = \alpha_m B(\mathbf{r}) + h\beta_1 (B(\mathbf{r}) - B_m)^2 \tag{1.7}$$

$$U_2(\mathbf{r}) = A_2 - A_1 + \alpha_m B(\mathbf{r}) + h\beta_2 (B(\mathbf{r}) - B_m)^2. \tag{1.8}$$

Here $A_2 - A_1 = \Delta E_{hfs} + h\Delta f_0$, where $\Delta E_{hfs}/h = 6.834\,682\,\mathrm{GHz}$, $\alpha_m = 1.001\,661 \times \mu_B/2$, $\Delta f_0 = -4497.31\,\mathrm{Hz}$ and $\beta = \beta_2 - \beta_1 = 431.3596\,\mathrm{Hz\,G^{-2}}$. The value of the magic field is $B_m = 3.228\,917\,\mathrm{G}$ [25].

The transition frequency between these two states reads

$$f_{|1\rangle \to |2\rangle} = \frac{\Delta E_{hfs}}{h} + \Delta f_0 + \beta (B(\mathbf{r}) - B_m)^2. \tag{1.9}$$

At B_m the magnetic trap is a pseudo-magic trap. It has features of both low dephasing and first order magnetic insensitivity of the transition frequency. It is the configuration of our experiment.

The atomic system The Trapped Atom Clock on a Chip uses ^{87}Rb atoms and the pair of states $|1\rangle$ and $|2\rangle$. Besides the existence of a magic field for this transition ^{87}Rb is also relatively convenient for laser and evaporative cooling, possesses a rather large hyperfine splitting and scattering lengths are almost equal for both states.

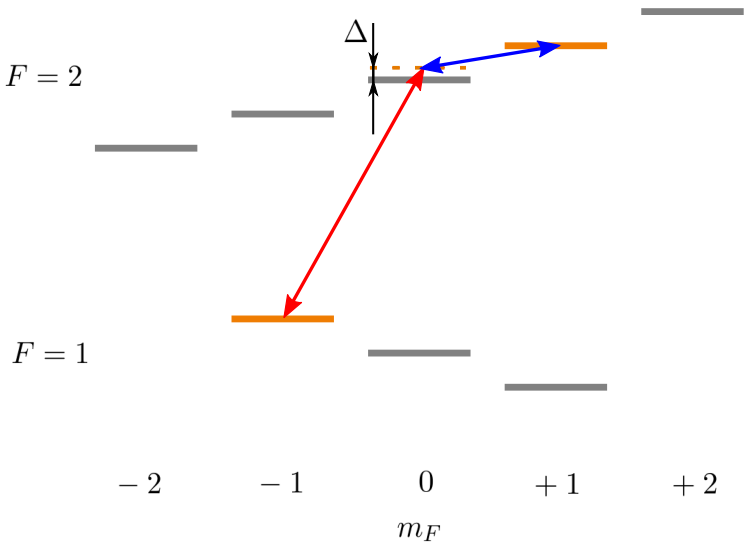

Figure 1.5: *Energy diagram of the hyperfine structure of ^{87}Rb in presence of a quantization magnetic field. Our two clock levels are displayed in orange. The transition can be addressed by the combination of two signals: microwave (red) and radiofrequency (blue). Both are detuned from the intermediate level (dashed orange) by* $\Delta \simeq +500\,\mathrm{kHz}$.

The transition between $|1\rangle$ and $|2\rangle$ must be addressed by two photons, each of them detuned from an intermediate level. We typically detune the two signals by 500 kHz from the $|F = 2, m_F = 0\rangle$ level. The total Rabi frequency of the coupling Ω can be expressed as a function of the one-photon Rabi frequencies Ω_{mw} and Ω_{rf} [26]:

$$\Omega = \frac{\Omega_{mw}\Omega_{rf}}{2\Delta}. \tag{1.10}$$

1.2.3 Magnetic microtraps

Atom trapping by a wire

An infinite wire carrying a current I produces a magnetic field of amplitude $B(r) = \mu_0 I/(2\pi r)$. When a homogeneous external field, B, perpendicular to the current flow is added the total magnetic field cancels at the point $z_0 = \mu_0 I/(2\pi B)$. Around this point the total magnetic field is a 2 dimensional quadrupole in which atoms can be confined.

Quadrupole trap

Confinement in the third direction can be obtained by adding two wires perpendicular to the first wire with contrapropagating currents. These wires add a field gradient in the x direction. A more convenient configuration is to use a single wire in a U shape in place of the three wires.

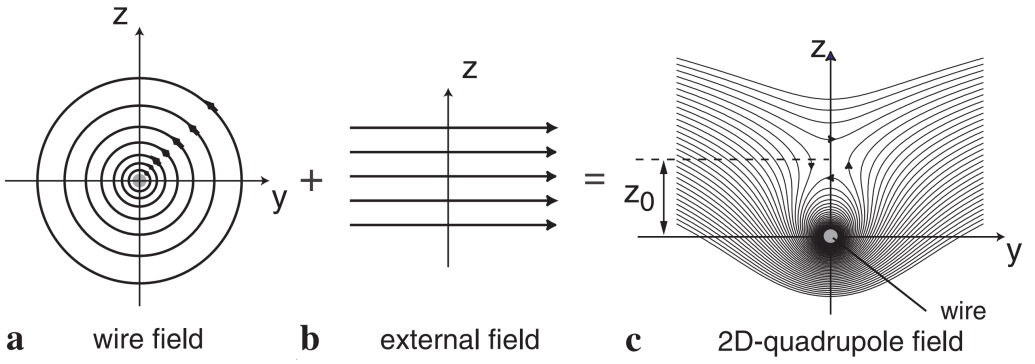

Figure 1.6: *A single wire carrying a current (a) combined with a homogeneous magnetic field (b) creates a 2 dimensional quadrupole magnetic trap (c). Figure taken from [27].*

A U wire combined with a homogeneous field provides a 3D quadrupole field: it is used to form the magneto-optical trap.

Dimple trap

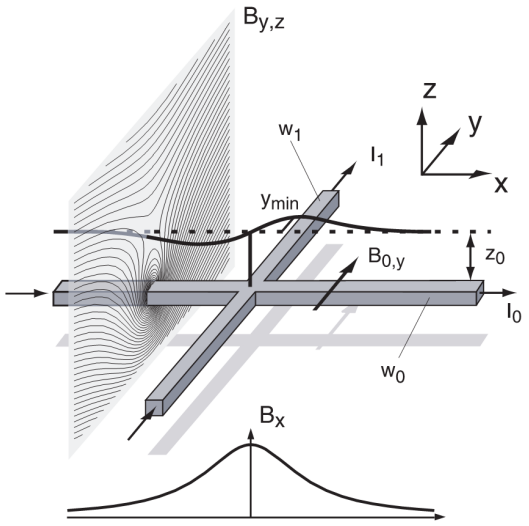

Figure 1.7: *Scheme of the dimple trap. The current I_0 combined to the homogeneous field B_y creates a 2-D quadrupole trap identical to figure 1.6. The current I_1 creates a field gradient along x and modifies the position of the field minimum along y (plain line). The dashed line indicates the field minimum for $I_1 = 0$. Here the potential is repulsive along x as shown by the plot of B_x. By adding a homogeneous field along x the potential can be tuned to become attractive [27]. Figure taken from [27].*

Instead of the two perpendicular wires, the confinement in the third direction can be obtained using only a single wire placed perpendicularly to the first wire (figure 1.7). If this new wire is combined with a large enough homogeneous field (perpendicular to it) the potential becomes confining in the x direction [27]. This Ioffe-Pritchard geometry dimple trap is used for both the evaporative cooling and the interrogation sequence (with different parameters).

If the pure 2D quadrupole trap minimum is along the x axis, the field minimum of the dimple trap is tilted in the xy plane.

Effect of the gravity The effect of gravity is to pull down the trapped atoms away from the point of minimum field. The gravitational sag is the distance z_0 between the cloud center $\mathbf{r_0} = (0, 0, 0)$ and the point of minimum field. It is defined by $\alpha_m(\partial B/\partial z)(\mathbf{r_0}) = mg$. The trap frequencies are given by $(\partial^2 B/\partial x_i^2)(\mathbf{r_0}) = m\omega_i^2/\alpha_m$. Around the cloud center, the magnetic field can be expressed

$$B(\mathbf{r}) = B(\mathbf{r_0}) + \frac{m\omega_x^2}{2\alpha_m}x^2 + \frac{m\omega_y^2}{2\alpha_m}y^2 + \frac{m\omega_z^2}{2\alpha_m}z^2 + \frac{mg}{\alpha_m}z. \tag{1.11}$$

1.3 Interactions between cold atoms

In this part we describe two effects arising from the interactions between atoms. The first one is a shift of the clock frequency also referred to as the *collisional shift*. The second one, the *identical spin rotation effect*, can be understood as an exchange of the atoms' internal states during a collision.

1.3.1 General framework: collisions at low energy

Atoms colliding at low energy can be described using the approach of [28]. In a dilute, cold gas the binary s-wave collisions are dominant and the interaction potential can be written

$$V(\mathbf{r} - \mathbf{r}') = g\delta(\mathbf{r} - \mathbf{r}') = \frac{4\pi\hbar^2 a}{m}\delta(\mathbf{r} - \mathbf{r}'). \tag{1.12}$$

a is the scattering length and depends on the internal state of the atoms involved in the collision. For the two states of ^{87}Rb which we use, the scattering lengths are $a_{11} = 100.44$, $a_{12} = 98.09$ and $a_{22} = 95.47$ in units of the Bohr radius a_0 [29].

The hamiltonian describing the system, in terms of the boson field operator $\hat{\psi}$, reads:

$$H = \int_V d^3\mathbf{r} \sum_\alpha \hat{\psi}_\alpha^\dagger(\mathbf{r}) \left(-\frac{\hbar^2\nabla^2}{2m} + U_\alpha(\mathbf{r}) \right) \hat{\psi}_\alpha(\mathbf{r}) + \frac{2\pi\hbar^2}{m} \int_V d^3\mathbf{r} \sum_{\alpha,\beta} a_{\alpha\beta} \hat{\psi}_\alpha^\dagger(\mathbf{r}) \hat{\psi}_\beta^\dagger(\mathbf{r}) \hat{\psi}_\alpha(\mathbf{r}) \hat{\psi}_\beta(\mathbf{r}). \tag{1.13}$$

Here α and β label the internal states of the atom. We have omitted the coupling between internal states by the interrogation field.

The interaction hamiltonian is treated as a perturbation. The field operator is expanded over the trap eigenstates with the help of the creation operators $\hat{c}_{\nu,\alpha}$ (creating an atom in the trap state $\varphi_\nu(\mathbf{r})$ and internal state α): $\hat{\psi}_\alpha(\mathbf{r}) = \sum_{\nu,\alpha} \varphi_\nu(\mathbf{r}) \hat{c}_{\nu,\alpha}$. The interaction part of 1.13 can be written

$$H_{int} = \frac{2\pi\hbar^2}{m} \sum_{\alpha,\beta} \sum_{\nu_1,\nu_2,\nu_3,\nu_4} a_{\alpha\beta} \hat{c}_{\nu_1,\alpha}^\dagger \hat{c}_{\nu_2,\beta}^\dagger \hat{c}_{\nu_3,\alpha} \hat{c}_{\nu_4,\beta} \int_V d^3\mathbf{r} \varphi_{\nu_1}^*(\mathbf{r}) \varphi_{\nu_2}^*(\mathbf{r}) \varphi_{\nu_3}(\mathbf{r}) \varphi_{\nu_4}(\mathbf{r}). \tag{1.14}$$

Lateral and forward collisions This form is useful for identifying two different collision processes: (1) for $\{\nu_1 = \nu_3, \nu_2 = \nu_4\}$ or $\{\nu_1 = \nu_4, \nu_2 = \nu_3\}$ the trap levels occupied by the atoms are unchanged. They are called *collisions in the forward direction*; (2) all other processes for which atoms are scattered to other trap states are called *lateral collisions*.

The balance between lateral and forward collisions is given by the cloud temperature. For $\{\nu_1, \nu_2\} \neq \{\nu_3, \nu_4\}$ it can be shown that $\int |\varphi_{\nu_1}|^2 |\varphi_{\nu_2}|^2 \gg |\int \varphi^*_{\nu_1} \varphi^*_{\nu_2} \varphi_{\nu_3} \varphi_{\nu_4}|$ [30]. The cloud temperature gives the number of trap levels that are populated and over which the sum in 1.14 must be calculated. The forward collisions will become dominant at temperatures low enough to maintain the inequality even after summing over the trap states ν_i.

We will now consider two effects arising from s-wave collisions: the first effect is a density-dependent shift of the clock frequency. It seems relevant to recall its expression for both the non-condensed and the condensed case. The second effect, the identical spin rotation effect, is specific to the non-degenerate case.

1.3.2 Collisional shift

The derivation of the collisional shift can be found in [28]. The authors derive the density-dependent shift of the clock frequency for a spatially homogeneous system:

$$\Delta f_{coll,nc} = \frac{4\hbar}{m} \left[a_{22} n_2 - a_{11} n_1 + a_{12}(n_1 - n_2) \right] \tag{1.15}$$

for a non-condensed gas and

$$\Delta f_{coll,c} = \frac{2\hbar}{m} \left[a_{22} n_2 - a_{11} n_1 + a_{12}(n_1 - n_2) \right] \tag{1.16}$$

for a pure condensate. n_1 and n_2 are the densities of states $|1\rangle$ and $|2\rangle$ respectively. The two expressions differ only by a factor 2: this is due to the absence of exchange interaction in a condensate. In a BEC all the atoms occupy the same spatial state and, therefore, no exchange process can occur during collisions, which reduces the number of processes involved in the interaction by a factor 2 [28]. This phenomenon was experimentally confirmed by a measurement of the ^{87}Rb clock frequency dependence on mean density in both the non-condensed and the condensed case [29].

1.3.3 Identical spin rotation effect (ISRE)

In this section we discuss the identical spin rotation effect. This effect arises from exchange interaction and, therefore, applies only to the non-degenerate case.

The two atoms model

Here we derive the identical spin rotation effect in the model of two atoms colliding [31]. We consider only the forward collision. In this case the problem reduces to two atoms with internal states $|1\rangle$ and $|2\rangle$ evolving in the subspace of their two wavefunctions before collision $\{\varphi_v, \varphi_w\}$. The interaction hamiltonian can be simplified to

$$H_{int} = \frac{2\pi\hbar^2}{m} \sum_{\substack{\{\alpha,\beta\}\in\{1,2\} \\ \{\nu_1,\nu_2\}\in\{v,w\}}} a_{\alpha\beta} \left(\hat{c}^\dagger_{\nu_1,\alpha}\hat{c}^\dagger_{\nu_2,\beta}\hat{c}_{\nu_1,\alpha}\hat{c}_{\nu_2,\beta} + \hat{c}^\dagger_{\nu_1,\alpha}\hat{c}^\dagger_{\nu_2,\beta}\hat{c}_{\nu_2,\alpha}\hat{c}_{\nu_1,\beta} \right) \int_V d^3\mathbf{r} |\varphi_{\nu_1}(\mathbf{r})\varphi_{\nu_2}(\mathbf{r})|^2. \tag{1.17}$$

The direct and exchange terms appears clearly. This hamiltonian is diagonal in the basis of symmetrized eigenstates:

$$\begin{aligned} |u\rangle &= \hat{c}^\dagger_{v,1}\hat{c}^\dagger_{w,1}|0\rangle \\ |d\rangle &= \hat{c}^\dagger_{v,2}\hat{c}^\dagger_{w,2}|0\rangle \\ |t\rangle &= \left(\hat{c}^\dagger_{v,2}\hat{c}^\dagger_{w,1} + \hat{c}^\dagger_{v,1}\hat{c}^\dagger_{w,2}\right)|0\rangle/\sqrt{2} \\ |s\rangle &= \left(\hat{c}^\dagger_{v,2}\hat{c}^\dagger_{w,1} - \hat{c}^\dagger_{v,1}\hat{c}^\dagger_{w,2}\right)|0\rangle/\sqrt{2}, \end{aligned} \tag{1.18}$$

or, in the language of first quantization, by labeling the two atoms a and b:

$$\begin{aligned} |u\rangle &= |1_a 1_b\rangle \left[\varphi_v(\mathbf{r}_a)\varphi_w(\mathbf{r}_b) + \varphi_w(\mathbf{r}_a)\varphi_v(\mathbf{r}_b)\right]/\sqrt{2} \\ |d\rangle &= |2_a 2_b\rangle \left[\varphi_v(\mathbf{r}_a)\varphi_w(\mathbf{r}_b) + \varphi_w(\mathbf{r}_a)\varphi_v(\mathbf{r}_b)\right]/\sqrt{2} \\ |t\rangle &= \left(|2_a 1_b\rangle + |1_a 2_b\rangle\right)\left[\varphi_v(\mathbf{r}_a)\varphi_w(\mathbf{r}_b) + \varphi_w(\mathbf{r}_a)\varphi_v(\mathbf{r}_b)\right]/2 \\ |s\rangle &= \left(|2_a 1_b\rangle - |1_a 2_b\rangle\right)\left[\varphi_v(\mathbf{r}_a)\varphi_w(\mathbf{r}_b) - \varphi_w(\mathbf{r}_a)\varphi_v(\mathbf{r}_b)\right]/2. \end{aligned} \tag{1.19}$$

The matrix elements of H_{int} read ${H_{int}}^{uu} = 8\pi\hbar^2 a_{11}\mathcal{I}/m$, ${H_{int}}^{dd} = 8\pi\hbar^2 a_{22}\mathcal{I}/m$, ${H_{int}}^{tt} = 8\pi\hbar^2 a_{12}\mathcal{I}/m$ ($\mathcal{I} = \int_V d^3\mathbf{r}|\varphi_v(\mathbf{r})\varphi_w(\mathbf{r})|^2$), and 0 everywhere else. The interactions shift the energy levels of the triplet states $|u\rangle, |d\rangle, |t\rangle$, but leave the singlet state $|s\rangle$ unaffected (figure 1.8.a).

In the special case of ^{87}Rb the situation is simple due to the fact that the scattering length for the three states $|d\rangle$, $|u\rangle$ and $|t\rangle$, respectively a_{11}, a_{22} and a_{12}, are nearly identical. The interactions produce a nearly identical shift of these three states by the amount $\hbar\omega_{ex}$ whereas $|s\rangle$ does not interact and is not shifted (figure 1.8.a):

$$\hbar\omega_{ex} = \frac{8\pi\hbar^2 a_{12}}{m} \int_V d^3\mathbf{r}|\varphi_v(\mathbf{r})\varphi_w(\mathbf{r})|^2 \tag{1.20}$$

Evolution of the atomic spins We now consider that the two atoms are placed by a $\pi/2$ pulse on the equator of the Bloch sphere and assume that they have acquired a different phase depending on their energy (figure 1.8.b). In the Bloch sphere the two spins are dephased by an angle, 2α. For simplicity we consider that the two atoms lie symmetrically on each side of the x axis, and make an angle α with it.

The initial wavefunction of the system before the collision reads

$$|\psi\rangle = \frac{\left(\hat{c}^\dagger_{v,1} + e^{i\alpha}\hat{c}^\dagger_{v,2}\right)}{\sqrt{2}} \frac{\left(\hat{c}^\dagger_{w,1} + e^{-i\alpha}\hat{c}^\dagger_{w,2}\right)}{\sqrt{2}}|0\rangle = \frac{1}{2}\left(|u\rangle + |d\rangle + \sqrt{2}\cos\alpha|t\rangle - i\sqrt{2}\sin\alpha|s\rangle\right). \tag{1.21}$$

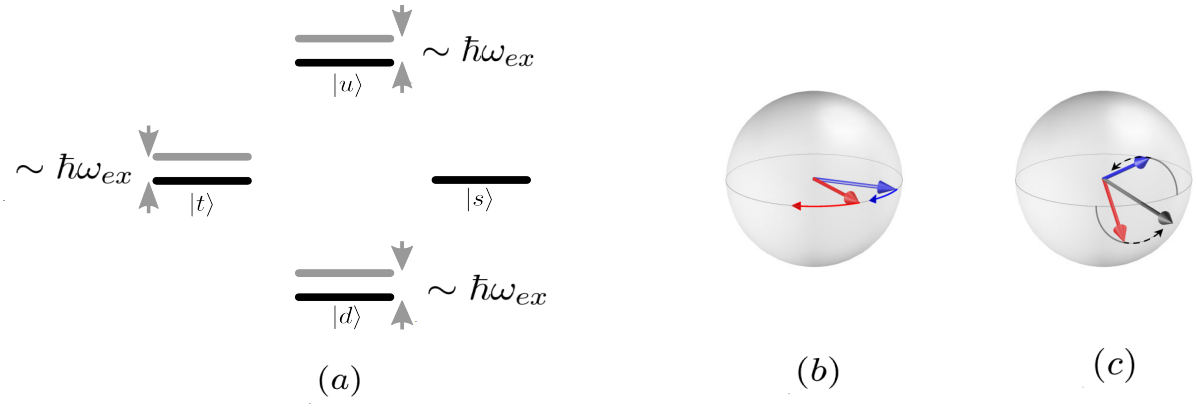

Figure 1.8: *(a) Energy scheme of the $|u\rangle, |d\rangle, |t\rangle$ and $|s\rangle$ states before (black) and during (grey) the collision for the case of ^{87}Rb. (b) Bloch sphere picture of the two atoms before the collision. They are dephased because their total energies are different: the red ("hot") atom precesses faster than the blue ("cold") one. (c) After the collision the atomic spins have rotated around each other, due to the fact that the $|s\rangle$ level is not shifted by the interactions. Figure adapted from [32].*

We note that dephasing causes the spins to be partially distinguishable, which populates the state $|s\rangle$. In the interaction picture this state evolves as:

$$|\psi(t)\rangle = \frac{e^{-i\omega_{ex}t}}{2}\left(|u\rangle + |d\rangle + \sqrt{2}\cos\alpha|t\rangle - ie^{i\omega_{ex}t}\sqrt{2}\sin\alpha|s\rangle\right). \tag{1.22}$$

In order to picture the two spins in the Bloch sphere we compute the Bloch vectors $\mathbf{B}_v$ and $\mathbf{B}_w$ associated with the wavefunctions φ_v and φ_w. By definition of the Bloch vector $\hat{\rho}_v(t) = (1 + \mathbf{B}_v(t)\cdot\hat{\boldsymbol{\sigma}})/2$ where $\{\hat{\sigma}_i\}$ are the Pauli matrices and $\hat{\rho}_v$ is the density matrix for the spin in φ_v. The three components of the Bloch vector can be calculated by noting that $B_i = \langle\hat{S}_i\rangle = \langle\hat{\sigma}_i\rangle/2$ where $\hat{\mathbf{S}}$ is the spin operator. For the spin state of the atom in φ_v we compute:

$$\mathbf{B}_v(t) = \begin{pmatrix} \cos\alpha \\ -\cos(\omega_{ex}t)\sin\alpha \\ -\sin(\omega_{ex}t)\sin\alpha\cos\alpha \end{pmatrix}. \tag{1.23}$$

This corresponds to an "elliptic" precession around the x axis. This is also the direction of the geometric sum of the two initial Bloch vectors (figure 1.8.c). A similar calculation holds for $\mathbf{B}_w(t)$. The identical spin rotation effect causes the two spins to rotate around their sum.

System entanglement We note that for the times $t = n\pi/\omega_{ex}$ the total state $|\psi(t)\rangle$ is separable, which corresponds to pure spin states for both φ_v and φ_w. At these times the Bloch vectors $\mathbf{B}_v(t)$ and $\mathbf{B}_w(t)$ have a norm 1. For all other times the system is in an entangled state and $|\mathbf{B}_{v,w}(t)| < 1$. That is, the two spins are correlated. Assuming we are able to discriminate between states φ_v and φ_w during the measurement, we could measure the probability of finding the φ_w atom in internal state $|2\rangle$ knowing that φ_v was measured in $|2\rangle$. This probability is given by

$$P(v:2|w:2) = \frac{1}{2 + 2\sin(2\alpha)\sin(\omega_{ex}t)}. \tag{1.24}$$

Degenerate gases It is interesting to note that if we consider two particles in the same internal state the model does not apply because we can no longer symmetrize or antisymmetrize the total wavefunction. In our description atoms cannot be in the same external state and have different spin states simultaneously. This is the case of a Bose-Einstein condensate for which, by definition, all particles occupy the same external state. Therefore, no exchange effects and no identical spin rotation are expected in a BEC.

The semiclassical description

A derivation of the spin rotation effect in the semiclassical description was given by Lhuillier and Laloë in [33]. They carefully treated the particle indistinguishability during a binary collision and showed that the internal state exchange occurs during a collision in the forward direction. For spin 1/2 atoms this effect is equivalent to a rotation of the individual spins around their sum [34]. The direction of rotation depends only on the statistical nature of the particles (bosons or fermions). It is purely caused by particle indistinguishability and does not involve any spin-dependant interaction. They also show that at low energies the spin rotation effect in the forward direction becomes the dominant process in the collision which is consistent with our model.

Lhuillier and Laloë derived a kinetic equation for the spin density and obtained for the rates of forward (ω_{ex}) and lateral (γ_c) collisions in the case of ^{87}Rb [34]:

$$\frac{\omega_{ex}}{2\pi} = \frac{2\hbar|a_{12}|\langle n\rangle}{m} \text{ and } \frac{\gamma_c}{2\pi} = \frac{32\sqrt{\pi}a_{12}^2\langle n\rangle}{3}\sqrt{\frac{k_BT}{m}}. \tag{1.25}$$

Since the direction of rotation only depends on the statistical nature of the particles, the spin rotation effect is *cumulative*. An atom crossing the atomic cloud will always undergo spin rotations in the same direction, independently of its direction of propagation. In this respect ISRE is similar to the Faraday effect for photons in a static magnetic field.

Consequences of the identical spin rotation effect

ISRE is the driving mechanism of spin waves observed in dilutes gases: in spin polarized hydrogen gas, ^{3}He, dilute ^{3}He-^{4}He solutions [34], and, more recently, in ultracold gas of ^{87}Rb bosons [35, 36, 37, 38, 39] and ^{6}Li fermions [40, 41, 42]. In our experiment ISRE has other expressions: it induces a self-rephasing of the spins which leads to extremely long dephasing times and contrast revivals in the atomic ensemble [11] (see also [19]). Its effect on the clock frequency itself is under investigation. Spin waves were observed under the application of inhomogeneous excitations [43].

Long dephasing times The evidence for spin-self synchronisation in our experiment was given by the observation of extremely long dephasing times (measured as the Ramsey contrast decay time) in the order of 58(12) s [11]. These spectacular dephasing times are the longest

ever observed on a collection of neutral atoms. For the ISRE to indeed act as a spin self-synchronisation mechanism the following conditions must be fulfilled:

$$\omega_{ex} \gg \Delta_0, \gamma_c. \tag{1.26}$$

Δ_0 is the typical inhomogeneity of the clock frequency over the cloud extension. The interpretation is straightforward: the spins need to dephase slowly enough for the synchronization mechanism to take place. Also, the lateral collision rate must be small enough for the forward collisions to be dominant and no rethermalization to take place during the exchange process.

Spin waves and collisional shift from inhomogeneous excitations A short inhomogeneous pulse spreads the atomic spins in the vertical plane of the Bloch sphere. A similar calculation as made above can be carried out and the spin rotation effect also takes place. In particular, our system was used to confirm predictions of a collisional shift in fermionic clocks arising from the inhomogeneity of the interrogation pulses [31, 43].

Chapter 2

Experimental methods

In this chapter we will give a brief description of the experimental setup and present experimental results that will be referred to throughout this manuscript. We will present the implementation of a new double-state detection scheme involving an adiabatic rapid passage. Finally we will discuss the problem of loading very shallow traps, as it is highly relevant to metrology with trapped atoms.

2.1 Overview of the experimental setup

In this section we briefly review the experimental setup. For a more in-depth explanation of the construction of the experiment we refer the reader to the works of my predecessors who, with great care and precision, designed and built this compact experiment under metrological constraints [26, 44, 32]. The purpose of this description is rather to emphasize the peculiarities of our experiment, give general conventions and indicate a few technical improvements that were made during this thesis.

2.1.1 The vacuum system and the chip

Vacuum cell The central part of the experiment is the vacuum cell (figure 2.1). The atom chip is glued onto it and plays the role of a cell wall, giving easy access to its electrical connections. Glued on the chip is a copper block that contains a macroscopic U and a macroscopic I wire. The copper block is cooled by temperature-regulated water. The chip is oriented horizontally and atoms are trapped below it. A commercial rubidium dispenser [45] continuously emits atoms into the cell.

The *atom chip* is made of two layers glued on top of each other (figure 2.2). Electrical connections were made by bond wires. An important feature of the science chip is the integrated microwave guide designed to interact with the atoms via its evanescent field. Because of this geometry, the microwave field is not homogeneous in space, a feature which will be used in chapter 5. The microwave guide is constituted of three parallel wires. The central wire, hereafter referred to as *stripline wire*, carries also a DC current. It is combined to the central wire of the base chip known as *dimple wire* to form a dimple trap (figure 2.2).

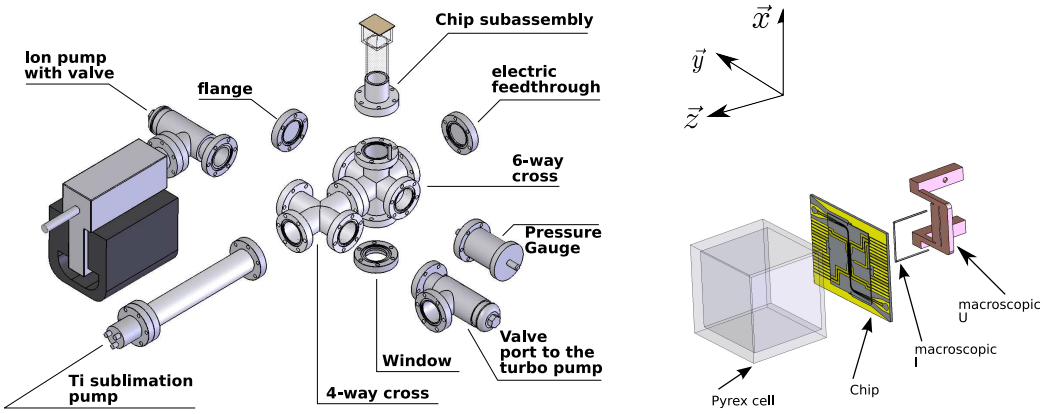

Figure 2.1: *Left: Expanded view of the vacuum system. Right: Expanded view of the cell only, together with the chip and the macroscopic U and I. We also show the axis convention that we will follow throughout this manuscript. In the experiment the chip is mounted horizontally such that gravity is along z. Pictures from [26].*

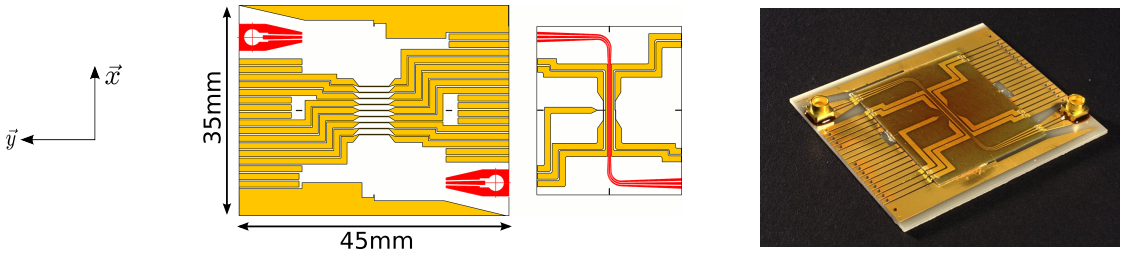

Figure 2.2: *Left: Scheme of the base chip. Middle: Scheme of the science chip, where the microwave guide is pictured in red. The central part of the microwave guide defines the x axis. Right: Photo of the two layers after gluing. Pictures from [26].*

2.1.2 Magnetic shielding and optical hat

An optical hat (figure 2.3) was designed to fit around the cell. It holds 3 pairs of coils and six fiber collimators and their polarization optics. Four beams are used for atom trapping and cooling in a mirror-MOT (magneto-optical trap) configuration: two along x and a further two in the yz plane pointing upwards at a 45 $^\circ$ angle to the vertical axis. Along the x and y axis are placed the two beams used for optical pumping and detection. An Andor iKon M 934-BRDD camera is placed on the x axis and PCO Sensciam QE on the y axis.

A double-layer MuMetal magnetic shield surrounds the optical hat and the cell and ensures attenuation of external magnetic perturbations.

2.1.3 The interrogation photons

A microwave synthesis chain was built to convert the 100 MHz from a hydrogen maser (distributed to all SYRTE laboratories) up to the hyperfine frequency of ^{87}Rb (~ 6.834 GHz). Figure 2.4 gives a schematic view. To evaluate the noise performances of such a device, it was compared to an identical chain. The measured performances [46] are equivalent to a frequency stability of 10^{-14} at 1 s. Recent measurements have confirmed that the noise added by the

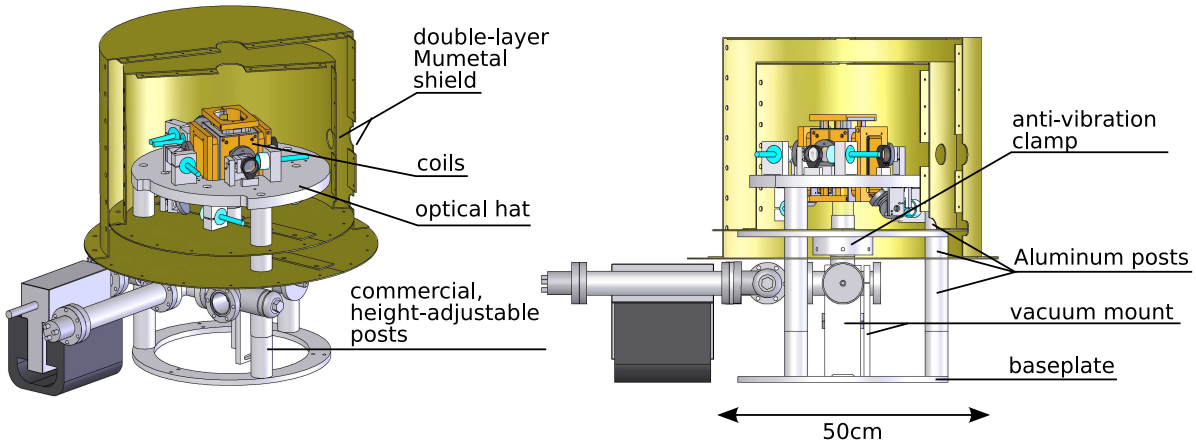

Figure 2.3: *Scheme of the mechanical structure of the experiment. The optical hat was designed to fit around the vacuum cell. It holds the coils and light collimators as well as some polarisation optics. Around the whole system a two-layer magnetic shield was placed, allowing only minimal access for cameras, electrical connections, water cooling pipes and vacuum cell body. Picture from [26].*

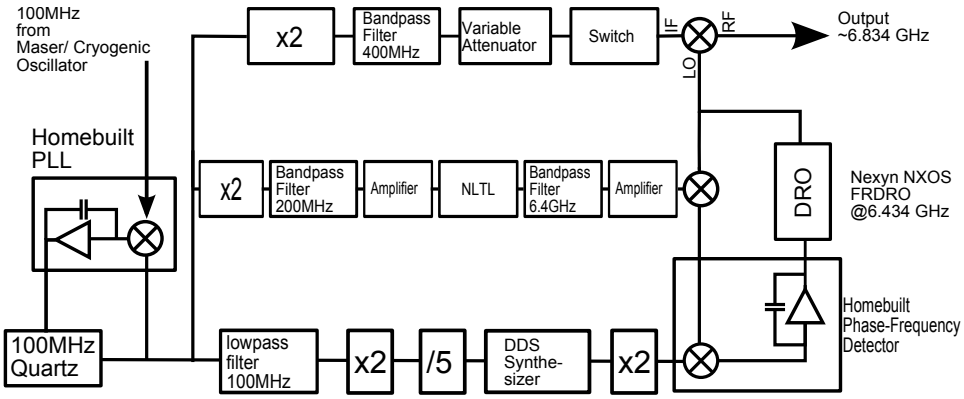

Figure 2.4: *Schematic view of the microwave synthesis chain. NLTL: Non-Linear Transmission Line; DDS: Direct Digital Synthesiser; DRO: Dielectric Resonator Oscillator. The middle arm provides a signal at* 6.4 GHz. *The top arm provides* 400 MHz *and allows control of the chain output power. The bottom arm gives fine tuning of the total frequency with a DDS clocked on a* 40 MHz *signal derived from the* 100 MHz *reference signal. Picture from [32]. See [26] for a complete description.*

synthesis chain to the maser signal is negligible.

The radiofrequency signal needed for the two-photon transition is provided by a DDS (Stanford Research System) clocked on the same 100 MHz reference signal. It is combined with adequate switches and amplifier (see details in [26]). The radiofrequency amplifier has not been characterized and in the rest of this report we will always give the radiofrequency power before the amplifier.

2.1.4 Low noise current sources

Specifically developed for the needs of our experiment, the low noise current sources deliver up to 3 A and show relative RMS noise of 2.5×10^{-6} for frequencies between 10 Hz and 100 kHz. The drift is below 4×10^{-5} during the first hour, and reduces to 10^{-5} when in continuous operation [26]. During the interrogation phase the magnetic trap is formed by low noise current sources exclusively whilst all other current sources are physically disconnected.

2.1.5 Optical bench

The optical bench consists of two extended-cavity laser diodes [47] (Master and Repump) and a slave diode. They provide the light for atom trapping and cooling, optical pumping and detection. The lock scheme works in the following way: the Repump laser is locked on a rubidium line thanks to a saturated adsorption spectroscopy. The Master laser is locked on the Repump laser by means of a beat between the two lasers. The Slave laser is injection-locked by the Master.

During this thesis the Repump laser was replacedin order to benefit from a design with better thermal stability with which the laser typically stays on lock for days. The Slave laser was also replaced once and its collimation optics adapted. The power splitting scheme of the Master laser was adjusted in order to send more power into the detection beam. The detuning scheme of the Repump laser was modified: its frequency is no longer changed throughout the cycle, reducing the chances of unlocking. The frequency of AOM 6 (controlling the optical pumping light derived from the Repump laser) was consequently adjusted to 73.5 MHz.

2.2 Typical cycle

The different steps of a typical experimental cycle are:

- **Mirror MOT** The $1/e$ loading time of the MOT is typically 8 s. Full loading of the MOT provides about 8×10^6 atoms. However, a loading time of 4 s gives good atom number (3.2×10^6 atoms) and reasonably short cycle times.

- The **compressed MOT** consists of a short (14 ms) compression of the captured cloud through increase of the magnetic gradient.

- The atoms are further cooled by 4 ms of **optical molasses**. The cloud final temperature is $< 10\,\mu$K.

- A short light pulse applied on the y axis together with a quantization magnetic field along y perform **optical pumping** of atoms in the $|1\rangle$ state.

- **Transfer to the magnetic trap** The magnetic trap is switched on and approximately 60 % of the atoms are captured.

- **Evaporative cooling** The cloud is compressed into a tight dimple trap (frequencies $\sim \{0.120, 1.2, 1.2\}$ kHz) and a radiofrequency ramp is applied on a chip wire. After 3.3 s an ultracold atomic cloud is obtained. By adjusting the final value of the radiofrequency ramp one can choose to reach quantum degeneracy (Bose-Einstein condensation) or stay above the condensation temperature.

- The **transfer to the interrogation trap** passes from a very tight trap to a very shallow one with frequencies $\{\omega_x, \omega_y, \omega_z\} = 2\pi \times \{2.9, 92, 74\}$ Hz. The transfer ramp takes 700 ms and is discussed further in section 2.4. Due to the low rethermalization rate in the dilute trap, the temperatures in all three axis are different. They typically read $\{T_x, T_y, T_z\} = \{40, 115, 100\}$ nK.

- **Interrogation of the atomic sample** Microwave and radiofrequency signals address the two-photon transition.

- **Double state detection** The atom distributions of both states are detected by absorption imaging after 5 ms*to*30 ms time of flight.

2.3 Double state detection methods

It is crucial to measure *both clock state populations* at each shot. This allows us to, among others, correct the clock frequency for shot-to-shot atom number fluctuations (see chapter 3).

Two different methods can be used to to this: *Double detection* and *Detection with adiabatic passage*. During this thesis the latter method was implemented. Both methods rely on the detection of the atoms on the cycling transition $|F = 2, m_F = 2\rangle \rightarrow |F' = 3, m'_F = 3\rangle$ of the D2 line. The imaging beam is set on resonance with the cycling transition and polarized σ^+ with respect to the quantization magnetic field.

2.3.1 Double detection: detection with Repump light

In this method the cloud is released and exposed to the imaging beam twice (figure 2.5). The first pulse images the atoms in $|2\rangle$, which are resonant with the detection light. They are rapidly pumped onto the cycling transition and scatter detection photons. A few milliseconds later a second pulse is applied together with the repump light which is sent through the 45 ° MOT beams. With this combination, atoms in state $|1\rangle$ are pumped into the $|F = 2\rangle$ state and then onto the detection transition. Between the two pulses a 200 µs pulse resonant with $|F = 2, m_F = 2\rangle \rightarrow |F' = 3, m'_F = 3\rangle$ is applied via the 45 ° beams to push the $|2\rangle$ atoms out of the way of the imaging beam.

This method requires a *fast transfer mode* on the camera: the two pulses are separated by a few milliseconds and this is not enough for the camera to read all the pixels. A fast transfer mode consists of taking two images successively and performing the read-out of both images at a later time.

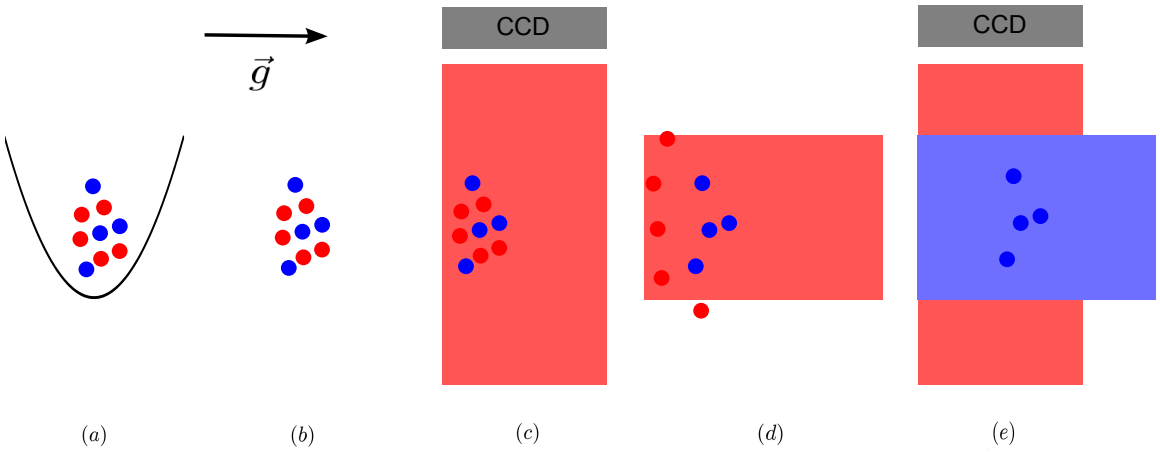

Figure 2.5: *Symbolic scheme of the double detection method. (a) Atoms in clock state* $|1\rangle$ *(blue) and* $|2\rangle$ *(red) are magnetically trapped. (b) The trap is released and the atoms fall. (c) The first light pulse (light red) resonant with the* $|2\rangle$ *state images of the* $|2\rangle$ *cloud distribution. (d) The push-out pulse ensures complete disappearance of the* $|2\rangle$ *atoms. (e) The second pulse is sent some* ms *later together with repump light coming from the side (light blue). This combination performs pumping of* $|1\rangle$ *atoms onto the cycling transition and provide an image of the* $|1\rangle$ *cloud.*

2.3.2 Detection with adiabatic passage

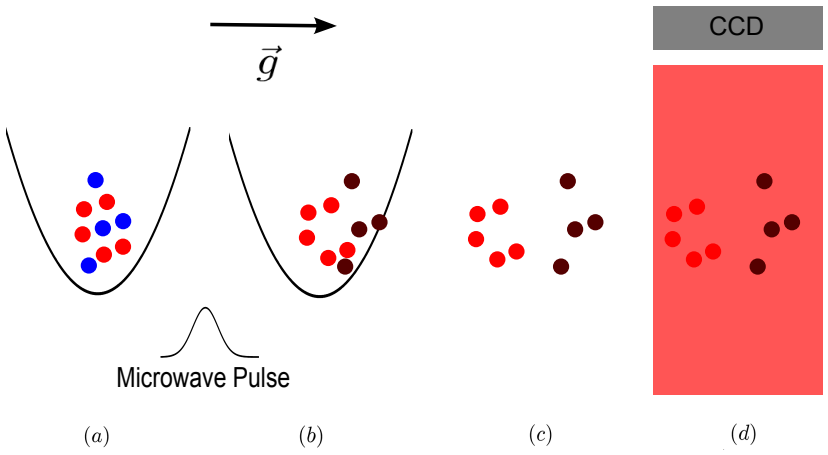

Figure 2.6: *Symbolic scheme of the detection with adiabatic passage. (a) Atoms in clock state* $|1\rangle$ *(blue) and* $|2\rangle$ *(red) are magnetically trapped. (b) A* 1 ms *microwave pulse transfers atoms from* $|1\rangle$ *to the* $|F = 2, m_F = 0\rangle$ *untrapped state (brown) with* 99.5 % *efficiency. Atoms in* $|3\rangle$ *begin to fall. (c) The trap is released some* ms *later and the* $|2\rangle$ *atoms also fall. (d) A single resonant pulse (light red) images both states that are spatially separated.*

An alternative to the double detection method involves transferring trapped $|1\rangle$ atoms to the untrapped $|F = 2, m_F = 0\rangle$ state. They will begin to fall whilst the $|2\rangle$ atoms remain trapped. Some milliseconds later the trap is released and a single imaging pulse is sent. All atoms are resonant with the imaging pulse and the two clouds are spatially discriminated (fi-

gure 2.6).

We will now focus on the transfer $|1\rangle \rightarrow |3\rangle = |F = 2, m_F = 0\rangle$ achieved with the use of a microwave pulse. A feature of the microwave is the inhomogeneity of the field produced. For the atoms to experience an almost homogeneous microwave field the transfer must occur on a short enough timescale. Given the typical spatial inhomogeneity of the microwave amplitude (the amplitude decreases exponentially along z on the scale $\delta \sim 33\,\mu\text{m}$ [43]) the field experienced by the falling atoms is approximately constant during the timescale $t < \sqrt{2\delta/g} \sim 3\,\text{ms}$. As explained in the following, it is possible to efficiently transfer the atoms during this time window with the *adiabatic rapid passage* technique provided the microwave power is large enough.

Theory of the adiabatic rapid passage The adiabatic passage is best understood in the formalism of the dressed atom. We consider a two-level atom (states $|1\rangle$ and $|3\rangle$) in interaction with the microwave field. Ω denotes the Rabi frequency and δ the detuning. In the dressed atom picture, the eigenstates of the $\{\text{atom} + \text{field}\}$ system read:

$$|+\rangle = \sin\theta|1, n\rangle + \cos\theta|3, n-1\rangle \tag{2.1}$$
$$|-\rangle = \cos\theta|1, n\rangle - \sin\theta|3, n-1\rangle, \tag{2.2}$$

where n is the number of photons in the field, and $\cot\theta = -\delta/\Omega$ [48]. The atom is initially in the $|1\rangle$ state. If δ is swept slowly across the resonance, the mixing angle θ turns from 0 to $\pi/2$, and consequently $|-\rangle$ evolves from $|1, n\rangle$ to $|3, n-1\rangle$ causing transfer of the atom from $|1\rangle$ to $|3\rangle$ (see figure 2.7). To ensure adiabaticity during the transfer, the following condition must be fulfilled [49]:

$$\frac{d\delta}{dt} \ll \Omega^2. \tag{2.3}$$

This equation can be summarized by the statement "the more microwave power, the more adiabatic". If equation 2.3 is fulfilled the adiabatic passage method bears the advantage of being insensitive to microwave power fluctuations.

Results for the adiabatic rapid passage in an inhomogeneous field In the experiment the detuning δ is controlled by the trap bottom field B_0. To minimize off-resonant excitations, we use Blackman shapes for both the magnetic field and the microwave pulse. Due to the response time and delays of the microwave attenuator (in the order of 1 ms), the microwave pulse has an unusual shape on the 1 ms timescale (figure 2.8).

Even with the maximum power provided by the microwave chain we were not able to reach full transfer *within* the interrogation trap and this was attributed to a lack of microwave power. The strategy employed involved moving the trap closer to the chip in order to benefit from larger microwave power. In the new trap, after experimental optimization of the timings and detuning sweep amplitude we were able to reach a transfer efficiency of 99.5 % which is comparable to the value of 99 % reported in [50].

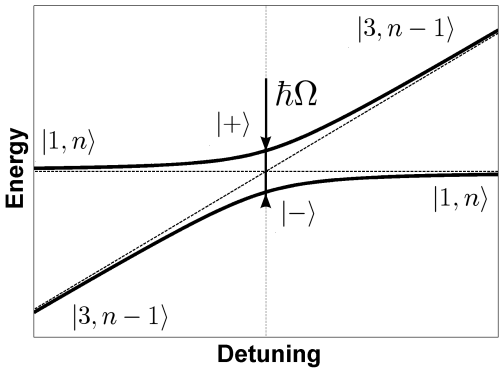

Figure 2.7: *Energy of the* $\{atom + field\}$ *eigenstates as a function of the microwave detuning. For low and large detunings they correspond to the atom being in* $|1\rangle$ *or* $|3\rangle$*. When the detuning is swept across resonance and if the Rabi frequency is high enough the atomic state is transferred adiabatically from* $|1\rangle$ *to* $|3\rangle$ *[48].*

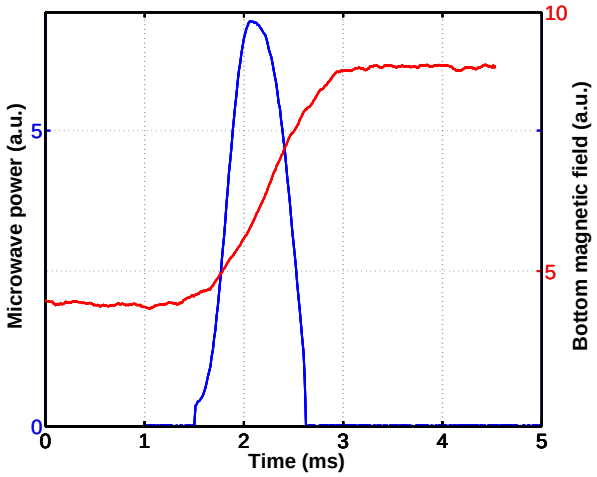

Figure 2.8: *Temporal profiles of the microwave power and bottom magnetic field sweep used for achieving adiabatic rapid passage. Ideally they have Blackman shapes, which minimizes off-resonant excitations. Due to the response time and delays of the microwave attenuator the microwave power has an unusual profile. Nevertheless, this configuration gives transfer efficiencies from* $|1\rangle$ *to* $|3\rangle$ *of* 99.5 % *within* 1.1 ms.

2.3.3 Comparison of the two methods

Double detection The double detection method can give rise to a lower detection efficiency for the state $|1\rangle$. This is because, in order for the atom to reach the imaging transition a certain number of repump photons need to be scattered: during the pumping time no detection photon is scattered. For dense clouds such as BECs, this effect is enhanced by the fact that atoms in the cloud center experience less light power.

In such a scheme laser frequency fluctuations might be problematic. As different pulses are used to image each state, the contribution to detection noise from laser frequency fluctuations

add independently. Although [32] mentions this effect, recent measurements show that this factor does not limit the detection noise (see section 3.3.1). Finally, as already stressed, a camera with a frame transfer mode is needed for this scheme.

Adiabatic rapid passage detection In this method none of the three effects mentioned above occurs. Detection laser frequency fluctuations are in common mode for the two states which renders the probability $P_2 = N_2/(N_1 + N_2)$ insensitive to these. However the current implementation requires that the trap be moved closer to the chip. This results in compression of the cloud causing its image after time of flight to be larger than for the double detection method. This leads to higher detection noise ($\sigma_{N_i} = 117$ atoms vs $\sigma_{N_i} = 59$ atoms, see chapter 3 for more details). An alternative would be to use a second microwave generator allowing higher output powers coupled to the atoms via an antenna placed within the magnetic shielding. An adequate shaping of the pulse should give even higher transfer efficiencies.

2.4 Loading very shallow traps

2.4.1 Motivations for producing very dilute clouds

Atomic clocks generally suffer from the collisional shift. In the trapped atomic clock this is even more problematic since large densities are reached. This shift can limit the long term stability of the clock, and prevent one from building highly accurate clocks. Finally its spatial dependence may cause dephasing of the atomic ensemble, leading to reduced contrast and sensitivity.

Another useful property of very dilute clouds is the reduced effect of asymmetric atomic losses, which affect both states unequally. They are density-dependent and lead to contrast loss and noise on the clock frequency (see chapter 3).

In order to reduce the density in single trap configurations, such as ours, very shallow traps are used. Two problems appear by having low trap frequencies: (1) the adiabaticity condition may not be fulfilled during the decompression and (2) the trap position becomes more and more sensitive to stray gradients as the trap frequency is lowered.

2.4.2 Adiabaticity

Decompression After the evaporative cooling the atoms need to be transferred from a tight trap (frequencies $\{0.120, 1.2, 1.2\}$ kHz) to a shallow trap (frequencies $\{2.9, 92, 74\}$ Hz). Adiabaticity during the decompression is required to minimize cloud excitations. For an isotropic harmonic trap of frequency $\omega/(2\pi)$ and a linear decompression ramp, the adiabaticity condition reads [51]

$$\frac{d\omega}{dt} \ll \omega^2. \tag{2.4}$$

Displacement It turns out that, during this transfer, not only do the trap frequencies change but also the trap position. The second adiabaticity condition with regards to the trap displacement can be formulated as [52]

$$\omega T_d \ll 1, \tag{2.5}$$

where T_d is the displacement time.

Our experimental situation Because of the low trapping frequency along x (2.9 Hz) the trap position is very sensitive to any stray field gradient that may exist along x. Indeed we observed that the interrogation trap is displaced by $\sim$ 130 µm along x from the theoretical prediction. The reason for this displacement could be a subtle effect of the x coils curvature, for example, if these coils were misaligned by $\sim$ 1 mm. The trap displacement of about 150 µm along z direction matches the expectation (see figures 2.9.a and 2.9.d).

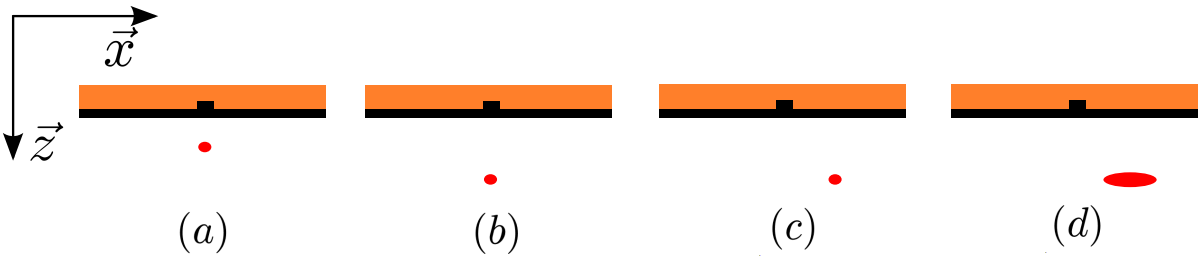

Figure 2.9: *Symbolic drawing of the trap positions (red). The stripline and dimple wires are pictured in black. (a) Cooling trap. (b) Intermediate trap used up to this point. (c) New intermediate trap. (d) Interrogation trap. The transfer used up to this point consisted of $a \to b \to d$ produces a residual oscillation along x, even with a* 600 ms *ramp. The new scheme consists of $a \to c \to d$, and permits to both cancel the cloud oscillation and reduce the ramp time. However, it excites unexplained oscillations in the y and z axis.*

Up to this point the strategy involved separating the transfer ramp into two moves: the first ramp (*displacement ramp*) brings the cloud to its final position along z while keeping it tight (figure 2.9.b). The second ramp (*decompression ramp*) performs the decompression at a constant position: typically this takes about 600 ms. This long ramp does not, however, fulfill condition 2.5 for the displacement along x as shown by our recent measurement of the cloud residual oscillation along x (figure 2.10). As the cloud oscillates we observe a temperature increase on a time scale comparable with the center-of-mass oscillation damping. This damping time (2 s) is comparable to the rethermalization time computed from the lateral collision rate (3.6 s). We note that the damping of the center-of-mass oscillation is a signature of the trap anharmonicity [53]. For a BEC we observe no damping of the center-of-mass oscillation within 2 s, in agreement with its superfluidity properties (figure 2.10).

2.4.3 Canceling the oscillation along x

One approach to avoid exciting oscillations during the displacement follows the philosophy explained above: the intermediate trap is displaced along x until the position of the inter-

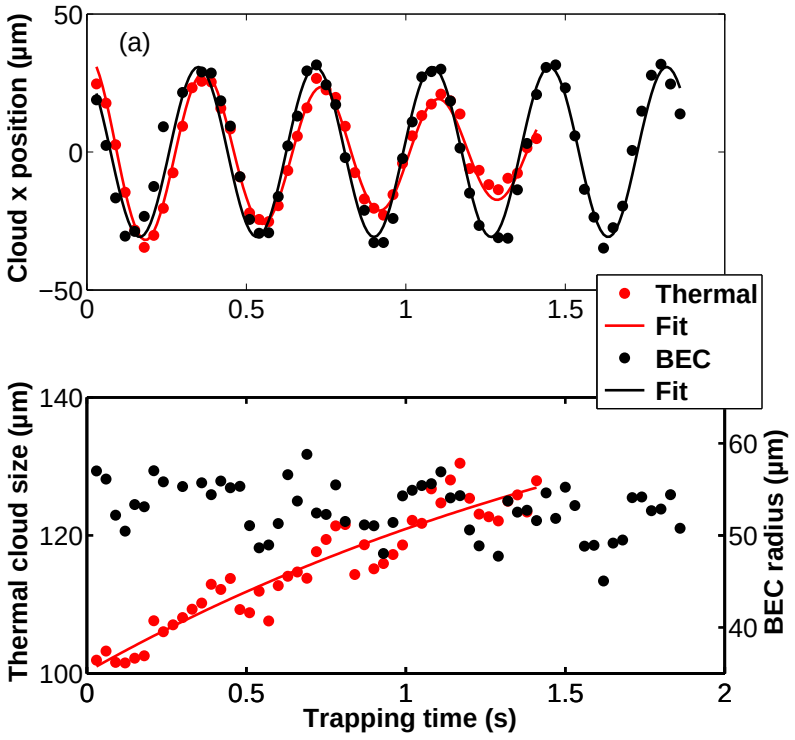

Figure 2.10: *Effect of the residual oscillation along x on the cloud center-of-mass position and size. The atoms are in $|2\rangle$ (a) Center of mass position. Damping is observed only for the thermal cloud since the BEC is superfluid. The damping is a signature of a trap anharmoniticity. We fit the data with $f(t) = A + B\sin(2\pi(t-t_0)f)\exp(-(t-t_0)/\tau_1)$. (b) Cloud size obtained from a gaussian fit for thermal clouds and a parabolic fit for BECs. For a thermal cloud the size increases with time as the cloud rethermalizes. We fit the data with $f(t) = A + B[1-\exp(-(t-t_0)/\tau_2)]$ and find $\tau_1 \sim \tau_2 \sim 2\,\mathrm{s}$, which is comparable to the expected value of $3.6\,\mathrm{s}$. For a BEC the size decreases in time as a consequence of the atom losses.*

rogation trap is reached (figure 2.9.c) and finally decompressed at constant position. The displacement is obtained by driving an additional chip wire oriented along y. The corresponding current is ramped up during the displacement ramp and eventually down to 0 during the decompression ramp. The latter ramp is adjusted point-by-point to maintain the trap at a constant position.

Figure 2.11 shows the results obtained with this method: it permits to almost cancel the residual oscillation along x. However, we observe increased oscillations in the two other directions. The origin of these excitations is not clear yet: as a result of higher trap frequencies in these directions we expect the adiabaticity criteria to be fulfilled. Further investigations of this problem are currently ongoing.

Reaching smaller ramp times Figure 2.11 shows that this approach is a way for reducing the decompression ramp time: for the 200 ms ramp with the extra wire the residual oscillation along x is already ~ 2 times smaller than for the 600 ms ramp without the extra wire. We are

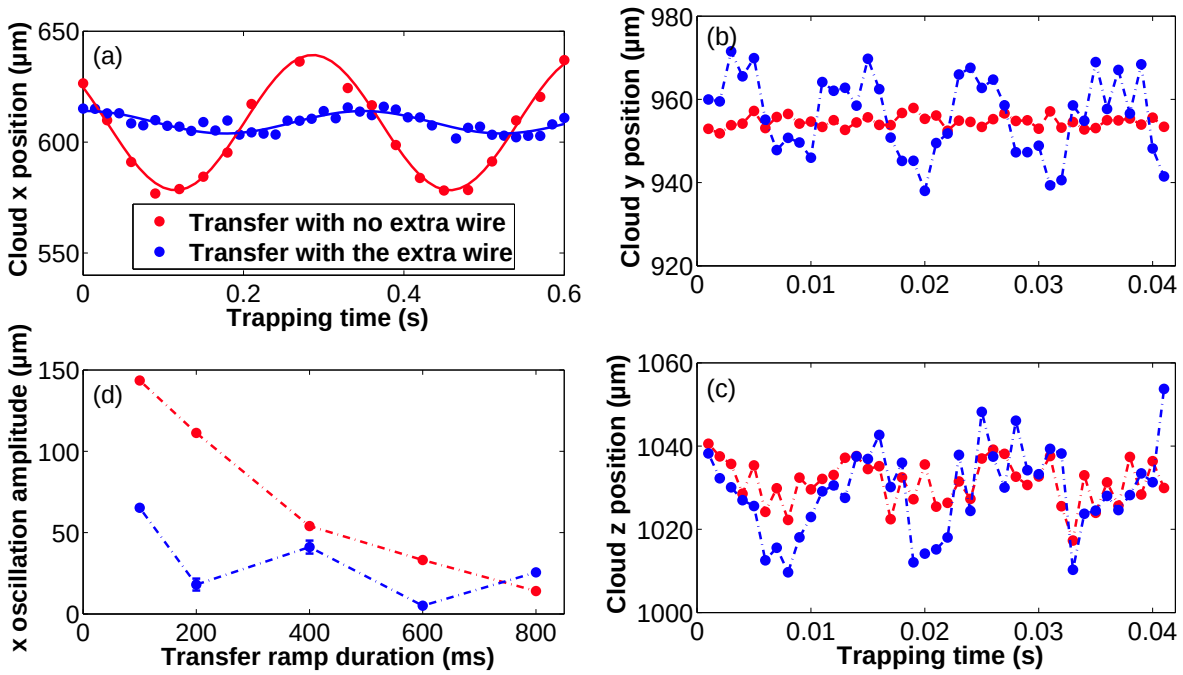

Figure 2.11: *(a) Oscillations along x can be reduced by adding an extra wire during the transfer ramp. (b) and (c) The new transfer ramp excites larger oscillations in the two other axis. This is not yet understood. (d) The new transfer ramp allows a reduction of the transfer time. Here the ramp was optimized for a ramp time of* 600 ms*. For other ramp times an optimization of the current ramp shape of the additional wire shall be done. Nevertheless, one observes that for the new ramp and a transfer time of* 200 ms*, even non optimized, the residual cloud oscillation is already smaller than for the* 600 ms *ramp with no extra wire.*

confident that with further optimization transfer times of 100 ms or less can be reached.

Chapter 3

Clock frequency stability

Earlier works [29, 54, 55] have anticipated the potential of using magnetically trapped cold ^{87}Rb atoms as an atomic frequency reference. High clock quality factors can be achieved with cold, non-condensed ensembles near the magic field for which coherence times of 2 s*to*3 s have been observed [29, 54]. With atom chip technologies the construction of a liter-sized atomic clock with a frequency stability in the low $10^{-13}/\sqrt{\tau}$ range have become a realistic project, with high potential for onboard applications. Since these predictions were made, the phenomenon of spin self-synchronization in cold atomic ensembles has been discovered [11]. This gives access to interrogation times of tens of seconds and opens the route to liter-sized atomic clocks with frequency stabilities below the value of $10^{-13}/\sqrt{\tau}$ mentioned above. In these estimations it is assumed that the clock is limited by the atomic shot noise. Before this fundamental limit can be reached a great amount of work is required in order to bring all technical noises below it.

In TACC the quantum projection limit has not yet been reached. The best observed frequency stability, $5.8 \times 10^{-13}/\sqrt{\tau}$, is still 4 times larger than the standard quantum limit ($1.5 \times 10^{-13}/\sqrt{\tau}$). In this chapter we give the current status of the characterization of the noises on the clock frequency and show that there are still unidentified noise(s). This chapter is organized as follows: the first part contains the general tools of noise analysis. The second part applies to the calculation of the known noises. In the third part we present an experimental investigation of the noise sources. Finally we comment on the best observed stability and discuss thermal effects.

3.1 Frequency stability analysis

3.1.1 Allan variance

The characterization of the frequency stability of oscillators is done with the Allan variance. Also called *two-sample variance*, it gives a classification of the noise types according to their spectral density. The frequency power spectral density admits a decomposition in powers of the frequency F:

$$S(F) = \sum_{\alpha} h_\alpha F^\alpha. \tag{3.1}$$

For example $\alpha = 0$ corresponds to a white frequency noise (see figure 3.1). Only the values $-2 < \alpha < 2$ are relevant to common noises.

If we consider a finite number N of frequency measurements $\{f_k\}$ spaced by the time interval T_c, the Allan variance of the normalized deviations $y_k = f_k/f_{at} - 1$ is defined by [12]:

$$\sigma_y^2(T_c) = \frac{1}{2(N-1)} \sum_{k=1}^{N-1} (y_{k+1} - y_k)^2 \tag{3.2}$$

The Allan variance at larger integration times $\tau = pT_c$ $(p > 1, p \in \mathbb{N})$ is obtained by constructing the dataset $\left\{ y'_m = (1/p) \sum_{k=(m-1)p+1}^{(mp)} y_k \right\}$ and computing 3.2 for it.

The plot $\sigma_y(\tau)$ gives information on the type of noise involved at each time scale according to the correspondence given in table 3.1. A linear drift of frequency $f(t) = f_0 + Dt$ can also be identified by the Allan variance: it gives a slope of +1 in the logarithmic plot of $\sigma_y(\tau)$ (figure 3.1).

α	Noise type	slope in $\sigma_y(\tau)$
2	white phase noise	-1
1	flicker phase noise	-1
0	white frequency noise	-1/2
-1	flicker frequency noise	0
-2	random walk frequency noise	1/2

Table 3.1: *Classification of noise types by their power spectral density and their slope in the log/log plot of $\sigma_y(\tau)$. The exact correspondence between the different descriptions can be found for example in [12].*

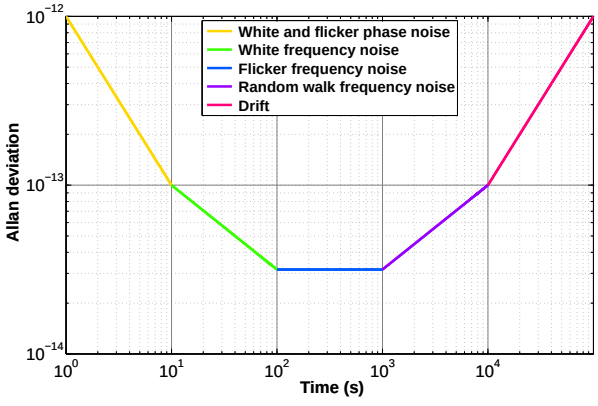

Figure 3.1: *Typical variations of the Allan deviation for an atomic clock and the corresponding noise types at each time scale.*

Shot-noise limited clock If dominated by the atomic shot noise (a white frequency noise) the clock frequency deviation takes the form [12, 56]

$$\sigma_{y,QPN} = \frac{1}{\alpha Q_{at} \sqrt{N_{at}}} \sqrt{\frac{T_c}{\tau}}. \tag{3.3}$$

Here N_{at} is the number of atoms detected, $Q_{at} = f_{at}/\Delta f$ is the atomic (or clock) quality factor with Δf the full width at half height of the atomic response. α is a numerical coefficient that depends only on the spectroscopic method ($\alpha = \pi$ for a Ramsey interrogation).

Short and long term stabilities In practice, the frequency noise is not white at all times. Typical clock stabilities integrate for some time and eventually reach a flicker floor or start to drift. We refer to **short term stability** as the white frequency noise extrapolated to 1 s. The quantity $\sigma_y(T_c)$ (computed with 3.2) is naturally called **stability at one shot**. The **long term stability** refers to the long term behavior of the frequency: spectral density of the dominant noise (typically flicker frequency noise on drift), lowest integrated value of the clock frequency Allan deviation.

3.1.2 Principle of the characterization of TACC

To characterize the frequency stability of our setup we benefit from a 100 MHz signal of the SYRTE hydrogen maser which is upconverted to ~ 6.834 GHz by TACC microwave chain. The characterization of the clock frequency stability is achieved by direct comparison with the frequency stability of the local oscillator (maser + microwave chain). The atomic clock is in open loop and no correction is applied on the local oscillator.

In the following Δf denotes the difference between the clock frequency f and the bare atomic frequency f_{at}.

3.2 Analysis of the sources of noise on the clock frequency

There are several ways to classify the noise sources. A natural choice is to distinguish the noises affecting the transition probability from those affecting the frequency. More specifically, there would be:

1. Noise of the transition probability P_2: it converts into frequency noise via the atomic response.

2. Fluctuations of Δf.

3. Fluctuations of the local oscillator frequency.

4. Noise added by the post-correction process.

For the fluidity of the presentation we have preferred, however, to order the noises according to their physical origin. In the following the frequency noise is always given at $\tau = T_c$ (noise at one shot).

3.2.1 Quantum projection noise

Also called atomic shot noise, it is of fundamental origin. Consider an atom in a quantum superposition of two states: quantum mechanics only predicts the probability of detecting the atom in either of the two states. For N uncorrelated atoms, each having the probability $p = P_2$ to be detected in state $|2\rangle$, the probability of measuring N_2 atoms in state $|2\rangle$ is given by the binomial law [57]:

$$p(N_2) = \frac{N!}{N_2!(N-N_2)!} p^{N_2}(1-p)^{N-N_2}, \tag{3.4}$$

whose mean value is $\langle N_2 \rangle = pN$ and variance $\sigma^2_{N_2} = Np(1-p)$.

The resulting noise on the transition probability $P_2 = N_2/(N_1 + N_2)$ is given by:

$$\sigma_{P_2,QPN} = \sqrt{\frac{p(1-p)}{N}} \tag{3.5}$$

For $p = 1/2$, corresponding to the steepest atomic response, we obtain $\sigma_{P_2,QPN} = 1/(2\sqrt{N})$.

Quantum projection noise for a reduced contrast If the contrast $C = 1$ it is obvious that all N atoms contribute to the signal, and equation 3.5 predicts the quantum noise. A reduced contrast $C < 1$ can arise from two mechanisms: decoherence or dephasing. Their signature on the quantum noise are different:

- In case of dephasing each atom is in a quantum state superposition and 3.5 can be used with the total number of atoms N. At the standard quantum limit the frequency stability for Ramsey interrogation would read, accordind to equation 3.3,

$$\sigma_{y,QPN} = \frac{1}{\pi C T_R f_{at} \sqrt{N}} \sqrt{\frac{T_c}{\tau}}. \tag{3.6}$$

- In case of decoherence, some atoms have been projected on either of the two states. Decohered atoms do not produce projection noise and 3.5 can be used, but with the atom number $C\,N$. In this case the frequency stability reads

$$\sigma_{y,QPN} = \frac{1}{\pi C T_R f_{at} \sqrt{CN}} \sqrt{\frac{T_c}{\tau}}. \tag{3.7}$$

Dephasing and decoherence are different mechanisms and the quantum noise measurement provides an interesting way of discriminating between them.

3.2.2 Detection noise

The detection noise is the uncertainty in measuring the atom number in a given cloud. The two contributions are: the photon shot noise and the optical disturbances from interference fringes in the image. The photon shot noise is determined by various parameters including imaging pulse intensity and duration, optics transmission and camera efficiency (see [32] for a full description). Influence of interference fringes is greatly reduced by numerically recomposing the reference image [32, 58]. For the other parameters the general rules are as follows:

the cloud image on the camera must be as small as possible (minimizing the number of pixels involved to reduce the photon shot noise) and the detection intensity must be at the saturation intensity. The pulses must be as long as possible and are in practice limited by saturation of the camera [32].

All of the contributions can be approximated by a constant noise on the atom number in state i, $\sigma_{N_i,det}$. Assuming the same value for both states the resulting noise on the probability P_2 for a 50/50 superposition takes the form [59]:

$$\sigma_{P_2,det} = \frac{\sigma_{N_i,det}}{\sqrt{2}N} \tag{3.8}$$

The noise of the total atom number is given by $\sigma_{N,det} = \sqrt{2}\sigma_{N_i,det}$.

Detection accuracy Recently we became aware of a problem in the atom number measurement. Due to light diffraction effects circular fringes appear around the cloud image for large optical densities. For large atom numbers we observe a reduced detectivity at short times of flight (see figure 3.2). This effect could become limiting in future experiments. As long as it is stable and repeatable it should not affect clock stability measurements.

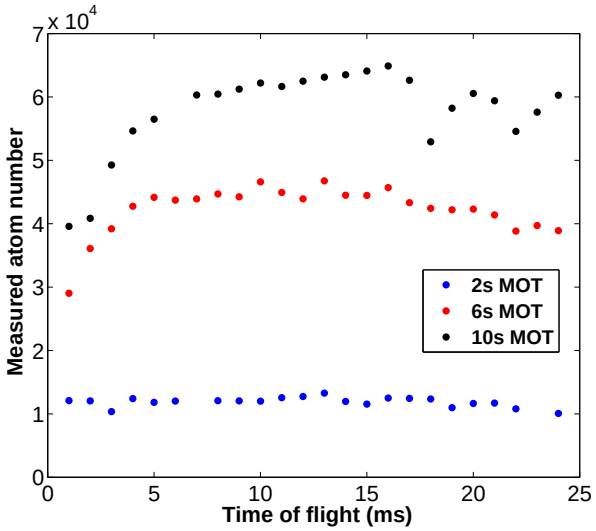

Figure 3.2: *Measured atom number as a function of the time of flight. For small atom numbers the measured value does not depend on the time of flight. For larger atom numbers the measured atom number depends on the time of flight. Cloud images show circular fringes which suggests an effect of light diffraction by the atomic cloud. Images are taken at resonance.*

3.2.3 Atom number fluctuations

The total atom number fluctuates shot-to-shot by typically $\sigma_{N,fluct}/N \simeq 1\,\%$ due to fluctuations in the MOT loading. It might also undergo drifts in the order of 50 % over several hours. The resulting fluctuations of the collisional shift can be corrected for, this will be explained in

section 3.3.2.

3.2.4 Temperature fluctuations

The cloud temperature is likely to fluctuate and drift. The impact of a cloud temperature fluctuation σ_T on the clock frequency shift Δf is twofold:

1. The temperature enters the cloud density and thus impacts the collisional shift.

2. The temperature determines the cloud extension in the trap. A change of temperature produces a change of the mean magnetic field experienced by the cloud, which directly translates to a change of the magnetic shift in Δf.

Assuming the same temperature $T = (T_x T_y T_z)^{1/3}$ in all three axis, the thermal gas model and equations 1.9 and 1.11 we predict

$$\sigma_{y,T} = \left| \frac{3\hbar(a_{22} - a_{11})\langle n \rangle}{m f_{at} T} + \frac{\beta k_B}{2\alpha_m \omega_z^2 f_{at}} \left[2mg^2 + \omega_z^2 (15 k_B T + 6\alpha_m \Delta B) \right] \right| \sigma_T, \tag{3.9}$$

where $\Delta B = B_0 - B_m$. We predict that the sensitivity to the cloud temperature vanishes for a field

$$B_0 = B_m - \frac{mg^2}{3\omega_z^2 \alpha_m} - \frac{5 k_B T}{2\alpha_m} - \frac{\hbar(a_{22} - a_{11})\langle n \rangle}{m\beta k_B T}. \tag{3.10}$$

With $T = 80\,\mathrm{nK}$ (measured for a cloud of 4×10^4 atoms) we obtain $B_0 = B_m - 35\,\mathrm{mG}$. At $B_0 = B_m$, $\sigma_T/T = 1\,\%$ leads to $\sigma_{y,T} = 1.6 \times 10^{-13}$.

3.2.5 Magnetic field fluctuations

We call σ_B the amplitude of magnetic field fluctuations. Using equation 1.9 we deduce the corresponding noise on the clock frequency:

$$\sigma_{y,B,magn} = \frac{\sqrt{2}\beta\sigma_B^2}{f_{at}} + \frac{2\beta\sigma_B(B_0 - B_m)}{f_{at}}. \tag{3.11}$$

The magnetic noise is averaged by the atoms during the interrogation sequence, therefore the relevant magnetic noise is the one averaged at the Ramsey time $\sigma_B(T_R)$. This noise is not known precisely. In section 3.3.5 we give an upper limit to $\sigma_B(3\,\mathrm{s})$ deduced from clock stability measurements.

3.2.6 Atomic losses

Symmetric losses

The lifetime of the atoms in the trap $\tau \sim 6\,\mathrm{s}$ (limited by the collisions with background atoms) is in the order of the typical Ramsey time (3 s). Therefore the number of trapped atoms significantly decays during the interrogation. Our imaging method is destructive and we have only access to the atom number N_f at the end of the sequence. Due to the random character of

the trap loss there is a statistical uncertainty on the initial atom number. It translates via the collisional shift into an uncertainty on the clock frequency we can *fundamentally not* correct for. In the following we estimate this error.

Forward distribution This discussion is inspired by the description of the decay of an ensemble of radioactive atoms [60]. We first consider a cloud of N_i trapped atoms with a trap decay constant $\gamma = 1/\tau$. γ can be reinterpreted as the (constant) probability rate for the atoms to be ejected from the trap. At the time t, the probability for a given atom to still be trapped is $e^{-\gamma t}$, and its probability to have left the trap is $1 - e^{-\gamma t}$. Starting with N_i atoms at $t = 0$, the probability of having n atoms at t is

$$p(N_f = n, t) = \frac{N_i!}{n!(N_i - n)!} e^{-n\gamma t}(1 - e^{-\gamma t})^{N_i - n}. \tag{3.12}$$

For $N_i \gg n$ (or equivalently $\gamma t \ll 1$) the distribution tends to a Poisson distribution of intensity $\mu = N_i\gamma$.

Reverse distribution In fact we are interested in the opposite case where we know the number N_f and want to know the initial atom number. If n_0 atoms were present in the trap at $t = 0$, $n_0 - N_f$ atoms have been ejected during the elapsed time t and N_f atoms are still trapped. The probability of such an event is proportional to $e^{-N_f\gamma t}(1 - e^{-\gamma t})^{n_0 - N_f}$ and to the number of possible combinations:

$$p(N_i = n_0, t) = A\frac{n_0!}{N_f!(n_0 - N_f)!} e^{-N_f\gamma t}(1 - e^{-\gamma t})^{n_0 - N_f}. \tag{3.13}$$

The normalization gives $A = e^{-\gamma t}$. A more rigorous derivation of this reverse distribution was done by C. Texier [61].

To compute the resulting noise on the clock frequency, we assume that the losses only affect the atom number and leave the temperature unchanged. The time-averaged clock frequency collisional shift reads

$$\Delta f_{coll} = k\frac{1}{T_R}\int_0^{T_R} N(t)\, dt, \tag{3.14}$$

where k is the dependance of the collisional shift with the atom number. This value could be computed from the theoretical prediction $k_{theo} = 2\hbar(a_{22} - a_{11})/(8m\sqrt{\pi^3\langle x^2\rangle\langle y^2\rangle\langle z^2\rangle})$, but a better estimation can be extracted from the f/N_f correlation which we will discuss in section 3.3.2. Doing so we assume that k does not change in time.

The distribution law of $N(t)$ is known at each time via 3.13. Approximating the binomial laws by gaussian distributions, it is possible to find an expression for the standard deviation of 3.14 [61]:

$$\sigma_{y,loss,stat} = \frac{k}{f_{at}\gamma T_R}\sqrt{N_f e^{2\gamma T_R}\left(1 - 2\gamma T_T e^{-\gamma T_R} - e^{-2\gamma T_R}\right)}. \tag{3.15}$$

Asymmetric losses

The calculation above relies on the assumption that all atoms have the same lifetime in the trap. In fact, due to the existence of spin-flip collisions, atoms in state $|2,1\rangle$ have a shorter lifetime. This is essentially due to the collision channel

$$2 \times |2,1\rangle \rightarrow |2,0\rangle + |2,2\rangle, \tag{3.16}$$

the equivalent of which does not exist for state $|1\rangle$ (we have adopted the convention $|F, m_F\rangle$). These collisions lead to the build up of incoherent population in the states $|2,2\rangle$ which remain trapped (N_2'). An incoherent population also builds up in $|1,-1\rangle$ (with $N_1' = 2N_2'$) arising from the $|1,-1\rangle$ part of atoms initially in a state superposition that have decohered through 3.16. Atoms in $|2,0\rangle$ are not trapped and do not play a role on the noise.

The rate of 3.16 is given by the lifetime difference between the two clock states. In our typical experimental conditions it amounts to $\gamma_{asym} \simeq 1/45\,\mathrm{s}^{-1}$. Asymmetric losses have several consequences:

1. The first parasitic effect is a fluctuation of the number of atoms detected in state $|2\rangle$: the $|2,2\rangle$ and $|1,-1\rangle$ populations fluctuate shot-to-shot because the total number of atoms fluctuates. The $|1,-1\rangle$ atoms are transferred by the second pulse into an equal superposition of the two clock states, and only contribute to the clock signal as decohered atoms. $|2,2\rangle$ atoms are not affected by the second pulse and create a noise on the transition probability P_2:

$$\sigma_{P_2,asym} = \frac{\sigma_{N,fluct}}{2N}(1 - e^{-\gamma_{asym}T_R}). \tag{3.17}$$

   For $\sigma_{N,fluct}/N = 1\,\%$ and $T_R = 3\,\mathrm{s}$ we find $\sigma_{P_2} = 3 \times 10^{-4}$, which is 10 times smaller than the quantum projection noise of 25×10^3 atoms.

2. Fluctuating populations in $|2,2\rangle$ and decohered $|1,-1\rangle$ produce fluctuations of the collisional shift. These are proportional to the total number of atoms N and are taken into account in our post-experiment correction procedure.

3. The third effect is the statistical noise associated with the asymmetric losses. Given $\gamma_{asym}T_R \ll 1$, the decay process can be approximated by a Poisson distribution and the statistical noise of the incoherent population N_2' is given by $\sqrt{N_2'}$. We assume that the system is an uncoherent mixture of constant populations, equal to their final values (this avoids the calculation of the integral 3.14 and overestimates the noise). Following [28] we find the corresponding frequency fluctuation:

$$\sigma_{y,asym,stat} = \frac{2\hbar}{m f_{at}}(a_{22} - 2a_{11} + a_{12})\frac{\sqrt{N_2'}}{8\sqrt{\pi^3\langle x^2\rangle\langle y^2\rangle\langle z^2\rangle}}. \tag{3.18}$$

   With the rough approximation $N_2' = N\gamma_{asym}T_R/2$ (doing so we neglect the losses of $|2,2\rangle$ and decohered $|1,-1\rangle$ atoms from collisions with the background gas, which overestimates the noise), we estimate $\sigma_{y,asym,stat} = 1.3 \times 10^{-14}$.

3.2.7 Rabi frequency fluctuations

Power fluctuations of the interrogation pulses affect the frequency stability at three different levels. It seems relevant to recall the calculations of these contributions [26, 32]:

1. The first effect is a noise on the pulse area that affects both the preparation and the phase readout in a Ramsey configuration. We call $\sigma_{P_2,Rabi}$ the noise in the preparation of the initial state superposition. This noise will be evaluated in section 3.3.1 to $\sigma_{P_2,Rabi} < 1 \times 10^{-4}$, which is more than 30 times smaller than the projection noise.

2. The second effect, related to the first one, concerns the collisional shift fluctuations induced by a noisy preparation. The resulting noise on the clock frequency reads

$$\sigma_{y,Rabi,Coll} = \frac{2\hbar}{m}(2a_{12} - a_{11} - a_{22})\langle n\rangle \frac{2\sigma_{P_2,Rabi}}{f_{at}}. \tag{3.19}$$

   With $\sigma_{P_2,Rabi} < 10^{-4}$ we anticipate $\sigma_{y,Rabi,Coll} < 10^{-16}$.

3. The third effect is a fluctuation of the AC Zeeman shift induced by the interrogation photon on the clock transition (during the Ramsey pulses). In a Ramsey interrogation this contribution can be expressed as a function of the π-pulse duration τ_π and the AC Zeeman shift Δf_{LS} on the transition [32]:

$$\sigma_{y,Rabi,LS} = \frac{8\Delta f_{LS}\sigma_{P_2,Rabi}}{\pi f_{at}\left(1 + \frac{\pi T_R}{2\tau_\pi}\right)}. \tag{3.20}$$

   With $\Delta f_{LS} = 0.2\,\mathrm{Hz}$, $T_R = 3\,\mathrm{s}$ and $\tau_\pi = 150\,\mathrm{ms}$ it amounts to $\sigma_{y,Rabi,LS} < 3 \times 10^{-16}$.

3.2.8 Local oscillator frequency

Fluctuations of the local oscillator frequency on time scales $\ll T_R$ are not detected as they are averaged by the atoms during the interrogation. LO frequency noise on time scales $\gtrsim T_R$ does affect the clock frequency. In fact pulsed atomic clocks are especially sensitive to the LO frequency noise at the harmonics of the inverse cycle time, $1/T_c$. This is called the *Dick effect* [62]. The *clock sensitivity function* [56, 63], which depends on the timings T_R, T_c and τ_π provides the link between the LO frequency noise spectra and the noise on the clock frequency.

A detailed analysis of our local oscillator frequency noise was carried out by Ramon Szmuk, who kindly provided the estimations of the LO Dick effect referred to in this manuscript. More details will surely be found in his PhD thesis.

3.2.9 Noise added by the post-correction

When applying the post-correction procedure one mechanically adds noise onto the clock frequency. This is due to the fact that the correcting parameter is not known with infinite accuracy. For the correcting parameter α_j, assuming it is distributed with a width σ_{α_j}, the corresponding noise on the frequency reads

$$\sigma_{y,corr,j} = \frac{1}{f_{at}} \left| \frac{\partial \Delta f}{\partial \alpha_j} \right| \sigma_{\alpha_j}. \tag{3.21}$$

For the correction with the atom number the relevant noise is the detection noise $\sigma_{N,det}$. This value is the measurement noise for a given cloud and should not be confused with the shot-to-shot atom number fluctuation $\sigma_{N,fluct}$.

3.3 Experimental investigation

In this section we present an experimental characterization of the technical noise on the clock frequency. We will start with a measurement of the detection and preparation noise, known as "noise on P_2". The second result is a study of the post-correction and shows that the best correction is achieved with the total atom number. We then estimate the effect of a residual oscillation of the cloud and of detectivity fluctuations: both appear to have negligible impact on the clock frequency stability. This will be followed by an analysis of the clock stability dependence with the bottom magnetic field. We finally present experimental optimizations of the Ramsey time and the atom number.

3.3.1 Measurement of the uncertainty on P_2

To characterize the uncertainty on the determination of the transition probability $P_2 = N_2/(N_1 + N_2)$ we performed a frequency-insensitive measurement ($T_R = 0$, no second pulse). Here a single $\pi/2$ pulse of 70 ms is applied to the cloud and the detection follows directly after. The standard deviation σ_{P_2} is obtained by repeating the experiment many times. Noise contributions are: the preparation $\sigma_{P_2,Rabi}$, the detection $\sigma_{P_2,det}$ and the projection noise $\sigma_{P_2,QPN}$. To discriminate between the three we make use of their different scaling with the total atom number N and repeat the experiment for various atom numbers (Figure 3.3). The total Allan deviation at one shot σ_{P_2} is given by the quadratic sum of the three contributions:

$$\sigma_{P_2} = \sqrt{\left(\frac{\sigma_{N_i,det}}{\sqrt{2}N}\right)^2 + \left(\frac{1}{2\sqrt{N}}\right)^2 + \sigma_{P_2,Rabi}}. \tag{3.22}$$

Experimental details The Double Detection method was used combined with bright frame recomposition. The times of flight were 8.5 ms for state $|1\rangle$ and 5.5 ms for $|2\rangle$. The fit of σ_{P_2} has two free parameters, $\sigma_{N_i,det}$ and $\sigma_{P_2,Rabi}$. We obtain $\sigma_{N_i,det} = 59$ atoms. The fit is consistent with $\sigma_{P_2,Rabi} < 1 \times 10^{-4}$ (see figure 3.3).

Effect of the atom number inaccuracy Figure 3.3 shows that the scaling at high atom numbers is consistent with the expected quantum projection noise. Since the latter depends on the atom number we conclude that the atom number inaccuracy does not affect the results shown here as times of flight larger than 5 ms were chosen, the threshold below which deviations occur (see figure 3.2).

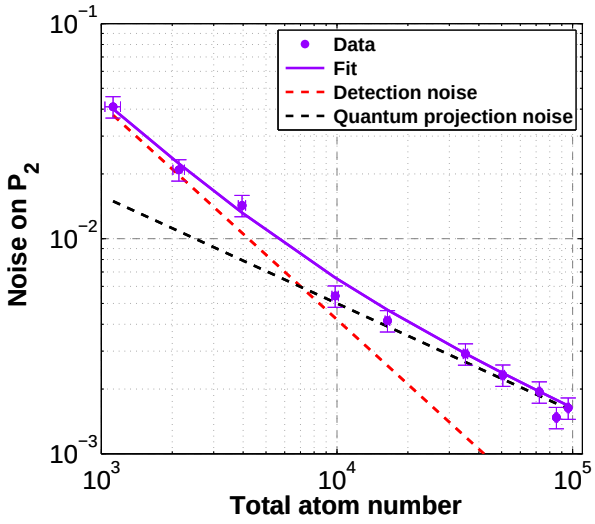

Figure 3.3: *P_2 Allan deviation at one shot as a function of the total atom number for times of flight of* 8.5 ms *for state* $|1\rangle$ *and* 5.5 ms *for* $|2\rangle$*. We fit the data with the quadratic sum of the detection noise* $\sigma_{P_2,det}$*, the quantum projection noise* $\sigma_{P_2,QPN}$ *and the preparation noise* $\sigma_{P_2,Rabi}$ *(equation 3.22). The fit gives* $\sigma_{N_i,det} = 59$ atoms *and is consistent with* $\sigma_{P_2,Rabi} < 1 \times 10^{-4}$*.*

Suggestion To measure the contribution $\sigma_{P_2,asym}$ of the asymmetric losses to the noise on P_2 (equation 3.17) a similar measurement should be carried out with a trapping time of T_R between the preparation pulse and the detection.

3.3.2 The best post-correction parameter

Figure 3.4 shows a comparison of the clock frequency Allan deviations for the same dataset with three different post-corrections: raw data, post-correction with the total atom number N, post-correction with the mean column density (i.e. correction with $N/(\sigma_y\sigma_z)$ where σ_i is the cloud gaussian size after TOF in the i direction).

The best correction is achieved with the total atom number, improving the stability at one shot from 3.1×10^{-13} to 1.8×10^{-13}. Further correcting with the cloud temperature worsens the clock frequency fluctuations. This indicates that even though we have cloud temperature fluctuations, our measurement of the cloud temperature is too noisy.

3.3.3 Cloud oscillation

If the cloud oscillates along x the interrogation frequency can be Doppler-shifted. A non-reproducible cloud oscillation would give a shot-to-shot noise on the clock frequency via the Doppler effect but also via the magnetic shift. Here we raise the question of the frequency noise caused by the residual oscillation along x that was identified (see section 2.4).

To do so we have performed a comparison of two clock frequency stability measurements: one with the usual $\{2.7, 92, 74\}$ Hz trap where the residual oscillation exists and one with a

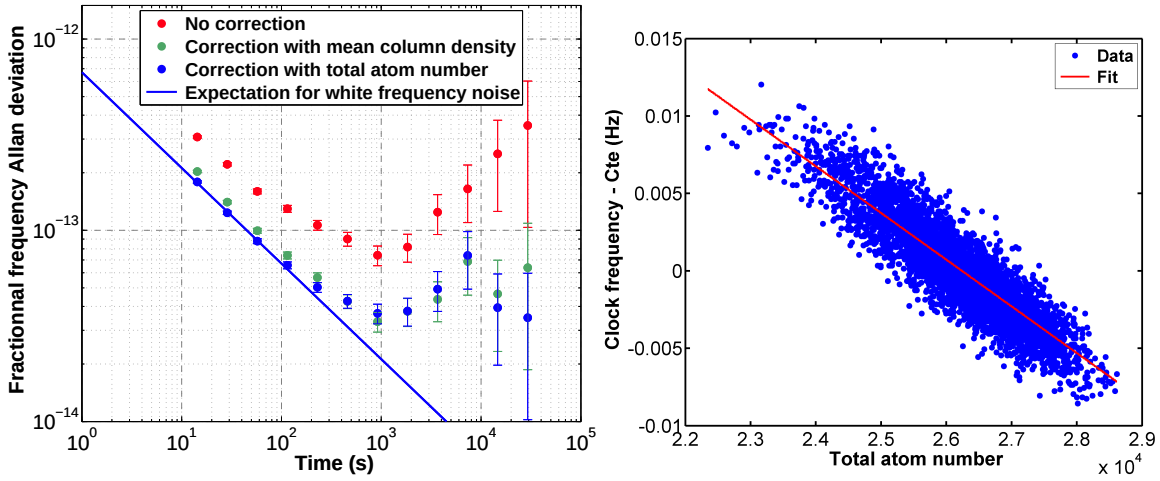

Figure 3.4: *(a) Allan deviation of the clock frequency after different treatments: raw data, post-correction with the total atom number and post-correction with the mean column density. The atom number post-correction reduces the frequency fluctuations at one shot from* 3.1×10^{-13} *to* 1.8×10^{-13}*. Further correcting with the cloud temperature makes them worse. We conclude that even though we have cloud temperature fluctuations we cannot correct for them because our measurement of the cloud temperature is not sensitive enough. (b) Typical correlation between the raw frequency data and the total atom number. A linear fit gives the post-correction function. The measured slope* $-3.1 \times 10^{-6}\,\mathrm{Hz\,atom^{-1}}$ *is* $\sim 50\,\%$ *larger that the theoretical prediction* $-1.9 \times 10^{-6}\,\mathrm{Hz\,atom^{-1}}$*, which is not yet understood.*

more confining trap of frequencies $\{17, 89, 76\}$ Hz where no oscillation was observed.

Changing the trap frequency changes the cloud density and affects all the noises that are density-dependent. To make a fair comparison between the two experiments we estimate and subtract all of the known noises that depend on density (correction, symmetric losses) and on atom number (detection, quantum projection noise). The comparison is shown in table 3.2. After the quadratic substraction, the rest is larger for the case with no oscillation. We conclude that the residual oscillation along x does not play a significant role in the frequency instability. Additionally, this result suggests the existence of an unidentified density-dependent noise: it could be caused by cloud temperature fluctuations.

3.3.4 Detectivity fluctuations

In this part we question the state detectivity fluctuation. In the double detection (DD) scheme the experiment is sensitive to the fluctuations of the Repump laser power and frequency. Conversely, in the adiabatic rapid passage (ARP) detection method such fluctuations do not play a role, whereas the imperfect transfer may play a role.

Table 3.3 shows a comparison of two stability measurements that differ only by the detection scheme: one was taken with the double detection and the other with the adiabatic rapid passage detection. As stressed previously the cloud image on the camera and therefore the detection noise are larger for the ARP detection. For a fair comparison we quadratically subtract the

Trap	Measured σ_y	$\partial f/\partial N$	$\sigma_{y,det}$	$\sigma_{y,QPN}$	$\sigma_{y,corr}$	$\sigma_{y,loss}$	Rest $\sigma_{y,rest}$
$\{17, 89, 76\}$ Hz	8.37	-7.5×10^{-6}	1.3	2.2	3.4	3.1	6.5
$\{2.7, 92, 74\}$ Hz	6.4	-2.6×10^{-6}	1.4	2.3	1.2	1.0	4.8

Table 3.2: *Comparison of clock frequency stability at* 1 s *(values given in the unit* $10^{-13}/\sqrt{\tau}$*) for two traps. In the tight trap there is no residual oscillation whereas there is one in the loose trap. The slope* $\partial f/\partial N$ *is given in* $\mathrm{Hz\,atom^{-1}}$*. We estimate the density-dependent and atom number-dependent noise.* $\sigma_{y,rest}$ *is obtained by (quadratic) subtraction of all known noises from the measured value. There is no striking difference in the rests between the two traps, which eliminates the residual oscillation from the list of dominant noise sources. The rest is even larger for the tight trap which suggests a density-dependent noise not yet identified.*

detection, correction and quantum projection noises from the measured frequency stability. After this operation the two rests have comparable amplitude: this indicates that Repump laser fluctuations are not a limiting contribution to the clock frequency noise.

Detection	Measured σ_y	$\partial f/\partial N$	$\sigma_{y,det}$	$\sigma_{y,QPN}$	$\sigma_{y,corr}$	Rest $\sigma_{y,rest}$
ARP	7.3	-2.39×10^{-6}	2.9	2.3	2.1	5.9
DD	6.8	-2.95×10^{-6}	1.1	2.0	1.3	6.3

Table 3.3: *Comparison of clock stability at* 1 s *(values given in the unit* $10^{-13}/\sqrt{\tau}$*) for the two detection schemes and comparable atom numbers. The slope* $\partial f/\partial N$ *is given in* $\mathrm{Hz\,atom^{-1}}$*. We estimate the detection, quantum projection and correction noise. After a quadratic subtraction the rests are nearly equal, showing that fluctuations of the Repump laser are to be erased from the list of dominating noise sources.*

3.3.5 Variation with the bottom magnetic field

List of the bottom field-dependent effects Magnetic noise is highly dependent on the value of the magnetic field at the trap bottom. When changing the field at the trap bottom, four effects are expected: (1) a direct fluctuation of the clock frequency $\sigma_{y,B,magn}$ caused by a variation σ_B of the magnetic field; (2) an indirect frequency fluctuation $\sigma_{y,T}$ caused by cloud temperature fluctuations; (3) changing the bottom field also changes the fringe contrast (see figure 3.5.b): if there is a remaining noise on P_2 it will translate into a magnetic-field dependent noise on the frequency; (4) the trap frequency change which impacts the cloud density.

The cloud density change (fourth effect) is on the order of 10 % over the range 3 G*to*3.3 G and can be neglected. The first effect is minimized at a field $\sim B_m - 5\,\mathrm{mG}$, the second one vanished for a field $\sim B_m - 35\,\mathrm{mG}$ whereas the third one is minimal at the compensation field $B_c \sim B_m - 35\,\mathrm{mG}$. The known noises on P_2 can be subtracted. In order to discriminate these contributions we have carried out a measurement of the clock frequency stability as a

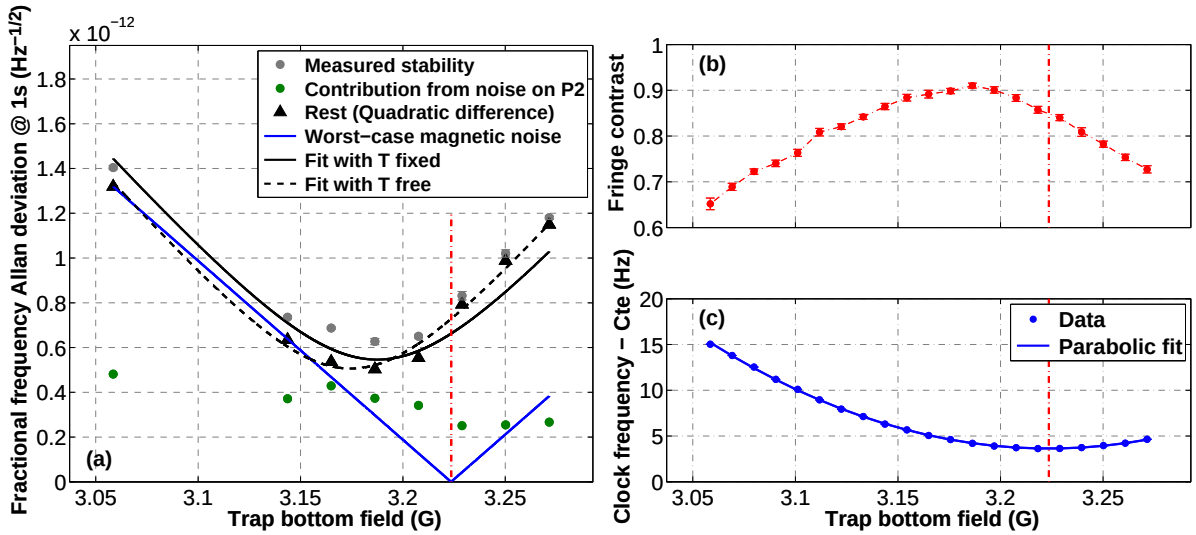

Figure 3.5: *(a) Stability at* 1 s *vs trap bottom magnetic field. For each point we subtract quadratically the noises on* P_2 *(detection and quantum projection noises) from the measured value. We can set a upper bound for the contribution of magnetic field fluctuations by attributing, for the highest point, all the remaining noise to* σ_B*. This gives the worst-case magnetic noise and* $\sigma_B(3\,\mathrm{s}) < 13\,\mu\mathrm{G}$*. Assuming the temperature fluctuations dominate we fit in the rest with the equation* $\sqrt{\sigma_0^2 + \sigma_{y,T}^2}$ *(*$\sigma_{y,T}$ *is given by equation 3.9 and* σ_0 *is a constant value). For a fixed cloud temperature* $T = (T_x T_y T_z)^{1/3} = 80\,\mathrm{nK}$ *we obtain* $\sigma_0 = 5.5 \times 10^{-13}/\sqrt{\tau}$ *and* $\sigma_T = 0.5\,\mathrm{nK}$ *but a bad convergence. Setting* T *free gives* $\sigma_0 = 5.1 \times 10^{-13}/\sqrt{\tau}$*,* $\sigma_T = 0.5\,\mathrm{nK}$ *and* $T = 125\,\mathrm{nK}$*, which is a reasonable value. (b) Fringe contrast as a function of the trap bottom magnetic field. The maximum contrast defines the compensation field* B_c*. (c) Clock frequency dependence with the trap bottom magnetic field, defining the magic field* B_m*.*

function of the bottom magnetic field. Figure 3.5.a shows the raw data together with data after quadratic subtraction of all the known noises on P_2 (detection and quantum projection noises). We observe that the rest is minimum for a field $\sim B_m - 40\,\mathrm{mG}$.

Upper bound for the magnetic noise We can first give an upper bound for $\sigma_B(3\,\mathrm{s})$ by considering the highest point and assuming all the remaining noise is magnetic. We obtain $\sigma_B(3\,\mathrm{s}) < 13\,\mu\mathrm{G}$ and we can put an upper bound for the contribution of magnetic field fluctuations for each point (see figure 3.5).

Upper bound for the cloud temperature noise We now assume that the effect of cloud temperature fluctuations dominates the two others. We fit the data with the function $\sqrt{\sigma_0^2 + \sigma_{y,T}^2}$ where $\sigma_{y,T}$ is given by 3.9 and σ_0 is constant and accounts for other noises that do not depend on B_0. If we force the mean temperature to $T = (T_x T_y T_z)^{1/3} = 80\,\mathrm{nK}$ the fit does not converge properly. If T is set free the fit converges towards $T = 125\,\mathrm{nK}$, $\sigma_0 = 5.1 \times 10^{-13}/\sqrt{\tau}$ and $\sigma_T = 0.5\,\mathrm{nK}$. These values are reasonable considering the atom number was not constant during the measurement but varied by factor ~ 2 between the two extremes: $T = 80\,\mathrm{nK}$ was measured for 4×10^4 atoms and we know that the atom number

plays a role in the cloud temperature.

Remaining noise on P_2 If the rest was an unidentified noise on P_2 one should observe a linear dependence with the fringe contrast C. With the present data we can not exclude such a contribution.

Conclusion Our data is consistent with a cloud temperature $T = 125\,\mathrm{nK}$, a fluctuation of $\sigma_T/T = 1.4\,\%$ and no additional noise on P_2. When summing up all the other effects (local oscillator, losses, correction) we obtain $3.3 \times 10^{-13}/\sqrt{\tau}$ which is sensibly smaller than σ_0. We conclude that if our assumption of pure temperature noise is true, there is still an unknown contribution to the clock frequency noise of amplitude $3.9 \times 10^{-13}/\sqrt{\tau}$. To confirm or quash this assumption one would need further measurements: for example a determination of the frequency sensitivity to cloud temperature as a function of the magnetic field.

3.3.6 Optimizing the Ramsey time

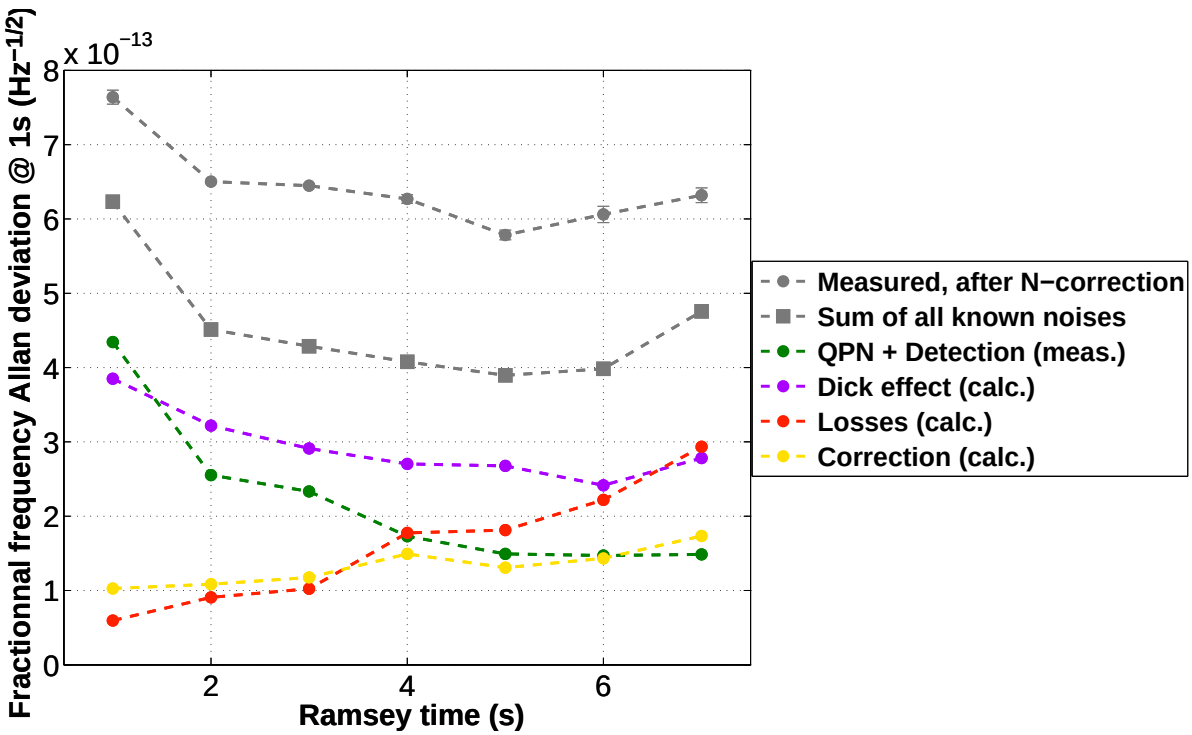

Figure 3.6: *Stability at* 1 s *vs Ramsey time* T_R*. The cycle time is* $T_c = T_R + 11\,\mathrm{s}$*. From left to right: the clock quality factor increases and the Dick effect decreases; the effect of atomic losses becomes more and more significant, and in the stability at one second the cycle time plays a role by the extrapolation to* 1 s *(effect of the factor* $\sqrt{T_c}$*). An optimal Ramsey time is observed at* 5 s.

An interesting feature of trapped atomic clocks is the possibility to change the interrogation time T_R. In a shot noise-limited clock for $T_R \ll T_c$ the stability scales as $1/T_R$ and whereas for

$T_R \sim T_c$ it scales as $1/\sqrt{T_R}$: in principle it is always profitable to increase the Ramsey time. In practice the Ramsey time is bounded by the fringe contrast decay time and atomic losses. The sampling of the local oscillator frequency noise is modified when the duty cycle T_R/T_c is changed.

To measure the optimal Ramsey time we repeated the experiment for T_R between 1 s and 7 s whilst keeping all other parameters constant (apart from the cycle time equal to $T_c = T_R + 11\,\mathrm{s}$). The results are shown in figure 3.6. From this measurement we conclude that our system is not yet sensitive to the Dick effect. We observe an optimum for $T_R = 5\,\mathrm{s}$ giving a short-term clock frequency stability of $5.8 \times 10^{-13}/\sqrt{\tau}$ (see section 3.4 for a detailed discussion of this result).

3.3.7 Optimizing the atom number

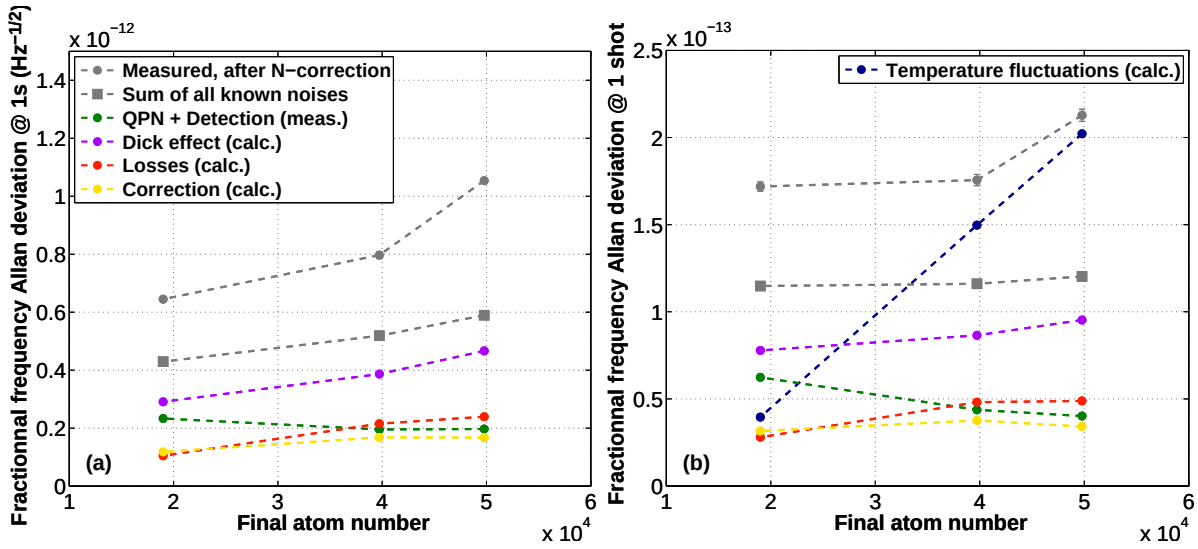

Figure 3.7: *Clock frequency stability for various atom numbers (a) extrapolated to* 1 s *and (b) at one shot. In the latter there is no effect of the cycle time increase. We observe an degradation of the frequency stability as the number of atoms increases, suggesting the presence of a density-dependent effect. A cloud temperature fluctuation of* 1.4 % *does not explain the missing noise, especially at low atom numbers.*

In this section we investigate the stability dependence with the number of interrogated atoms, which may help to identify the remaining unknown noise. All other parameters are equal apart from the MOT loading time (and therefore the cycle time). We observe on figure 3.7.a that the missing contribution at 1 s increases with the atom number. This could simply be an effect of the increased cycle time. Figure 3.7.b shows the stability at one shot where the latter effect is not included. A similar behavior is observed which suggests that the unknown noise depends on the cloud density. A temperature fluctuation of 1.4 % computed with the mean atom number does not explain the unidentified noise: it is too high at large atom numbers and too small at small atom numbers. By repeating this measurement on a wider range of atom numbers and densities and with a constant cycle time (to keep the Dick effect constant) one must be able to get more insight on the missing noise.

3.4 Best frequency stability up-to-date

In this section we present in more detail the best frequency stability observed so far. It was acquired for $T_R = 5\,\mathrm{s}$ and $N = 4 \times 10^4$ atoms initially obtained with the bottom magnetic field at compensation value B_c and a cycle time of 16 s. The data are the same as in figure 3.6).

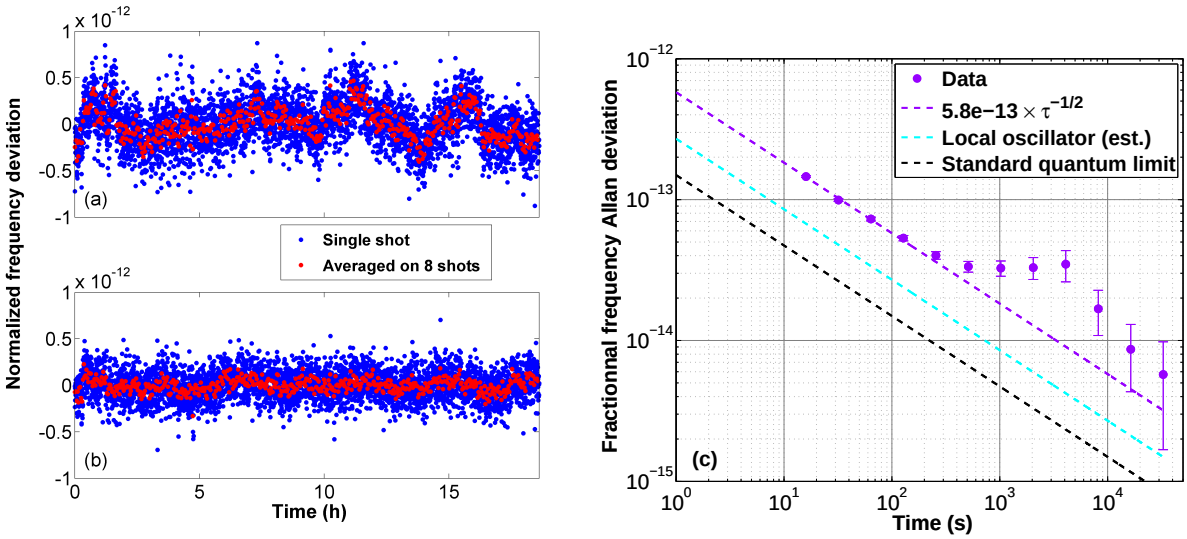

Figure 3.8: *Clock frequency fluctuations for a stability measurement with* $T_R = 5\,\mathrm{s}$ *and* $N = 4 \times 10^4$ atoms *initially. (a) normalized frequency deviation before the correction with the atom number and (b) after the correction. (c) Allan deviation of the clock frequency after correction that shows a white frequency noise until* $\sim 130\,\mathrm{s}$*, corresponding to* 8 *shots. On (a) and (b) we report the value averaged on* 8 *shots, which exhibits the long-term fluctuations. Long term fluctuations on the time scale of* $\sim 1\,\mathrm{h}$ *can be seen on both (b) and (c). It may be a thermal effect.*

Contribution	**Amplitude** σ_y @1 s
Measured, after correction	5.8×10^{-13}
Local oscillator	2.7×10^{-13}
Symmetric losses	1.8×10^{-13}
Quantum projection	1.5×10^{-13}
Correction	1.3×10^{-13}
Detection	9×10^{-14}
Missing	4.3×10^{-13}

Table 3.4: *Summary of the contributions of the dominant noise sources for the best measured clock frequency stability at* 1 s*. All values are given in the unit* $Hz^{-1/2}$*. The missing contribution could be a cloud temperature fluctuation or an additional noise on* P_2*.*

Figure 3.8 shows the time variations of the raw frequency data and after the post-correction,

as well as the Allan deviation of the corrected frequency. It integrates as white frequency noise up to 8 shots ($\sim 130\,\mathrm{s}$). In figure 3.8.b we have also reported the data averaged over 8 shots, which gives a better sensitivity to search for long term drifts or fluctuations. Long term fluctuations on the time scale $\sim 1\,\mathrm{h}$ appear and correspond to the bump at 4000 s of the Allan deviation. They could be thermal effects.

Table 3.4 gives a breakdown of the relevant contributions to the clock frequency noise at 1 s. The missing contribution amounts to $\sigma_y = 4.3 \times 10^{-13}/\sqrt{\tau}$. Our analysis permits to exclude magnetic frequency noise, detectivity fluctuations and effects of the cloud residual oscillation. Cloud temperature fluctuations must have low impact in these conditions. An unidentified noise on P_2 could be explain this remaining noise.

3.5 Long term thermal effects

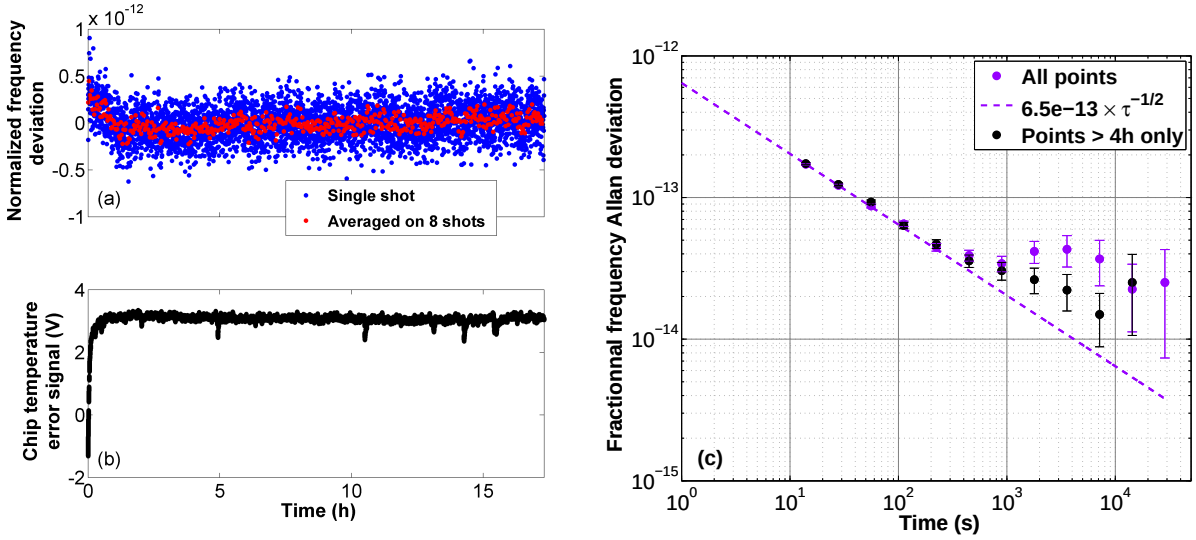

Figure 3.9: *(a) Normalized frequency deviation for a stability measurement with* $T_R = 3\,\mathrm{s}$ *and* $N = 4 \times 10^4$ atoms *initially, where the experiment was initially cold at rest for some hours. (b) Image of the temperature of the copper bloc glued on the atom chip. The heating of the experiment can be clearly seen during the first hour. Spikes at later times correspond to irregularities of the clock cycle time. (c) Allan deviation of the corrected fractional frequency. When removing the first* 4 h *of data the oscillation at* 1 h *reduces, suggesting a thermal effect of the chip.*

If the experiment was off for some hours before a stability measurement is started we observe an initial drift of the clock frequency. It is correlated to the signal of a thermistance placed on the copper bloc that holds the chip (figure 3.9). The corresponding Allan variance is shown in figure 3.9.c.

When removing the first 4 h of data one reduces the amplitude of the oscillation at $\sim 4000\,\mathrm{s}$ (figure 3.9.c). It suggests that this oscillation is caused by a thermal effect on the chip.

3.6 Conclusion

In this chapter we have given a detailed description of all possible sources of noise on the clock frequency identified so far. We have carried out an experimental investigation of the unidentified technical noise.

Our measurements show that this noise is not predominantly due to magnetic field fluctuations. We have shown that the missing noise is dominated neither by an effect of the residual cloud oscillation nor by a fluctuation of the Repump laser. A good candidate for most of this noise is a cloud temperature fluctuation: a shot-to-shot fluctuation of 1.4 % would be enough to explain part of it. We have suggested measurements that could be done in the future to confirm or infirm this hypothesis. Cloud temperature fluctuations can be caused by fluctuations of the atom number(but in this case they would be eliminated by the post-correction procedure) or fluctuations of the cooling parameters (laser detuning, magnetic field, radiofrequency power...). Even with the assumption of a cloud temperature noise of 1.4 % (an upper limit), a noise of amplitude $\sim 4 \times 10^{-13}/\sqrt{\tau}$ remains to be identified. This noise could be appearing on P_2 at long trapping times (for example, an effect of the asymmetric losses, or another decoherence effect which has not been identified). To verify this point a frequency-insensitive measurement of P_2 noise for long trapping times is needed.

We have nevertheless performed an optimization of the clock Ramsey time and found an optimum of the best short-term stability of $5.8 \times 10^{-13}/\sqrt{\tau}$ for $T_R = 5\,\mathrm{s}$. At this working point contributions from the symmetric losses and noise of the local oscillator were found to be significantly higher than the projection noise.

The effects of trap losses will be mechanically smaller with a better quality vacuum. The Dick effect contribution would be lowered by referencing the interrogation signals to a sapphire cryogenic oscillator instead of the maser. It could also be reduced by increasing the T_R/T_c ratio, currently equal to $\sim 20\,\%$. This would require an acceleration of the cloud preparation time: MOT loading time, evaporative cooling time and ramp times.

For shortening the MOT loading time two options are available: (1) a double-chamber setup for example with the well-established technique of the 2D-MOT; (2) a single-chamber setup where the rubidium pressure is modulated in time. The latter bears the two advantages of compactness and simplicity. In chapter 7 we present an experimental study of fast rubidium pressure modulation for this purpose and discuss its limitations. To speed up the evaporation step (currently: 3.3 s) one could go to tighter traps. Cooling times of 1 s have been demonstrated on atom chip setups [64]. Finally the transfer ramp could be shorten by using a new trap that is not displaced along x. There are methods to shortcuts the adiabaticity during the decompression [65].

The frequency noise from symmetric atom losses may at some point become a limiting factor. Assuming a total preparation time of 1 s, comparable densities, trap lifetimes of 1 min, $T_R = 20\,\mathrm{s}$ and $C = 0.9$ this noise amounts to $7 \times 10^{-14}/\sqrt{\tau}$, equivalent to the projection noise of 8×10^3 atoms. Only a further reduction of the density would make this contribution lower.

Chapter 4

Bose-Einstein condensates for time metrology

Since Bose-Einstein condensates in dilute gases were obtained in 1995 [66, 67], a large amount of theoretical and experimental work has been done to understand their coherence properties. Thought of as macroscopic matter waves, Bose-Einstein condensates (BECs) behave in many ways like coherent radiation fields, and can exhibit interferences. However, unlike photons of a laser field, atoms in a BEC interact strongly with each other, which has consequences for their spatial dynamics and coherence properties.

A particularly interesting problem is the evolution of the coherence between two condensates initially prepared in a state with a well defined relative phase, as in a Ramsey interrogation. The coherence defines the fringe contrast C and the clock stability at the standard quantum limit which scales as $1/(C\sqrt{N})$. Due to evaporative cooling BECs typically contain fewer atom than thermal clouds. They have much higher densities (typically a factor 100 more) than thermal clouds, which enhances the role of interactions and the corresponding frequency noise. As a consequence of their small atom numbers and high densities one might expect BECs to be less efficient timekeepers than thermal clouds. However, one advantage of BECs is the possibility of creating interaction-driven spin-squeezed states [68], opening the path for metrology beyond the standard quantum limit.

Another key advantage of using BECs for precision measurements lies in their small size making them the best suited for high spatial resolution experiments: for example in the magnetic field cartography [69] or measurement of deviations from Newton's law at short distances [70]. At LNE BECs were chosen for application in their absolute atomic gravimeter because their small size will reduce systematic effects from the laser's wavefront curvature [71].

Our experimental setup is particularly well suited for the study of the coherence in BECs as it was built under metrological constraints. These constraints include fast production rate (typically every 20 s), repeatability, extremely good control over the magnetic fields and an ultra-low noise local oscillator. Recently, Ramsey contrasts of 0.75 at 1.5 s were measured in BECs of 5.5×10^4 ^{87}Rb atoms and modeled by a combination of state-dependent spatial dynamics, technical noise and quantum phase diffusion (or phase collapse) [72]. The direct observation of the latter is a particularly exciting experimental challenge.

In this chapter we present a study of the coherence of BEC superpositions. We will begin

by introducing the Gross-Pitaevskii equation as well as its numerical modeling. Following this we will describe measurements of the BEC properties including condensed fraction and state lifetimes. We will then report on our observations of the state-dependent spatial dynamics which is qualitatively reproduced by a numerical simulation. We shall investigate the phase coherence of BECs using Ramsey spectroscopy, in particular, as a function of the interrogation time, number of atoms and clock frequency spatial inhomogeneity. We will also report on the existence of a sweet spot for the clock frequency with respect to atom number fluctuations across the condensation threshold. Finally, we discuss the effects of interactions of the collective spin dynamics and give theoretical predictions to explain these.

4.1 Theory of a dual component BEC

We begin this chapter with a general description of BEC. Firstly we will describe the general hypotheses used in the explanation of a single component BEC, and from this an extension of the theory applying to a dual component BEC. Secondly we will introduce the phenomenon of state-dependent spatial dynamics. Finally we shall describe the numerical modeling that we have developed.

4.1.1 The Gross-Pitaevskii equation for a single component

As in [73] we start with the hamiltonian governing the evolution of the field operator (equation 1.13) derived in the Born approximation, for a single component. We decompose the field operator $\hat{\psi}$ in the basis of single-particle wavefunctions $\{\varphi_i\}$:

$$\hat{\psi}(\mathbf{r}) = \varphi_0(\mathbf{r})\hat{a}_0 + \sum_{i\neq 0} \varphi_i(\mathbf{r})\hat{a}_i. \tag{4.1}$$

The Bogoliubov approximation consists of ignoring the noncommutativity of $\hat{a}_0$ and $\hat{a}_0^\dagger$ and is valid in the case $N = \langle \hat{a}_0^\dagger \hat{a}_0 \rangle \gg 1$ (BEC corresponds to a macroscopic occupation of the state φ_0). In this approximation the $\varphi_0\hat{a}_0$ component is treated as a classical field $\psi_0 = \sqrt{N}\varphi_0$, also called the BEC order parameter. It is a complex number, $\psi_0(\mathbf{r}) = |\psi_0(\mathbf{r})|e^{i\theta(\mathbf{r})}$. If we approximate that $\delta\hat{\psi}(\mathbf{r}) = \sum_{i\neq 0} \varphi_i(\mathbf{r})\hat{a}_i$ is negligible (system at zero temperature), the time evolution is given by the Gross-Pitaevskii equation (GPE):

$$i\hbar\partial_t\psi_0(\mathbf{r},t) = \left(\frac{-\hbar^2\nabla^2}{2m} + U(\mathbf{r}) + g|\psi_0(\mathbf{r},t)|^2\right)\psi_0(\mathbf{r},t), \tag{4.2}$$

where $g = 4\pi\hbar^2 a/m$ and a is the scattering length. The many-body wave function of the system takes the form:

$$\Phi(\mathbf{r}_1, ..., \mathbf{r}_N) = \left(\frac{1}{\sqrt{N}}\psi_0(\mathbf{r}_1)\right) ... \left(\frac{1}{\sqrt{N}}\psi_0(\mathbf{r}_N)\right). \tag{4.3}$$

Stationary states

Stationary solutions are of the form $\psi_0(\mathbf{r})e^{-i\mu t/\hbar}$, where $\mu = \partial E/\partial N$ is the chemical potential.

4.1.2 Gross-Pitaevskii system for a dual component BEC

The case of a mixture of two states leads to a set of coupled Gross-Pitaevskii equations for the order parameters. A new inter-component interaction term appears:

$$i\hbar\partial_t\psi_1(\mathbf{r},t) = \left(\frac{-\hbar^2\nabla^2}{2m} + U_1(\mathbf{r}) + g_{11}|\psi_1(\mathbf{r},t)|^2 + g_{12}|\psi_2(\mathbf{r},t)|^2\right)\psi_1(\mathbf{r},t) \tag{4.4}$$

and symmetrically for state $|2\rangle$;

$$i\hbar\partial_t\psi_2(\mathbf{r},t) = \left(\frac{-\hbar^2\nabla^2}{2m} + U_2(\mathbf{r}) + g_{22}|\psi_2(\mathbf{r},t)|^2 + g_{12}|\psi_1(\mathbf{r},t)|^2\right)\psi_2(\mathbf{r},t). \tag{4.5}$$

Collisional shift of the clock frequency In the spatially homogeneous case the phase difference between the two wavefunctions equals

$$\theta_2 - \theta_1 = \Big([g_{22}n_2 - g_{11}n_1 + g_{12}(n_1 - n_2)] + (U_2 - U_1)\Big)\frac{t}{\hbar}, \tag{4.6}$$

where the term in square brackets is nothing more than the collisional shift (equation 1.16).

Atom losses Three-body recombination losses dominate in a pure $|1\rangle$ BEC (with the rate γ_{111}), but two-body inelastic collisions dominate in a pure $|2\rangle$ BEC (with the rate γ_{22}) and in a mixed BEC (with the rate γ_{12}) [74]. To account for the losses, one can add the phenomenological terms $-i\hbar[\gamma_{111}|\psi_1(\mathbf{r},t)|^4 + \gamma_{12}|\psi_2(\mathbf{r},t)|^2]\psi_1(\mathbf{r},t)/2$ into equation 4.4 and $-i\hbar[\gamma_{22}|\psi_2(\mathbf{r},t)|^2 + \gamma_{12}|\psi_2(\mathbf{r},t)|^2]\psi_1(\mathbf{r},t)/2$ into equation 4.5.

4.1.3 State-dependent spatial dynamics

Two quantum fluids will be miscible or immiscible, depending on the values of the interaction parameters. Phase separation of quantum fluids was observed long ago in ^{3}He-^{4}He mixtures. For binary mixtures of BECs, which can be thought of as two interacting quantum fluids, phase separation also occurs.

We consider a dual component BEC and make the additional assumptions that (1) the gases are confined in a square box and that (2) the Thomas-Fermi approximation can be made. We also neglect, for now, any energy difference between the two spin states. For a uniform mixture of the two components the energy of the system reads [73]:

$$E_{unif} = \frac{g_1}{2}\frac{N_1^2}{V} + \frac{g_2}{2}\frac{N_2^2}{V} + g_{12}\frac{N_1N_2}{V} \tag{4.7}$$

and for a phase-separated configuration, where the two components do not overlap at all:

$$E_{separ} = \frac{g_1}{2}\frac{N_1^2}{V_1} + \frac{g_2}{2}\frac{N_2^2}{V_2}, \tag{4.8}$$

where V_1 and V_2 are the volumes occupied by the two components ($V = V_1 + V_2$). When writing the condition of mechanical equilibrium between the two phases ($\partial E_{separ}/\partial V_1 = \partial E_{separ}/\partial V_2$) we can express E_{separ} as

$$E_{separ} = \frac{g_1}{2}\frac{N_1^2}{V} + \frac{g_2}{2}\frac{N_2^2}{V} + \sqrt{g_1 g_2}\frac{N_1 N_2}{V}. \tag{4.9}$$

When comparing with equation 4.7 one can see that the condition for having phase separation ($E_{separ} < E_{unif}$) is

$$g_{12} > \sqrt{g_1 g_2}. \tag{4.10}$$

In this condition the ground state of the system is made up of two wavefunctions that are separated in space. If the two wavefunctions are initially superimposed, the system will undergo state demixing and remixing.

In the case of a non-uniform gas (for example in a harmonic trap), there is no analytical treatment.

Prior observations of demixing for ^{87}Rb The first observations of demixing of a BEC mixture of ^{87}Rb in the spin states $|1\rangle$ and $|2\rangle$ goes back to 1998 [75]. The atoms were initially in $|1\rangle$ and were prepared in the ground state of the potential. A $\pi/2$ pulse was applied to place the BEC in a state superposition. The system relaxed to a state where species $|1\rangle$ had the spatial form of a shell, creating a crater in which the atoms in $|2\rangle$ could reside. Due to the hierarchy $a_{11} > a_{22}$ in the scattering lengths, atoms in the $|1\rangle$ state tend to stay at the periphery of the trap. This is in agreement with the prediction of 4.10, although derived for homogeneous BECs.

More recently, [74] reports the observation of demixing of the same states. The author's experiment can be reproduced with very good accuracy by a numerical resolution of the coupled Gross-Pitaevskii equations that include the loss terms . In [50] the same experiment was reproduced on an atom chip setup and analyzed using the same model. Finally, such a state demixing was also observed in a dipole trap with the magnetic-insensitive clock transition of ^{87}Rb [76, 77].

Consequences for the fringe contrast When the second $\pi/2$ pulse is applied to the atomic cloud, it only drives those atoms in the wavefunction overlap region. That is, if states demix and remix, one must observe oscillations of the contrast driven by the state dynamics.

4.1.4 Numerical modeling

To the best of our knowledge there is no analytical treatment for the spatial dynamics of a BEC superposition. Due to the intrinsic non-linearity of the interaction term a numerical simulation is required.

We perform a 3-dimensional numerical integration of the coupled GPEs with the time-splitting spectral method [78]. We use a $\{x, y, z\}$ grid of $\{60 \times 10 \times 10\}$ points spaced by $\{0.5, 0.2, 0.2\} \times a_{ho,x}$ ($a_{ho,x} = \sqrt{\hbar/(m\omega_x)}$). Trap frequencies are $\{2.9, 92, 74\}$ Hz (measured). The mesh is chosen to be smaller than the typical healing length in the center of the BEC, $\xi = 1/\sqrt{8\pi n(0) a_{11}}$ ($1.2 \times a_{ho,x}$ for 10^4atoms in $|1\rangle$). Time steps of $2 \times 10^{-4}/\omega_x$ ensure negligible numerical noise: we have checked that the simulation conserves the norm of the wavefunction

to the $< 1 \times 10^{-11}$ level up to 5 s of evolution.

The ground state of the system is obtained by propagation in imaginary time. As this evolution is non-unitary the wavefunction is renormalized at each time step. This approach causes exponential damping of all modes but the ground state.

For now we neglect the term $\beta(B(\mathbf{r}) - B_m)$ and give the two states an identical trapping potential. The values for two-body and three-body loss coefficients are take from [74]=. A one-body loss term with a time constant $\tau = 6$ s is added to account for the losses from collisions with atoms from the background.

In the case $\omega_x \gg \omega_\perp = \omega_y = \omega_z$ [79] the 3D equation can be approximated using a 1-dimensional model. We chose $\omega_\perp = \sqrt{\omega_y \omega_z}$ and find that this approximate model gives data that are close to the 3-dimensional solution. This 1D model gives a first approximation of the physical behavior and is particularly useful if a fine grid is needed. In fact, as exposed in the following, the dynamics in the experiment is essentially 1D.

These numerical simulations are valuable tools required to understand the experimental data presented in the subsequent sections of this chapter.

4.2 Preparing Bose-Einstein condensates

In this part we detail the procedure and results of the characterization of our BECs including: temperature and condensed fraction measurements, critical temperature and lifetimes of the clock states.

4.2.1 Condensed fraction measurements

A common method used to determine the condensed fraction is to fit a bimodal distribution of the cloud density profile. In the Thomas-Fermi limit, the BEC density profile is well approximated by a reversed parabola, whereas the cloud shape of the thermal phase is given by a gaussian profile.

We perform the BEC purity analysis in a tighter trap (frequencies $\times \{264, 266, 274\}$ Hz). In this trap the Thomas-Fermi approximation is valid and the bimodal fit is justified. The transfer into the dilute trap ($\{2.9, 92, 74\}$ Hz) is adiabatic such that it lowers the cloud temperature. Thus, the results given here are upper bounds for the temperature and lower bounds for the condensed fraction in the dilute trap.

There is an issue with bimodal fit of small BECs; the Thomas-Fermi profile is indeed only valid for the central part of the condensate, where the density is large [73]. On the wings of the condensate the cloud profile is smooth, much like the wings of a gaussian. This can lead to bad convergence of a bimodal fit, resulting in the gaussian profile converging on the condensate. To circumvent this, we use the following procedure inspired by [80]: (1) the image is split into two parts: a central region larger than the expected size of the condensate and an outer region containing only the thermal part; (2) we fit a gaussian profile onto the second region, this

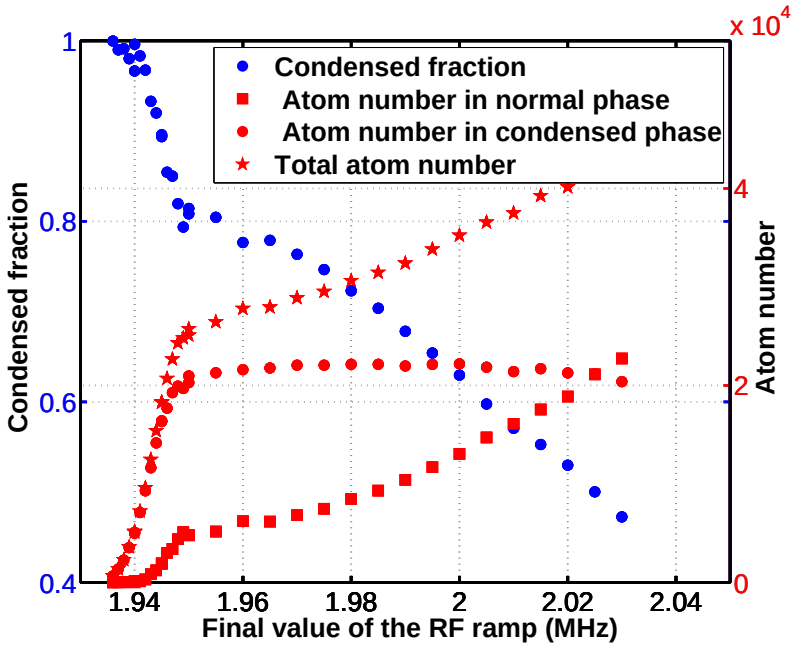

Figure 4.1: *Condensed fraction and atom number in each phase as a function of the final value of the RF cooling ramp F_{stop}. The analysis is done in a tighter trap with frequencies $\sim 2\pi \times 268$ Hz in all three axes. We demonstrate the production of BECs of 10^4atoms with a purity level exceeding 95 %. Thanks to adiabatic decompression the purity level is equal or higher in the dilute trap. For $F_{stop} < 1.95$ MHz the radiofrequency starts to outcouple atoms from the BEC itself.*

gives an estimation of the thermal part; (3) we fit the central part with a pure parabolic profile.

The results of this analysis can be seen in figure 4.1 as a function of the final value of the radiofrequency cooling ramp F_{stop}. For all the data points, the number of atoms loaded into the initial trap was at the maximum (MOT loading time of 20 s). On this figure one can clearly see the point at which the radiofrequency starts to outcouple atoms from the BEC itself ($F_{\text{stop}} < 1.95$ MHz).

4.2.2 Critical temperature

To check the validity of our results we have compared them to the non-interacting theory. The thermodynamics of the non-interacting Bose gas confined in a 3 dimensional harmonic potential gives the well-known formula for the critical temperature T_c, below which a macroscopic occupation of the ground state occurs [73]:

$$T_c = \frac{\hbar\overline{\omega}}{k_B}\left(\frac{N}{\zeta(3)}\right)^{1/3} \simeq 0.94\frac{\hbar\overline{\omega}}{k_B}N^{1/3}, \tag{4.11}$$

as a function of the total number of particles N and the geometric mean of the trap frequencies $\overline{\omega}/(2\pi)$. The number of condensed atoms N_0 is related to the temperature T via

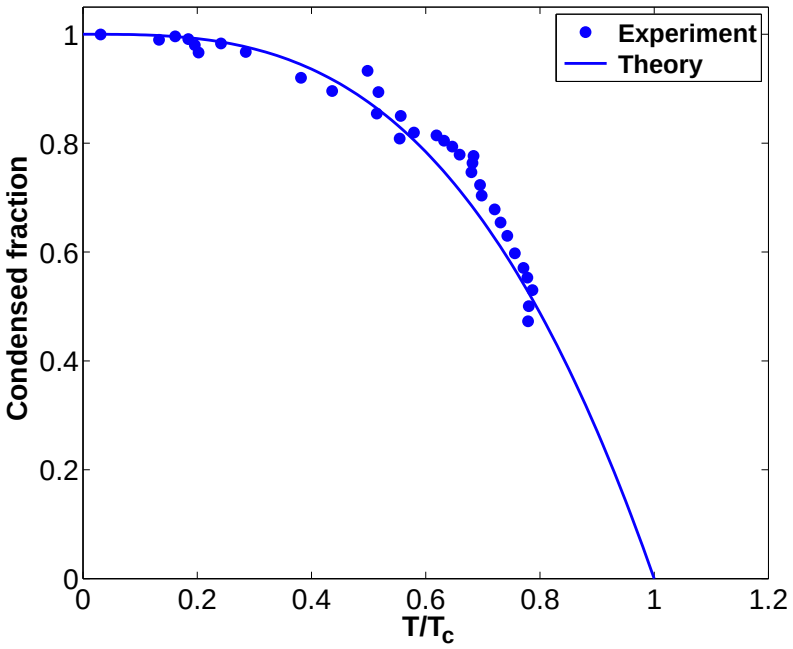

Figure 4.2: *Condensed fraction as a function of the ratio T/T_c. The theory is given by 4.12 and 4.11 and contains no adjustable parameter.*

$$\frac{N_0}{N} = 1 - \left(\frac{T}{T_c}\right)^3 . \tag{4.12}$$

We show on figure 4.2 the condensed fraction N_0/N as a function of the ratio T/T_c. Our data shows qualitative agreement with the independent prediction for the non-interacting Bose gas. For an interacting Bose gas containing a finite number of atoms data points are expected below the interaction-free theory curve. In [81] it was shown that this shift is about 20 % for 5×10^3 atoms confined in a spherical trap of frequency 236 Hz. Adopting this number, since our experimental conditions are fairly comparable, we conclude that our method overestimates the condensed fraction by $\sim 20\,\%$. The number given above must be refined: our BECs of $< 1 \times 10^4$ atoms have a purity level of $> 75\,\%$.

In fact, as stated before, the cloud temperature is much lower in the dilute trap. The lower bound given above is thus a conservative number for the dilute trap. A more qualitative but widely used approach is to quantify the thermal phase by looking at the the cloud image. In the dilute trap and for $N < 1 \times 10^4$ atoms we see no thermal atoms, suggesting that the BECs are almost pure.

4.2.3 BEC lifetimes

Lifetime measurements are done by preparing a 50/50 state superposition and counting the remaining atoms as a function of the trapping time. We obtain typical lifetimes of 5 s for state $|1\rangle$ and 2 s for state $|2\rangle$ (see figure 4.3). For comparison the values measured with a thermal cloud are both in the order of 6 s, limited by collisions with the background gas. We conclude

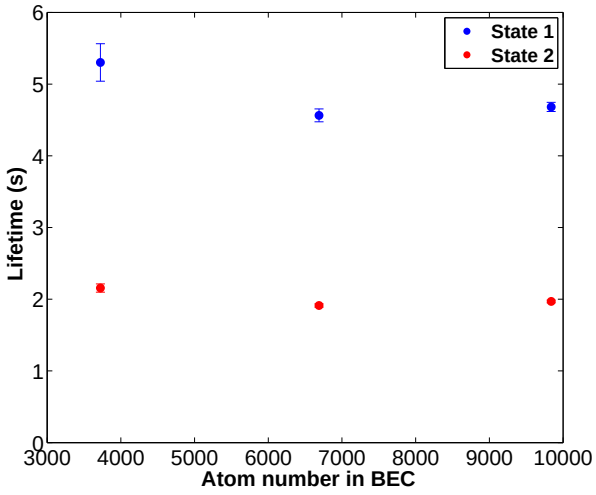

Figure 4.3: *BEC lifetimes in the dilute trap for an initial* 50/50 *state superposition and their dependence on the number of atoms. The background-limited lifetime is* 6 s*, such that the BEC lifetimes in this trap are dominated by inelastic collisions.*

that both lifetimes are limited by the two-body and three-body inelastic collisions in the BEC.

To be able to give numbers for these rates one needs to measure the decay constant of a pure $|2\rangle$ cloud, which has not yet been done. For our simulation we will rely on the values reported in [74], although these values give lifetimes (typically: 3.5 s for $|1\rangle$ and 1.4 s for $|2\rangle$) that are shorter than our experimental values.

4.3 State-dependent spatial dynamics

In this part we present our studies of the BECs spatial dynamics after preparing the system in an equal state superposition. Because of the differences in the scattering lengths the ground states are different for N atoms in state $|1\rangle$ or $N/2$ atoms in each clock state. The preparation procedure is as follows: first a BEC is created in state $|1\rangle$ in the ground state of the potential; a resonant $\pi/2$ pulse of 12.5 ms is applied, this prepares the system in an excited, non-stationary state. The atoms are kept in the trap for some time t and are finally imaged along the y axis after a 30 ms time of flight.

4.3.1 Experimental observations

We only observe dynamics in the x direction, corresponding to the weakest confinement. Figure 4.4 shows the typical density profiles integrated along y and z for a BEC of 1×10^4 atoms initially. State $|1\rangle$ tends to occupy the periphery of the trap and splits into two parts after $\sim$ 0.6 s. Conversely $|2\rangle$ is attracted towards the trap center and becomes denser in the same timescale. After $\sim$ 1.1 s a remixing of the states is observed. This is followed by a second demixing/remixing.

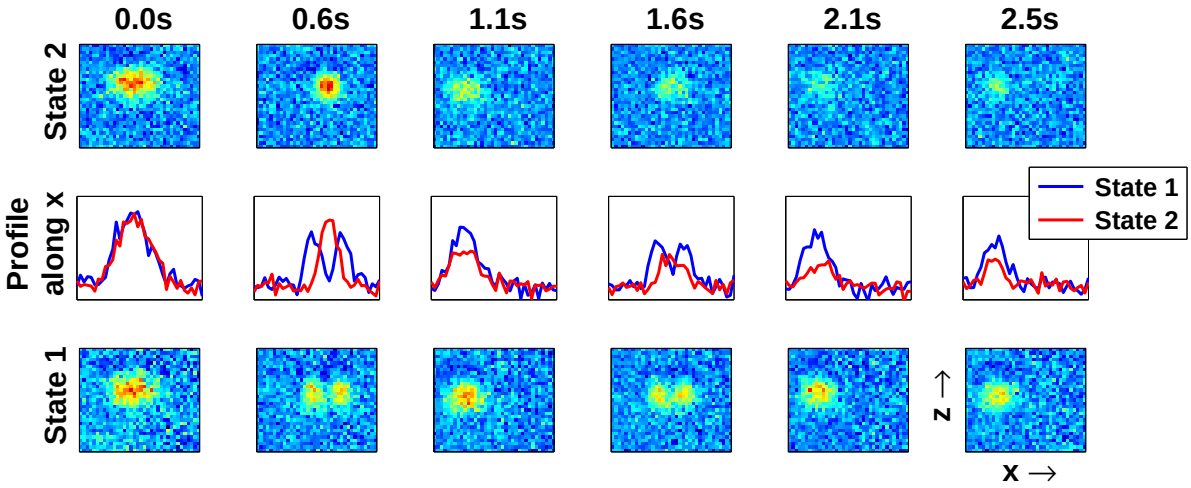

Figure 4.4: *Typical cloud profiles integrated along y after a* 30 ms *time of flight. In this experiment a BEC of* 10^4 *atoms is produced in its ground state. A resonant* $\pi/2$ *pulse prepares in an equal superposition of the two states and the cloud dynamics are monitored in time.*

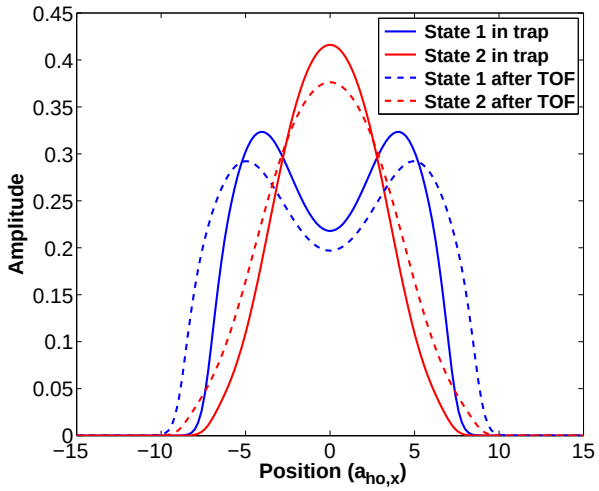

Figure 4.5: *Wavefunctions along x calculated with a one-dimensional approximation of the coupled GPEs for* $N_1 = N_2 = 5 \times 10^3$ atoms. *We show the ground state in the trap and the shape after* 30 ms *of time of flight. The cloud remain of the same shapes during the expansion and are larger by a factor* ~ 1.20.

Cloud expansion during the time of flight For a single-component BEC in the Thomas-Fermi regime the cloud expansion during the time of flight has an analytical solution [82]. In the case of a dual component BEC there is no straightforward extension of this calculation. To estimate the effect of the time of flight on the cloud profiles we have used the one-dimensional approximation of the coupled GPEs. Starting from the ground state with 5×10^3 atoms in each state we calculate the cloud expansion for a time of flight of 30 ms (figure 4.5). It is observed that the cloud maintains the same shape and expands by a factor ~ 1.20 during this time. We used this number to make the link between in-trap results of the simulation and

after-time-of-flight experimental results.

4.3.2 Data modelling

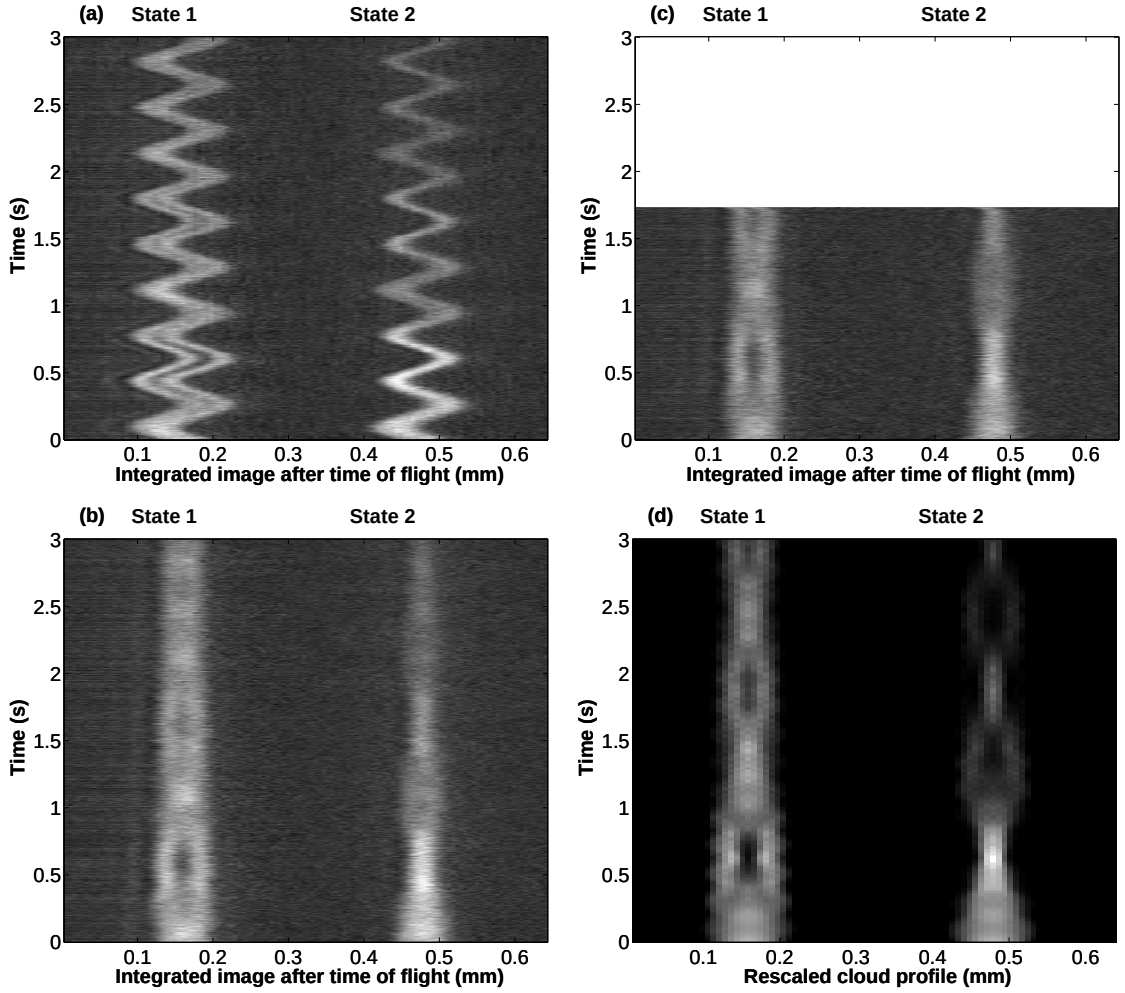

Figure 4.6: *Cloud profiles after TOF integrated along y and z for a BEC of* 10^4 atoms *prepared in an equal superposition of the two states. Abscissa correspond to the x axis in the experiment. (a) Raw experimental data. We observe the common mode residual oscillation of the two clouds in the trap. We fit this oscillation. (b) Experimental data after subtracting the residual cloud oscillation. (c) Experimental data after substraction of the residual oscillation for* 7×10^3 atoms. *(d) Reproduction of the cloud dynamics from our 3D numerical integration of the coupled Gross-Pitaevskii equations for* 10^4 atoms. *Our simulation gives the cloud profiles within the trap and to account for the expansion during time of flight we have rescaled the data by a factor of* 1.20. *We observe that the simulation reproduces qualitatively the data. However, it overestimates the remixing time by* $\sim 20\,\%$.

Figure 4.6.a shows the density profile of both clouds integrated along y and z as a function of time for a condensate of 10^4 atoms initially. We observe the residual common-mode cloud oscillation resulting from the non-adiabatic transfer discussed in section 2.4. We fit the data with a sine function and subtract this oscillation (figure 4.6.b). The state-dependent dynamics

appears clearly with cloud $|1\rangle$ splitting into two parts while in cloud $|2\rangle$ density sharpening. The two states remix after 1.1 s. We then observe a second demixing and a second remixing after 2.1 s.

We reproduce the experimental data using the 3D numerical simulation (figure 4.6.d). Since the simulation gives the cloud shapes within the trap, we rescale the numerical results by a factor 1.20 to account for their expansion during time of flight. We observe a qualitative agreement bewteen the data and the simulation. However, the simulation overestimates the first remixing time by $\sim 20\,\%$. This discrepancy could be caused by a default in the detection: however, if this was the case our detection would have to overestimate the number of atoms by more than a factor 2, which is unreasonable.

Adding finer details in the simulation We tried introducing to the simulation a potential difference $h\beta(B(\mathbf{r})-B_m)$ between the two states and found that this had no visible effect on the cloud dynamics. Secondly we tried taking loss constants 20 % smaller than the value reported in [74] and observed that it had not effect on the remixing time. Next we tried using the 1D numerical model to include the residual oscillation along x and found that it did not impact on the remixing time either. As we believe the atom number calibration is reliable this discrepancy could be caused by other effects that have not been modeled yet, for example: small non-adiabaticity of the decompression ramp causing the initial BEC to be far from the trap ground state; or the influence of a residual non-condensed part, although this is invisible on the images.

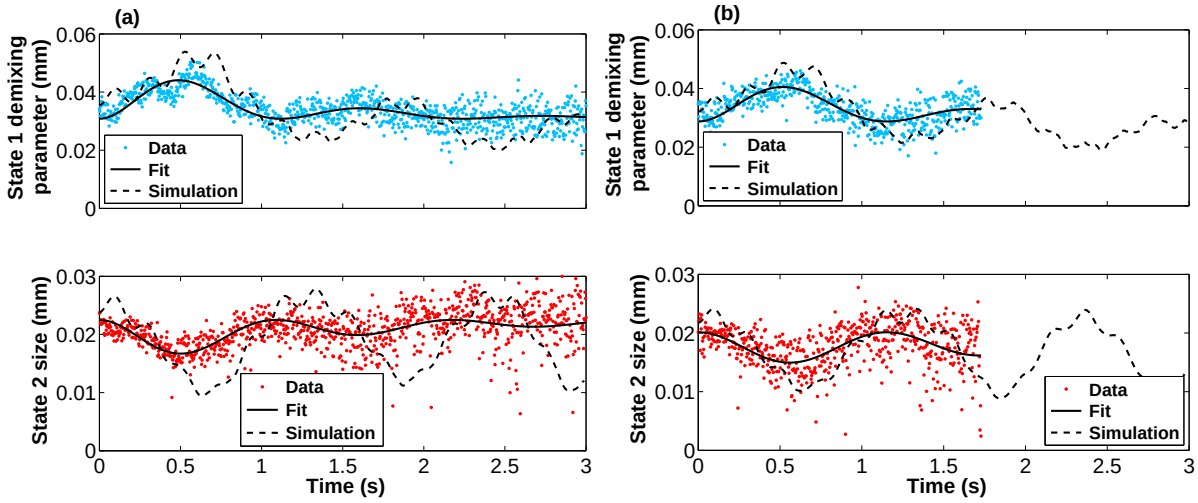

Figure 4.7: *Demixing parameter and cloud size along x extracted from figure 4.6 for (a)* 10^4 atoms *and (b)* 7×10^3 atoms *initially. The demixing parameter is defined by the distance between the left and right centers of mass of state $|1\rangle$ (defined with respect to the median line). We fit the data with the function $A+Be^{-t/\tau_d}\sin^2(\pi f_d t)$ and find for (a) $f_d=0.89(2)$ Hz, $\tau_d=0.86(12)$ s and for (b) $f_d=0.87(2)$ Hz, $\tau_d=1.13(20)$ s. We have also reported the results of the 3D numerical simulation. As stressed previously the demixing dynamics is slower by $\sim 20\,\%$ in the simulation.*

Demixing parameter We define the *demixing parameter* as follows: we artificially separate the cloud into two halves along x and compute the distance between the left-hand side and right-hand side centers of mass. This distance is the demixing parameter. It is a measurement of how much the system is demixed. For state $|2\rangle$ the relevant parameter is the cloud size along x. Figure 4.7 shows state $|1\rangle$ demixing parameter and state $|2\rangle$ cloud size, extracted from the data of figure 4.6, for both 10^4 atoms and 7×10^3 atoms. The data can be fitted with a damped oscillation, $A + Be^{-t/\tau_d} \sin^2(\pi f_d t)$. We obtain $f_d = 0.89(2)\,\text{Hz}$ and $\tau_d = 0.86(12)\,\text{s}$ for 10^4 atoms, and $f_d = 0.87(2)\,\text{Hz}$ and $\tau_d = 1.13(20)\,\text{s}$ for 7×10^3 atoms. As previously mentioned, the simulation does not reproduce exactly, this is particularly true for the value of the demixing frequency f_d.

In conclusion, our simulation qualitatively reproduces our observations. For a more quantitative agreement one would, perhaps, have to include other effects in the model, such as a residual non-condensed phase, or the excitation of collective modes of the condensate during the decompression. Our observations of demixing are in qualitative agreement with the results published by other groups [74, 50, 76, 77]. As it modulates the overlap between the two wavefunctions, the state demixing must have consequences for the Ramsey contrast. This is the focus of the next section.

4.4 Coherence of a BEC superposition

The study of coherence is carried out using Ramsey interrogation. The experiment begins similarly to that detailed above but with a second $\pi/2$ pulse is applied which closes the interferometer. The contrast corresponds to the amplitude of the Ramsey fringes.

4.4.1 In time domain

In the first experiment the interrogation signal was detuned by $\sim 10\,\text{Hz}$ and we acquired Ramsey fringes in time domain.

Figure 4.8 shows the experimental results for three different atom numbers: 10^4 atoms, 7×10^3 atoms and 2.5×10^3 atoms initially. On the same graphs we have plotted the fitted values of the demixing parameters for state $|1\rangle$, which are identical to figure 4.7. The demixing parameter is a measurement of the overlap of the two wavefunctions. We observe revivals of the Ramsey contrast at the remixing times, which shows explicitly that the fringe contrast depends on the overlap of the two wavefunctions. We also observe that the contrast hardly decays over 5 s for the smallest atom number. It does decays for larger atom numbers, however, it does not reach zero and seems to saturate at a constant value. At the same time, we observe the appearance of a jitter on the signal. We will discuss this phenomenon in section 4.5. In the following section we present, among others, a more in-depth study of the contrast evolution in time.

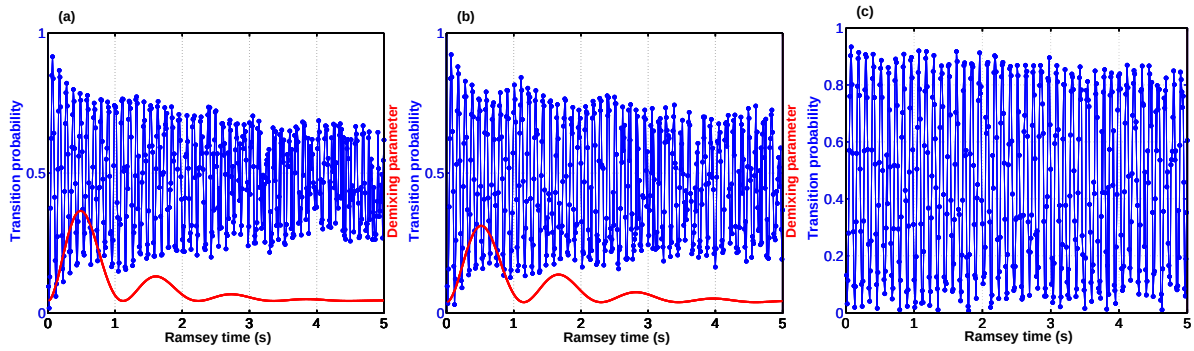

Figure 4.8: *Ramsey fringes in time domain for a BEC of (a)* 10^4 atoms, *(b)* 7×10^3 atoms *and (c)* 2.5×10^3 atoms *initially. The fitted demixing parameter are also reported and gives a measurements of the overlap of the two wavefunctions. The atomic response does not reach 1 at* $t = 0$, *this is a consequence of the AC Zeeman shift induced by the interrogation photons on the clock transition. We observe revivals of the atomic response at the same times the system remixes (corresponding to the minima of the demixing parameter). This result shows explicitly that the Ramsey contrast depends on the overlap of the two wavefunctions. We observe that the contrast decay is slower for smaller atom numbers; in fact the contrast hardly decays over* 5 s *in (c). Lastly, in (a) and (b), for times* > 2 s, *we observe a jitter of the signal which is not visible in (c). We will discuss this phenomenon in section 4.5.*

4.4.2 In frequency domain

In the second experiment we worked with a fixed Ramsey time and varied the interrogation frequency.

Ramsey spectra

Figure 4.9 shows typical Ramsey spectra. We recorded 28 points over 4 fringes, this was enough to extract the contrast from a sinusoidal fit with a good precision. The fit also provides the value f of the clock frequency.

On figure 4.9 we observe the appearance of noise for increasing atom numbers and Ramsey times. This noise is further discussed in section 4.5.

Contrast evolution in time

In this experiment the bottom field was set at B_m. The contrast measurement was repeated for several Ramsey times T_R and with BECs of different sizes. The data is shown in figure 4.10 and compared with the results for a thermal cloud. The behavior related to the number of atoms is exactly opposite in each case: in BECs larger densities lead to faster contrast loss whereas in thermal clouds larger densities imply better spin-synchronization and thus slower contrast decay. The physical phenomena are different: in thermal clouds the contrast loss is caused by dephasing of the atomic ensemble; in BECs it is a combined effect of the overlap and the relative phase of the two wavefunctions. It is, however, difficult to distinguish between these two effects. Our model includes both contributions.

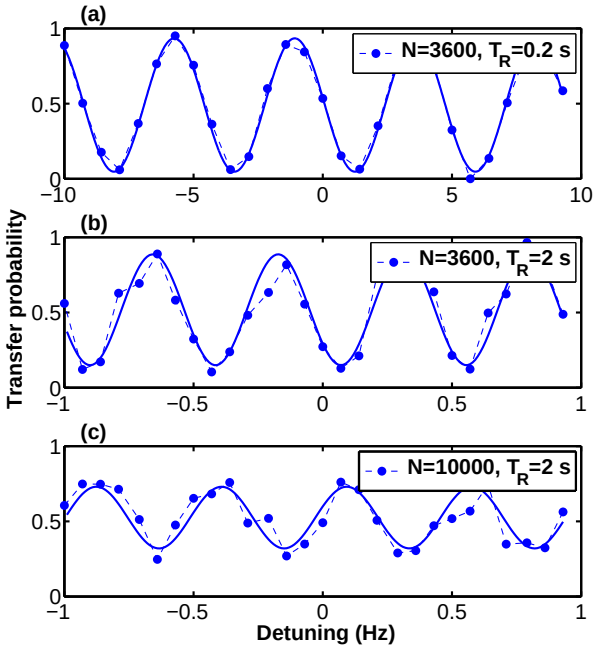

Figure 4.9: *Typical Ramsey spectra. The Ramsey time is constant and the detuning of the local oscillator is scanned. We typically record* 28 *points over* 4 *fringes. A sinusoidal fit gives access to the contrast C which is also the fringe amplitude. The noise appearing for increasing atom numbers and Ramsey times is discussed further in section 4.5.*

Displayed on the same graph is the calculated contrast $C = 2|\int \psi_2(\mathbf{r},t)^*\psi_1(\mathbf{r},t)d\mathbf{r}|/\int(|\psi_2(\mathbf{r},t)|^2+|\psi_2(\mathbf{r},t)|^2)d\mathbf{r}$ where $\psi_i(\mathbf{r},t)$ are the order parameters before the second pulse. The numerical contrast is multiplied by a factor 0.94 to account for the additional contrast reduction from the interrogation photon AC Zeeman shift. The data for small atom numbers, and in particular the contrast revival at the remixing time is well reproduced by the model. For larger atom numbers ($N > 3600$ atoms), the numerical model does not reproduce the experiment. The reason of this discrepancy at high atom numbers is under investigation.

Contrast dependence on the clock frequency spatial inhomogeneity

An interesting question is the dependance of the contrast on the clock frequency spatial inhomogeneity. This inhomogeneity is given by the difference of the trapping potential of the two states, which can be tuned using the bottom field B_0. $B_0 = B_m$ gives almost identical trapping potentials for the two states.

For thermal clouds it is known that the contrast is maximized at the compensation field $B_c < B_m$, whose value depends on the cloud and trap parameters, these include: temperature, density, trap frequencies. This compensation can be understood in a model of independent atoms: it is the field for which the clock frequency spatial inhomogeneity arising from the collisions is best compensated by the clock frequency spatial inhomogeneity arising from the trapping potential. It corresponds to the point where dephasing of atoms from different energy classes is minimized. It can also be seen as the point at which the two contributions cancel

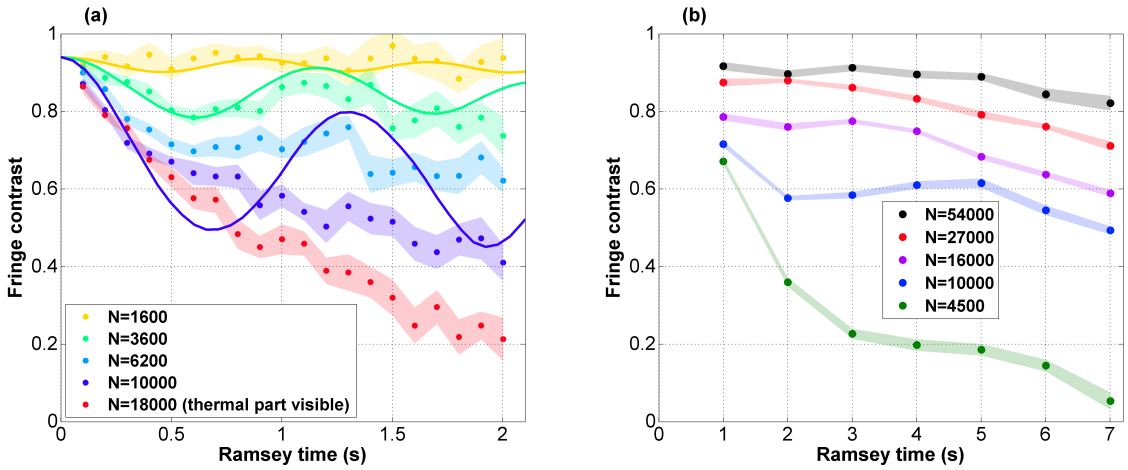

Figure 4.10: *Contrast evolution in time for (a) BECs and (b) thermal clouds. The lighter colors illustrate the statistical uncertainty given by the fit. In both graphs the contrast is not* 1 *at* $t = 0$ *which is a consequence of the interrogation photon AC Zeeman shift. In (a) we observe that the contrast decays faster for larger BECs. There are contrast revivals for* $N = 3600$ atoms *and* $N = 6200$ atoms. *On the same graph we report the results of our numerical model multiplied by a factor* 0.94 *to account for the contrast reduction due to the interrogation photon AC Zeeman shift (full lines). The model reproduces the data for the smallest atom numbers and diverges from the experiment for larger atom numbers. For* $N = 18\,000$ atoms *we have no theoretical prediction since the BEC is not pure. In (b) we observe the typical behavior of a ISRE-synchronized gas [11], in the same trap: as the number of atoms (or density) increases the exchange rate* ω_{ex} *becomes larger and the spin synchronization stronger, leading to higher contrasts. The dependence with the atom number is the exact opposite as for BECs.*

each other out to second order in position.

In BECs one can make an approximate calculation by considering only the x axis and assuming the Thomas-Fermi approximation. In this case the position dependent collisional shift reads:

$$\Delta f_{coll}(x) = \left(\frac{\mu}{g_{11}} - \frac{m\omega_x^2 x^2}{2g_{11}}\right)\frac{\hbar}{m}(a_{22} - a_{11}) \tag{4.13}$$

and the position dependant magnetic shift expanded to second order in x:

$$\Delta f_{magn}(x) = \beta\,(B_0 - B_m)^2 - \beta\,(B_0 - B_m)\,\frac{m\omega_x^2 x^2}{\alpha_m}. \tag{4.14}$$

Here B_0 is the field at the trap bottom, $g_{11} = 4\pi/\hbar^2 a_{11}/m$, $\alpha_m \simeq \mu_B/2$ (cf chapter 1) and μ is the chemical potential of the BEC in $|1\rangle$. The cancelation of the x^2 terms requires

$$(B_0 - B_m) = -\frac{\alpha}{4\pi\beta\hbar}\left(1 - \frac{a_{22}}{a_{11}}\right). \tag{4.15}$$

The value of the right-hand side is -10 G, it is neither dependent on the trap frequency nor on the atom number. This working point is not accessible since $B_m = 3.23$ G. For comparison, we find for a thermal cloud of 5×10^4 atoms at 100 nK in our usual trap: $(B_0 - B_m) = -70$ mG,

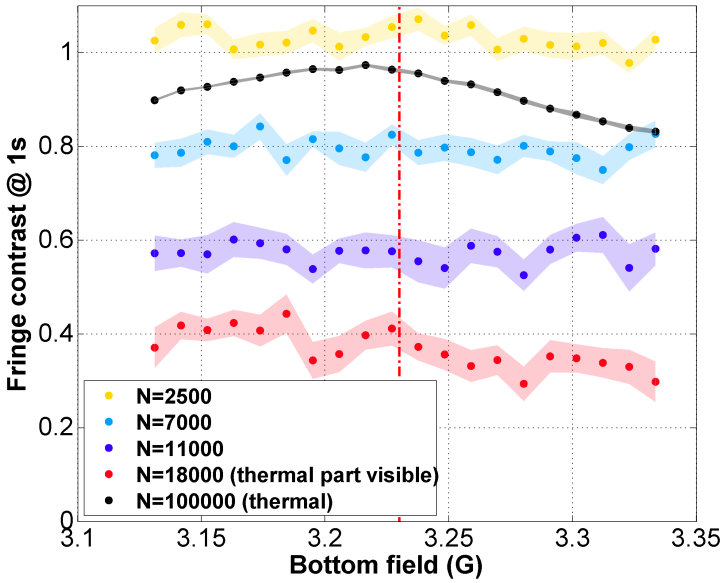

Figure 4.11: *Contrast of the Ramsey fringes at* 1 second *as a function of the trap bottom field, that controls the spatial inhomogeneity of the clock frequency. The measurement was repeated for BECs of several sizes. An asymmetry in the detection leads to contrasts larger than* 1 *for small BECs, which is not physical. We have also recalled the typical curve obtained for a thermal cloud, for which the existence of a compensation field that maximizes the contrast is well understood. From this measurement we learn that no spatial clock shift compensation happens in BECs in the explored range of inhomogeneity. Rather, the contrast is entirely driven by the atomic interactions.*

which is in the order of the experimental measurement $(B_0 - B_m) = -35\,\mathrm{mG}$.

To check this prediction we performed a measurement of the BEC contrast at $T_R = 1\,\mathrm{s}$ as a function of the trap bottom field (figure 4.11). The measurement was repeated for BECS of various sizes. On the same graph we present the results obtained for a thermal cloud of 10^5 atoms initially for which the fringe contrast is at a maximum at a bottom field $B_c \sim B_m - 15\,\mathrm{mG}$. For BECs, however, no such compensation is observed and the contrast remains flat over the range of the bottom field. These results show that a difference between the trapping potential of the two states plays a negligible role on the coherence of a BEC superposition. Therefore, we conclude that the coherence of a BEC superposition is entirely governed by the interactions.

Clock frequency: a sweet spot across the condensation threshold

The clock frequency exhibits an interesting behavior across the condensation threshold. In this measurement only the final value F_{stop} of the radiofrequency cooling ramp was varied. For each value of F_{stop} a Ramsey spectra was recorded from which the central frequency was extracted. We observe (figure 4.12) that the clock frequency admits a minimum for a total atom number $N \sim 10^4$ atoms. This is, potentially, an interesting feature for making an atomic clock which is first-order insensitive to atom number fluctuations.

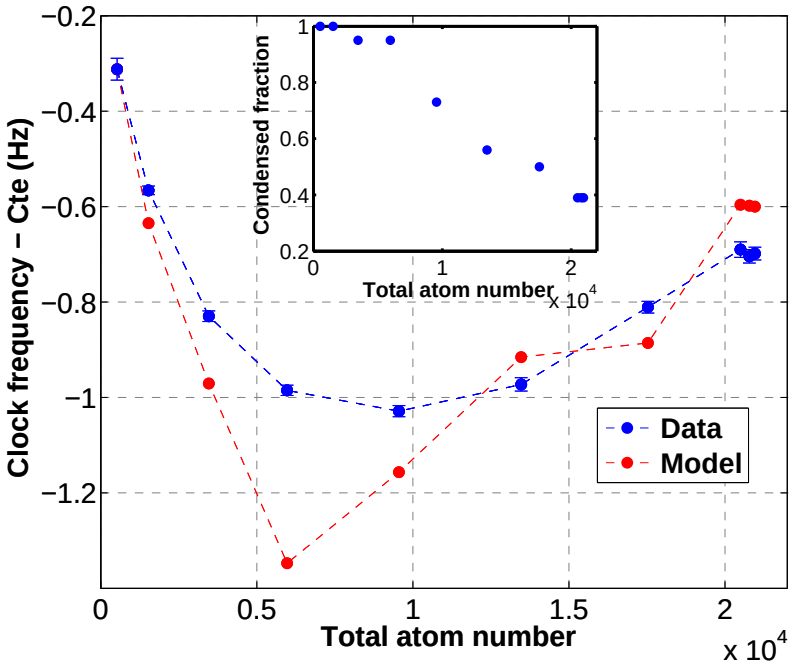

Figure 4.12: *Clock frequency across the condensation threshold as a function of the total atom number. This was measured for a Ramsey time of* 200 ms. *The experimental curve admits a minimum around* $\sim 10^4$ atoms. *We also show the results of our approximated model of an independent BEC-thermal cloud mixture. The parameters of this model (atom numbers and temperature) are taken from a bimodal fit on the cloud images. The prediction of the model were shifted by an arbitrary constant in order to match the first point. Our model qualitatively reproduces the shape of the curve. For a more detailed explanation one would have to take into account the interactions between condensed and non-condensed phase, which was neglected here.*

To understand this behavior in greater detail we used the following approximate model: the cloud is constituted of an independent mixture of BEC and thermal cloud. Interactions between the two are neglected such that we anticipate the model to be accurate only for the two limits of a pure BEC and a pure thermal cloud. For each constituent the clock frequency is shifted by two contributions: (1) the collisional shift and (2) the magnetic shift coming from the cloud extension. The total clock frequency is computed by weighting the contribution of each phase by its fraction.

This model used the values of the atom number in each phase and of the cloud temperature extracted from a bimodal fit on the cloud profiles. Figure 4.12 shows that it qualitatively reproduces the measured data, indicating that our approach is on the right path to explaining these data. For a more complete analysis one would have to take into account the interactions between the condensed and the non-condensed phase.

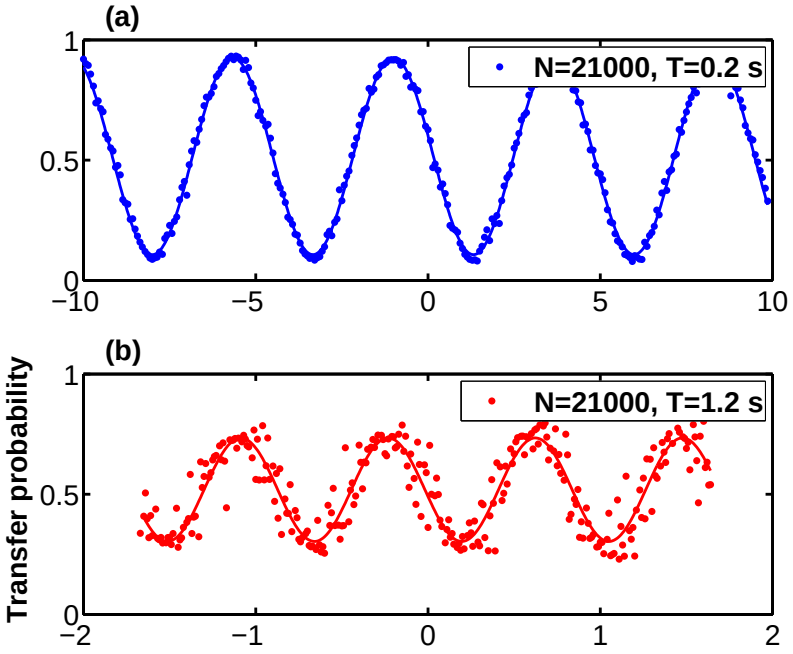

Figure 4.13: *Fine Ramsey spectra for a cloud of* $N = 2.1 \times 10^4$ atoms, *condensed at* 80 %, *for interrogation times of* 0.2 s *and* 1.2 s. *There is an increase in noise as the Ramsey time increases. As noted in this section the technical noises do not give a complete explanation for the amplitude of this noise. We conclude that we may be seeing a collective spin state deformed by the non-linear spin dynamics.*

4.5 Evidence for increased noise on the atomic response

In this section we discuss, in greater detail, the increased noise on P_2 observed in figure 4.9. The noise increase can also be seen in figure 4.10.a where the error bars on the contrast increase with interrogation time. The same process probably causes the jitter observed for the largest atom numbers in figure 4.8.

Figure 4.13 shows a fine scan in the frequency domain, for a BEC condensed at $\sim 80\,\%$. We observe that the data are much noisier after 1.2 s than after 0.2 s of interrogation. We compute two numbers to characterize this noise: (1) the noise on P_2, that is, the standard deviation of the difference between the data points and the mean value (given by the fit); (2) the noise on the detuning, that is, the same quantity for the abscissa. From figure 4.13.b we obtain $\sigma_{P_2,\mathrm{mes}} = 7.5 \times 10^{-2}$ and $\sigma_{\Delta,\mathrm{mes}} = 0.15\,\mathrm{Hz}$. These quantity are the noise we have to explain for. In the following we give an estimation of the amplitude of all the technical noise contributions that we expect.

Detectivity The data, acquired with the Double Detection method, were corrected for a detectivity difference between the two states. After this correction the measured shot-to-shot atom number fluctuation is $\sigma_N/N = 2.3\,\%$.

4.5.1 Estimation of the technical noise contributions

Here we give estimations for the amplitudes of all the known sources of technical noise. We discriminate bewteen the noise on P_2 and the noise on the detuning Δ.

Noise on P_2

Detection noise If this noise was dominant we would observe an equal amplitude on both graphs of figure 4.13. In fact we estimate $\sigma_{P_2,\mathrm{det}} = 2 \times 10^{-3}$.

Noise on P_2 arising from the asymmetric losses For shot-to-shot atom number variations of $\sigma_N/N = 2.3\,\%$ we compute that this effect leads to fluctuations $\sigma_{P_2} = 7 \times 10^{-3}$, making it smaller than the measured noise.

Noise of the preparation We use the upper bound of 10^{-4} for $\sigma_{P_2,\mathrm{Rabi}}$ measured for thermal clouds and 70 ms pulses. We rescale it to take into account the change in pulse length (12.5 ms): this gives a preparation noise of $\sigma_{P_2} = 6 \times 10^{-4}$.

As can be seen all three contributions are far too small to explain the observed noise on P_2 of $\sigma_{P_2,\mathrm{mes}} = 7.5 \times 10^{-2}$.

Noise on Δ

The calculations presented here use the mean density of a fully condensed BEC of 2.1×10^4 atoms, $n = 1.6 \times 10^{13}\,\mathrm{atoms\,cm^{-3}}$, this is an overestimation considering the cloud is not fully condensed in the experiment. The description of the noise contributions was done in chapter 3.

Collisional shift from shot-to-shot atom number fluctuations We compute $\sigma_{f,\sigma_{N_{\mathrm{fluct}}}} = 70 \times 10^{-3}\,\mathrm{Hz}$. If the noise that we observed was dominated by shot-to-shot atom number fluctuations, we should be able to reduce the noise amplitude by proceeding to a post-selection of the data according to the final atom number. Figure 4.14 shows the results of such a post-selection; we observe the post-selection does not reduce the noise, suggesting that this noise is not caused by atom number fluctuations.

Noise on the collisional shift from a noisy preparation We use the upper bound of 10^{-4} for $\sigma_{P_2,\mathrm{Rabi}}$ measured for thermal clouds and 70 ms pulses. We rescale it to take into account the change in pulse length (12.5 ms): this gives a frequency noise of $\sigma_{f,\sigma_{N_{\mathrm{fluct}}}} = 4 \times 10^{-4}\,\mathrm{Hz}$.

Frequency uncertainty due to symmetric atom losses To compute this noise we consider the worst case scenario by taking the smallest lifetime of the two clouds. We find $\sigma_{f,\mathrm{loss,stat}} = 13 \times 10^{-3}\,\mathrm{Hz}$.

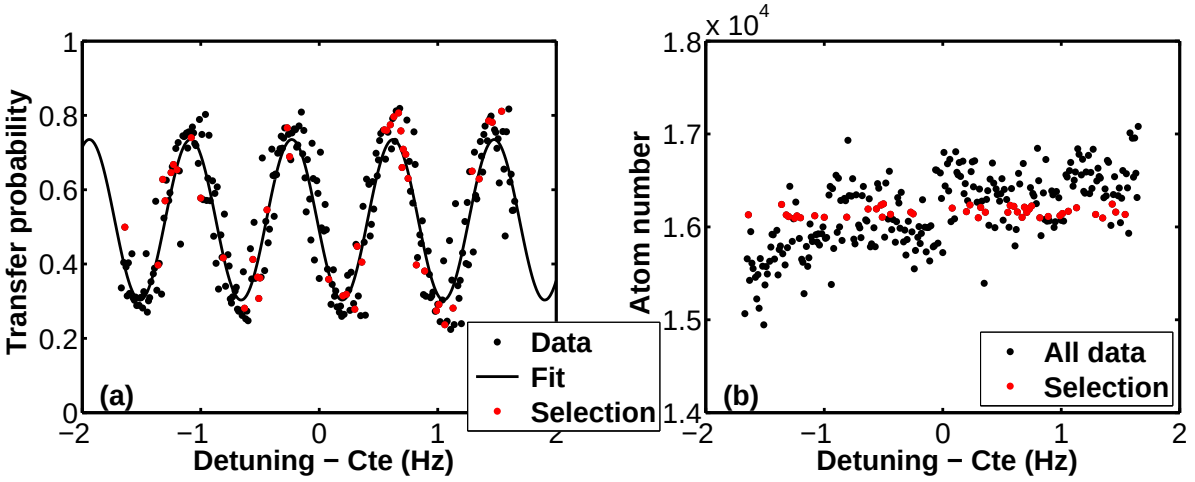

Figure 4.14: *Post-selection of the data from figure 4.13.b. according to the total atom number. (a) Ramsey fringes as a function of the detuning. (b) Final atom number as a function of the detuning for the same data. We have post-selected the data corresponding to atom number fluctuations of* $< 0.5\,\%$ *deviation from the mean. The post-selected data are indicated in red on both graphs. In (a) we observe that post-selecting the data does not reduce the observed noise, showing that the noise is not dominated by shot-to-shot frequency noise, which is consistent with our estimation (*$70 \times 10^{-3}\,\mathrm{Hz} < 150 \times 10^{-3}\,\mathrm{Hz}$*).*

Frequency uncertainty due to asymmetric atom losses We estimate this contribution to $\sigma_{f,\mathrm{asym,stat}} = 13 \times 10^{-3}\,\mathrm{Hz}$ (conservative estimation).

Fluctuations of the bottom magnetic field With $\sigma_B(3\,\mathrm{s}) = 60\,\mu\mathrm{G}$ (worst case estimation) and assuming white noise for the magnetic field for $\tau < 3\,\mathrm{s}$ we estimate that magnetic field fluctuations give frequency fluctuations in the order of $4 \times 10^{-4}\,\mathrm{Hz}$.

Shot-to-shot fluctuations of the magnetic shift by the BEC extension The magnetic shift of the clock transition depends on the cloud extension in the trap. In a pure BEC the cloud extension is determined by the number of atoms. With our simulation we compute the dependence of this shift on the atom number in the region of $N = 2 \times 10^4$ atoms: $\Delta f_{mag,N} = AN$ with $A = 6.5 \times 10^{-8}\,\mathrm{Hz\,atoms^{-1}}$. For $\sigma_N/N = 2.3\,\%$ this leads to shot-to-shot frequency fluctuations of $3 \times 10^{-3}\,\mathrm{Hz}$ typically.

Shot-to-shot fluctuations of the magnetic shift by the thermal cloud extension The cloud we analyzed was not fully condensed. With $\sigma_T/T = 1.4\,\%$ and by considering the cloud to be half condensed we estimate the effect of shot-to-shot temperature fluctuations to amout to $\sim 2 \times 10^{-3}\,\mathrm{Hz}$.

Noise of the local oscillator Its contribution to the shot-to-shot noise on the detuning is estimated to be $6 \times 10^{-4}\,\mathrm{Hz}$.

At this point we reach the conclusion that all these contributions are too small to explain the observed noise on the data. Another possibility is that there is an increased noise of the atomic response P_2 driven by a fundamental process. This could be caused by a deformation of the BEC collective spin state on the Bloch sphere. The next section focuses on this phenomenon.

4.5.2 Non-linear spin dynamics in a dual component BEC

Up to now we have considered that, after the preparation pulse, the system can be described as having $N/2$ atoms in each spin state, this is known as the Fock state description. In fact we have to consider that *each atom is in a state superposition*. If ϕ_0 is the wavefunction before the pulse and all the atoms are in the spin state $|1\rangle$, the state of the system directly after the pulse reads [83] $|\psi(0)\rangle = [c_1|1,\phi_0\rangle + c_2|2,\phi_0\rangle]^N$ where $c_1 = c_2 = 1/\sqrt{2}$ for a $\pi/2$ pulse (assuming the pulse is short on the BEC dynamics timescale). This *phase* state (the two components have a well-defined relative phase) is equal to a superposition of Fock states: $|\psi(0)\rangle = \sum_{N_1=0,N_2=N-N_1}^{N} \left(\frac{N!}{N_1!N_2!}\right)^{1/2} c_1^{N_1} c_2^{N_2} |N_1:\phi_0, N_2:\phi_0\rangle$. The notation $|M:\phi_0, L:\phi_0\rangle$ stands for M atoms in internal state $|1\rangle$ and external state ϕ_0 and L atoms in internal state $|2\rangle$ and external state ϕ_0.

Because of the intrinsic non-linearity of the GPEs, each of the states $|N_1:\phi_0, N_2:\phi_0\rangle$ evolves with its own dynamics: $|N_1:\phi_1(N_1,N_2,t), N_2:\phi_2(N_1,N_2,t)\rangle$. In principle the propagation of state $|\psi(0)\rangle$ would require one to solve N independent sets of coupled Gross-Pitaevskii equations.

Fortunately, approximations can be made using the fact that the distributions peak around the mean atom numbers $\overline{N_i} = |c_i|^2\overline{N}$. In this approach the hamiltonian ruling the spin dynamics can be approximated by [84, 85]:

$$H = \delta S_z + \hbar\chi S_z^2, \tag{4.16}$$

where δ is the local oscillator detuning from resonance and the non-linearity takes the form

$$\chi = \frac{1}{2}[(\partial_{N_1} - \partial_{N_2})(\epsilon_1 - \epsilon_2)](\overline{N}_1, \overline{N}_2), \tag{4.17}$$

where ϵ_i is the energy per atom of state i ($\epsilon_i = \mu_i$ for stationary states).

Stationary states The effect of such an hamiltonian in the case of stationary states is depicted on figure 4.15. The system is initially in a phase state prepared by a $\pi/2$ pulse. The non-linear evolution creates a twist of the state on the collective Bloch sphere. When the state is elongated to the point that it covers almost the entire equator of the Bloch sphere, the information on the phase gets lost: this is the *phase collapse*. A second effect of this hamiltonian is to create spin-squeezed states: at certain times there is a direction Θ along which the width of the state is inferior to the standard quantum limit. To represent a metrological interest the gain by spin-squeezing has to be larger that the loss in contrast: the metrological interest is best quantified by the squeezing parameter ξ defined as $\xi^2 = N\Delta S_{\theta,\min}^2/\langle S_x\rangle^2$, where $\mathbf{S}$ is

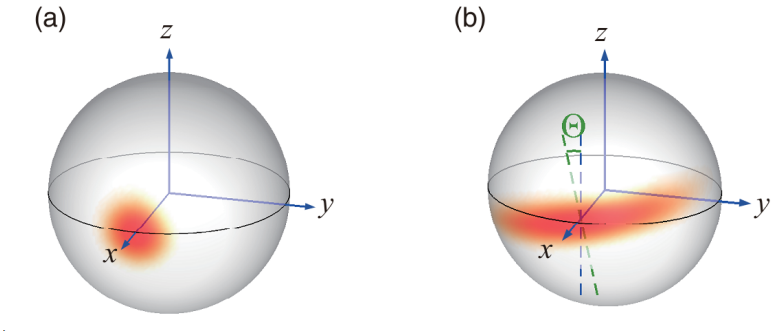

Figure 4.15: *Effect of the twisting hamiltonian 4.16 in the collective Bloch sphere picture for* $N = 100$. *The probability of measuring the spin in a given direction is given by the color intensity. (a) At* $t = 0$ *the system in is a phase state, prepared by a* $\pi/2$ *pulse. A measurement of the spin state is limited by the standard quantum limit. (b) State after evolution under the non-linear hamiltonian during* $t = 0.05/\chi$ *(corresponding the the predicted best squeezing time for stationary states). The spin state becomes elongated along the angle defined by* Θ. *In the* Θ *direction one can measure a noise below the standard quantum limit (spin-squeezing). Picture from [68].*

the collective spin, N the atom number and $\Delta S^2_{\Theta,\min}$ the variance calculated in the direction Θ. The stability of a spin-squeezed clock would be improved by a factor ξ compared to the standard quantum limit.

Non-stationary states In the case of non-stationary states, such as in our situation, the parameter χ has a time dependence. The effect on the dynamics of the collective spin state may be somewhat different than in the stationary case. We are currently calculating the consequences that the non-linear spin dynamics should have in our system.

4.6 Perspectives

The results presented here on the coherence of a BEC superposition opens the path to new studies.

A finer simulation As explained before there is a discrepancy between our theoretical predictions for a pure BEC and the observed behavior. In particular, the calculation overestimates the remixing time by $\sim 20\,\%$ when carried out for the measured atom number. To quantitatively explain the data one needs to artificially reduce the number of atoms. This suggests the existence of a non-negligible thermal phase, although none can be observed on the cloud images. This could also explain the mismatch between the measured and calculated contrast. Our simulation reproduces the behavior of a BEC in the trap ground state. At this point we cannot exclude the excitation of collective modes in the condensate during the decompression ramp affecting the BEC dynamics.

Quantum correlations In order to check our predictions we would need to perform a quantum tomography of the BEC state. In this experiment the state is rotated by a variable angle θ. For each angle one records a large number of points in order to compute the noise on the collective spin measurement. If this noise shows variations with the angle θ one can conclude that the collective spin state has been deformed by the non-linear dynamics. In order to reduce the frequency noise associated with shot-to-shot atom number fluctuations, this measurement should be carried out using a post-selection of the data according to the total atom number. It may even be possible to observe a noise below the standard quantum limit (spin squeezing). It would also be interesting to measure Ramsey fringes for times longer than 2 s: one might be able to experimentally observe the phase collapse, this should manifest itself by the appearance of noisy Ramsey fringes on which it is no longer possible to fit a sine function.

Fighting the demixing State demixing happens naturally because of the difference in scattering length between the two states, it would be interesting to change the demixing properties by tuning the scattering length. In fact, the control of demixing in dual condensates has a broader range of application: for example it is a key step toward the creation of ultracold heteronuclear molecules in the lower vibrational state. The use of broad Feshbach resonance to control demixing was demonstrated for mixed species in [86, 87].

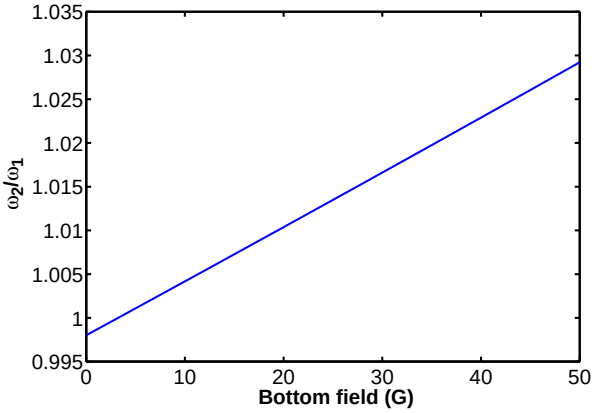

Figure 4.16: *Ratio of the trap frequencies experienced by the two states as a function of the trap bottom field, calculated with the Breit-Rabi formula.*

Alternatively, one might think that the demixing could be avoided by achieving greater confinement of species $|1\rangle$. For purely static magnetic fields, only a small range of ratios $\omega_2/\omega_1 < 1$ are accessible (see figure 4.16). Also, if the trap frequencies are different for each state the gravitational sag would also be state-dependent. However, by using microwave or radiofrequency state-dependent potentials one could control the trap frequencies independently for the two clock states.

Clock shifts in non-homogeneous systems For inhomogeneous systems, the clock shift dependance on the cloud density should differ from the homogeneous case. It would be interesting to investigate this problem experimentally, and to determine the conditions required

for the predictions of the homogeneous theory to stay valid for the cloud mean density. In particular one may wonder whether the clock frequency is modulated as the system demixes.

Exchange collisions in partially condensed samples As observed by measuring the clock frequency across the condensation threshold, mixed samples of BEC and thermal clouds can exhibit complex and interesting features. It may be interesting to consider the effect exchange collisions. In a mixed system the situation is more complex and requires both a theoretical and an experimental investigation. Exchange collisions lead to ISRE in non-condensed clouds and must spin exchange must also occur during collisions between condensed and non-condensed atom. For example, one could imagine that the collective spin of a small condensate surrounded by a spin self-synchronized thermal component would undergo a spin-locking effect mediated by spin exchange collisions with the non-condensed part.

Chapter 5

Coherent sideband transition by a field gradient

In this chapter we report on the use of inhomogeneous microwave and radiofrequency pulses in the manipulation of the external state of trapped atoms.

Control of the motion of trapped atoms is the first step towards integrated atom interferometry for measuring forces. It is usually performed with laser beams in Raman configuration. Lasers bear the advantage of having strong phase gradients (i.e. strong wavevector $\mathbf{k}$) in comparison to plane microwaves. Consequently they are more efficient in driving transitions between external states. Microwaves, however, have the advantage of a simple synthesis and handling. Here we show that they can drive transitions between external states if there is a large amplitude gradient.

Large microwave gradients can be realized in the evanescent field of a coplanar waveguide. This approach has been used to create on-chip state-dependent potentials [88]. Recently it has also been used to drive sideband transitions and produce entanglement in systems of ions trapped above a microstructure [89]. It seems to be a promising way to replace Raman beams and gain in simplicity and compactness.

In our experiment both the radiofrequency (RF) and the microwave (MW) interrogation signals have position-dependent amplitudes as they are produced by microstructures on the chip. Here we study how they can be combined to control the external state of a cloud of $\sim 4 \times 10^4$ atoms trapped atoms in the thermal regime. In particular, we show that it is possible to reach a regime where only one sideband (blue or red) is excited. We will also show that the sidebands are driven coherently, in the sense that the atoms transferred on the carrier and on the sideband maintain a phase relation.

This chapter is organized as follows: first we give the formulae used to describe sideband transitions. Secondly we give experimental results on the sideband excitation and demonstrate the cancelation of the red sideband. Thirdly we examine the coherence of the process by looking at interferences between the sideband and the carrier.

5.1 Theory of the sideband excitation by an inhomogeneous field

Fundamentally, driving transitions between external states requires an inhomogeneity of the coupling field. The magnetic field responsible for the coupling takes the generic form

$$\mathbf{B}(\hat{\mathbf{r}})e^{i\mathbf{k}\cdot\hat{\mathbf{r}}-[\omega-\omega_0(\hat{\mathbf{r}})]t} \tag{5.1}$$

The inhomogeneity of the coupling field can arise from the inhomogeneity of the amplitude $\mathbf{B}(\hat{\mathbf{r}})$, phase $\mathbf{k}\cdot\hat{\mathbf{r}}$ or detuning $[\omega-\omega_0(\hat{\mathbf{r}})]\,t$. We estimate each contribution. We will limit the calculation to first order in position, which, as we will see further in this chapter, corresponds to single sideband excitations.

5.1.1 Field inhomogeneity

Phase inhomogeneity

The inhomogeneity of the phase is given by the wavevector $k = 50\,\mathrm{m}^{-1}$ [26].

Clock frequency inhomogeneity

The inhomogeneity of the clock frequency comes from the combination of the static trapping field and the collisional shift. Figure 5.1 shows the calculated spatial profile of the clock frequency for typical cloud parameters and for a bottom field equal to the magic field. In this case the clock frequency varies quadratically in space to lowest order. Thus, the clock frequency inhomogeneity will only contribute to multiple sideband transition processes.

Amplitude inhomogeneity

The spatial dependence of the field amplitude can be expressed as a spatial dependence of the Rabi frequency. The two-photon Rabi frequency takes the form

$$\Omega(\mathbf{r}) = \frac{\Omega_{mw}(\hat{\mathbf{r}})\Omega_{rf}(\hat{\mathbf{r}})}{2\Delta(\hat{\mathbf{r}})}. \tag{5.2}$$

Figure 5.2 shows the calculated profile of the microwave field of the waveguide in space. The inhomogeneity of the microwave field is predominantly along z. For the radiofrequency field, as the radiating wire is oriented along x, the inhomogeneity is predominantly along y and z. To lowest order we may write

$$\Omega_{mw(rf)}(\hat{\mathbf{r}}) = \Omega_{mw(rf),0}\left(1+\boldsymbol{\delta}_{mw(rf)}\cdot\hat{\mathbf{r}}\right). \tag{5.3}$$

and

$$\Delta(\hat{\mathbf{r}}) = \Delta_0\left(1+\boldsymbol{\delta}_{\Delta}\cdot\hat{\mathbf{r}}\right). \tag{5.4}$$

$\boldsymbol{\delta}_{mw}$, $\boldsymbol{\delta}_{rf}$ and $\boldsymbol{\delta}_{\Delta}$ are the typical inhomogeneities. Estimations of their amplitudes are as follows:

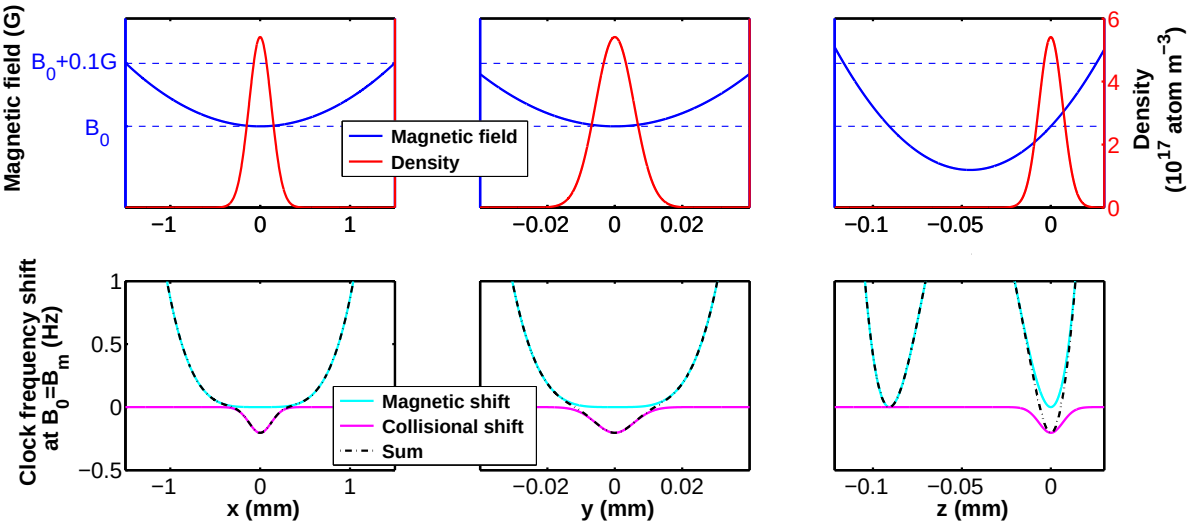

Figure 5.1: *Variation of the magnetic field, density and clock frequency in space calculated for* $B_0 = B_m$, $N = 4 \times 10^4$ atoms, $T_x = 46\,\mathrm{nK}$, $T_y = 114\,\mathrm{nK}$ *and* $T_z = 100\,\mathrm{nK}$. *Top: Variation of the magnetic field and the cloud density. Along* z *the cloud is shifted away from the magnetic minimum by the gravity. Bottom: Spatial variation of the magnetic and collisional shifts of the clock frequency. To lowest order in position, their sum varies quadratically in all directions.*

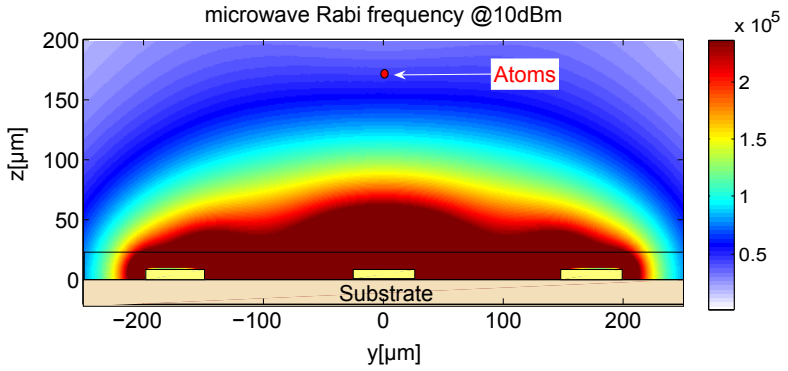

Figure 5.2: *Calculated profile of the one-photon resonant microwave Rabi frequency. The amplitude inhomogeneity of the microwave field emitted by the waveguide is predominantly along* z. *We estimate* $\delta_{mw,z} \sim 3 \times 10^4\,\mathrm{m}^{-1}$ *[43].* $\delta_{mw,z}$ *is zero by symmetry. Picture adapted from [26].*

- **Rabi frequency along** x**:** The microwave may be partially stationary. The maximum typical inhomogeneity along x is given by the wavevector k: $\delta_{mw,x} \sim k = 50\,\mathrm{m}^{-1}$ [26]. The RF field inhomogeneity along x is negligible.

- **Rabi frequency along** y**:** In the magnetostatic approximation, for a wire placed along the x axis the field around the point $\mathbf{r}_0 = (y_0, z_0)$ the field reads:

$$B(y,z,t) = \frac{\mu_0 I(t)}{2\pi r_0}\left(1 - \frac{y_0}{r_0^2}(y-y_0) - \frac{z_0}{r_0^2}(z-z_0)\right). \tag{5.5}$$

$y_0 \sim 500\,\mu\text{m}$ and $z_0 \sim 330\,\mu\text{m}$ give $\delta_{rf,y} \sim 1.3\times 10^3\,\text{m}^{-1}$. This number is only an estimation as the RF field is not only determined by the radiating wire. In fact we have evidence for inductive coupling in the other chip wires. $\delta_{mw,y}$ is zero by symmetry (figure 5.2).

- **Rabi frequency along z:** The magnetostatic approximation gives $\delta_{rf,z} \sim 9\times 10^2\,\text{m}^{-1}$. The MW inhomogeneity of our waveguide along z was estimated in [43]. It involves the measurement of the fringe contrast decay under the application of pulses of variable duration. The measurement gives $\delta_{mw,z} \sim 3\times 10^4\,\text{m}^{-1}$.

- **Detuning inhomogeneity** The detuning from the intermediate level $|2,0\rangle$, $\Delta(\mathbf{r})$, may also have some spatial inhomogeneity due to the trap:

$$\Delta(\mathbf{r}) = \Delta_0 + \frac{\alpha_m}{\hbar}B_t(\mathbf{r}). \tag{5.6}$$

B_t is the trapping magnetic field and α_m refers to the convention of equation 1.8. In the x and y directions the field varies quadratically and the corresponding spatial inhomogeneity of the detuning is 0 to our level of approximation. In the z direction the magnetic field across the cloud is linear due to the gravitational sag. We estimate the typical inhomogeneity to be

$$\delta_{\Delta,z} = \frac{mg}{\hbar\Delta_0} \sim 4.3\times 10^3\,\text{m}^{-1}. \tag{5.7}$$

At this point we can summarize the results by saying that the inhomogeneity along z is dominated by the inhomogeneous one-photon microwave Rabi frequency. Along y it is dominated by the inhomogeneous one-photon radiofrequency Rabi frequency. Along x the typical inhomogeneity is given by the wavevector $\mathbf{k}$. Experimentally we did not observe sidebands at the x trapping frequency.

5.1.2 Calculation of the total coupling element

In this part we compute the total coupling element between the initial state $|1,n\rangle$ (we have adopted the convention: $|\text{internal state}, \text{external state}\rangle$) and the final state $|2,n'\rangle$. We will restrict ourselves to the z direction, however, a similar derivation applies for the other directions. We also use a generic notation that applies to both the MW and RF fields. There are two effects to be considered: the first one is the spatial inhomogeneity of the two-photon Rabi frequency. The second effect is specific to our two-photon transition: the effect of an inhomogeneous AC Zeeman shift is to produce a displacement of the trap centers.

Effect of an inhomogeneous Rabi frequency

If $\hat{a}^\dagger$ is the ladder operator of the harmonic trap along z the Rabi frequency can be expressed as

$$\Omega(\hat{z}) = \Omega_0 \left(1 + \delta_z \hat{z}\right) = \Omega_0 \left(1 + \delta_z \sqrt{\frac{\hbar}{2m\omega}} (\hat{a} + \hat{a}^\dagger)\right). \tag{5.8}$$

Effect of an inhomogeneous AC Zeeman effect: trap displacement

The effect of the dressing by an inhomogeneous AC Zeeman effect is to displace the trap centers. We call Δz_i the distance between the centers of the dressed and undressed traps for state i. A detailed calculation of the AC Zeeman shift of both interrogation signals can be found in appendix A. We consider the generic energy shift of state i: $\hbar\Omega(z)^2/(4\Delta)$. Here the spatial dependence of Δ is neglected, as it is of second order in position in the x and y direction, and along z the inhomogeneity is dominated by $\Omega(z)^2$. The trap center displacement resulting from this shift is given by

$$\Delta z_i = \frac{\hbar\, \Omega_0^2\, \delta_z}{\Delta\, (m\, \omega_z^2)}. \tag{5.9}$$

The two-photon pulse drives a transition between traps that are separated by $d_z = \Delta z_2 - \Delta z_1$. If $|n[i]\rangle$ denotes the trap levels for an atom in the internal state $|i\rangle$ we obtain the following equality:

$$|n[2]\rangle = e^{-\frac{i d_z \hat{p}_z}{\hbar}} |n[1]\rangle. \tag{5.10}$$

The distance d_z can be expressed:

$$d_z = \frac{\hbar}{\Delta m \omega_x^2} (\alpha \Omega_{rf,z}^2 \delta_{rf,z} - \Omega_{mw,z}^2 \delta_{mw,z}), \tag{5.11}$$

where α is a coefficient that takes into account the polarization of the RF field at the atoms' position (see appendix A).

Total coupling element

The total coupling element between the states $|1, n[1]\rangle$ and $|2, n'[2]\rangle$ can be expressed as

$$\Omega_{n,1\to n',2} = \langle 2, n'[1] | \Omega(\hat{z}) e^{\frac{i d_z \hat{p}_z}{\hbar}} |1, n[1]\rangle. \tag{5.12}$$

In terms of ladder operators we obtain, to first order:

$$\Omega_{n,1\to n',2} = \langle n', [1], 2 | \Omega_0 \left(1 + \sqrt{\frac{\hbar}{2m\omega_z}} \left[\delta_z + \frac{d_z m \omega_z}{\hbar}\right] \hat{a} + \sqrt{\frac{\hbar}{2m\omega_z}} \left[\delta_z - \frac{d_z m \omega_z}{\hbar}\right] \hat{a}^\dagger\right) |n, [1], 1\rangle. \tag{5.13}$$

On this expression it is clear that a field gradient can drive sideband transitions. We note that the coupling element for the red sideband is proportional to $\sqrt{n-1}$ and the coupling for the blue sideband to $\sqrt{n}$.

Sideband extinction We also observe that the combination of the two effects can give rise to sideband cancelation. From equation 5.13 we derive the condition for the red (−) or blue (+) sideband extinction:

$$\delta_z = \pm \frac{d_z \, m \, \omega_z}{\hbar}, \tag{5.14}$$

which does not depend on the trap level $|n\rangle$.

In the succeeding sections we present the experimental realization of sideband transitions.

5.2 Spectra of trapped thermal atoms under inhomogeneous excitation

In all the following the atomic cloud is interrogated with Rabi pulses. The trap used for these experiments is characterized by the frequencies $\{f_x, f_y, f_z\} = \{\omega_x, \omega_y, \omega_z\}/(2\pi) = \{2.9, 92, 74\}$ Hz.

5.2.1 Typical data

Figure 5.3 shows an example of the typical spectra acquired. The central structure corresponds to a transfer on the carrier. On both sides of the carrier we observe the appearance of sharp peaks located at the detunings $-f_y$, f_z and f_y. We can also distinguish smaller peaks at detunings of $2f_z$ and $f_z + f_y$. As the power is increased we observe the emergence of extra sidebands at: $2f_y$ and $-f_z$. This result gives the demonstration that trap sideband can be driven in our system.

There are several other comments to be made on this figure: first, we observe a strong asymmetry of the spectra. This point is discussed further in section 5.2.3. Second, we observe that the position of the sidebands does not correspond exactly to the trap frequencies. For example, their location depends on the microwave power applied. We consider this phenomenon in section 5.2.4.

5.2.2 Transfer efficiency

For a given wire geometry and trap position the field inhomogeneities are constant. An increase in coupling on the sideband can be achieved by increasing the interaction time, power or the mean state index n (for a given state $|n\rangle$).

Figure 5.4 shows a comparison of the sideband transitions obtained for 1 s and 2 s interaction times. We observe that longer interrogation times can increase the sideband amplitude, giving transfer efficiencies up to 65 %.

Figure 5.5 shows the dependence of the blue sideband amplitude as a function of the final frequency of the RF cooling ramp (controlling the cloud temperature and thus the mean occupation number $\langle n \rangle$). For this measurement we used pulses of 50 ms, $P_{rf} = -12$ dBm and

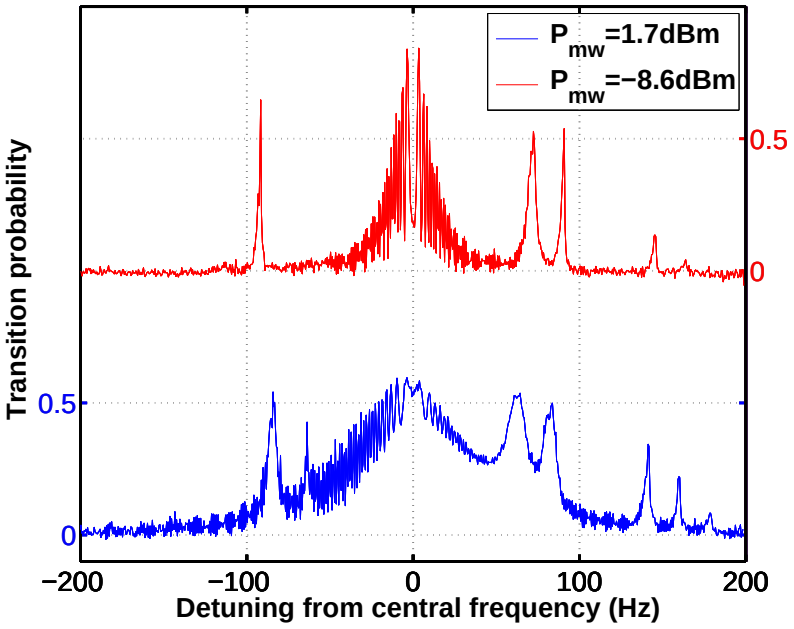

Figure 5.3: *Rabi spectra for* 1 s *pulses and* $P_{rf} = -12$ dBm. *We choose the carrier frequency as* 0. *The ensemble of peaks around zero corresponds to a transfer on the carrier. Top: We observe the existence of sharp peaks located at detunings of* $-f_y$, f_z *and* f_y *as well as* $2f_z$ *and* $f_z + f_y$. *These peaks correspond to single and double sideband transitions. Bottom: as the MW power is increased we observe the emergence of the* $-f_z$ *and* $2f_y$ *sidebands. This result demonstrates the possibility to drive sideband transitions in our system. We also observe a strong asymmetry of the spectra, as well as a displacement of the sideband location as the MW power increases. These two points will be investigated further.*

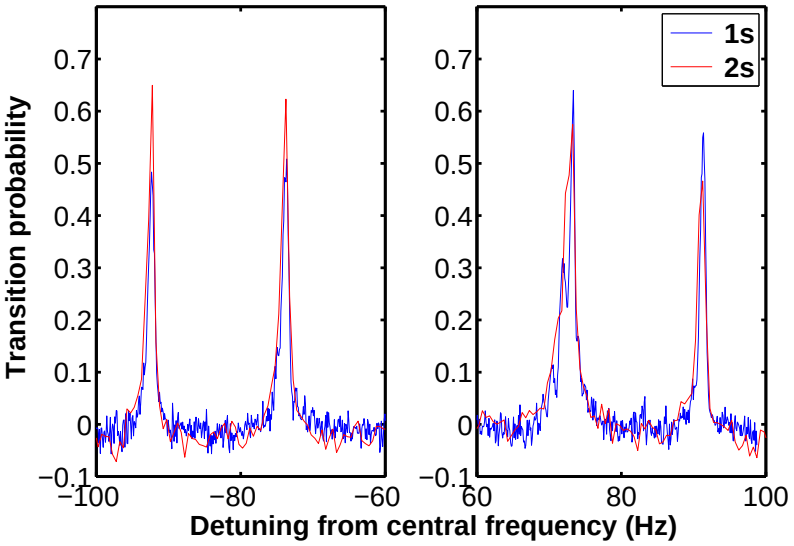

Figure 5.4: *Rabi spectra taken with identical MW and RF powers (*−8.6 dBm *and* −17 dBm *respectively) but for interrogation times of* 1 s *and* 2 s. *Longer interrogation times can increase the sideband amplitude.*

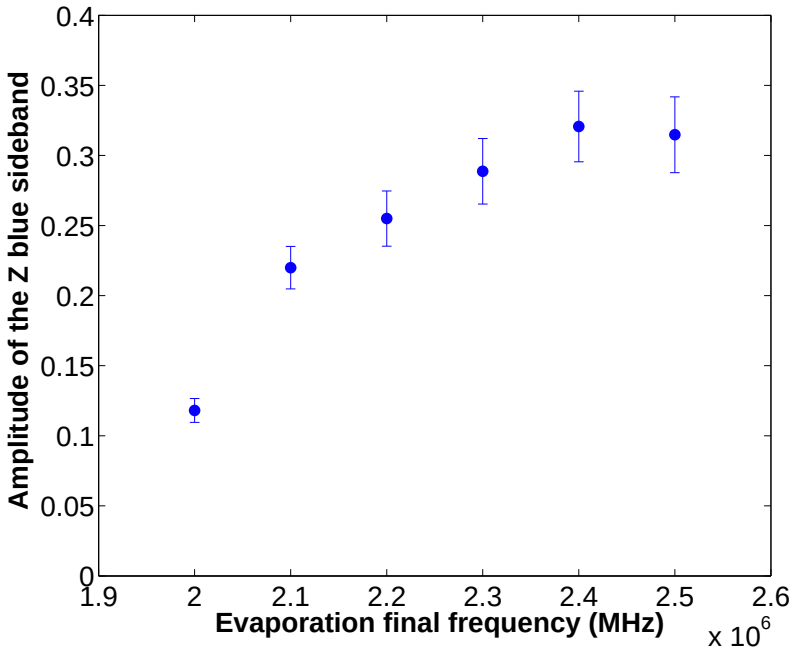

Figure 5.5: *The amplitude of the z blue sideband as a function of the evaporation final frequency (the evaporation final frequency is an increasing function of the cloud temperature). For this measurement we used pulses of* 50 ms, $P_{rf} = -12$ dBm *and* $P_{mw} = 1.7$ dBm. *For constant powers, the sideband amplitude increases with the cloud temperature, which is consistent with the fact that the coupling element of a given state* $|n\rangle$ *is proportional to* $(n+1)$.

$P_{mw} = 1.7$ dBm. We observe that the sideband amplitude increases with cloud temperature. This is consistent with the fact that the coupling element of a given state $|n\rangle$ is proportional to $(n+1)$.

5.2.3 Observation of the sideband cancelation

In the experiment the inhomogeneity δ_z cannot be easily adjusted (it would require one to change the trap position). Conversely, the trap displacement d_z can be adjusted as it is determined by the MW and RF power.

An interesting feature of the two-photon transition lies in the ability to change the RF and MW power while keeping the two-photon Rabi frequency constant. Figure 5.6 compares two measurements taken with 1 s pulses and different RF and MW powers. We observe that the blue z sideband is extinguished at $P_{rf} = -12$ dBm whilst the amplitude of all other peaks remains comparable. As the two-photon Rabi frequency of the two experiments were quite similar we attribute this extinction to the combined effect of the inhomogeneous two-photon Rabi frequency and the inhomogeneous one-photon AC Zeeman shift explained previously.

Thus, by tuning the RF power we can achieve the extinction of the red z sideband. In the sideband extinction condition, the only parameter that can be tuned is the trap center displacement d_z. From the fact that tuning the RF power changes the amplitude of the red z

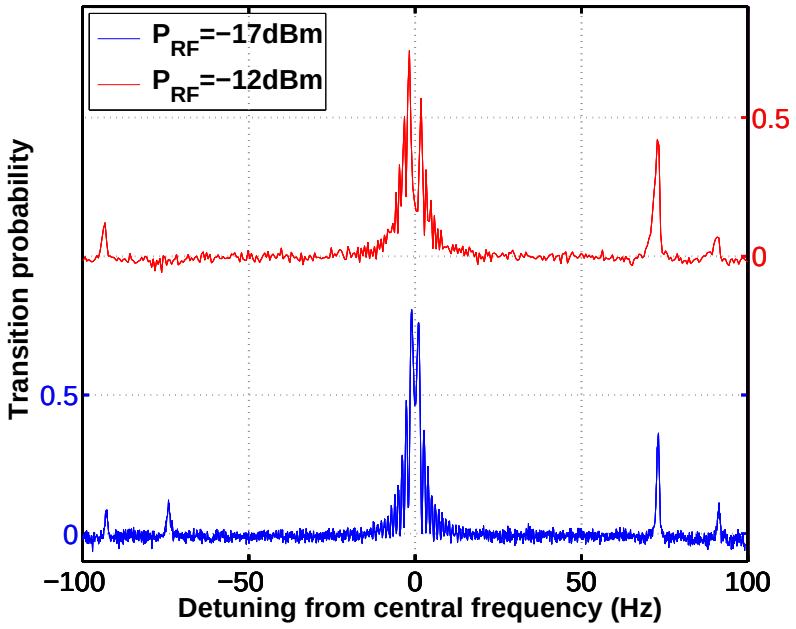

Figure 5.6: *Rabi spectra for pulses where $T = 1\,\mathrm{s}$, different RF/MW power configurations and comparable two-photon Rabi frequencies. Top: P_{rf}−17 dBm, P_{mw}−18.7 dBm and $\Omega_0/(2\pi) = 2.98\,\mathrm{Hz}$. Bottom: P_{rf}−12 dBm, P_{mw}−21.9 dBm and $\Omega_0/(2\pi) = 2.23\,\mathrm{Hz}$. On the upper spectrum we observe the extinction of the z red sideband while all other peaks remain of comparable amplitude. Since the Rabi frequencies are comparable we attribute the sideband extinction to the cancelation condition 5.14. We also learn from this experiment that the trap displacement along z is dominated by the RF power, i.e. ${\Omega_{mw,0}}^2\delta_{mw} \ll {\Omega_{rf,0}}^2\alpha\delta_{rf}$.*

sideband we conclude that the displacement d_z is dominated by the RF contribution, that is, ${\Omega_{mw,0}}^2\delta_{mw} \ll {\Omega_{rf,0}}^2\alpha\delta_{rf}$.

We have observed in data that are not shown here that the z red sideband remains canceled up to two-photon Rabi frequencies of $\Omega_0/(2\pi) = 22.5\,\mathrm{Hz}$. Coming back to figure 5.3 we observe for $\Omega_0/(2\pi) = 39.3\,\mathrm{Hz}$ a weak coupling of the z red sideband, this might be the effect of higher order terms of the inhomogeneity.

Assuming ${\Omega_{mw,0}}^2\delta_{mw} \ll {\Omega_{rf,0}}^2\alpha\delta_{rf}$ the z red sideband cancelation condition reads:

$$-\frac{\Omega_{rf,0}^2\alpha}{2\omega_z\Delta} = 1 + \frac{\delta_{mw,z}}{\delta_{rf,z}}. \tag{5.15}$$

In this experiment $\alpha < 0$ and $\Delta > 0$ which is consistent with the extinction of the red sideband. The blue sideband extinction should happen for a detuning $\Delta' = -\Delta$. We compute the left-hand side of equation 5.15 and get ~ 1.75 (see appendix A), which is fairly close to the independent estimation of the right-hand side (~ 1.6).

We also note that the sideband extinction condition cannot be fulfilled at the same time as in the z and y directions: as $\delta_{rf,y} \simeq \delta_{rf,z}$, $\delta_{mw,z} \gg \delta_{mw,y}$ and $\omega_y \sim \omega_z$, no extinction of the y sideband can be observed within the power range used to demonstrate the z sideband

cancelation.

5.2.4 Sideband dressing by the carrier

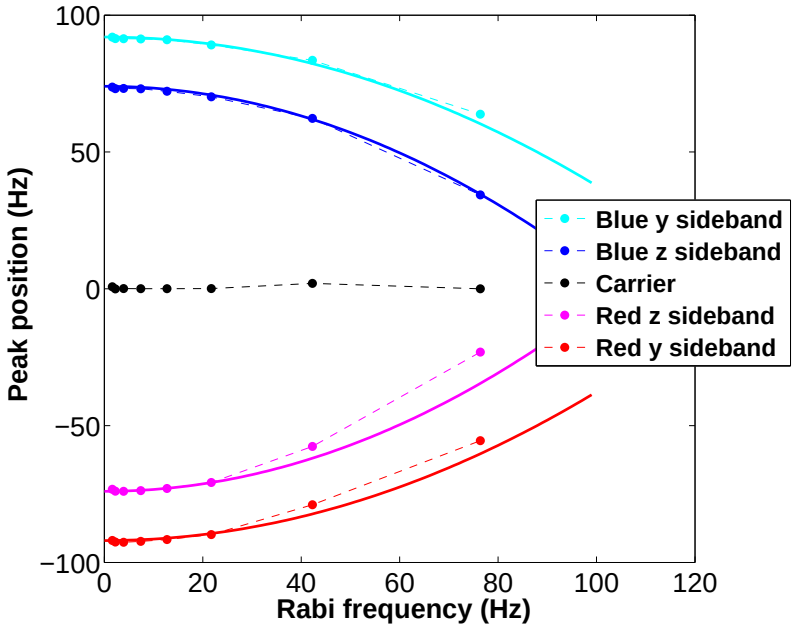

Figure 5.7: *Peak position as a function of the carrier Rabi frequency. Full lines sketch the model* Ω_0/w_i^2 *which describes a dressing of the sideband transitions by the carrier. We find good agreement between data and prediction. The deviation from the red sideband prediction at high power remains unexplained.*

An intriguing phenomenon is the attraction of the sideband frequencies toward the carrier at high powers. Figure 5.7 shows a systematic measurement of the sideband position with respect to the carrier as a function of the two-photon Rabi frequency. We interpret this attraction as the dressing of the sideband transitions by the carrier. In fact, our results agree closely with the expectation for this effect, given by the AC Zeeman shift Ω_0/w_i^2.

5.3 Cloud dynamics induced by sideband excitations

5.3.1 Non sideband-resolved regime

Full spectrum

The non sideband-resolved regime, $\Omega_0 \gg \omega_z, \omega_y$ corresponds to the carrier transition being so broad that it is no longer possible to separate the sideband and the carrier spectra (figure 5.8). As a first approximation we fit the data with a sum of two Rabi spectra, that is to say, we neglect the coherence between the carrier and the sidebands for now. This fit gives an idea of the amount of atoms that are transferred on the carrier or on the sideband.

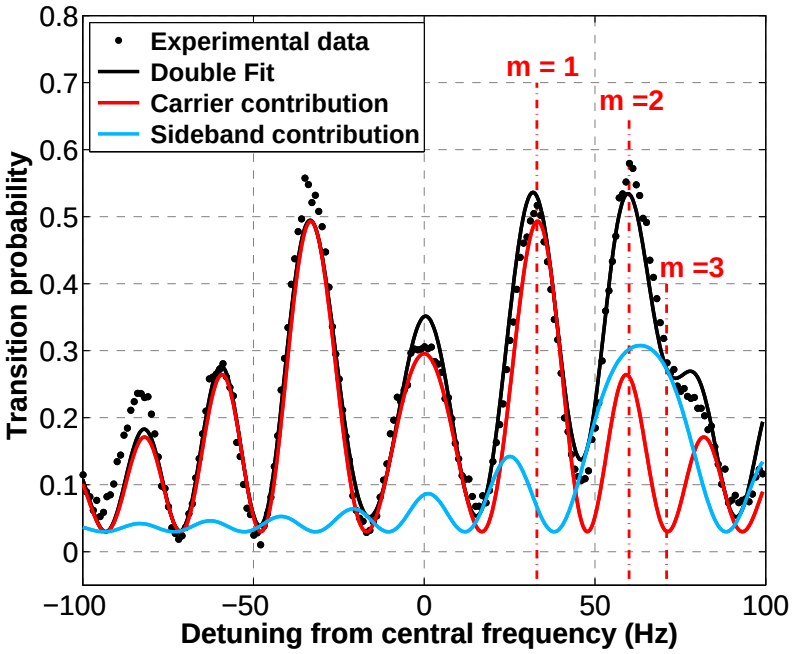

Figure 5.8: *Rabi spectrum obtained for* $P_{mw} = 1.7\,\mathrm{dBm}$, $P_{rf} = -12\,\mathrm{dBm}$ *and* $T = 50\,\mathrm{ms}$. *As a first approximation we fit the spectra with a sum of two Rabi spectra. This gives an indication of the amount of atoms that are transferred on the sideband and on the carrier.*

At several points of this spectrum, we have recorded the cloud dynamics of state $|1\rangle$ and $|2\rangle$ by repeating the experiment with a variable trapping time $t = 0\,\mathrm{ms} to 50\,\mathrm{ms}$ after the interrogation. Then the clouds are imaged after 20 ms of time of flight.

$m = 1$: Excitation on the carrier only

Figure 5.9 shows the cloud profiles after time of flight as a function of the holding time for a quasi-pure excitation on the carrier ($m = 1$ in figure 5.8). We observe that both $|1\rangle$ and $|2\rangle$ clouds have a gaussian shape.

$m = 2$: Mixed carrier/sideband excitation

Figure 5.10.a shows the cloud profiles after time of flight as a function of the holding time for a mixed carrier/sideband excitation ($m = 2$ in figure 5.8). About half of the atoms in the $|2\rangle$ are transferred on the carrier and half on the sideband. On the state $|2\rangle$ cloud shape we observe a beat dynamics at the frequency 74 Hz, which corresponds to the z trapping frequency. We interpret this signal as the interference between the wavefunctions of the carrier and the sideband.

We model, for now, the data by assuming that the state transferred on the carrier has a gaussian profile $\Psi_0(z) = Ae^{-z^2/(2\sigma_z^2)}$ whereas the state transferred on the sideband has a profile of the form $\Psi_1(z) = Bze^{-z^2/(2\sigma_z^2)}$. We consider the sum

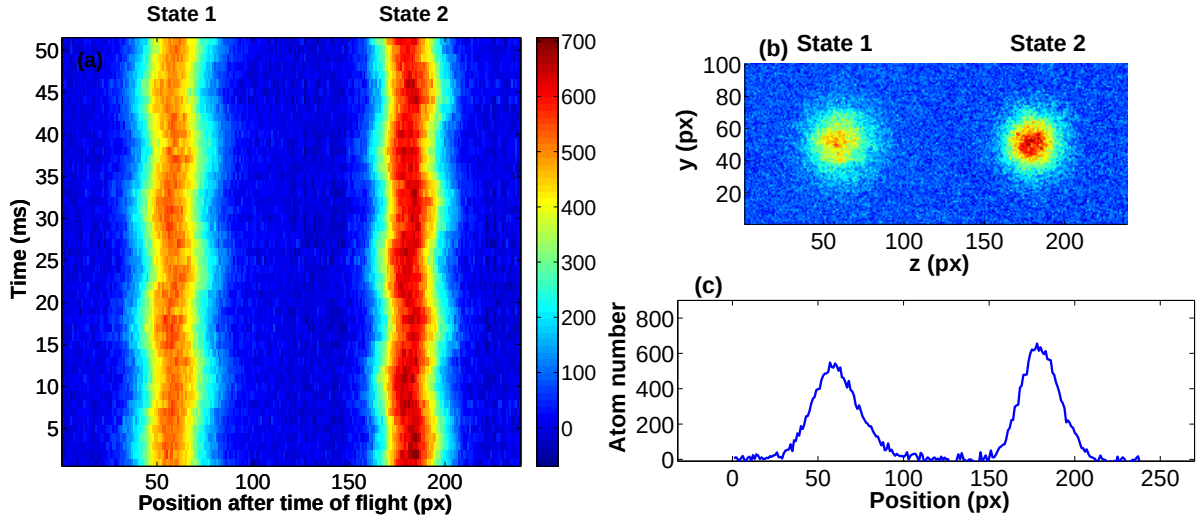

Figure 5.9: *Excitation on the carrier only ($m = 1$ in figure 5.8). (a) Cloud profiles after time of flight integrated along y and x as a function of the holding time after the pulse. The scale is given in atoms. (b) Cloud profiles integrated along x and (c) along x and y for* 10 ms *holding time. Both cloud profiles are gaussian.*

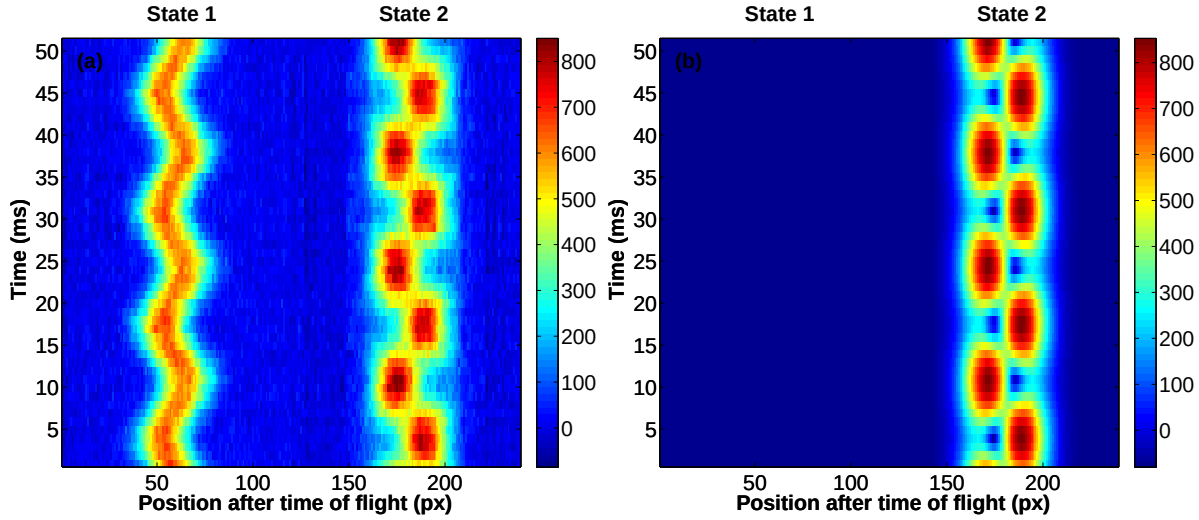

Figure 5.10: *Excitation by a mixed carrier-sideband pulse ($m = 2$ in figure 5.8). (a) Cloud profiles after time of flight integrated along y and x as a function of the trapping time after the pulse. The scale is given in atoms. We observe a beat dynamics on the cloud shape of the $|2\rangle$ state at the frequency* 74 Hz. *We interpret this beat as an interference between atoms transferred on the carrier and on the sideband. At the same time state $|1\rangle$ undergoes out-of-phase oscillations in the trap. (b) Reproduction of the $|2\rangle$ cloud profile with the approximate model described in the text.*

$$\psi_{tot}(z,t) = \Psi_0(z) + \Psi_1(z)e^{i\omega_z t}. \tag{5.16}$$

and find that the function $A_0 + |\Psi_{tot}|$ reproduces the experimental data fairly well with

$A_0 = -80$, $A = 352$, $B/A = 0.25e^{-1.1i}$, $\omega_z = 2\pi \cdot 74\,\mathrm{Hz}$ and $\sigma_z = 11.18\,\mathrm{px}$ (see figure 5.10.b). Our modeling may seem somewhat arbitrary. We give in section 5.3.3 a qualitative justification. The derivation of a more rigorous explanation based on the Wigner function formalism is currently ongoing in our team. It would also have to explain the oscillation of state $|1\rangle$ that we observe.

$m = 3$: Excitation on the sideband only

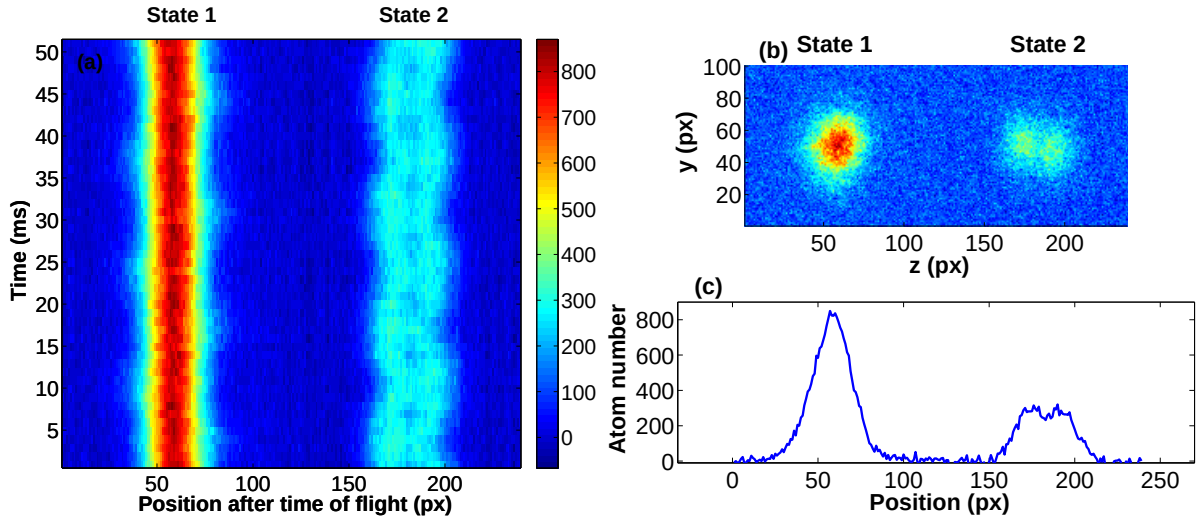

Figure 5.11: *Excitation on the sideband only ($m = 3$ in figure 5.8). (a) Cloud profiles after time of flight integrated along y and x as a function of the holding time after the pulse. The scale is given in atoms. (b) Cloud profiles integrated along x and (c) along x and y for 22 ms holding time. Whilst state $|1\rangle$ profile remains gaussian, state $|2\rangle$ profile exhibits a double-peak structure which qualitatively corresponds to the function $|\Psi_1(z)|^2$. In (a) we observe an out-of-phase oscillation of the two clouds at the trap frequency.*

Figure 5.11 shows the cloud profiles after time of flight as a function of the holding time for a quasi pure excitation on the sideband ($m = 3$ in figure 5.8). We observe that state $|1\rangle$ profile is gaussian. State $|2\rangle$ profile has a double-peak structure, which qualitatively corresponds to the function $|\Psi_1(z)|^2$. In figure 5.11.a we observe an oscillation of both clouds at the z trap frequency. This could be a similar beat signal as observe in the mixed sideband/carrier situation, and would mean that the transfer is not purely on the sideband.

By going to the sideband-resolved regime one should reduce such an effect.

5.3.2 Sideband-resolved regime

Figure 5.12.a shows the cloud profiles after time of flight as a function of the holding time for a pure excitation on the sideband, in the sideband-resolved regime. We used $P_{mw} = -3.5\,\mathrm{dBm}$, $P_{rf} = -17\,\mathrm{dBm}$ and $T = 1\,\mathrm{s}$. We clearly observe a double structure for state $|2\rangle$ profile. State

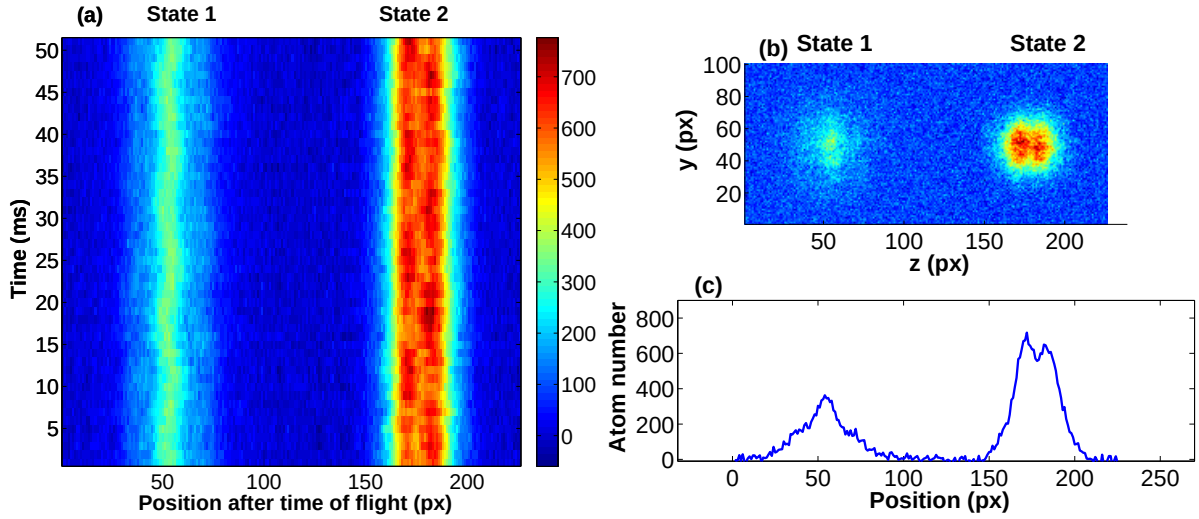

Figure 5.12: *Sideband excitation in the sideband-resolved regime for* $P_{mw} = -3.5\,\mathrm{dBm}$, $P_{rf} = -17\,\mathrm{dBm}$ *and* $T = 1\,\mathrm{s}$. *(a) Cloud profiles after time of flight integrated along* y *and* x *as a function of the trapping time after the pulse. The scale is given in atoms. (b) Cloud profiles integrated along* x *and (c) along* x *and* y *for* $22\,\mathrm{ms}$ *holding time. Whilst state* $|1\rangle$ *profile remains gaussian, state* $|2\rangle$ *profile exhibits a double-peak structure which qualitatively corresponds to the function* $|\Psi_1(z)|^2$. *In (a) we do not observe cloud oscillations.*

$|1\rangle$ profile has a sharper, non-gaussian structure along z.

5.3.3 Interpretation

We have shown the existence of a cloud dynamics when driving sideband transitions in our system. The interpretation of these observations is not straightforward, as we are dealing with a thermal cloud of mean occupation number $\langle n\rangle \sim 30$. Thus, many different trap states are occupied by the atoms and it is not obvious that we must observe such interferences. The approximate model we have used suggests that our system reproduces the behavior of a quantum harmonic oscillator reduced to its ground and first excited states. However, the link between the thermal cloud and the quantum harmonic oscillator must be clearly established.

A detailed modeling of the data is currently ongoing in our team. Here we would like to justify the use of a function of the form $\Psi_1(z) = Bze^{-z^2/(2\sigma_z^2)}$ to describe the atoms transferred on the sideband. We consider the density matrix of a thermal gas

$$\hat{\rho} = \sum_{n=0}^{\infty} p_n |\varphi_n\rangle\langle\varphi_n|, \tag{5.17}$$

where p_n is given by the Bolztmann distribution. The corresponding cloud profile in the momentum space is gaussian. The sideband transition corresponds the application of the $\hat{a}^\dagger$ ladder operator to the state. After the application of this operator the new density matrix takes the form

$$\hat{\rho}' = \sum_{n=1}^{\infty} n p_{n-1} |\varphi_n\rangle\langle\varphi_n|. \tag{5.18}$$

The distribution np_{n-1} is peaked around a finite value of n, as opposed to the distribution p_n, peaked around $n = 0$. We are currently calculating whether this could explain the double-peak profile observed. In a next step, one would have to model the beat dynamics. Moving to the Heisenberg picture, one can intuitively see that the beat will be provoked by the time evolution of the $\hat{a}^\dagger$ operator. This calculation is also ongoing.

5.4 Conclusion

In this chapter we have given an experimental demonstration of the coherent manipulation of the external state of trapped atoms in the thermal regime. We have demonstrated that, due to the existence of field gradients, we are able to drive sideband transitions.

A special feature of the two-photon transition is the existence of an AC Zeeman shift. We have shown both theoretically and experimentally that, by tuning the balance between the effect of an inhomogeneous AC Zeeman shift and an inhomogeneous two-photon Rabi frequency, it is possible to control the asymmetry between the blue and the red sideband or even have complete extinction of one of them.

When exciting the sideband the cloud profiles dynamics reveals unexpected features: for a pure sideband excitation we observe a double-peak structure whilst we observe a gaussian structure for a pure transition on the carrier. When the excitation mixes the sideband and the carrier, we observe a beat signal at the trap frequency. Due to the fact that we deal with a thermal cloud, many trap states are occupied and the exact modeling of this behavior remains to be done. Nevertheless, the observation of a beat signal confirms the coherence of the transfer process.

By engineering the RF and microwave fields one could reach extinction of the carrier itself: this could be done by creating quadrupole fields that cancel at the trap center [89]. In this configuration pure sidebands could be excited with broad spectrums (large powers, short pulses) which is adapted to the realization of an on-chip atom interferometer.

Chapter 6

An atomic microwave powermeter

Today's primary standards for measuring radiofrequency or microwave powers are based on a comparison of the heat produced by a RF signal with that of a DC signal [90]. This approach gives uncertainties that are dominated by the differences in the RF and DC heat dissipation processes. The general trend in metrology is to define all the units by fundamental properties of quantum systems, according to the philosophy of atomic clocks.

A proof of principle of a primary microwave power standard with an atomic fountain was reported Crowley at al. [91]. Atoms were launched through a microwave cavity and Rabi oscillations between the two states were observed as a function of microwave field strength. With this approach the microwave power measured using atoms agreed to within less than 5 % with the value given by a conventional device.

Exact knowledge of the field distribution is required to build an absolute microwave power standard. With this aim in mind a dedicated microwave transmission line was designed at the National Research Council of Canada. By probing the field with a cloud of cold atoms passing through the transmission line, an agreement of 1.3 % with the value of a conventional powermeter was obtained [92].

In this chapter we will give an experimental proof of principle of a cold atom-based microwave powermeter. It does not measure the absolute power but confirms the linearity of another device over 80 dB. Working with trapped atoms, i. e. disposing of timescales from 1 ms to 5 s enables one to explore a large range of microwave powers. We investigate three different methods: (1) based on the measurement of the Rabi frequency in frequency domain; (2) based on the measurement of the Rabi frequency in time domain; (3) based on the measurement of the AC Zeeman frequency shift on the clock transition induced by the microwave.

All the experiments presented here were carried out with a thermal cloud in the interrogation trap of frequencies $\{\omega_x, \omega_y, \omega_z\}/(2\pi) = \{2.9, 92, 74\}$ Hz. The radiofrequency power during interrogation is equal to -12 dBm unless otherwise specified. The power at the output of the microwave guide was measured by a conventional powermeter (Agilent E4418B) used for the comparison.

6.1 Rabi spectra

6.1.1 Principle of the experiment

The aim of the experiment is to record Rabi spectra for various input microwave powers. By using a fit of the form 1.2 one determines two quantities: the Rabi frequency Ω_0 and the central frequency f_0 (figure 6.1). The central frequency is displaced by the AC Zeeman shift of the microwave photon (see section 6.3). In this section we only consider the Rabi frequency.

Typical spectra An example of typical spectra is shown on figure 6.1.a. The statistical error from the fit gives the error on the measurement of Ω_0.

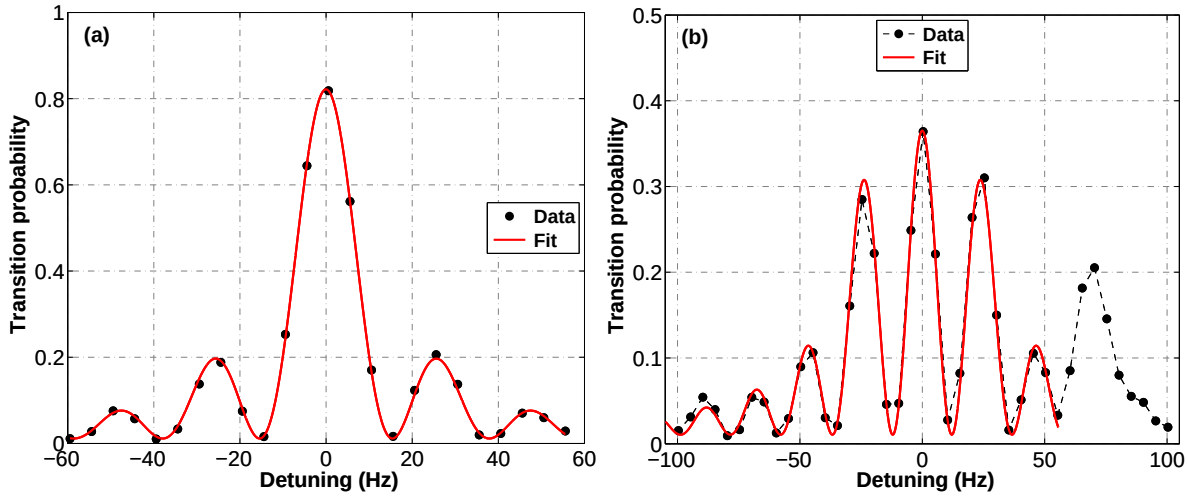

Figure 6.1: *(a) A typical Rabi spectra for a* 50 ms *interrogation. The fit gives the two-photon Rabi frequency* $\Omega_0 = 12.74(6)$ Hz *for a contrast* $C = 0.98$. *(b) A typical Rabi spectra where the blue sideband is excited at* $\sim \omega_z$. *The best fit of the data is obtained when ignoring the sideband.*

Excitation of the trap sidebands The existence of field gradients for both the microwave and the radiofrequency signals can lead to excitation of trap sidebands, which may add noise when trying to determine the fit parameters. In some cases ($\Omega_0 \ll \omega_z$) we can ignore them when fitting the data (see figure 6.1.b). In a purpose built device one would avoid such effects.

Contrast loss for high powers At high microwave powers we observe typical spectra as shown in figure 6.2. Around the resonance the signal does not decrease down to zero. The same phenomenon is observed in the Rabi interrogation in time domain (see section 6.2). We discuss possible causes of this contrast loss in section 6.4. Here we would like emphasize that the Rabi frequency can, nevertheless, be extracted from such a spectra since the periodicity with Ω_0 is well visible.

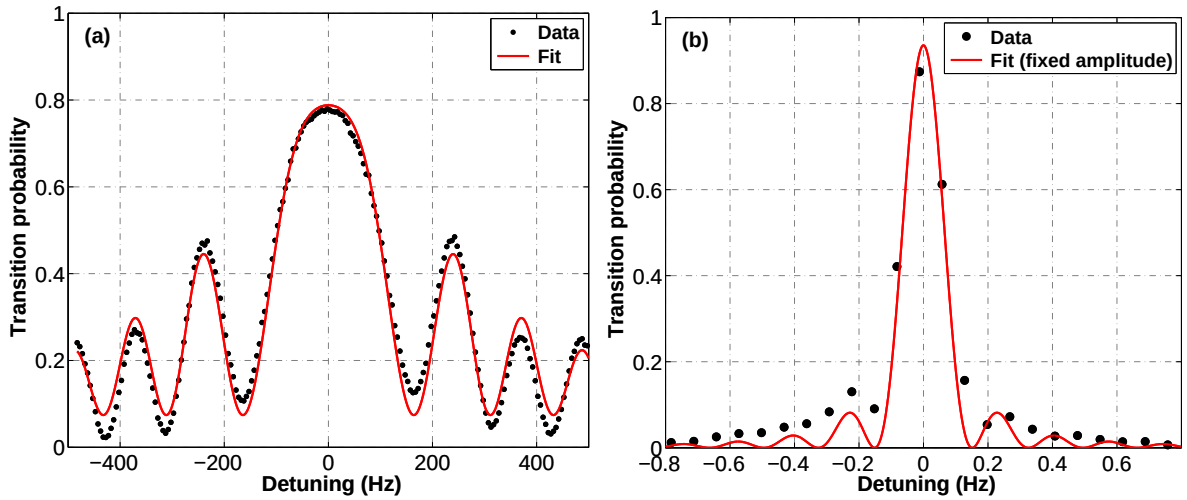

Figure 6.2: *(a) Rabi spectra for* $\Omega_0/(2\pi) = 251.1(4)$ Hz *and* 10 ms *pulse duration. Around the resonance, the signal does not decrease to zero, this effect is discussed further in section 6.2. Further away from the resonance, it does. Consequently, the fit with eq 1.2 does not match the data points exactly. However, the Rabi frequency can be determined with a small error since it only depends on the fringe period. (b) Rabi spectra for* $\Omega_0/(2\pi) = 75$ mHz *and a* 6 s *interrogation. This is the smallest Rabi frequency observed so far. It gives an atomic linewidth of* 0.2 Hz.

Pulse asymmetry at very low powers We have demonstrated Rabi interrogations up to 6 s giving a typical linewidth of 0.2 Hz (figure 6.2.b) and a Rabi frequency of 75 mHz. This is the smallest Rabi frequency observed so far. Under these conditions we observe asymmetric Rabi spectra on which the simple Rabi pedestal function does not fit the data well. To extract the Rabi frequency one has to force the signal amplitude to $C = 0.9$. It is not clear what causes this asymmetry. On this timescale a certain number of significant phenomena occur, including: trap losses, spin-exchange collisions, lateral collision and cloud rethermalization. Further investigation is needed to explain these observations.

The data shown in figure 6.2.b were taken with a radiofrequency power $P_{rf,2} = -35$ dBm. To be able to compare them with data taken at $P_{rf,1} = -12$ dBm we proceed to a rescaling of the microwave power assuming somewhat artificially that the radiofrequency amplitude responds perfectly to the programmed power.

6.1.2 Results

The Rabi frequency Ω_0 is expected to vary with the microwave power x expressed in dBm as

$$\Omega_0 \propto 10^{x/20}. \tag{6.1}$$

Figure 6.3 shows the results over a span of 80 dB. On the same graph we have plotted the expected slope of 0.05. We observe that the experimental data is in good agreement with the expected slope in the range -23 dBm$to-10$ dBm. At high power we observe deviations from

linearity of up to 30 %. Possible reasons for such deviations are discussed in section 6.4.

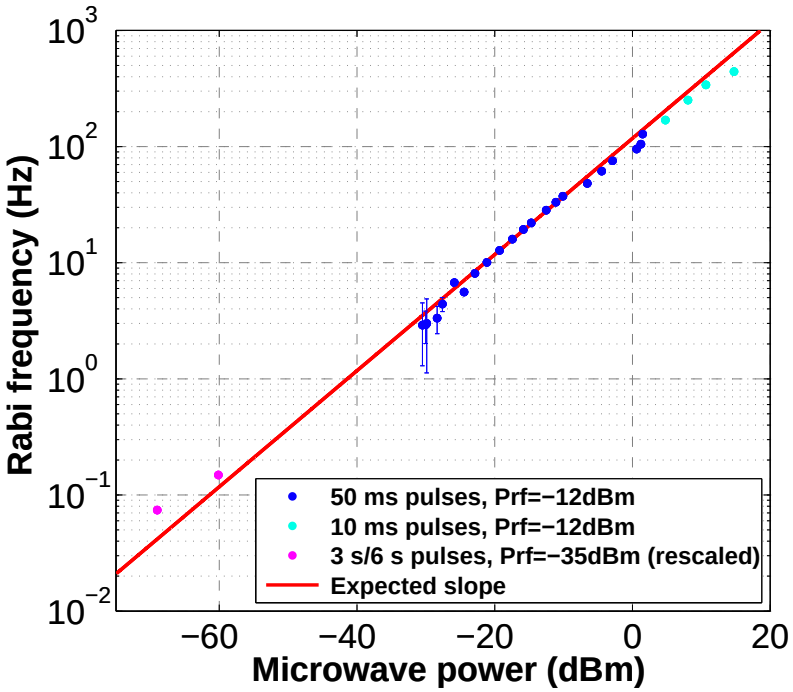

Figure 6.3: *Comparison of the Rabi frequency measured from spectra and the microwave power measured with a commercial microwave powermeter: Agilent E4418B. The magenta points were acquired with a* 23 dB *lower radiofrequency power and are shown rescaled for comparison. We expect the slope* 0.05 *(full red line). The experimental data agree only within the range* −23 dBm*to*−10 dBm*. Possible causes for the deviations from linearity at high power are discussed in section 6.4.*

6.2 Temporal Rabi oscillations

6.2.1 Principle of the experiment

Following this we conducted an experiment in which we measured the Rabi frequency by recording Rabi oscillations in the time domain. For each microwave power the interrogation frequency was set on resonance and the Rabi oscillations in time were recorded by changing the pulse length.

6.2.2 Typical experimental data

Figure 6.4 shows data for a Rabi frequency $\Omega_0 = 38.4\,\mathrm{Hz}$. The contrast decreases and revives once at $T_1 = 365(4)\,\mathrm{ms}$ and a second time at $T_2 = 808(2)\,\mathrm{ms}$. We also show the Fourier spectrum on which peaks at $\omega_0/(2\pi) =\sim 38\,\mathrm{Hz}$, $\omega_z/(2\pi) = 74\,\mathrm{Hz}$, and $(-\omega_y + \omega_z + \Omega_0)/(2\pi) \sim 18.5\,\mathrm{Hz}$ can be observed. Although the fringe contrast varies in time, which is not yet fully understood, the Rabi frequency given by the Fourier spectra can be extracted with a good resolution.

The shape of the Rabi oscillations contrast qualitatively changes with the microwave power applied. Here we present another three typical behaviors (figures 6.5, 6.6 and 6.7). One these graphs we observe Rabi oscillations and contrast revivals. The Fourier spectra show peaks which can be identified as the Rabi frequency and its mixing with the trap frequencies.

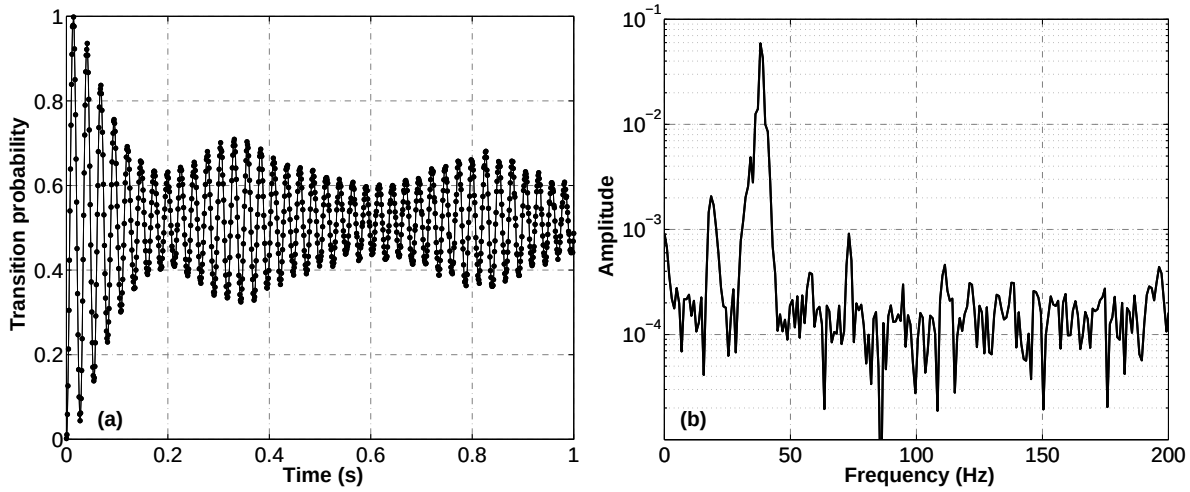

Figure 6.4: *(a) Rabi oscillations at resonance for a Rabi frequency* $\Omega_0/(2\pi) = 38\,\mathrm{Hz}$. *We observe contrast revivals at* $T_1 = 365(4)\,\mathrm{ms}$ *and at* $T_2 = 808(2)\,\mathrm{ms}$. *(b) Fast Fourier transform of the signal after subtracting its mean. Peaks appear at* $\Omega_0/(2\pi) = 38\,\mathrm{Hz}$, $\omega_z = 74\,\mathrm{Hz}$, $(-\omega_y + \omega_z + \Omega_0)/(2pi) \sim 18.5\,\mathrm{Hz}$.

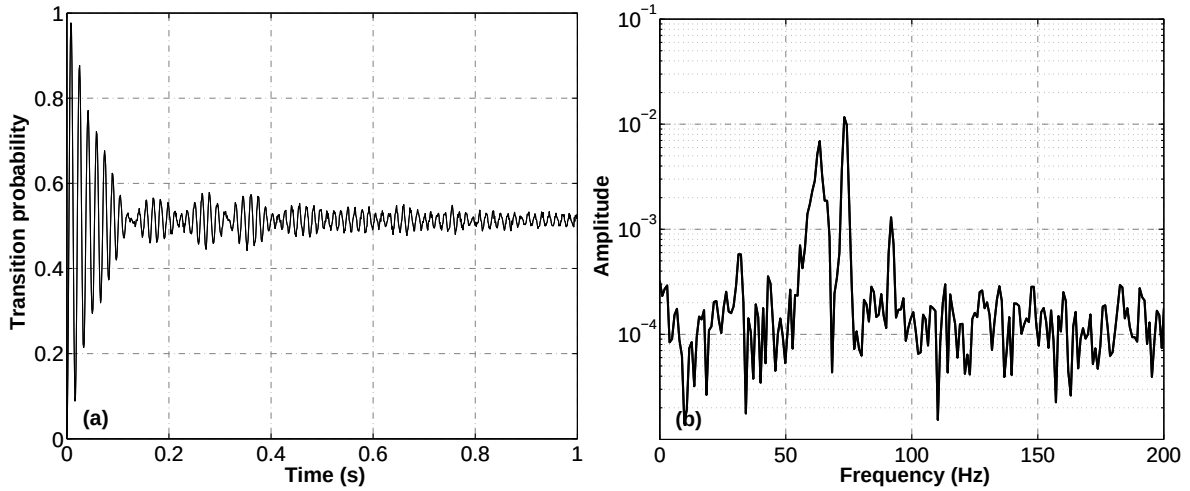

Figure 6.5: *(a) Rabi oscillations for* $\Omega_0/(2\pi) = 63\,\mathrm{Hz}$. *We observe contrast revivals with a period of* $\sim 100\,\mathrm{ms}$, *corresponding to the* $\omega_z - \Omega_0$. *(b) Fast Fourier transform after subtraction of the mean. We identify peaks at* $\Omega_0/(2\pi) = 63\,\mathrm{Hz}$, $\omega_z = 74\,\mathrm{Hz}$ *(*ω_z*) and* $\omega_y 92\,\mathrm{Hz}$. *There is also a peak at* $(\omega_y - \Omega_0)/(2\pi) \sim 30\,\mathrm{Hz}$.

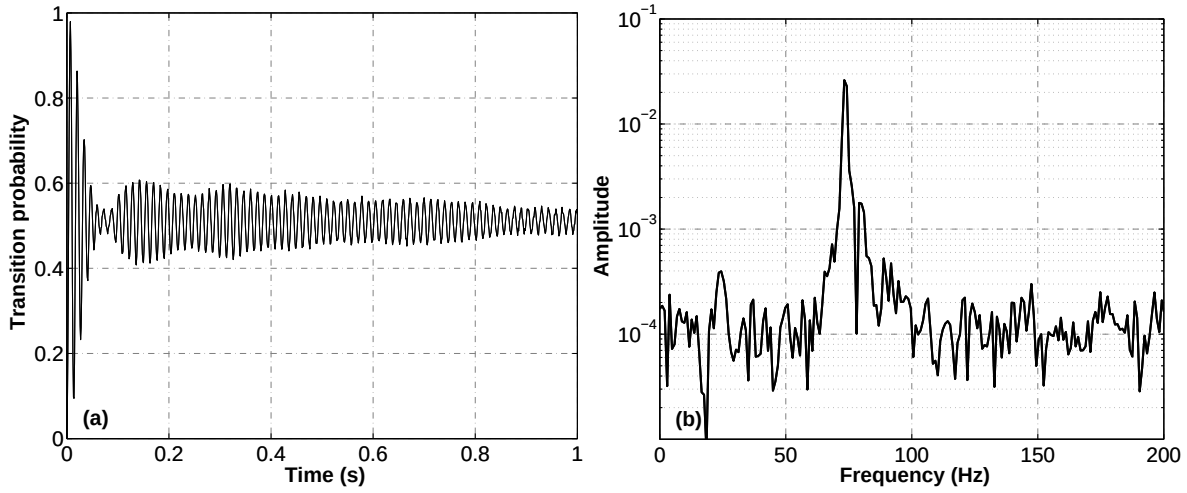

Figure 6.6: *(a) Rabi flopping for* $\Omega_0/(2\pi) = 75\,\mathrm{Hz}$. *(b) Fast Fourier transform after subtracting the mean. It exhibits a double peaked structure including* $\omega_z = 74\,\mathrm{Hz}$.

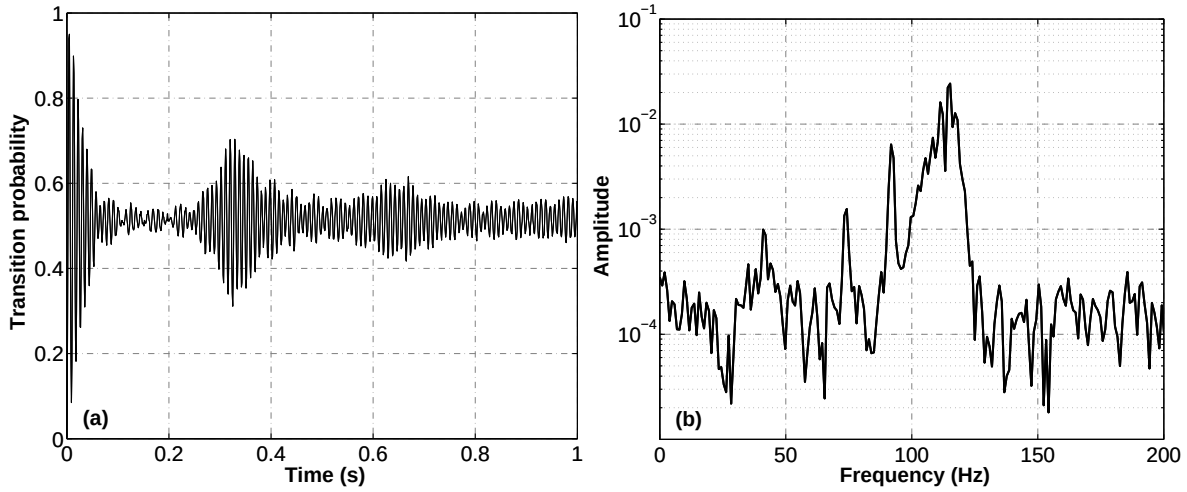

Figure 6.7: *(a) Rabi flopping for* $\Omega_0/(2\pi) = 115\,\mathrm{Hz}$. *We observe contrast revivals with a period of* $\sim 50\,\mathrm{ms}$, *corresponding to* $\Omega_0 - \omega_y$. *The signal revives at* $T_1 = 330(10)\,\mathrm{ms}$, *and also at* $T_2 = 650(30)\,\mathrm{ms}$. *(b) Fast Fourier transform of the signal after subtraction of the mean. We identify peaks at* $\omega_z = 74\,\mathrm{Hz}$, $\omega_y = 92\,\mathrm{Hz}$ *and* $\Omega_0/(2\pi) = 115\,\mathrm{Hz}$ *(*Ω_0*). The peak at* $\sim 40\,\mathrm{Hz}$ *corresponds to* $\Omega_0 - \omega_z$.

Possible driving mechanisms The modeling of these data remains to be done. The reason for the appearance of beat frequencies is probably due to the existence of microwave or radiofrequency field gradients. In the case of a rabi frequency gradient one can use the model of non-interacting thermal clouds to demonstrate that the atomic response has a tendency to decay and then revive at the trap periods. This suggests that the revival observed on some graphs at $\sim 350\,\mathrm{ms}$ is caused by a field gradient along x. The revival times depend on the microwave power, this could be caused by a trap deformation by the field gradient. The same phenomenon can explain the appearance of peaks in the Fourier spectra at the beat frequencies between Ω_0, ω_y and ω_y, as well the contrast loss. In the model of the non-interacting thermal

cloud, however, the contrast equals 1 at the revival times, which is not observed. This model is thus too naive and ISRE certainly plays a determining role as it does for Ramsey interrogation with identical interrogation times.

6.2.3 Results

For each Rabi oscillation the Rabi frequency is deduced from a gaussian fit of the Fourier spectrum and the error is taken equal to the gaussian width. The data we obtained is shown in figure 6.8. We observe that there is a good agreement with the expected slope in the range $-30\,\mathrm{dBm} to -10\,\mathrm{dBm}$. At higher power we observe a deviation from linearity of $\sim 10\,\%$. We discuss its possible causes in section 6.4.

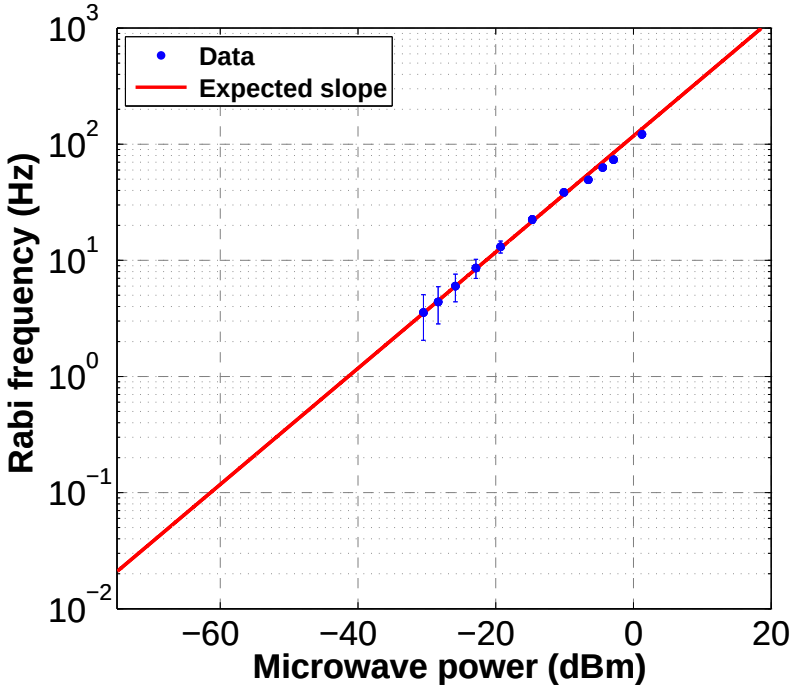

Figure 6.8: *Comparison of Rabi frequency measured from temporal Rabi oscillations and the reading given by the conventional powermeter. The error bars correspond to the peak width in the Fourier space. We observe good agreement with the expected slope for the range* $-30\,\mathrm{dBm} to -10\,\mathrm{dBm}$. *Possible explanations for the deviation of* $\sim 10\,\%$ *at higher power will be discussed in section 6.4.*

6.3 Clock frequency shift measurements

In a third experiment we used the shift of the clock frequency induced by the microwave photon. These data are extracted from the same Ramsey spectra used in section 6.1.

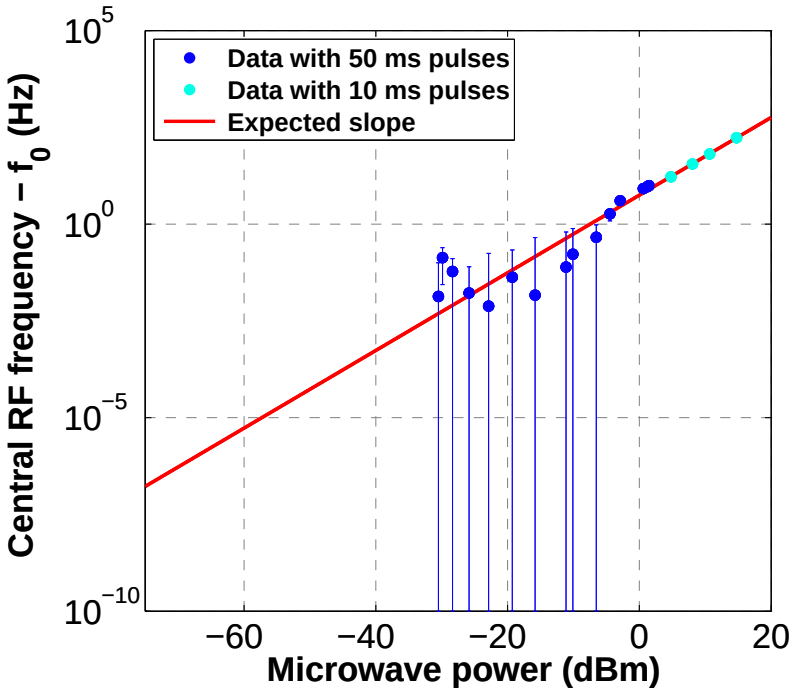

Figure 6.9: *Frequency AC Zeeman shift $f_f 0$ of the clock transition induced by the microwave as a function of the microwave power. The frequency f was obtained from the fit of the Rabi spectra. f_0 is obtained by averaging f over the 5 points of lowest Rabi frequency. We also plot the expected slope. We observe a good agreement within the error bars.*

6.3.1 Principle of the experiment

Through the AC Zeeman effect, the microwave photon produces a frequency shift of the clock transition of the form

$$\Delta f_{mw,|1\rangle\to|2\rangle} = -\frac{\hbar\Omega_{mw}^2}{4\Delta}. \tag{6.2}$$

Here Ω_{mw} is the one-photon Rabi frequency of the microwave and Δ the detuning from the intermediate level, $|2,0\rangle$, as explained in chapter 1.

The outcome of our measurement is the clock frequency $f = f_0 + \Delta f_{mw,|1\rangle\to|2\rangle}$ where f_0 depends on the magnetic field, the cloud density and the radiofrequency photon power. Thus, we expect the quantity $f - f_0$ to scale as $10^{x/10}$ (x is the microwave power in dBm). We obtain f_0 by averaging f over the five points of lowest Rabi frequency, for which no frequency shift is visible.

6.3.2 Results

Figure 6.9 shows the comparison of $f - f_0$ with the microwave power given by the conventional powermeter. We observe a good agreement with the expected slope within the error bars.

6.4 Discussion

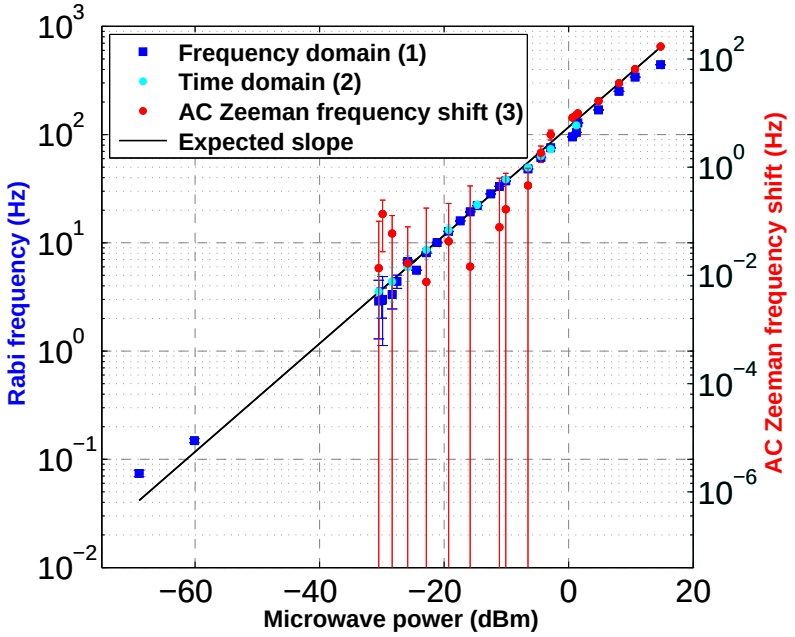

Figure 6.10: *Comparison of the three methods for realizing an atomic microwave powermeter. Dark (1) and light (2) blue points correspond to Rabi frequency measurements and plotted on the left axis. The expected slope (black) is the same one as the one of figures 6.3 and 6.8. On the right axis we have reported the results from the clock frequency shift measurements (3). The span of the right axis is exactly twice as large as the span of the left axis. We have adjusted the lower value of the right axis for the data points to sit approximately on the expected slope. We observe that, at high power, data (1) and (2) begin to deviate from the expected slope at the same point, this suggests a common bias.*

We have investigated three different methods for realizing an atomic microwave powermeter. Figure 6.10 is an accumulation of the results in order to make a comparison. We observe that, at high power, the methods (1) and (2) deviate identically from the expected behavior, suggesting that the bias is common for both experiments. We also note that, at very low power, the points are significantly away from the expectation.

Deviation at high power The deviation could be a deviation of the conventional powermeter: we have checked its reading against a synthesizer (Agilent E8267D) and found an agreement within 0.5 % within the whole range of power explored. Thus, the deviation must be attributed to the atomic device. We now discuss possible causes for the deviation of the atomic device at high power: trap center displacement, state-selective trap center displacement, non-linear effect in the transmission line:

- **Trap center displacement** As explained in the previous chapter a microwave gradient displaces the trap center experienced by state $|1\rangle$. At the position of the displaced trap the Rabi frequency is different from the one experienced at the initial position. The higher the microwave power the stringer the shift and the error on the Rabi frequency.

We make an overestimation for the amplitude of this effect by considering the value of the Rabi frequency at the displaced trap position. It can be written $\Omega_{mw,0}(1+\eta)$ where

$$\eta_i = \frac{\hbar\Omega_{mw,0}\delta_{mw,i}^2}{2\Delta m\omega_i^2} \tag{6.3}$$

for the direction i. We estimate that an error of 1 % corresponds to $\Omega_{mw,0} \sim 100\,\mathrm{kHz}$. This effect is too small to explain our data.

- **State-selective trap center displacement** The effect leads to a reduction of the wavefunction overlap between the two states, which reduces the coupling element. This effect causes underestimation of the actual microwave power. We estimate its amplitude by computing the missoverlap η_i' between the cloud density profiles in the i direction:

$$\eta_i' = \exp -\frac{{\delta_{mw,i}}^2\hbar^2{\Omega_{mw}}^4}{4\Delta^2 k_B T m\omega_i^2}. \tag{6.4}$$

  We estimate that the density overlap starts to differ from 1 by more than 1 % for $\Omega_{mw} > 17\,\mathrm{kHz}$. Thus, this effect is far too small to explain quantitatively the deviation at high microwave power.

- **Non-linear affect in the transmission line** We cannot exclude a non-linear affect in the transmission line. A power-dependent loss coefficient, or a power-dependence of the microwave field polarization would modify the Rabi frequency experienced by the atoms.

Limit at low power To measure low power the limiting factor becomes the interrogation time of the atoms. We have demonstrated interrogation times up to 6 s showing, however, intriguing asymmetry in the spectra. On the timescale of several seconds collective effects such as spin rotation effect, symmetric and asymmetric atom losses play a non-negligible role and must impact the power measurement.

Conclusion We have carried out a preliminary characterization of an atomic microwave powermeter. The data show that the powermeter is sensitive to microwave power over a range of at least 80 dB. Further experimental and theoretical investigation is needed in order to understand the characterize completely the powermeter at low powers and to understand the deviations from linearity observed at high powers. Our measurement confirms that trapped atoms have a potential for metrology of microwave and radiofrequency powers. To conclude, we note that atoms can also be used for microwave power stabilization [93], imaging of the magnetic field distribution around a microwave guide [94, 95] or microwave electrometry [96].

Chapter 7

Fast alkali pressure modulation

The sensitivity of atomic sensors at the standard quantum limit increases with the number of interrogated atoms N, the interrogation time and the measurement rate. As most cold atom experiments begin with loading a MOT (magneto-optical trap), it is necessary that the MOT loading is fast and efficient. There is also a need for long lifetimes of the cold clouds, implying low background pressures. This can be done by using two-chamber systems, such as 2D-MOTs, where loading and trapping are spatially decoupled.

An alternative approach is to separate the MOT loading and the trapping *in time*. This approach is compatible with single-chamber systems making it well suited for compact experiments and, eventually, industrial applications, for which simplicity is an important criteria. In this chapter we investigate the possibility of rapidly modulating the ^{87}Rb pressure (also applicable to any alkali) in a glass cell. The target is to reach modulation frequencies $> 1\,\mathrm{Hz}$ as it is where the method becomes relevant to atom chip setups. We will begin by presenting the concepts mentioned above in greater detail. We will then establish a list of technical requirements of atom sources that are needed in order to obtain fast modulation. We will show that a commercial rubidium dispenser attached to a properly designed heat sink fulfills these requirements. We investigate both its short and long term behavior. Finally we will present the characterization of alternative fast sources, among which laser-heated dispensers, light-induced atom desorption and dispensers with a reduced thermal mass are included.

7.1 Optimizing the preparation of cold atomic clouds

7.1.1 Reminders: MOT loading and trap decay

MOT loading

In the case of a low density MOT where two-body losses and light assisted collisions are negligible processes [97], the number of trapped atoms N_{mot} is described by the rate equation

$$\frac{dN_{mot}}{dt} = R - \gamma N_{mot}. \tag{7.1}$$

The equation is driven by a gain term R and a loss term $-\gamma N_{mot}$. If the trap is loaded from a background vapor the gain term R is proportional to the ^{87}Rb density $n_{^{87}Rb}$ in the cell:

$$R(t) = An_{^{87}Rb}(t), \tag{7.2}$$

where the factor A depends on the magnetic field geometry and laser beam shapes, geometries and intensities. It has no analytical derivation. [98] proposes an approximative model for A.

The decay constant can be expressed as

$$\gamma(t) = \sum_i \sigma_i \overline{v_i} n_i(t), \tag{7.3}$$

where σ_i stands for the collisional cross-section between a trapped ^{87}Rb atom and an untrapped atom of species i, $\overline{v}_i$ the mean velocity and n_i the density of the atoms of species i.

Trap decay

We now consider a conservative trap, for example a magnetic or dipolar trap. If the trap losses are dominated by collisions with the background gas, the number of trapped atoms $N_{trap}(t)$ obeys

$$\frac{dN_{trap}}{dt} = -\gamma N_{trap}, \tag{7.4}$$

with a loss term identical to that of the MOT loading equation.

7.1.2 Constant background pressures case

If all pressures in the cell are constant, we get the following expression for the MOT atom number, for trapping starting at $t = 0$:

$$N_{mot}(t) = \frac{R}{\gamma}(1 - e^{-\gamma t}). \tag{7.5}$$

At a given time (t_0) a fraction (α) of the atoms are transferred into the conservative trap. The trapped atom number reads

$$N_{trap}(t) = \alpha N_{mot}(t_0) e^{-\gamma(t-t_0)}. \tag{7.6}$$

Lifetime The time $\tau_{bkg} = 1/\gamma$ is called "background-limited lifetime". We note that it is equal to the MOT loading time.

Balancing N and τ_{bg} Equation 7.5 shows that large MOTs and short loading times are achieved for high ^{87}Rb background pressures. Conversely, equations 7.3 and 7.6 indicate that long trapping times require low background pressures. Thus, if the ^{87}Rb background pressures are increased in order to boost the MOT atom number, one automatically shortens the trap lifetime.

For atom chip experiments this compromise corresponds to a ^{87}Rb pressure of a few $\sim 10^{-10}$mbar. It enables one to capture millions of atoms in the MOT while preserving trap lifetimes on the order of 5 s. This limitation can be overcome in two ways: (1) by a *spatial* separation of the loading and trapping processes or (2) by a *temporal* modulation of the pressure. The latter is more appropriate for compact experiments.

7.1.3 Solutions with a double-chamber setup

In double chamber setups the vacuum system one of the chambers is maintained at "high" pressure (typically $10^{-8}/10^{-9}$ mbar). The second chamber, the "science chamber", is maintained at lower background pressure ($< 10^{-10}$ mbar) and provides long trapping times. The two chambers are connected by a small hole which makes it possible to maintain a pressure difference of several orders of magnitude thanks to differential pumping. There are two main configurations for a double chamber system:

Trap transport The atoms are trapped in the first chamber and physically transported to the science chamber. This is done by moving the trapping potential and requires a translation stage or an adjustable magnetic trap.

Cold atom beams The high pressure chamber delivers a collimated beam of cold atoms that is directed towards a magneto-optical trap in the science chamber. With this approach most of the atoms entering the science chamber are trapped. The beam of cold atoms can be produced by a *Zeeman slower* or a *two-dimensional MOT*. Two-dimensional MOTs can deliver fluxes of 10^{10} atoms s^{-1}, allowing for loading of a three-dimensional MOT in ~ 100 ms.

A disadvantage of double-chamber setups is the increased complexity of the system: not only is a more sophisticated vacuum system needed, but also additional cooling power and/or moving potentials. Pressure temporal modulation, however, can be performed in simple cells and is well adapted to compact experiments. This is what motivated our work on fast pressure modulation.

7.1.4 Fast pressure modulation: a solution for single-cell setups

Review of previous experiments

Dispenser current modulation The idea of temporal pressure modulation is not new. In [99] the authors report a modulation of the rubidium pressure by controlling the current in a commercial dispenser. They achieved the loading of 10^7atoms in the MOT in less than 2 s whilst keeping trap lifetimes of ~ 30 s (in this paper the lifetime is assumed to be equal to the MOT decay time). When the source is turned off the pressure does not decay to zero even after 45 s, it is qualitatively explained that this is a result of atom desorption from the cell surfaces.

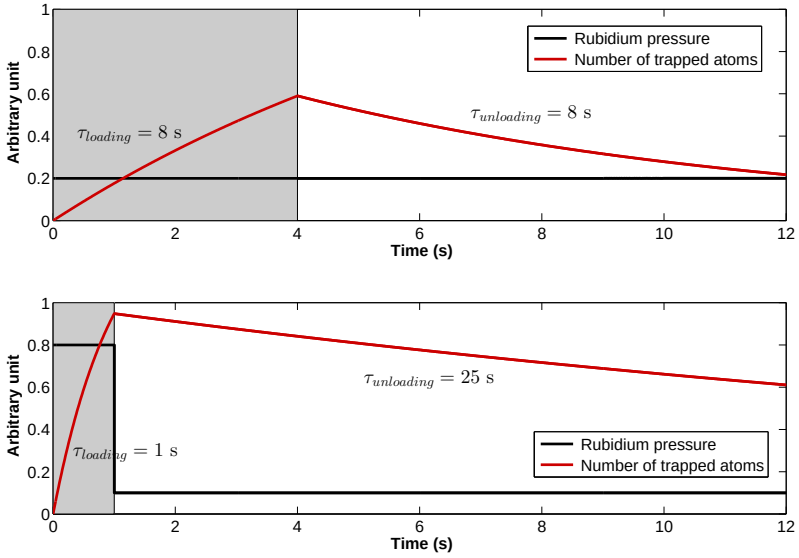

Figure 7.1: *Illustration of the principle of temporal modulation of the ^{87}Rb. The MOT loading phase is colored in grey and the trapping phase in white. Top: for constant background pressures, there is equality between loading time and background-limited decay time. Bottom: by modulating the pressure, one can achieve shorter loading times, larger numbers of atoms and longer background-limited decay time.*

Light-Induced Atom Desorption (LIAD) In this approach atom desorption from the cell surface is stimulated by the application of light, generally in the blue or UV range. LIAD is simple to implement, but suffers from a lack of theoretical understanding and reproducibility [100]. The behavior is known to vary from one experiment to another, this is probably due to the combined influence of the nature and state of the surfaces and the pumping time of the cell. Nevertheless, Light-Induced Atom Desorption contributed to the achievement of Bose-Einstein condensation in dilute gases in several experiments [101, 102, 103]

Collimated dispensers There have been attempts to collimate an atomic beam and direct it towards the MOT in order to increase the ratio between trapped and untrapped atoms. In [104] a rubidium dispenser was combined with a cold copper shroud with the aim of capturing the untrapped atoms. The authors explain that this method does not enable them to reduce the experimental cycle time to under 20 s due to too high a background pressure in the chamber. More recently, [105] reports on the MOT loading by a directional atomic beam using an alkali metal dispenser and a collimation nozzle. The authors demonstrate MOT loading times of 7 s and show that the source can be turned off in 1.8 s.

Our approach: dispenser cooling

It is well known that dispensers take a few seconds to stop emitting atoms after the heating current is switched off [106, 107, 108]: this turn-off time gives the upper limit for the frequency of the pressure modulation. Our approach is inspired by the results and conclusions from [99] where it is mentioned that the dispenser turn-off time in a vacuum is dominated by radiative heat losses. Our idea involves shortening the dispenser cooling time by increasing its *conductive*

heat losses.

Requirements

At this point it is important to recall a few numbers in order to elaborate on the list of technical requirements of the atom source. The MOT loading time in TACC is typically $4\,s to 12\,s$ and the evaporative cooling time is currently 3.3 s. The useful part of the cycle, the interrogation phase, typically takes $1\,s to 10\,s$. The trap lifetime is 6 s.

Pressure decay time When the source is turned off, the evolution of pressure in the cell is determined by two quantities:

- *The evacuation time* τ_{ev} which is the time needed to pump atoms away from the cell.
- *The source turn-off time* τ_s which is the time taken for the source to stop emitting atoms.

Whichever is the largest determines the cell pressure decay time τ_{off}. The pressure decay time must be much shorter than evaporative cooling time, such that we require $\tau_{\text{off}} < 1\,\text{s}$.

Source turn-on time To represent a substantial improvement with respect to the current MOT loading time, the source turn-on time τ_{on} must equally be much shorter than one second: $\tau_{on} < 1\,\text{s}$.

Release The source must enable us to load $\sim 10^7$ atoms in the MOT. However, we keep in mind that the number of trapped atoms depends greatly on the trapping beams' size and power, which may vary from one experiment to another.

Trap lifetime The source must preserve trap lifetimes of at least 6 s.

Reproducibility From the perspective of integration into continuously operating devices, the atom source must be repeatable both in the mid term (hours) and in the long term (days).

7.2 Experimental methods

In this section we provide some details about the measurement system used for characterizing the fast sources. We will also describe the method we used for monitoring pressures in the cell based on the MOT loading.

Our system consists of a three-dimensional MOT for ^{87}Rb.

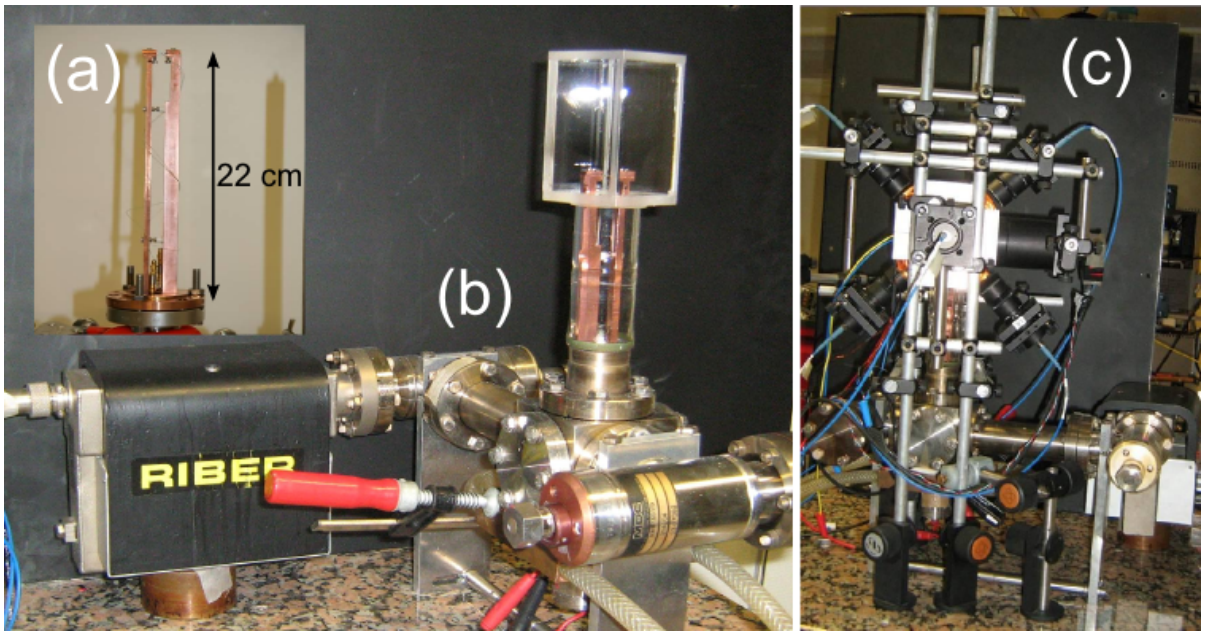

Figure 7.2: *Overview of the experimental setup used for fast alkali pressure modulation experiments. (a) Full view of the copper heat sink designed to cool the dispenser (described in section 7.3.1). (b) Full view of the vaccum system, including a* $25\,\mathrm{L\,s^{-1}}$ *ion pump and a glass cell. Inside the glass cell one can see the copper mount (a). (c) Side view of the vacuum system after adding the aluminium structure holding the MOT components.*

7.2.1 Vacuum system

The vacuum system is simple, along the line of atom chips experiments performed in our group. A quartz cell of $50 \times 50 \times 90\,\mathrm{mm^3}$ is bound to a glass-to-metal transition that is connected to a 6-way cross. Connected to the cross are: an electrical feedthrough, an all-metal valve, a $25\,\mathrm{L\,s^{-1}}$ ion pump separated from the cross by an all metal valve and a steel tube (see figure 7.2.b).

7.2.2 Optics and coils

The MOT An aluminium structure holds 6 beam collimators composed by of 60 mm focal length, 1 in diameter aspherical lens followed by a quarterwave plate (figure 7.2.c). Each beam carries 1.6 mW of cooling light and 250 µW of Repump light. Two coils create a magnetic field gradient of $\sim 10\,\mathrm{G\,cm^{-1}}$.

The upper face of the cell constitutes another optical access that was used to focus a powerful laser (10 W) onto the dispenser (see section 7.4).

The lasers The laser system consists of two extended-cavity laser diodes [47] and a slave laser diode (see figure 7.3). The cooling light is detuned by $\delta = -13\,\mathrm{MHz}$ from the cooling

transition. Locking loops lend them a stability of several days.

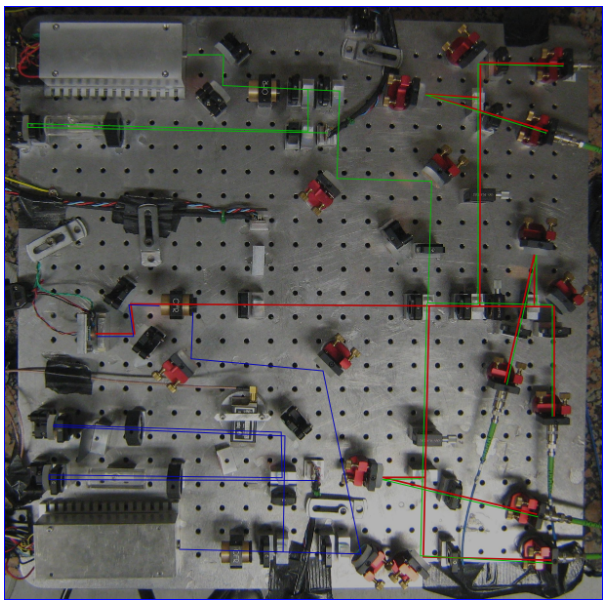

Figure 7.3: *Picture of the optical bench. Symbolic colors sketch the path of the three lasers: blue for the master, red for the slave and green for the repumper.*

The detection The atomic fluorescence is detected using a $1\,\mathrm{cm}^2$ photodiode on which the MOT is imaged by a lens. The photocurrent is converted into a voltage through a transimpedance circuit with the conversion factor $R = 3.9\,\mathrm{M}\Omega$. Combined with the photodiode capacity $C_{PD} = 1100\,\mathrm{pF}$ it gives a response time of $4\,\mathrm{ms}$.

The number of atoms in the MOT, N_{mot}, is calculated using the power, P_{PD}, received by the photodiode [109]:

$$P_{PD} = \hbar\omega\gamma N_{mot}\frac{\Omega}{4\pi}T^2, \tag{7.7}$$

with

$$\gamma = \frac{s_0\Gamma/2}{1 + s_0 + (2\delta/\Gamma)^2}. \tag{7.8}$$

Here $\omega/(2\pi)$ is the frequency of the cooling transition, T is the transmission coefficient at the air/glass interface (our cell is not coated) and Ω the solid angle of detection. $s_0 = I/I_{sat}$ is the saturation parameter, I the intensity of the 6 beams, I_{sat} the saturation intensity and Γ the linewidth of the transition.

The calibration gives:

$$C = 7.3 \times 10^6\,\mathrm{atoms\,V}^{-1}. \tag{7.9}$$

The photodiode is also sensitive to the fluorescence of untrapped atoms from the background gas. This signal is directly proportional to the ^{87}Rb pressure in the cell.

7.2.3 Pressure measurements

Pressure in the cell can be estimated with the MOT loading curve. According to equations 7.5, 7.2 and 7.3, the MOT loading curve in an environment of constant pressure gives us two pieces of information [110]:

- **The loading rate** R: this is also the initial slope of the curve. It is *directly proportional* to the ^{87}Rb pressure in the cell, with a proportionality constant that depends only on the MOT parameters (beam power and diameter, magnetic field gradient).

- **The background-limited lifetime** $\tau_{bkg} = 1/\gamma$: this is a decreasing function of the total pressure in the cell.

These two quantities allow us to follow the evolution of the ^{87}Rb pressure and the total pressure in the cell. This will be particularly useful in the study of long-term evolution when the fast source is emitting.

If the pressures in the cell are not constant but are approximately constant on the timescale t_p, equations 7.5, 7.2 and 7.3 still hold for times $t \ll t_p$.

7.3 A device for sub-second alkali pressure modulation

In this part we present the main results of this chapter. These results concern the design and characterization of a fast atom source obtained by fastening the dispenser thermal dynamics using a heat sink.

7.3.1 Presentation and design

Commercial dispensers

Several properties explain the popularity of alkali metal dispensers in the field of cold atoms: ultra-high vacuum compatibility, easy handling, reliability and reproducibility. One dispenser contains enough atoms to supply an atom chip experiment for several years.

To our knowledge two companies sell rubidium dispensers, each with differing working principles. Our work focused on the ones by SAES Getters, therefore, the information given in this thesis refers to their dispensers.

These dispensers are made of a NiChrome shell filled with a mixture of rubidium chromate and St101 getter [45]. The reduction reaction between the two produces rubidium atoms in the vapor phase. The chemical reaction is inhibited at room temperature but can be activated by elevating the temperature of the medium. This is done by running a current through the metallic shell: due to the high resistivity of nickel-chrome, relatively low currents ($\sim 3\,\mathrm{A} to 5\,\mathrm{A}$)

are sufficient to reach the alkali vapor emission temperature ($\sim 500\,°\mathrm{C}$).

According to the company, the dispensers release almost exclusively rubidium, a statement which is confirmed by the measurements of [111]. The level of purity of the emissions surely depends on the emission rate: it is well known that in cold atom experiments where low emission rates are used, dispensers do not only emit rubidium atoms but also a significant amount of impurities.

Alkali metal dispensers can also be made in the laboratory with only basic chemical requirements [112].

Fastening the dispenser thermal dynamics

Dispensers are usually electrically connected to copper wires inside the vacuum. In [107] the dispenser turn-on and turn-off times were measured. The authors observed that rubidium atoms appear some tens of seconds after the current is turned on. When the current is switched off, the rubidium density in the cell follows an exponential decay with a time constant of $\sim 3\,\mathrm{s}$, independent of the value of the current. Similar observations were reported in [106, 108].

This rather long turn off time can be explained by the thermal inertia of the dispenser. In fact, in a vacuum environment and with a mounting on thin copper wires, the heat loss of a dispenser is governed by thermal radiation: the authors of [99] have observed that the temperature of a cooling dispenser follows a law of the form: $dT/dt = CT^4$ where C is a constant.

We adopt the following model for the thermal dynamics of the dispenser: we assume that the temperatures T (of the dispenser) and T_0 (of the copper wires) are homogeneous. T_0 is also the room temperature. The thermal conductivity of the copper is taken to be infinite, and the thermal contact between the dispenser and the copper is characterized by the thermal conductance h. In this case T obeys:

$$c\frac{dT}{dt} = P(t) - h(T - T_0) - \sigma\epsilon S_d(T^4 - T_0^4). \tag{7.10}$$

We label c the thermal capacity of the dispenser, $P(t)$ the supplied (Joule) power, S_d the dispenser total surface, ϵ its emissivity and σ the Stefan-Boltzmann constant. Our measurements give $c = 0.089\,\mathrm{J\,K^{-1}}$.

Conductive cooling time The conductance h for a bar of section S, length L and thermal conductivity k reads $h = kS/L$. In our case the relevant length L is half the length of the dispenser, and S the contact surface with the copper wire. With $k = 15\,\mathrm{W\,m^{-1}\,K^{-1}}$ (NiChrome alloy), $L = 5\,\mathrm{mm}$, $S = 0.1\,\mathrm{mm^2}$, we estimate the $1/e$ cooling time by pure conduction to be $\sim 300\,\mathrm{s}$.

Radiative cooling time With $T(0) = 700\,\mathrm{K}$ and $\epsilon = 1$ we estimate the $1/e$ cooling time for pure radiation to be $45\,\mathrm{s}$. This confirms that the dispenser cooling is dominated by radiation losses [99].

We conclude from this qualitative analysis that an increase of the contact surface S by a factor > 10 will reduce the cooling time of the dispenser.

Source design

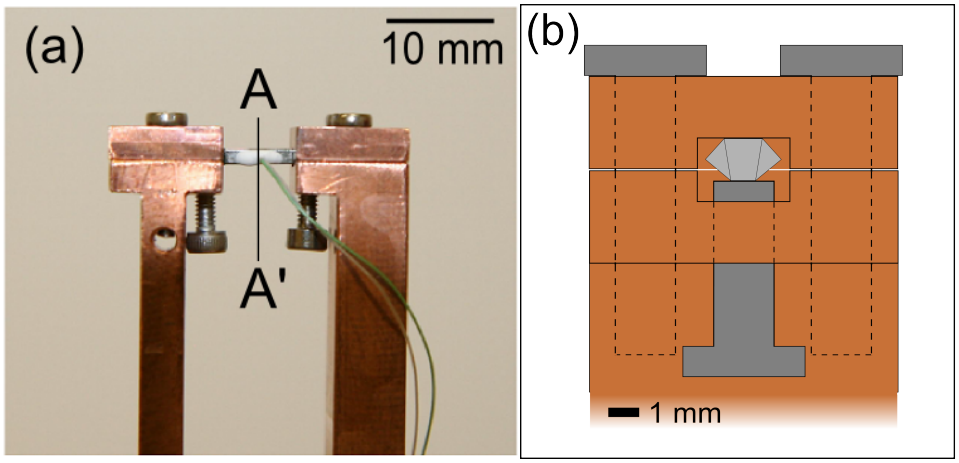

Figure 7.4: *Copper heat sink designed to fasten the dispenser thermal dynamics. (a) Picture of the copper mount. It is used for both cooling and electrically contacting the dispenser. On this picture we can see a thermocouple that was glued onto the dispenser (white spot and thin wires): it was not present under vacuum. 6 screws ensure squeezing of the dispenser against the copper. (b) Scheme of the section along AA'. The dispenser is sketched in light grey, the screws in darker grey and the copper in orange.*

We have designed a copper heat sink to increase the contact surface between the dispenser and the copper (figure 7.4). The heat sink consists of two 20 cm copper rods (see figure 7.2). One of them is attached to a home-made copper flange which is also the vacuum seal for the electrical feedthrough. In this configuration the vacuum body is in good thermal contact with the copper and plays the role of a thermal reservoir. The second rod is connected to a pin from the electrical feedthrough.

Source turn-off time In the first experiment we turned off the MOT coils and applied short current pulses to the dispenser. The photodiode delivers a signal directly proportional to the fluorescence of the ^{87}Rb atoms in the cell. For 1 s pulses, we found that the rubidium emission threshold lies at around 18 A. Figure 7.5 shows the fluorescence signal for a pulse of 20.2 A. After the current pulse the rubidium density in the cell decays exponentially with the time constant $\tau = 112$ ms. This time is shorter by a factor > 20 than the values reported for bare dispensers [107, 106]. This result opens the way to fast modulation of the rubidium pressure in a vacuum cell.

7.3.2 MOT loading by a pulse

In the second experiment we turned on the MOT coils at the same time as the current pulse (figure 7.6.a). The MOT is loaded in ~ 1.2 s, a time that includes the dead time constituted

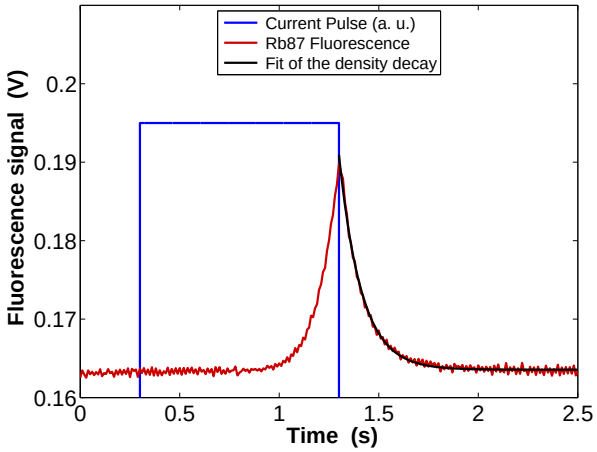

Figure 7.5: *Fluorescence signal of the* ^{87}Rb *vapor when driving the source with current pulses of* 20.2 A *and* 1 s. *The data are averaged over* 29 *shots. We fit the* ^{87}Rb *decay with the function* $A + Be^{-t/\tau}$ *and find* $\tau = 112$ ms.

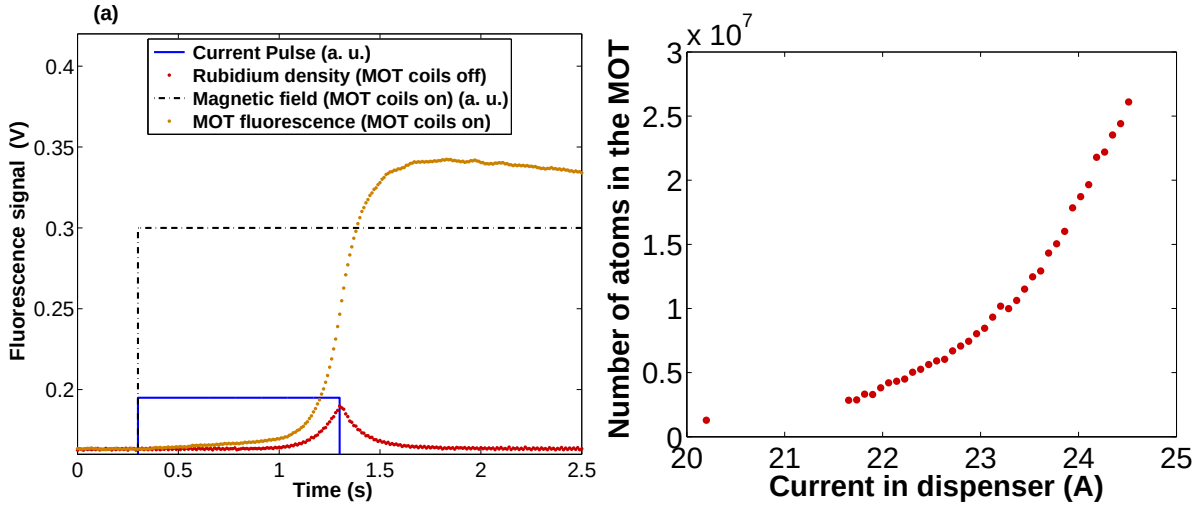

Figure 7.6: *(a) Fluorescence signal from the MOT when driving the source with current pulses of* 20.2 A *and* 1 s. *The data are averaged over 10 shots. On the same graph we present the density peak from 7.5. (b) Number of atoms loaded in the MOT as a function of the dispenser current for* 1 s *pulses. We demonstrate loading of* $> 2.5 \times 10^7$ atoms *into the MOT over approximately* 1.2 s *(including the pulse duration).*

by the current pulse. Most of the loading happens within 0.5 s.

When increasing the current in the dispenser we observe that the number of atoms in the MOT increases, meaning that the MOT saturation has not yet been reached. We demonstrate loading of $> 2.5 \times 10^7$ atoms into the MOT over approximately 1.2 s.

7.3.3 Sensitive measurement of the pressure decay

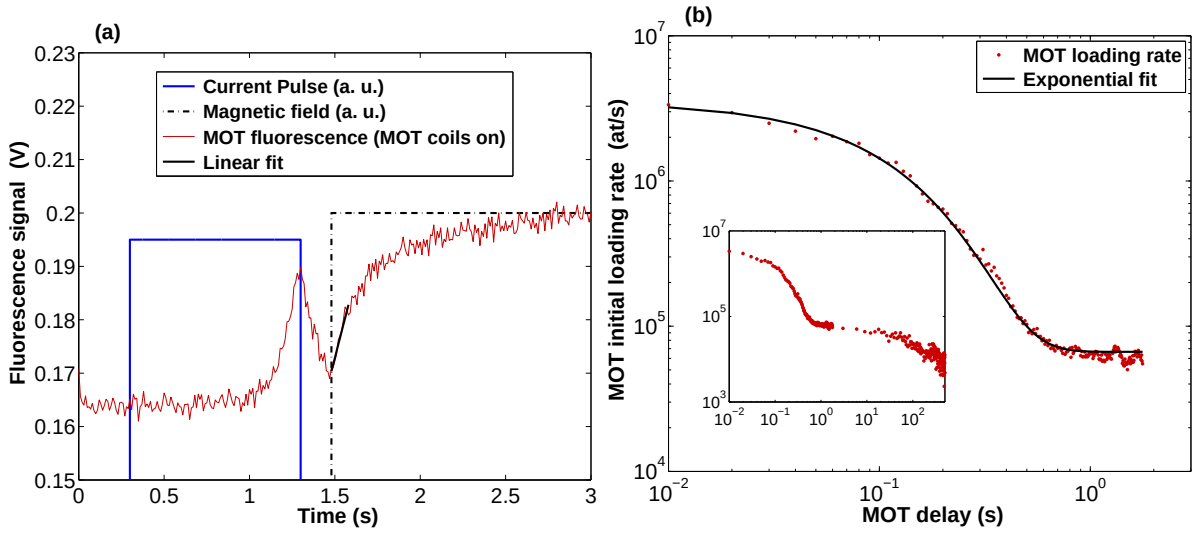

Figure 7.7: *(a) MOT loading curve by a ^{87}Rb pulse with a MOT delay* 0.19 s. *The MOT delay is defined as the time between the end of the current pulse and the start of the magnetic field. (b) Initial MOT loading rate as a function of the MOT delay. This is the direct image of the ^{87}Rb density in the cell. The density decays to a constant value n_b. An exponential fit with the decay time $\tau = 108$ ms, in agreement with* 112 ms *reported above. Inset: on longer term n_b is not constant and decays. This phenomenon is further analyzed in the next section.*

The photodiode is not sensitive to low ^{87}Rb densities. The MOT gives more sensitive measurements of the density. As stressed previously, the MOT initial loading rate is proportional to the ^{87}Rb density in the cell.

We repeated the last experiment with a variable delay Δt_B between the end of the current pulse and the time that the magnetic field is turned on ($\Delta t_B = -1$ s in figure 7.6.a). At the end of each shot, the magnetic field was turned off for 0.3 s in order to allow the trap to be emptied. For each shot we extract the initial slope of a MOT loading curve by a linear fit.

Short term The results of this experiment are shown in figure 7.7.b. For the short term ($\Delta t_B < 2$ s) we fit the data with the function $n_b + Be^{-t/\tau}$ and find $\tau = 108$ ms, this is in agreement with the value of 112 ms reported above.

Long term On the long term (inset of figure 7.7.b) we observe that the floor n_b is indeed not constant but decays on the time scale ~ 100 s. We explain the existence of this floor by the slow desorption of ^{87}Rb atoms from the surfaces. This is discussed further in the next sections.

7.3.4 Rate equations for the adsorption/desorption dynamics

The adsorption and desorption of ^{87}Rb atoms from the inner walls of the cell play a dominant role. Here we introduce a model following the approach of [113] that reports a study of the adsorption/desorption dynamics of rubidium atoms on a gold surface.

Model The adsorption phenomenon is characterized by a rate C_a and the desorption by a rate C_d. The ion pump evacuates atoms from the cell with the rate C_p. We call $N_v(t)$ the number of atoms in the vapor phase and $N_a(t)$ the number of atoms adsorbed on the surface. We also introduce the production rate $R_s(t)$ equal to the number of ^{87}Rb emitted by the source per second.

In this approach the number of adsorbed atoms obeys:

$$\frac{dN_a}{dt} = C_a N_v - C_d N_a. \tag{7.11}$$

The number of atoms in the vapor phase follows:

$$\frac{dN_v}{dt} = -C_a N_v + C_d N_a - C_p N_v + R_s. \tag{7.12}$$

We now give estimations for the three independent parameters of our model. For this we will refer to another fast source involving a high-power laser diode focused onto the dispenser active powder (see section 7.4.3). This source will be introduced later in this chapter.

Estimation of the pumping constant We compute the pumping speed at the cell using the conventional formulae: after multiplication by the cell volume we find $C_p = 15\,\mathrm{s}^{-1}$ ($1/C_p = 66\,\mathrm{ms}$).

Estimation of the adsorption probability The adsorption constant is related to the sticking probability p_0

$$C_a = \frac{\overline{v} S p_0}{4V}, \tag{7.13}$$

with V and S the volume and internal surface of the cell and $\overline{v}$ the mean velocity of the ^{87}Rb atoms.

On the short term, the ^{87}Rb density decay is governed by the smallest of C_a, C_p and $1/\tau_s$ (τ_s is the source turn-off time). The idea for measuring C_a is to use a very fast atom source, for which the ^{87}Rb density decay would be dominated by the adsorption process. By considering our fastest source, obtained by focusing a powerful laser directly onto the dispenser active power, we obtain a lower bound for C_a. From the measured pressure decay time of 9 ms we infer $C_a > 111\,\mathrm{s}^{-1}$ and $p_0 > 0.02$.

Estimation of the desorption constant Desorption is the slowest process. By solving equations 7.11 and 7.14 for $R = 0$ and $C_d \ll C_a$, C_p one shows that at times $t \gg 1/C_a$, $1/C_p$ the number of atoms in the cell evolves as:

$$N_v(t) \propto e^{-Ct}, \tag{7.14}$$

with $C = C_d C_p/(C_a + C_p)$. The situation $R = 0$ is realized by turning off the source and observing the long-term pressure decay in the cell. Figure 7.8 shows the evolution of the MOT loading rate in time after the source was turned off. The decay observed is not exponential, which indicates that our model for desorption is too naive. Nevertheless, this data gives the timescale on which the base pressure in the cell responds to a change of the source parameters: $\sim 200\,\mathrm{s}$ ($1/e$ time).

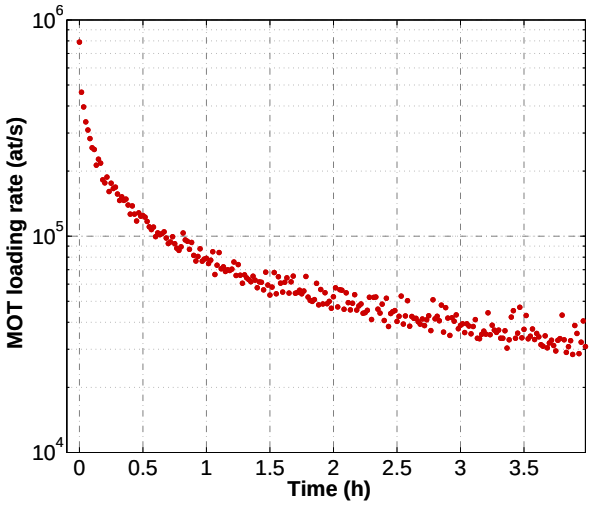

Figure 7.8: *Evolution of the MOT loading rate ($\propto p_{^{87}Rb}$) in time. The source was emitting over a number of hours and turned off at $t = 0$. The source used here is the laser-base fast source but similar results were obtained with the current-driven dispenser on a copper sink. The pressure decay is not exponential, which shows that our adsorption/desorption model is too simple. Nevertheless, this data gives the timescale on which the base pressure in the cell responds to a change of the source parameters: $\sim 200\,\mathrm{s}$ ($1/e$ time).*

Vacuum system curing It is well known that a freshly baked vacuum system in which an alkali is introduced undergoes curing during a period of several weeks [114]. This transitory regime can be interpreted as the time taken for the atoms to form (on the walls) the first adsorption layer, which is tightly bound and does not desorb. All the experiments presented in this chapter were carried out long after the system had cured (i.e. after several months of operation).

7.3.5 Long term evolution of the pressure

We are now equipped to study the long-term behavior of the current-driven dispenser on a copper sink.

Time to steady-state

In the first experiment we measured the time taken for the system to reach its steady-state whilst maintaining the bottom copper flange at a temperature of 15 ° using water flow. Current pulses were applied to the dispenser every $T = 5\,\mathrm{s}$. Each pulse loaded atoms into the MOT, and the trap was emptied at each cycle by turning off the magnetic field. Every $N_p = 150$ pulses we stopped the source for $T_{cm} = 60\,\mathrm{s}$ and recorded a MOT background loading in order to monitor the pressure in the cell. We call this a *check MOT*. The sequence was repeated over several hours until the steady-state was reached. By choosing $T_{cm} \ll N_p T$ we ensured that the system's behavior is similar to that of a continuously pulsed dispenser (where $T_{cm} = 0$).

Figure 7.9 shows typical behavior. The steady-state is reached after $\sim 6\,\mathrm{h}$. The transitory regime is not a simple exponential growth, showing evidence for a process more complex than a simple thermal equilibrium. We interpret this shape and especially the "bump" observed at $\sim 1.5\,\mathrm{h}$ as being caused by atoms desorbing from the cell walls during the system heating.

The second observation we make is that, in the steady-state, the values of the total pressure and of the ^{87}Rb pressure are higher than in the initial state. This is discussed further in the next part.

Limits to modulation imposed by atom desorption

In order to better understand the existence of a slowly decaying base pressure we repeated the previous experiment for various current pulse amplitudes. For each setting we waited until the steady-state was reached and recorded the parameters. Figure 7.10 summarizes the data. They are plotted as a function of the number of atoms loaded by a pulse in the MOT $N_{\mathrm{MOT,stat}}$, which is an increasing function of the mean number of atoms released by the source per pulse, $\langle R_S \rangle$. The main observation is that both the ^{87}Rb and the total pressure increase with the mean number of atoms released by the source.

Modulation factor We also plot the modulation factor, defined as:

$$\eta = \frac{N_{\mathrm{MOT,stat}}}{R_{\mathrm{bkg}} T}, \tag{7.15}$$

where R_{bkg} is the loading rate in absence of pulse (from background), T, the pulse duration and, $N_{\mathrm{MOT,stat}}$, the number of atoms loaded per pulse in the MOT. From the adsorption/desorption model we expect R_{bkg} to be proportional to the mean atom release rate of the source $\langle R_S \rangle$ (since the steady-state number of atoms in the vapor phase reads $N_{\mathrm{v,stat}} = \langle R_S \rangle / C_p$). From the dependence of η on $N_{\mathrm{MOT,stat}}$ we conclude that either $N_{\mathrm{MOT,stat}}$, R_{bkg} or both are not proportional to $\langle R_S \rangle$.

Composition of the background gas It would be interesting to know whether the background gas is predominantly composed of rubidium or other gases. In the case of dominance by other gases, work on the source purity could further push the modulation limit. In the current system, however, it impossible for us to give a precise estimation of the background

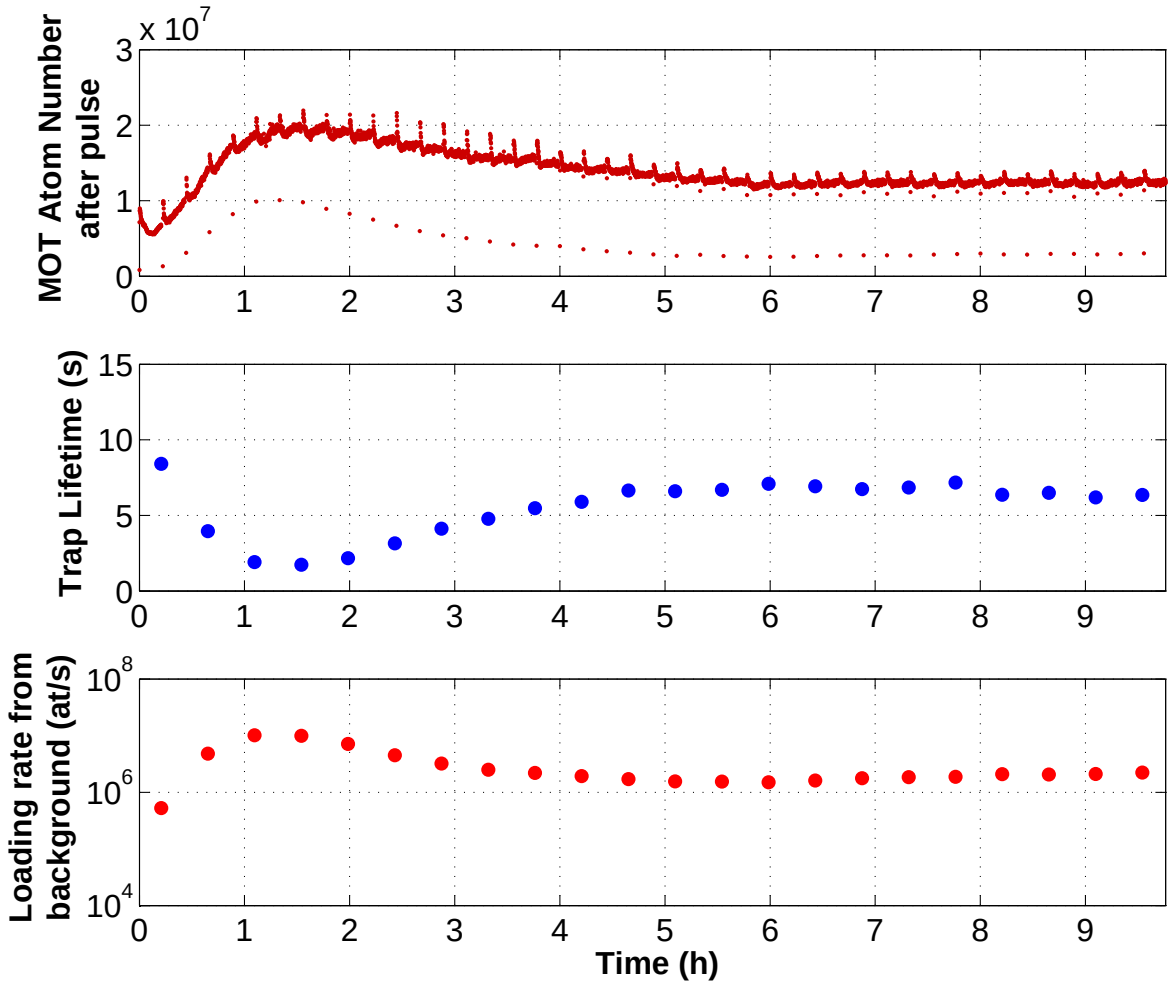

Figure 7.9: *System evolution to steady-state. We applied* 1 s *current pulses every* $T = 5$ s. *Each pulse loads atoms into the MOT. The trap was emptied at the end of each cycle. Every* $N_p = 150$ *pulses we recorded "check MOT" over* 60 s *to monitor the pressure in the cell. The system takes* ~ 6 h *to reach its steady-state. The transitory regime has an unusual "bump" shape that we interpret as being caused by atoms desorbing from the heating surfaces.*

gas composition.

Origin of the background gas Thus, we are confident that the background gas originates from atom desorption from the walls. There are two possible explanations for the origin of these atoms: (1) they are atoms that were stuck on the walls initially. As the surface temperature rises the desorption rate of these atoms increases and so does the background pressure; (2) they are atoms that were not initially present on the walls. They were produced by the source and adsorbed on the walls earlier. We show in section 7.4.3 evidence for the predominance of phenomenon (2). This is obtained by considering a laser-based source of rubidium, which dissipates considerably less power to the system in the form of heat.

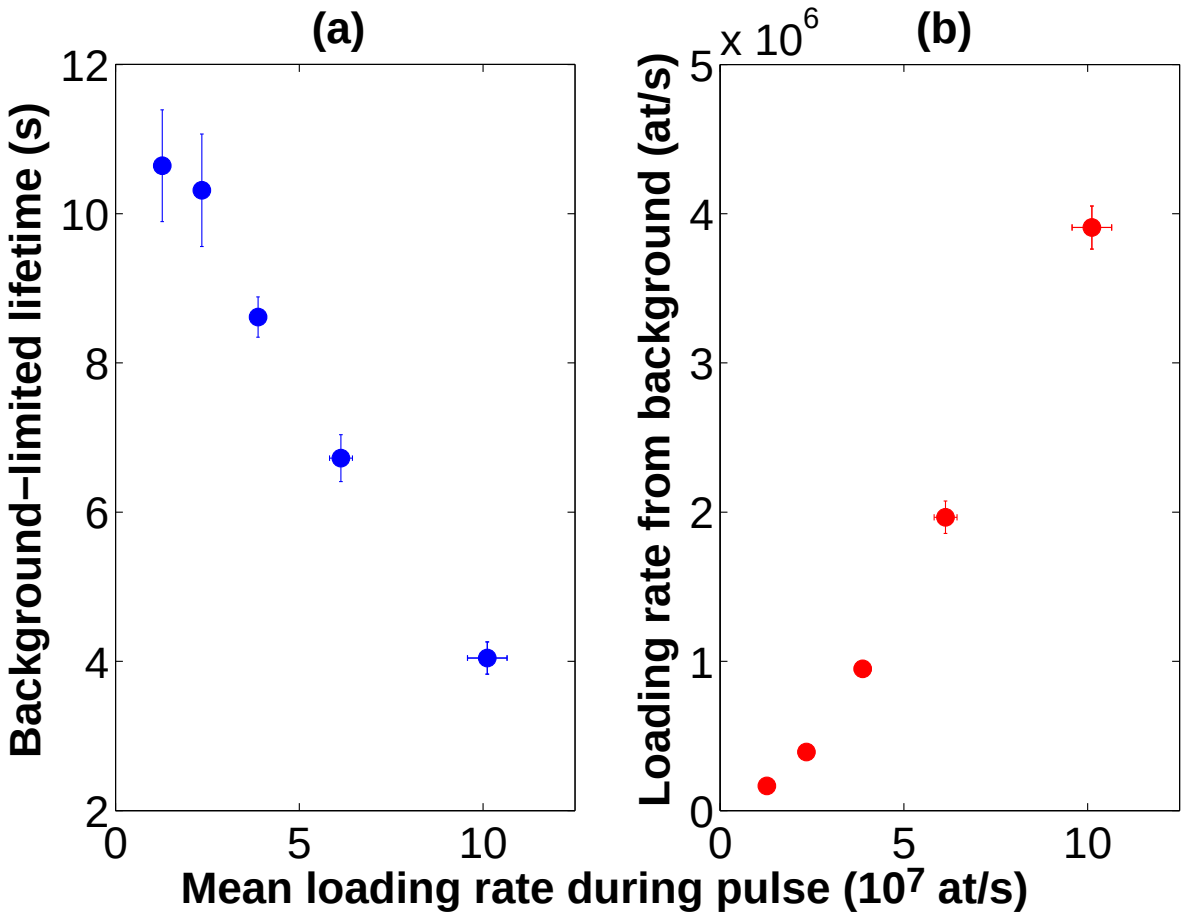

Figure 7.10: *Evolution of the steady-state parameters as a function of the number of atoms loaded per pulse, $N_{MOT,stat}$, which is a measurement of the mean release rate of the source, $\langle R_S \rangle$. In these experiments the timings were all identical and the source release was tuned by the pulse current amplitude. (a) Background-limited lifetime. (b) MOT loading rate from background. (c) Modulation factor. As the production rate of atoms in the cell increases both the total pressure and the ^{87}Rb pressure in the cell increase. We interpret this dependence as being mediated by the atom desorption from the cell walls. The fact that the modulation factor depends on $N_{MOT,stat}$ indicates that either $N_{MOT,stat}$, R_{bkg} or both are not proportional to $\langle R_S \rangle$.*

7.4 Other fast sources

7.4.1 Local heating with a laser

Motivations

A second option for reducing the source turn-off time is through local heating: the less energy brought to the system, the shorter the recovery time. [115] reports on heating of a rubidium dispenser using a Nd:YAG laser focused on 35 µm. After switching off the laser, the authors observed pressure decay times < 10 ms. The authors of the study note that after working on the same spot for several weeks, a decrease of 10 %*to*20 % of the MOT atom number was observed. This was attributed to the depletion of the local rubidium concentration in the

dispenser. However, this experiment did not further investigate the potential of laser heating for fast pressure modulation.

A systematic study of a pulsed, laser-heated dispenser had to be carried out. To do so we installed a 10 W, laser diode emitting at 915 ± 10 nm [1], focused on the dispenser. A special feature of our laser diode is the possibility of "hard-pulsing", that is to say, the laser diode switching at ~ 1 Hz rates, leading to high thermal stress. We estimated the laser spot size to ~ 67 µm.

This laser has been used to activate two different dispensers: a commercial dispenser and an open dispenser that gives direct access to the active power inside it.

7.4.2 Laser heating of a commercial Dispenser

The heating laser was focused onto a commercial dispenser. Even after isolating the detection photodiode with a narrow band filter at 780 nm, a significant amount of heating light was reaching the photodiode. The source characterization involved measuring reference signals and subtracting them in order to obtain the ^{87}Rb contribution only.

Short-term Figure 7.11 shows a measurement of the rubidium density during a laser pulse. We observe that the rubidium decay after the heating pulse can be fitted with a double exponential function, yielding the two time constants of 9 ms and 70 ms.

Source release It appeared that this source gives rather modest release, even at full power 4 s are needed to provide 10^7atoms in the trap. Due to this unfavorable property the long-term behavior of the source has not been investigated any further.

7.4.3 Laser heating of the dispenser active powder

In the previous configuration most of the laser light is reflected by the dispenser. Most of the energy absorbed by the dispenser is wasted in heating the NiChrome shell rather than the active powder. We constructed a new source with direct optical access to the power by removing the upper half of the NiChrome shell of a commercial dispenser (figure 7.12.a).

Short term Figure 7.12.b shows a measurement of the source dynamics, carried out in the same way as explained above. Very short turn on times in the order of ~ 100 ms could be achieved. The source turn-off follows a double-exponential decay with two time constants of 11 ms and 90 ms.

1. 10W 9xxnm Uncooled Multimode Laser Diode Module, Ref. BMU10A-915-01-R (*Oclaro*).

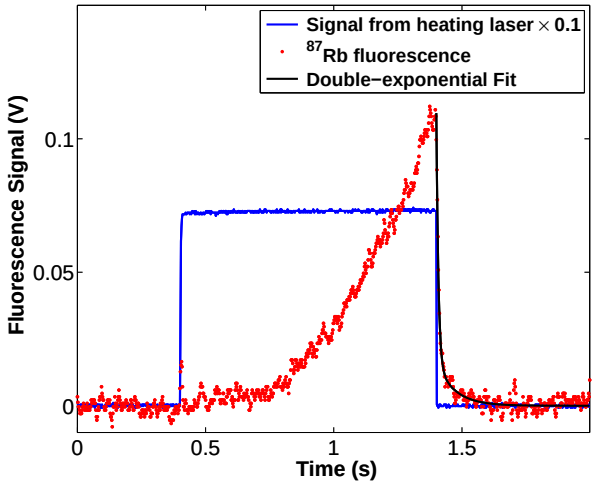

Figure 7.11: *Speed of the the laser-heated dispenser. The heating laser light is detected by the photodiode. The ^{87}Rb fluorescence is obtained by subtracting the heating laser signal. The ^{87}Rb density decay can be fitted with a double-exponential of time constants* 9 ms *and* 70 ms.

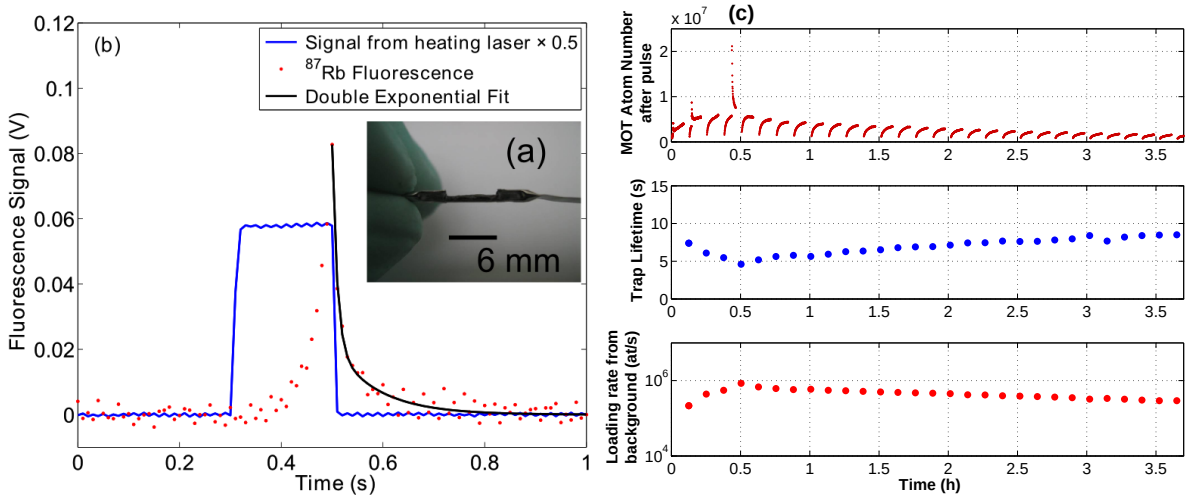

Figure 7.12: *(a) Picture of the open-dispenser obtained by removing the upper half of the central part of the NiChrome shell. (b) Source speed. A double-exponential fit gives the time constants* 11 ms *and* 90 ms. *(c) In the long term we observe that the rubidium release tends to decrease, which we attribute to the local depletion of the source. We observe a clear correlation between N_{MOT} and the pressures. This indicates unambiguously that the background gas is composed of desorbing atoms that have been emitted by the source, confirming the statement made in section 7.3.5.*

Long term In the long term this source shows a depletion behavior which we attribute to the local reduction in rubidium (figure 7.12.c). It also exhibits random spikes that might be caused by fluctuations of the laser position. This is a disadvantage of local heating. We observe a clear correlation between N_{MOT} and the pressures. This indicates unambiguously that the background gas is composed of desorbing atoms that have been emitted by the source, confirming the statement made in section 7.3.5.

7.4.4 Light-induced atom desorption

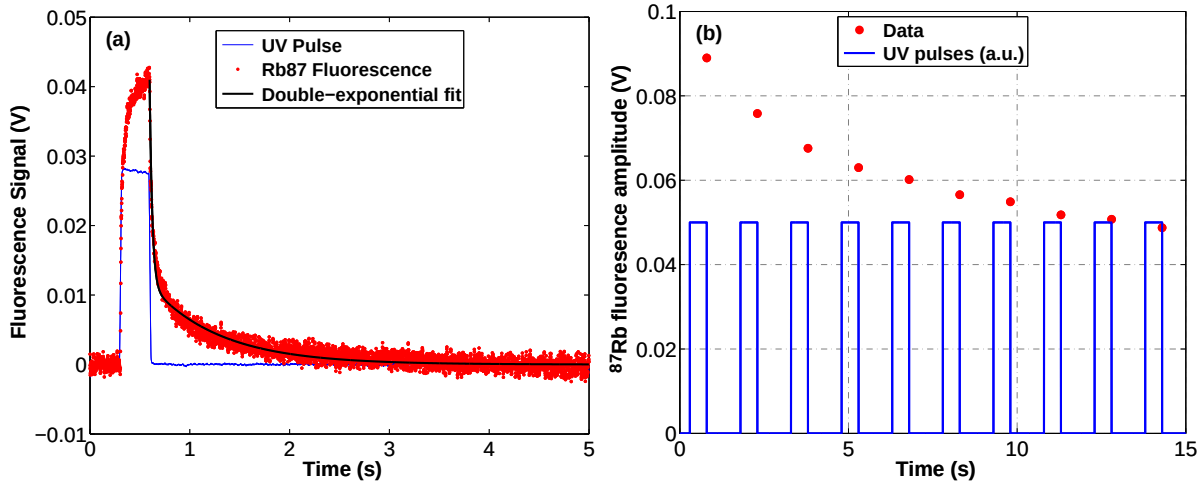

Figure 7.13: *(a) Rubidium pulse obtained when applying a UV pulse on the cell. The decay can be fitted with a double-exponential of time constants* 31(2) ms *and* 0.7(1) s. *The reasons for this behaviour are not understood. (b) Amplitude of the* ^{87}*Rb signal in time when applying repeated UV pulses. The rubidium release decays rapidly with the number of pulses, showing that, on its own, LIAD is a poor atom source in our geometry.*

Light-induced atom desorption has been demonstrated with rubidium [116] and sodium, [117]. As previously stressed LIAD behavior is known to depend, amongst other things, on the cell geometry and nature. In the glass cells used in our group LIAD is known to give poor results. Atom vapor production reduces significantly after a few desorption pulses, which prevents it from being a reproducible atom source. However, as we will show here, it can be used as a complementary source. In particular, LIAD can help to push the limit to modulation imposed by the atom desorption.

Figure 7.13.a shows the behavior of the rubidium density in the cell during application of a UV light pulse. The density decay shape consists of a double exponential of time constants $32(2)\,\mathrm{s}^{-1}$ and $1.3(1)\,\mathrm{s}^{-1}$, this is not yet understood. On figure 7.13.b we show how the LIAD release efficiency decreases with the number of pulses applied. We understand this behavior as the atoms in vapor phase being pumped away from the cell (the pumping time is estimated to 67 ms).

Table 7.1 compares two experiments carried out with a laser-based atom source. In the first experiment no LIAD was applied. In the second experiment LIAD was applied during the laser pulse. The comparison shows that for an identical number of atoms trapped in the MOT the background pressure is lower in the second experiment. This observation is consistent with the fact that the background gas originates from atom desorption: the application of LIAD cleans the surfaces at the same time as it increases the rubidium pressure in the cell. Thus, LIAD can be used as a complementary source.

Here we would like to point out that UV light does not desorb only rubidium atoms, which may constitute a limit to the amount of UV light that is used for assisting the main source. This effect should be reduced by preparing cleaner vacuum systems: applying UV light during the bakeout procedure may be one way to reduce the effect.

	Without LIAD	With LIAD
Atom number loaded per pulse	1.6×10^6	1.6×10^6
Lifetime (s)	7.4	8.5
Loading rate from background (at/s)	1.0×10^6	0.66×10^6
Modulation factor	3.2	4.8

Table 7.1: *Comparison of two experiments carried out with* 0.5 s *pulses of heating laser onto the active powder. In the second experiment only, UV light was added during the laser pulses. We compare the experiments at a point where the number of atoms loaded in the MOT after the pulse are equal. We observe that LIAD enables us to increase the modulation factor. UV pulses can be used as a complementary source: they desorb some of the adsorbed atoms, allowing for a lower background pressure.*

7.4.5 Reduced thermal mass dispenser

At this point our conclusions can be summarized as follows: laser-based sources are fast but not reproducible on the long term; on its own, LIAD is not efficient in our cells; the current-driven dispenser is fast and reproducible but suffers from the long time needed to reach the steady-state. It also requires a considerable amount of power (typically 40 W). A way to reduce the two last effects is to reduce the dispenser thermal mass.

Attempts During close inspection of commercial dispensers one realizes that most of their heat capacity arises from the NiChrome shell. We have made two attempts to reduced the amount of NiChrome involved in the dispenser: one is the open dispenser presented in section 7.4.3. The second one is a home-made dispenser: this was constructed by placing the active powder inside a 25 µm thin NiChrome envelope. With these two sources we have observed that the source turn-off time was reaching a rather high steady-state value of $\sim$ 600 ms, making them too slow to modulate the pressure. Our understanding is that this behavior is caused by poor thermal contact within the active powder itself and between the active power and the NiChrome shell. In fact, in these two configurations the powder was simply placed and manually squeezed into its shell, consequently it does not reach the compactness of commercial dispensers.

Proposal for a new fast source These considerations lead us to propose the following design for a low-thermal mass, current driven atom source. It involves a combination of a thin NiChrome layer, a copper heat sink and the possibility of mechanically maintaining the powder against the NiChrome with a system of screws. With this design it may be that the thermal conductance between the dispenser and the heat sink becomes too high. This could be adjusted

by digging stripes in the copper holders (see figure 7.14).

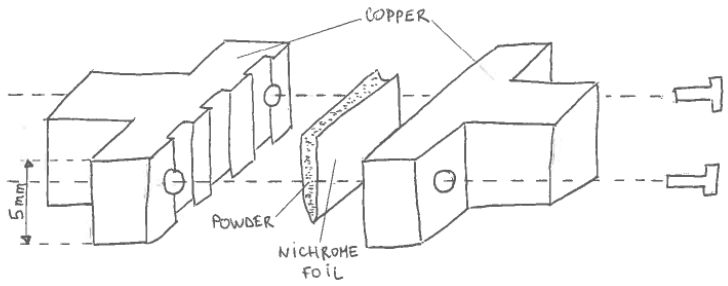

Figure 7.14: *Proposal for a new low-thermal source. It involves a* 25 µm *thin NiChrome envelope where the active powder sits. The dispenser is squeezed by two screws between two pieces of copper. The thermal conductance can be adjusted by digging stripes into the copper pieces as sketched on the left-hand-side diagram. This source should allow us to perform fast modulation with good reproducibility whilst requiring lower activation power than the commercial dispenser on copper.*

7.5 Conclusions and perspectives

In conclusion we have studied a large variety of sources for achieving rubidium pressure modulation on the sub-second timescale in a vacuum cell. The commercial dispenser on copper, the laser-heated dispenser and the laser-heated active powder are all suitable sources for this task. Our attempts towards a reduced-thermal mass dispenser were unsuccessful regarding the source speed. Besides the source speed, reproducibility is an important criteria of choice. Only the commercial dispenser on copper fulfills the latter criteria. Laser-based sources appeared to suffer from either a poor rubidium release or a fast depletion of the powder concentration in rubidium.

We have studied in detail the long-term behavior of the commercial dispenser on a copper heat sink and concluded that a limit to modulation is set by the atoms slowly desorbing from the cell walls and contributing to the background pressure. We have evidence to suggest that these atoms originate predominantly from the source. We have also shown that LIAD can help to further push the limit set by the atom desorption.

Atom adsorption on the walls explains why we are able to observe density decay times as short as 10 ms. If there was no adsorption the density decay time would be limited by the pumping speed created by the ion pump, giving pumping times of ~ 67 ms. This pumping time is, however, short enough to allow for a sub-second pressure modulation. This means that chemical treatment of the surfaces could be performed to reduce the rubidium atoms sticking time, with this one should be able to improve the modulation factor.

With the commercial dispenser on a copper heat sink we have demonstrated the loading of $> 2.5 \times 10^7$ atoms in the MOT within 1.2 s. Our MOT volume is, however, rather small and

the relevant parameter is the modulation factor in the steady-state, that reaches values of up to 16. This modulation factor decreases when the mean atom release per pulse is increased. This may be due to the release of gases other than ^{87}Rb by the source.

A new source was proposed that would combine speed, reproducibility and lower activation power. A smaller heat sink could be designed in order to reduce the time to thermal equilibrium.

Conclusion

In this thesis we have presented several experiments carried out with either degenerate or non-degenerate atoms trapped on a chip.

Degenerate gases As shown by our study, degenerate and non-degenerate clouds obey a dramatically different physics. The first key difference is the absence of exchange collisions in pure BECs. Exchange collisions combined to particle indistinguishability are the driving mechanism of the identical spin rotation effect, which leads to dephasing times on the order of a minute. With such incredibly long dephasing times an atomic clock with a stability below $10^{-13}/\sqrt{\tau}$ becomes realistic, surpassing the initially anticipated performances. Conversely, interactions dominate the BEC physics. As a result of the difference in scattering length between the two clock states, a state-dependent spatial dynamics occurs. This dynamics affects both the overlap and the relative phase of the two states' wavefunction, which translates into a modulation of the fringe contrast. We note that in the case of BECs it is not possible to discriminate between the role of the phase and the role of the wavefunction overlap in the interference term. The two effects drive each other. However, the accurate description of the Ramsey interferometer must be treated with the phase state formalism. In the case of BECs, as the evolution hamiltonian depends on the number of atoms in each state, a deformation of the collective spin state occurs. Strongly correlated systems, BECs create naturally spin-squeezed states. Such natural spin-squeezed states have not yet been observed. TACC is the ideal experiment for observing this effect given its metrological features. Another question is the possibility of directly observing the BEC phase diffusion. In particular one should be able to observe the phase collapse, predicted in [83]. It is a consequence of the collective spin state being so elongated that the information on the phase is completely lost. Our results on interfering BECs open exciting new perspectives.

Clock stability Non-degenerate gases can be interrogated for seconds. Thanks to this property we could perform Ramsey interrogations of 5 s and demonstrate a clock stability of $5.8 \times 10^{-13}/\sqrt{\tau}$, integrating down to 2×10^{-14}. Our study shows that the experiment is affected by shot-to-shot cloud temperature fluctuations. However, these cloud temperature fluctuations have a negligible contribution to the best measured clock frequency stability, as it was acquired at a field of minimum sensitivity to them. Magnetic noise appears not to be a limiting factor to the clock performance. Rather, we suspect the existence of a shot-to-shot, density-dependent noise on the clock states populations. This could arise from the phenomenon of asymmetric losses, or from another process of atomic decoherence that remains to be identified.

Atomic microwave powermeter As another application of these long dephasing times, we have demonstrated Rabi interrogations up to 6 s. We have characterized the response of the system over 80 dB of microwave power. The results deviate from the expected scaling at high powers which is attributed to the atomic device. With further investigation we could determine the reason for such a deviation, possible explanations include: a non-linear effect in the transmission guide, a consequence of atomic interactions or a subtle effect from the interrogating field inhomogeneity.

Sideband transitions The inhomogeneity of the interrogation field is a special feature of our experiment and can be exploited to control the atoms' external dynamics. This approach was already used for ions trapped on a chip, although it greatly differs from our system by the atom's confinement. This prevents us from performing, for example, sideband cooling. Nevertheless, we have demonstrated sideband transition with efficiency of up to 70 % and we have also demonstrated that the transitions are driven coherently. This technique opens new perspectives and may contribute to the demonstration of an on-chip atom interferometer.

Fast modulation We have concluded the manuscript with the investigation of fast alkali pressure modulation and its application to high-repetition rate atom loading. Our study started with the design of a fast atom source that enables one to modulate the rubidium pressure in a sub-second timescale. With such a source we have determined that the current limitation to the modulation amplitude is set by the slow desorption of atoms (stuck during the source emission) from the cell surfaces. Sticking is a fast process and partly explains the efficient pumping of the atoms. However, we estimate that the ion pump on its own would be sufficient to reach sub-second modulation. We have investigated numerous fast sources and concluded that the best compromise between long-term reproducibility and simplicity would be a reduced thermal mass dispenser, assisted by UV desorption pulses. Such a device remains to be designed and tested. A second research axis is the modifications of the cell surface sticking properties to further push the limit set by desorption.

Perspectives We conclude this manuscript with an overview of future tests and experiments that could be carried out on TACC. Firstly, as already stated, a more in-depth study of the non-linear evolution of the BEC collective spin should provide exciting fundamental results as well as, perhaps, a starting point for quantum metrology beyond the standard limit [85]. Non-degenerate gases can also be used for quantum metrology as entanglement has been demonstrated in coupled atom-cavity systems [118]. However, in our experiment, and in order to take full advantage of spin-squeezed states for metrology, one would first need to reduce the technical noise to below the standard quantum limit.

Appendix A

AC Zeeman shifts of the clock frequency

In this appendix we compute the AC Zeeman shift of the clock frequency induced by both the microwave and the radiofrequency photons. We use this calculation to provide a measurement of the radiofrequency polarization imbalance.

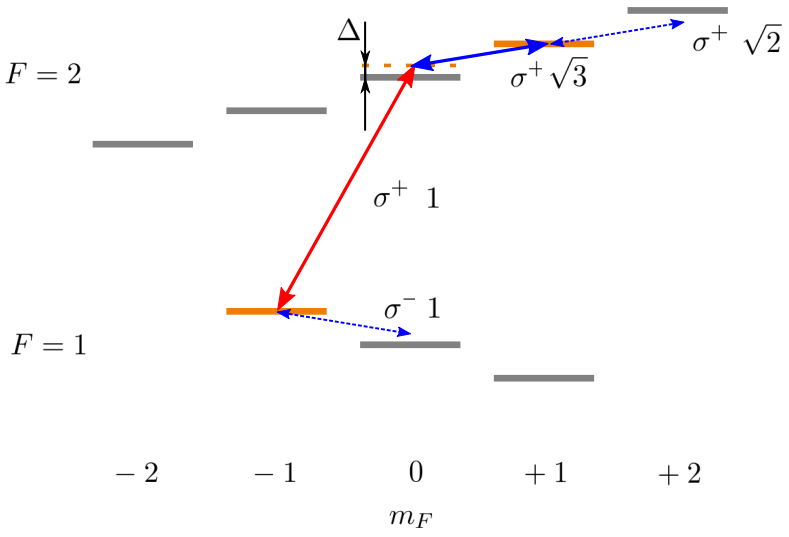

Figure A.1: *Energy diagram of ^{87}Rb hyperfine structure in the presence of a quantization magnetic field. The clock levels are displayed in orange. The full arrows sketch the two-photon transition. Dotted arrows indicate transitions that we also take into account to compute the AC Zeeman shift. We neglect contributions from other levels which are far detuned. For each transition we have indicated the relevant component of the field as well as the relevant component of the transition strength $\langle F', m'_F|\hat{\mathbf{J}}|F, m_F\rangle$ [26]. The detuning Δ is defined as the microwave field detuning from the $|F = 1, m_F = -1\rangle \rightarrow |F = 2, m_F = 0\rangle$ transition.*

Figure A.1 is a scheme of the levels involved in the AC Zeeman shift together with the relevant components of the magnetic field and of the transition strengths $\langle F', m'_F|\hat{\mathbf{J}}|F, m_F\rangle$.

The **microwave photon** only affects the $|1\rangle$ level and via its σ^+ component. The corresponding freuency shift of the level reads

$$\Delta E_{mw,|1\rangle} = \hbar\frac{\hbar\Omega_{mw}}{4\Delta_0}. \tag{A.1}$$

The **radiofrequency photon** affects both $|1\rangle$ and $|2\rangle = |F = 2, m_F = 1\rangle$ levels. Having defined the detuning Δ for the microwave photon, the detuning of the radiofrequency photon from the intermediate level is $-\Delta$. If we express the RF magnetic field $\vec{B}(t) = \sum_{\{q=-,0,+\}} B_q\vec{e}_q e^{i\omega t} + h.c.$ in the $\left\{\vec{e}_\pm = (\vec{e}_x + \vec{e}_y)/\sqrt{2}, \vec{e}_0 = \vec{e}_z\right\}$ basis [94] (here $\vec{e}_z$ is the direction of the quantization axis) we obtain the following expressions:

$$\Delta E_{rf,|1\rangle} = -\frac{\hbar}{4(-\Delta)}\left(\frac{2g_J\mu_B}{\hbar^2}B_-\right)^2. \tag{A.2}$$

and

$$\Delta E_{rf,|2\rangle} = -\frac{\hbar}{4(-\Delta)}\left(\frac{2g_J\mu_B}{\hbar^2}B_+\sqrt{3}\right)^2 + \frac{\hbar}{4(-\Delta)}\left(\frac{2g_J\mu_B}{\hbar^2}B_+\sqrt{2}\right)^2 \tag{A.3}$$

Measurement of the RF polarization imbalance Here we give a measurement of the RF polarization imbalance $\kappa = B_-/B_+$ as an application of the Ac Zeeman shift calculations. This measurement is only possible because the microwave photon affects the transition exclusively via its B_+ component. Ω_{RF} is defined by $2g_J\mu_B B_+\sqrt{3}/\hbar^2$. We can reformulate the net RF Ac Zeeman shift on the clock transition as:

$$\Delta E_{RF,|1\rangle\to|2\rangle} = \Delta E_{rf,|2\rangle} - \Delta E_{rf,|1\rangle} = \frac{\hbar\Omega_{RF}^2}{4\Delta}\frac{\left(1-\kappa^2\right)}{3}. \tag{A.4}$$

We define $\alpha = \left(1-\kappa^2\right)/3$. It turns out that the RF AC Zeeman shift is 0 for $\kappa = 1$. This corresponds to the field radiated by a single wire. Although only one wire is driven in the experiment we have evidence to suggest that inductive RF coupling in neighboring wires modifies the field. The chip reflective coating at 780 nm may also influence the field configuration and lead to $\kappa \neq 1$.

The total AC Zeeman shift on the clock transition reads $\Delta E_{tot,|1\rangle\to|2\rangle} = \frac{\hbar}{4\Delta}\left(-\Omega_{mw}^2 + \Omega_{rf}^2\alpha\right)$. If we call P_{mw} and P_{rf} the MW and RF input powers respectively, we can define the proportionality constants a and b by $\Omega_{mw} = a\sqrt{P_{mw}}$ and $\Omega_{rf} = b\sqrt{P_{rf}}$. The two-photon Rabi frequency takes the form

$$\Omega = \frac{ab\sqrt{P_{mw}P_{rf}}}{2\Delta}, \tag{A.5}$$

and the total AC Zeeman shift on the clock transition

$$\Delta E_{tot,|1\rangle\to|1\rangle} = \frac{\hbar}{4\Delta}\left(-a^2P_{mw} + b^2\alpha P_{rf}\right). \tag{A.6}$$

a^2 and $b^2\alpha$ can be measured by the AC Zeeman shift dependence on P_{mw} and P_{rf}. ab is given by the dependence of Ω on $\sqrt{P_{rf}P_{mw}}$ (figure A.2). Using this method we estimate the value of κ in two configurations:

- with the RF interrogation signal plugged into the "Sc−1" chip wire: $\kappa_1 = 1.45$. Here the AC Zeeman shift produced by the RF radiation on the clock transition is negative.

- with the RF interrogation signal plugged into the "Sc+1" chip wire: $\kappa_2 = 0.63$, with a positive AC Zeeman shift produced by the RF photon.

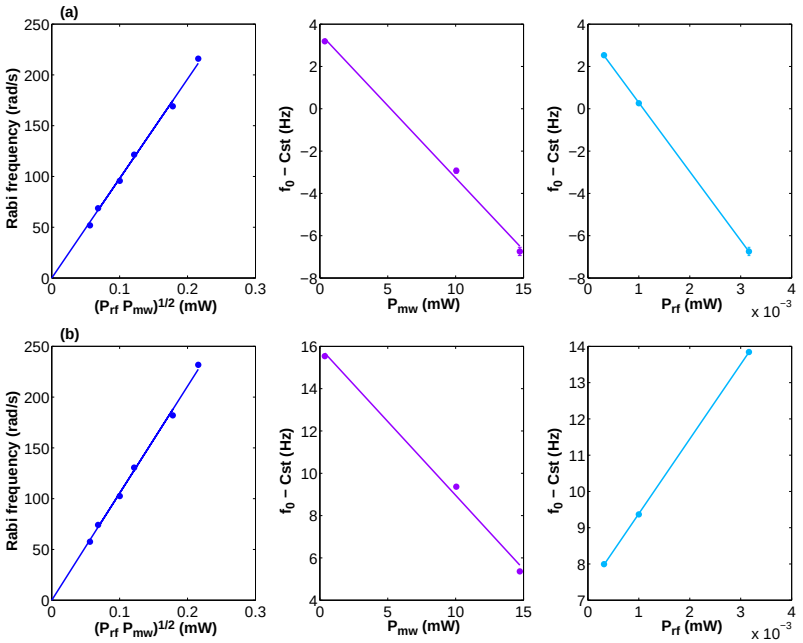

Figure A.2: *Data used for measurement of the RF polarization imbalance κ. The RF interrogation signal was plugged into the (a) "Sc−1" and (b) "Sc+1" chip wire. For each configuration we plot the Rabi frequency dependence on $\sqrt{P_{rf} P_{mw}}$ (blue) and the clock frequency AC Zeaamn shift dependence of P_{mw} (purple) and P_{rf} (cyan). A fit of the slopes gives κ.*

Appendix B

List of abbreviations and symbols

symbol	meaning
h	Planck constant
$\hbar$	Reduced Planck constant
μ_B	Bohr magneton
k_B	Boltzmann constant
m	Mass of a ^{87}Rb atom
BEC	Bose-Einstein condensate
MOT	Magneto-optical trap
RF	Radiofrequency
MW	Microwave
$TACC$	Trapped Atom Clock on a Chip
$ISRE$	Identical Spin Rotation Effect
ARP	Adiabatic Rapid Passage
AOM	Accousto-Optical Modulator

Bibliography

[1] J. Terrien. News from the international bureau of weights and measures. *Metrologia*, 4(1):41–45, 1968.

[2] Bureau international des poids et mesures. *The International System of Units SI 8e edition*, 2006.

[3] S. Bize, Y. Sortais, M. S. Santos, C. Mandache, A. Clairon, and C. Salomon. High-accuracy measurement of the 87 Rb ground-state hyperfine splitting in an atomic fountain. *Europhysics Letters*, 45(5):558, 1999.

[4] S Bize, P Laurent, M Abgrall, H Marion, I Maksimovic, L Cacciapuoti, J Grünert, C Vian, F Pereira dos Santos, P Rosenbusch, P Lemonde, G Santarelli, P Wolf, A Clairon, A Luiten, M Tobar, and C Salomon. Cold atom clocks and applications. *Journal of Physics B: Atomic, Molecular and Optical Physics*, 38(9):S449, 2005.

[5] A. D. Ludlow, T. Zelevinsky, G. K. Campbell, S. Blatt, M. M. Boyd, M. H. G. de Miranda, M. J. Martin, J. W. Thomsen, S. M. Foreman, Jun Ye, T. M. Fortier, J. E. Stalnaker, S. A. Diddams, Y. Le Coq, Z. W. Barber, N. Poli, N. D. Lemke, K. M. Beck, and C. W. Oates. Sr lattice clock at 1×10–16 fractional uncertainty by remote optical evaluation with a Ca clock. *Science*, 319(5871):1805–1808, 2008.

[6] C. W. Chou, D. B. Hume, J. C. J. Koelemeij, D. J. Wineland, and T. Rosenband. Frequency comparison of two high-accuracy Al^+ optical clocks. *Phys. Rev. Lett.*, 104:070802, Feb 2010.

[7] C. W. Chou, D. B. Hume, T. Rosenband, and D. J. Wineland. Optical clocks and relativity. *Science*, 329(5999):1630–1633, 2010.

[8] M.P. Heß, L. Stringhetti, B. Hummelsberger, K. Hausner, R. Stalford, R. Nasca, L. Cacciapuoti, R. Much, S.Feltham, T. Vudali, B.Leger, F. Picard, D. Massonnet, P. Rochat, D. Goujon, W. Schäfer, P. Laurent, P. Lemonde, A. Clairon, P. Wolf, C. Salomon, I. Prochazka, , U. Schreiber, and O. Montenbruck. The ACES mission: System development and test status. *Acta Astronautica*, 69:929–938, 2011.

[9] EMRP. Compact microwave clocks for industrial applications, Call 2012 – Open Excellence, Industry and SI Broader Scope, 2012. www.emrponline.eu.

[10] Jakob Reichel and Vladan Vuletic. *Atom Chips*. Wiley-VCH, 2011.

[11] C. Deutsch, F. Ramirez-Martinez, C. Lacroûte, F. Reinhard, T. Schneider, J. N. Fuchs, F. Piéchon, F. Laloë, J. Reichel, and P. Rosenbusch. Spin self-rephasing and very long coherence times in a trapped atomic ensemble. *Phys. Rev. Lett.*, 105(2):020401, Jul 2010.

[12] Jacques Vanier and Claude Audoin. *The quantum physics of atomic frequency standards.* Adam Hilger, 1989.

[13] http://www.beyonddiscovery.org.

[14] François-Xavier Esnault. *Etude des performances ultimes d'une horloge compacte à atomes froids: optimisation de la stabilité court terme.* PhD thesis, Université Paris VI, 2009.

[15] S Micalizio, C E Calosso, A Godone, and F Levi. Metrological characterization of the pulsed Rb clock with optical detection. *Metrologia*, 49:425–436, 2012.

[16] Jean-Marie Danet. Private communication.

[17] J.D. Prestage, S.K. Chung, R.J. Thompson, and P. MacNeal. Progress on small mercury ion clock for space applications. In *Proceedings of the Frequency Control Symposium, 2009 Joint with the 22nd European Frequency and Time forum. IEEE International*, pages 54 –57, april 2009.

[18] F.X. Esnault, N. Rossetto, D. Holleville, J. Delporte, and N. Dimarcq. Horace: A compact cold atom clock for Galileo. *Advances in Space Research*, 47:854–858, 2011.

[19] G. Kleine Büning, J. Will, W. Ertmer, E. Rasel, J. Arlt, C. Klempt, F. Ramirez-Martinez, F. Piéchon, and P. Rosenbusch. Extended coherence time on the clock transition of optically trapped rubidium. *Phys. Rev. Lett.*, 106:240801, Jun 2011.

[20] Savas Dimopoulos, Peter W. Graham, Jason M. Hogan, and Mark A. Kasevich. Testing general relativity with atom interferometry. *Phys. Rev. Lett.*, 98:111102, Mar 2007.

[21] L. Zhou, Z.Y. Xiong, W. Yang, B. Tang, W.C. Peng, K. Hao, R.B. Li, M. Liu, J. Wang, and M.S. Zhan. Development of an atom gravimeter and status of the 10-meter atom interferometer for precision gravity measurement. *General Relativity and Gravitation*, 43:1931–1942, 2011.

[22] H. Katori. Spectroscopy of strontium atoms in the Lamb-Dicke confinement. In *Proceedings od the 6th Symposium on Frequency Standards and Metrology*, pages 323–330. World Scientic, 2002.

[23] V. V. Flambaum, V. A. Dzuba, and A. Derevianko. Magic frequencies for cesium primary-frequency standard. *Phys. Rev. Lett.*, 101:220801, Nov 2008.

[24] Claude Cohen-Tannoudji. Ions piégés, refroidissement radiatif et applications. In *Cours au Collège de France*, 1985-1986.

[25] Daniel Adam Steck. *Rubidium 87 D Line Data Version 2.1.4*, 2010.

[26] Friedmann Reinhard. *Design and Construction of an Atomic Clock on an Atom Chip.* PhD thesis, Université Paris VI, 2009.

[27] J. Reichel, , W. Hänsel, P. Hommelhoff, and T.W. Hänsch. Applications of integrated magnetic microtraps. *Appl. Phys. B*, 72:81–89, 2001.

[28] M. Ö. Oktel and L. S. Levitov. Collective dynamics of internal states in a Bose-Einstein gas. *Phys. Rev. A*, 65:063604, May 2002.

[29] D. M. Harber, H. J. Lewandowski, J. M. McGuirk, and E. A. Cornell. Effect of cold collisions on spin coherence and resonance shifts in a magnetically trapped ultracold gas. *Phys. Rev. A*, 66(5):053616, Nov 2002.

[30] A. M. Rey, A. V. Gorshkov, and C. Rubbo. Many-body treatment of the collisional frequency shift in fermionic atoms. *Phys. Rev. Lett.*, 103:260402, Dec 2009.

[31] Kurt Gibble. Decoherence and collisional frequency shifts of trapped bosons and fermions. *Phys. Rev. Lett.*, 103:113202, Sep 2009.

[32] Christian Deutsch. *Trapped Atom Clock on a Chip. Identical Spin Rotation Effects in an Ultracold Trapped Atomic Clock.* PhD thesis, Université Paris VI, 2011.

[33] C. Lhuillier and F. Laloë. Transport properties in a spin polarized gas. *J. Phys. France*, 43:197–224, 1982.

[34] J.N. Fuchs, , D.M. Gangardt, and F. Laloë. Large amplitude spin waves in ultra-cold gases. *Eur. Phys. J. D*, 25:57–75, 2003.

[35] H. J. Lewandowski, D. M. Harber, D. L. Whitaker, and E. A. Cornell. Observation of anomalous spin-state segregation in a trapped ultracold vapor. *Phys. Rev. Lett.*, 88:070403, Jan 2002.

[36] J. M. McGuirk, H. J. Lewandowski, D. M. Harber, T. Nikuni, J. E. Williams, and E. A. Cornell. Spatial resolution of spin waves in an ultracold gas. *Phys. Rev. Lett.*, 89:090402, Aug 2002.

[37] M. Ö. Oktel and L. S. Levitov. Internal waves and synchronized precession in a cold vapor. *Phys. Rev. Lett.*, 88:230403, May 2002.

[38] J. N. Fuchs, D. M. Gangardt, and F. Laloë. Internal state conversion in ultracold gases. *Phys. Rev. Lett.*, 88:230404, May 2002.

[39] J. E. Williams, T. Nikuni, and Charles W. Clark. Longitudinal spin waves in a dilute bose gas. *Phys. Rev. Lett.*, 88:230405, May 2002.

[40] X. Du, L. Luo, B. Clancy, and J. E. Thomas. Observation of anomalous spin segregation in a trapped fermi gas. *Phys. Rev. Lett.*, 101:150401, Oct 2008.

[41] F. Piéchon, J. N. Fuchs, and F. Laloë. Cumulative identical spin rotation effects in collisionless trapped atomic gases. *Phys. Rev. Lett.*, 102:215301, May 2009.

[42] X. Du, Y. Zhang, J. Petricka, and J. E. Thomas. Controlling spin current in a trapped fermi gas. *Phys. Rev. Lett.*, 103:010401, Jul 2009.

[43] Wilfried Maineult, Christian Deutsch, Kurt Gibble, Jakob Reichel, and Peter Rosenbusch. Spin waves and collisional frequency shifts of a trapped-atom clock. *Phys. Rev. Lett.*, 109:020407, Jul 2012.

[44] Clément Lacroute. *Développement d'une horloge atomique sur puce à atomes: optimisation de la durée de cohérence et caractérisation préliminaire.* PhD thesis, Université Paris VI, 2010.

[45] *SAES Getters S.p.A., 20151 Milano, Italy.*

[46] F. Ramírez-Martínez, C. Lacroûte, P. Rosenbusch, F. Reinhard, C. Deutsch, T. Schneider, and J. Reichel. Compact frequency standard using atoms trapped on a chip. *Advances in Space Research*, 47:247 – 252, 2011.

[47] X. Baillard, A. Gauguet, S. Bize, P. Lemonde, Ph. Laurent, A. Clairon, and P. Rosenbusch. Interference-filter-stabilized external-cavity diode lasers. *Optics Communications*, 266:609–613, 2006.

[48] Claude Cohen-Tannoudji, Jacques Dupont-Roc, and Gilbert Grynberg. *Processus d'interaction entre photons et atomes*. Editions du CNRS, 1988.

[49] F. Pereira Dos Santos, H. Marion, M. Abgrall, S. Zhang, Y. Sortais, S. Bize, I. Maksimovic, D. Calonico, J. Grunert, C. Mandache, C. Vian, P. Rosenbuch, P. Lemonde, G. Santarelli, P. Laurent, A. Clairon, and C. Salomon. 87Rb and 133Cs laser cooled clocks: testing the stability of fundamental constants. In *Proceedings of the Frequency Control Symposium and PDA Exhibition Jointly with the 17th European Frequency and Time Forum, 2003. IEEE International*, pages 55 – 67, may 2003.

[50] R. P. Anderson, C. Ticknor, A. I. Sidorov, and B. V. Hall. Spatially inhomogeneous phase evolution of a two-component Bose-Einstein condensate. *Phys. Rev. A*, 80:023603, Aug 2009.

[51] Xi Chen, A. Ruschhaupt, S. Schmidt, S. Ibanez, and J. G. Muga. Shortcut to adiabaticity in harmonic traps. *J. At. Mol. Sci.*, 1:1–17, 2010.

[52] A. Couvert, T. Kawalec, G. Reinaudi, and D. Guéry-Odelin. Optimal transport of ultracold atoms in the non-adiabatic regime. *EPL (Europhysics Letters)*, 83(1):13001, 2008.

[53] Jean Dalibard. Collisional dynamics of ultra-cold atomic gases. In *Proceedings of the International School of Physics Enrico Fermi, Course CXL: Bose-Einstein condensation in gases*. Societa Italiana di Fisica, 1998.

[54] Philipp Treutlein, Peter Hommelhoff, Tilo Steinmetz, Theodor W. Hänsch, and Jakob Reichel. Coherence in microchip traps. *Phys. Rev. Lett.*, 92(20):203005, May 2004.

[55] P. Rosenbusch. Magnetically trapped atoms for compact atomic clocks. *Applied Physics B*, 95:227–235, 2009.

[56] Pierre Lemonde. *Pharao: étude d'une horloge spatiale utilisant des atomes refroidis par laser ; réalisation d'un prototype*. PhD thesis, Université Paris VI, 1997.

[57] W. M. Itano, J. C. Bergquist, J. J. Bollinger, J. M. Gilligan, D. J. Heinzen, F. L. Moore, M. G. Raizen, and D. J. Wineland. Quantum projection noise: Population fluctuations in two-level systems. *Phys. Rev. A*, 47:3554–3570, May 1993.

[58] C. F. Ockeloen, A. F. Tauschinsky, R. J. C. Spreeuw, and S. Whitlock. Detection of small atom numbers through image processing. *Phys. Rev. A*, 82(6):061606, Dec 2010.

[59] Sébastien Bize. *Tests fondamentaux à l'aide d'horloges à atomes froids de rubidium et de césium*. PhD thesis, Université Paris VI, 2001.

[60] Hong Qian. Exponential distribution and the process of radioactive decay. 2010. http://depts.washington.edu/amath/courses/423-winter-2010/note2.pdf.

[61] Christophe Texier. Random escape from a trap. Unpublished, 2012.

[62] G. Santarelli, C. Audoin, A. Makdissi, P. Laurent, G.J. Dick, and A. Clairon. Frequency stability degradation of an oscillator slaved to a periodically interrogated atomic resonator. *Ultrasonics, Ferroelectrics and Frequency Control, IEEE Transactions on*, 45(4):887 –894, july 1998.

[63] P. Lemonde, G. Santarelli, P. Laurent, F.P. Dos Santos, A. Clairon, and C. Salomon. The sensitivity function: a new tool for the evaluation of frequency shifts in atomic spectroscopy. In *Frequency Control Symposium, 1998. Proceedings of the 1998 IEEE International*, pages 110 –115, may 1998.

[64] T. van Zoest, N. Gaaloul, Y. Singh, H. Ahlers, W. Herr, S. T. Seidel, W. Ertmer, E. Rasel, M. Eckart, E. Kajari, S. Arnold, G. Nandi, W. P. Schleich, R. Walser, A. Vogel, K. Sengstock, K. Bongs, W. Lewoczko-Adamczyk, M. Schiemangk, T. Schuldt, A. Peters, T. Könemann, H. Müntinga, C. Lämmerzahl, H. Dittus, T. Steinmetz, T. W. Hänsch, and J. Reichel. Bose-Einstein condensation in microgravity. *Science*, 328(5985):1540–1543, 2010.

[65] J.-F. Schaff, X.-L. Song, P. Capuzzi, P. Vignolo, and G. Labeyrie. Shortcut to adiabaticity for an interacting Bose-Einstein condensate. *Europhysics Letters*, 93(2):23001, 2011.

[66] M. H. Anderson, J. R. Ensher, M. R. Matthews, C. E. Wieman, and E. A. Cornell. Observation of Bose-Einstein condensation in a dilute atomic vapor below 200 nanokelvins. *Science*, 269, 1995. JILA Pub. 5466.

[67] K. B. Davis, M. O. Mewes, M. R. Andrews, N. J. van Druten, D. S. Durfee, D. M. Kurn, and W. Ketterle. Bose-Einstein condensation in a gas of sodium atoms. *Phys. Rev. Lett.*, 75:3969–3973, Nov 1995.

[68] Yun Li. *Spin squeezing in Bose-Einstein condensates.* PhD thesis, Université Paris VI, 2010.

[69] C Ockeloen and P. Treutlein. To be published.

[70] F. Pereira Dos Santos, S. Bize, P. Lemonde, S. Reynaud, A. Clairon, M.-C. Angonin, A. Landragin, P. Wolf, A. Lambrecht, and B. Lamine. Measurement of short range forces using cold atoms. In Lute Maleki, editor, *Proceedings of the 7th Symposium for Frequency Standards and Metrology*, pages 44–52. World Scientific Publishing Co. Pte. Ltd., 2008.

[71] Franck Pereira Dos Santos. Private communication, 2012.

[72] M. Egorov, R. P. Anderson, V. Ivannikov, B. Opanchuk, P. Drummond, B. V. Hall, and A. I. Sidorov. Long-lived periodic revivals of coherence in an interacting Bose-Einstein condensate. *Phys. Rev. A*, 84:021605, Aug 2011.

[73] Lev. P. Pitaevskii and Sandro Stringari. *Bose-Einstein condensation.* Oxford University Press, USA, 2003.

[74] K. M. Mertes, J. W. Merrill, R. Carretero-González, D. J. Frantzeskakis, P. G. Kevrekidis, and D. S. Hall. Nonequilibrium dynamics and superfluid ring excitations in binary Bose-Einstein condensates. *Phys. Rev. Lett.*, 99:190402, Nov 2007.

[75] D. S. Hall, M. R. Matthews, J. R. Ensher, C. E. Wieman, and E. A. Cornell. Dynamics of component separation in a binary mixture of Bose-Einstein condensates. *Phys. Rev. Lett.*, 81:1539–1542, Aug 1998.

[76] P A Altin, G McDonald, D Döring, J E Debs, T H Barter, J D Close, N P Robins, S A Haine, T M Hanna, and R P Anderson. Optically trapped atom interferometry using the clock transition of large 87 Rb Bose–Einstein condensates. *New Journal of Physics*, 13(6):065020, 2011.

[77] P A Altin, G McDonald, D Döring, J E Debs, T H Barter, N P Robins, J D Close, S A Haine, T M Hanna, and R P Anderson. Optically trapped atom interferometry using the clock transition of large 87 Rb Bose–Einstein condensates. *New Journal of Physics*, 13(11):119401, 2011.

[78] Russel Anderson. *Nonequilibrium dynamics and relative phase evolution of two-component Bose-Einstein condensates*. PhD thesis, Swinburn University, Australia, 2010.

[79] L. Salasnich, A. Parola, and L. Reatto. Effective wave equations for the dynamics of cigar-shaped and disk-shaped Bose condensates. *Phys. Rev. A*, 65:043614, Apr 2002.

[80] Fabrice Gerbier. *Condensats de Bose-Einstein dans un piège anisotrope*. PhD thesis, Université Paris-Sud XI, 2003.

[81] S. Giorgini, L. P. Pitaevskii, and S. Stringari. Condensate fraction and critical temperature of a trapped interacting Bose gas. *Phys. Rev. A*, 54:R4633–R4636, Dec 1996.

[82] Y. Castin and R. Dum. Bose-Einstein condensates in time dependent traps. *Phys. Rev. Lett.*, 77:5315–5319, Dec 1996.

[83] A. Sinatra and Y. Castin. Binary mixtures of Bose-Einstein condensates: Phase dynamics and spatial dynamics. *The European Physical Journal D*, 8:319–332, 2000.

[84] Yun Li, P. Treutlein, J. Reichel, and A. Sinatra. Spin squeezing in a bimodal condensate: spatial dynamics and particle losses. *The European Physical Journal B*, 68:365–381, 2009.

[85] Max F. Riedel, Pascal Böhi, Yun Li, Theodor W. Hänsch, Alice Sinatra, and Philipp Treutlein. Atom-chip-based generation of entanglement for quantum metrology. *Nature*, 464:1170–1173, 2010.

[86] S. B. Papp, J. M. Pino, and C. E. Wieman. Tunable miscibility in a dual-species Bose-Einstein condensate. *Phys. Rev. Lett.*, 101:040402, Jul 2008.

[87] G. Thalhammer, G. Barontini, L. De Sarlo, J. Catani, F. Minardi, and M. Inguscio. Double species Bose-Einstein condensate with tunable interspecies interactions. *Phys. Rev. Lett.*, 100:210402, May 2008.

[88] Pascal Böhi, Max F. Riedel, Johannes Hoffrogge, Jakob Reichel, Theodor W. Hänsch, and Philipp Treutlein. Coherent manipulation of Bose-Einstein condensates with state-dependent microwave potentials on an atom chip. *Nature Physics*, 5:592–597, 2009.

[89] C. Ospelkaus, U. Warring, Y. Colombe, K. R. Brown, J. M. Amini, D. Leibfried, and D. J. Wineland. Microwave quantum logic gates for trapped ions. *Nature*, 476:191–194, 2011.

[90] A. Fantom. *Radio Frequency and Microwave Power Measurement*. Pergrinus, London, 1990.

[91] T. P. Crowley, E. A. Donley, and T. P. Heavner. Quantum-based microwave power measurements: Proof-of-concept experiment. *Review of Scientific Instruments*, 75(8):2575–2580, 2004.

[92] D.C. Paulusse, N.L. Rowell, and A. Michaud. Accuracy of an atomic microwave power standard. In *Proceedings of the Conference on Precision Electromagnetic Measurements Digest, 2004*, pages 410 –411, june 2004.

[93] J. C. Camparo. Atomic stabilization of electromagnetic field strength using rabi resonances. *Phys. Rev. Lett.*, 80:222–225, Jan 1998.

[94] Pascal Bohi, Max F. Riedel, Theodor W. Hansch, and Philipp Treutlein. Imaging of microwave fields using ultracold atoms. *Applied Physics Letters*, 97(5):051101, 2010.

[95] Pascal Bohi and Philipp Treutlein. Simple microwave field imaging technique using hot atomic vapor cells. *Applied Physics Letters*, 101(18):181107, 2012.

[96] J. Sedlacek, A. Schwettmann, H. Kübler, R. Löw, T. Pfau, and J.P. Shaffer. Quantum assisted electrometry using bright atomic resonances. *Nature Physics Advanced online Publication*, 2012.

[97] Christopher D. Wallace, Timothy P. Dinneen, Kit-Yan N. Tan, Timothy T. Grove, and Phillip L. Gould. Isotopic difference in trap loss collisions of laser cooled rubidium atoms. *Phys. Rev. Lett.*, 69:897–900, Aug 1992.

[98] C. Monroe, W. Swann, H. Robinson, and C. Wieman. Very cold trapped atoms in a vapor cell. *Phys. Rev. Lett.*, 65:1571–1574, Sep 1990.

[99] J. Fortagh, A. Grossmann, T. W. Hänsch, and C. Zimmermann. Fast loading of a magneto-optical trap from a pulsed thermal source. *J. Appl. Phys.*, 84:6499, 1998.

[100] Atsushi Hatakeyama, Markus Wilde, and Katsuyuki Fukutani. Classification of light-induced desorption of alkali atoms in glass cells used in atomic physics experiments. *e-Journal of Surface Science and Nanotechnology*, 4:63–68, 2006.

[101] S. N. Atutov, R. Calabrese, V. Guidi, B. Mai, A. G. Rudavets, E. Scansani, L. Tomassetti, V. Biancalana, A. Burchianti, C. Marinelli, E. Mariotti, L. Moi, and S. Veronesi. Fast and efficient loading of a Rb magneto-optical trap using light-induced atomic desorption. *Phys. Rev. A*, 67(5):053401, May 2003.

[102] B. P. Anderson and M. A. Kasevich. Loading a vapor-cell magneto-optic trap using light-induced atom desorption. *Phys. Rev. A*, 63(2):023404, Jan 2001.

[103] W. Hänsel, P. Hommelhoff, T. W. Hänsch, and J. Reichel. Bose–Einstein condensation on a microelectronic chip. *Nature*, 413:498–501, 2001.

[104] Kevin L. Moore, Thomas P. Purdy, Kater W. Murch, Sabrina Leslie, Subhadeep Gupta, and Dan M. Stamper-Kurn. Collimated, single-pass atom source from a pulsed alkali metal dispenser for laser-cooling experiments. *Rev. Sci. Instrum.*, 76:023106, 2005.

[105] Peter D. McDowall, Tzahi Grünzweig, Andrew Hilliard, and Mikkel F. Andersen. An atomic beam source for fast loading of a magneto-optical trap under high vacuum. *Rev. Sci. Instrum.*, 83:055102, 2012.

[106] Umakant D. Rapol, Ajay Wasan, and Vasant Natarajan. Loading of a Rb magneto-optic trap from a getter source. *Phys. Rev. A*, 64(2):023402, Jun 2001.

[107] S. Bartalini, I. Herrera, L. Consolino, L. Pappalardo, N. Marino, G. D'Arrigo, and F.S. Cataliotti. Full characterization of the loading of a magneto-optical trap from an alkali metal dispenser. *Eur. Phys. J. D*, 36:101–104, 2005.

[108] David R. Scherer, David B. Fenner, and Joel M. Hensley. Characterization of alkali metal dispensers and non-evaporable getter pumps in ultrahigh vacuum systems for cold atomic sensors. *J. Vac. Sci. Technol. A*, 30:061602, 2012.

[109] H. J. Lewandowski, D. L. Whitaker, and E. A. Cornell. Simplified system to create a Bose-Einstein condensate. *Journal of Low Temperature Physics*, 132:309, 2003.

[110] T. Arpornthip, C. A. Sackett, and K. J. Hughes. Vacuum-pressure measurement using a magneto-optical trap. *Phys. Rev. A*, 85:033420, Mar 2012.

[111] B. Grüner, M. Jag, A. Stibor, G. Visanescu, M. Häffner, D. Kern, A. Günther, and J. Fortágh. Integrated atom detector based on field ionization near carbon nanotubes. *Phys. Rev. A*, 80:063422, Dec 2009.

[112] B. DeMarco, H. Rohner, and D. S. Jin. An enriched 40K source for fermionic atom studies. *Rev. Sci. Instrum.*, 70:1967, 1999.

[113] C Stehle, H Bender, F Jessen, C Zimmermann, and S Slama. Ad- and desorption of Rb atoms on a gold nanofilm measured by surface plasmon polaritons. *New Journal of Physics*, 12(8):083066, 2010.

[114] J. Ma, A. Kishinevski, Y.-Y. Jau, C. Reuter, and W. Happer. Modification of glass cell walls by rubidium vapor. *Phys. Rev. A*, 79:042905, Apr 2009.

[115] P. F. Griffin, K. J. Weatherill, and C. S. Adams. Fast switching of alkali atom dispensers using laser-induced heating. *Rev. Sci. Instrum.*, 76:093102, 2005.

[116] C. Klempt, T. van Zoest, T. Henninger, O. Topic, E. Rasel, W. Ertmer, and J. Arlt. Ultraviolet light-induced atom desorption for large rubidium and potassium magneto-optical traps. *Phys. Rev. A*, 73(1):013410, Jan 2006.

[117] Emmanuel Mimoun, Luigi De Sarlo, David Jacob, Jean Dalibard, and Fabrice Gerbier. Fast production of ultracold sodium gases using light-induced desorption and optical trapping. *Phys. Rev. A*, 81(2):023631, Feb 2010.

[118] Monika H. Schleier-Smith, Ian D. Leroux, and Vladan Vuletić. States of an ensemble of two-level atoms with reduced quantum uncertainty. *Phys. Rev. Lett.*, 104:073604, Feb 2010.

Resumé Le piégeage d'atomes sur puce ouvre de nouvelles possibilités pour la métrologie temps-fréquence et l'interférométrie atomique intégrée. L'expérience TACC (Trapped Atomic Clock on a Chip) a pour but d'étudier le potentiel des gaz quantiques, dégénérés ou non, pour la métrologie, et d'élaborer de nouveaux outils pour la manipulation des atomes. Elle vise notamment la réalisation d'un étalon secondaire de fréquence avec une stabilité de quelques 10-13 à une seconde. Cette thèse s'inscrit dans ce contexte. Nous y présentons les résultats de quelques expériences de métrologie réalisées avec des nuages thermiques ou des condensats de Bose-Einstein. Dans un premier temps nous démontrons une stabilité de 5.8 x 10-13 à une seconde et caractérisons les bruits techniques limitant cette stabilité. Nous présentons ensuite une étude de la cohérence des condensats et en particulier l'effet des interactions. Les données sont comparées à un modèle numérique. Dans un deuxième temps nous présentons quelques outils développés pour la production et la manipulation d'atomes sur puce. Nous démontrons d'abord la réalisation d'un puissancemètre atomique pour la micro-onde et estimons les limites actuelles de ses performances. Nous démontrons ensuite que des champs micro-onde ayant des gradients élevés permettent la manipulation cohérente de l'état externe des atomes. Enfin nous présentons et caractérisons un nouveau dispositif pour la production de nuages d'atomes froids à haute cadence consistant en la modulation rapide de la pression de rubidium dans une cellule.

Mots-Clé Horloge atomique compacte - Gaz quantiques - Condensation de Bose-Einstein - Puce à atomes - Métrologie - Puissancemètre - Modulation rapide de la pression.

Abstract Atom trapping on chip opens new perspectives for time and frequency metrology and integrated atom interferometry. The TACC experiment (Trapped Atomic Clock on a Chip) was built to study the potential of degenerate and non-degenerate quantum gases for metrology and to develop new tools for atom manipulation. One of the aims is the demonstration of a secondary frequency standard with a stability of a few 10-13 at one second. This is the context of this thesis. We report on several metrology experiments carried out with thermal clouds or Bose-Einstein condensates. Firstly, we demonstrate a stability of 5.8 x 10-13 at one second and characterize the limiting technical noise. We then present a study of the coherence of Bose-Einstein condensates and, in particular, the effect of interactions. The data is compared with a numerical model. Secondly, we introduce several tools for producing and manipulating atoms on a chip. We show the realization of an atomic microwave powermeter and assess the current limits of its performance. We then demonstrate that high-gradient microwave fields allow one to coherently manipulate the atoms' external motion. Finally, we present and characterize a new device for high-repetition rate atom loading involving fast modulation of the rubidium pressure.